Bio-inspired Polymer-Supported Nitrido Molybdenum(VI) Complexes for Ammonia Synthesis − Reactivity towards protons and electrons

EPR investigations on paramagnetic molybdenum(V) and copper(II) complexes

Dissertation
zur Erlangung des Grades
„Doktor der Naturwissenschaften"
im Promotionsfach Chemie

am Fachbereich Chemie, Pharmazie und Geowissenschaften
der Johannes Gutenberg-Universität Mainz

vorgelegt von
Anica Wünsche von Leupoldt
geboren in Bad Dürkheim

Mainz, 2014

Die vorliegende Arbeit wurde unter Betreuung von ██████████████ in der Zeit von November 2009 bis August 2014 am Institut für Anorganische Chemie und Analytische Chemie der Johannes Gutenberg-Universität Mainz angefertigt.

Mainz, August 2014

Dekan: ████████████████

1. Berichterstatter: ████████████████

2. Berichterstatter: ████████████████

Tag der mündlichen Prüfung: 18. September 2014

D77

Short abstract

The mechanism of biological nitrogen fixation by Mo-dependent nitrogenases is of considerable interest. Dinitrogen activation at metal centers, which involves sixfold protonation and reduction as well as N–N cleavage to finally produce ammonia via a wealth of intermediates, presents a very complex reaction. Molybdenum complexes in particular have been very successful models for single N_2 activation steps and even catalytic cycles with molybdenum have been devised by Schrock *et al*. with triamidoamine ligands. Despite the use of bulky substituents, the turnover of this homogeneous catalyst is limited due to its deactivation by intermolecular reactions, such as dimerization and disproportionation. This work aims to tackle some of these challenges by immobilization of the active species onto a solid support to reduce intermolecular reactions by site isolation.

The synthesis of a polymer-immobilized analogue of the Schrock nitrido molybdenum(VI) complex is presented using a new pathway consisting of only a single step to introduce the "MoN" functional group. Protonation of the immobilized nitrido molybdenum(VI) complex $LMo^{VI}N$, with L = polymer-supported triamidoamine ligand, by 2,6-lutidinium yields the respective imido molybdenum(VI) complex. Subsequent one-electron reduction by cobaltocene gives the polymer-supported imido molybdenum(V) complex $LMo^{V}NH$ as proven by EPR spectroscopy ($g_{1,2,3}$ = 1.989, 1.929, 1.902). Due to the immobilization and the effective separation of the reaction centers onto the solid support, bimolecular side reactions which often occur in homogeneous systems are suppressed. This enables the preparation of the imido molybdenum(V) intermediate of the Schrock cycle for the first time.

EPR spectra of immobilized nitrato copper(II) complexes, introduced as spin label, were recorded under different conditions (solvent, temperature) revealing a strong dependence of the accessibility and the reactivity of the immobilized reaction centers on the type of solvent. Thus the reactivity of $LMo^{VI}N$ towards protons and electrons leading to NH_3 formation was investigated and optimized using different types of solvent. Protonation and reduction of $LMo^{VI}N$ proceeds section by section within the polymer bead. Active sites located at the "outer shell" of the polymer are well accessible and react rapidly upon H^+/e^- addition, whereas active sites located at the "inner volume" of the polymer are less accessible undergoing slow diffusion-controlled reactions. Three H^+/e^- steps followed by one ligand exchange reaction are required to release NH_3 from these "inner shells", corresponding to the reaction steps: $LMo^{VI}N \rightarrow LMo^{V}NH \rightarrow LMo^{IV}NH_2 \rightarrow LMo^{III}NH_3$ with subsequent ligand exchange to release NH_3.

In a second project, a bis(ddpd) copper(II) complex was studied by EPR spectroscopy with regards to Jahn−Teller distortion and Jahn−Teller dynamics. EPR spectra were recorded at variable temperatures ranging from 70−293 K. In the solid state at T < 100 K the copper(II) complexes appear as Jahn–Teller elongated polyhedral, while at higher temperatures EPR spectra show g-values corresponding to pseudo-compressed octahedral copper(II) species. This fact is ascribed to an intramolecular dynamical Jahn−Teller phenomenon, which is frozen at 100 K.

Mein Dank gilt

██████████████

für die wissenschaftliche Betreuung und die stete Diskussionsbereitschaft, sowie für die gewährten Freiheiten bei der Bearbeitung dieses Forschungsthemas.

Meiner Familie

„DREI DINGE MACHEN EINEN GUTEN MEISTER:

WISSEN, KÖNNEN UND WOLLEN."

-- deutsches Sprichwort

CONTENTS

Abbreviations

δ	chemical shift
λ	wavelength in UV/Vis spectroscopy, spin orbit coupling constant in EPR spectroscopy
μ_B	Bohr magneton = 9.2740×10^{-24} J/T
$\tilde{\nu}$	wavenumber
A	hyperfine coupling constant in EPR spectroscopy
ADP	adenosine diphosphate
Ar	aryl
$[^{Ar}N_3N]H_3$	2,2′,2″-tris(arylamino)triethylamine
ATP	adenosine triphosphate
B	magnetic field
rac-BINAP	racemic 2,2′-bis(diphenylphosphanyl)-1,1′-binaphthyl
^tBu	*tert*-butyl
°C	degree Celsius
calcd.	calculated
cat.	catalyst
CEPT	coupled electron proton transfer
Cp	cyclopentadienyl (η^5-C_5H_5)
Cp*	pentamethylcyclopentadienyl (η^5-C_5Me_5)
CV	cyclic voltammetry
CW	continuous wave
Cys	cysteine
d	day
dba	dibenzylideneacetone
DCM	dichloromethane
ddpd	*N,N′*-dimethyl-*N,N′*-dipyridin-2-yl-pyridin-2,6-diamine
diphos	diphosphane
DMF	dimethylformamide
dpph	2,2-diphenyl-1-picrylhydrazyl
eq.	equivalent

EPR	electron paramagnetic resonance
Et	ethyl
Fca	1-aminoferrocene-1′-carboxylic acid
Fd_{red}	ferredoxin
G	Gauss
$g_\parallel$	g-value parallel to the magnetic field
$g_\perp$	g-value orthogonal to the magnetic field
Δg	g-anisotropy
Ghosez' reagent	1-chloro-N,N,2-trimethyl-1-propenylamine
h	hour
ΔH_b	bond-dissociation energy
HIPT	hexaisopropylterphenyl (= 3,5-(2,4,6-^{i}Pr$_3$C$_6$H$_2$)$_2$C$_6$H$_3$)
His	histidine
HOMO	highest occupied molecular orbital
Hypogel 400 PHB	Hypogel resin (polystyrene/divinylbenzene grafted with PEG chains, 10 units) with a *para*-hydroxybenzyl alcohol (PHB) linker
I	nuclear spin
ICP-MS	inductively coupled plasma mass spectrometry
IR	infrared
J	coupling constant in NMR spectroscopy
K	Kelvin
L	ligand
LUMO	lowest unoccupied molecular orbital
[2,6-LutH][BAr$^F_4$]	[2,6-lutidinium][B(3,5-{CF$_3$}$_2$C$_6$H$_3$)$_4$]
[2,6-LutH][Al(OR^F)$_4$]	[2,6-lutidinium][Al(OC{CF$_3$}$_3$)$_4$]
M	molar (mol L^{-1})
M	metal
Me	methyl
min	minute
mT	Millitesla (= 10 Gauss)
(N′N)H	polystyrene-Si(^{i}Pr)$_2$-O-[4-({1H-pyrrole-2-ylmethylene}-amino)-phenyl]
CN-(N∩N′)	4-(isocyanophenyl)pyridine-2-ylmethylene amine

IV

NMR	nuclear magnetic resonance
OAT	oxygen atom transfer
P_1-^{t}Bu	*tert*-Butylimino-tris(dimethylamino)phophorane
Ph	phenyl
P_i	inorganic phosphate, PO_4^{3-}
PS	polystyrene
^{i}Pr	isopropyl
R	alkyl
r.t.	room temperature
S	electron spin
SOMO	singly occupied molecular orbital
SPPS	solid phase peptide synthesis
T	temperature
THF	tetrahydrofuran
TON	turn over number
tpy	2,2′;6′,2′′-terpyridine
UV/Vis	ultraviolet-visible
V	volt
X-band	frequency range in EPR measurements ($\nu \sim 9.5$ GHz)
xyl	3,5-dimethylphenyl

1. INTRODUCTION

With an amount of 78% molecular dinitrogen is the most common component of the Earth's atmosphere.[1] Therefore, air represents on the one hand the main nitrogen source and on the other hand the start and the end point of the nitrogen cycle. Molecular dinitrogen is an unreactive molecule because the highest occupied molecular orbital (= HOMO) is low in energy and the LUMO (= lowest unoccupied molecular orbital) has a high energy level, and the triple bond is with ΔH_b = 945 kJ mol^{-1} very stable. Thus molecular dinitrogen is often used as an efficient inert gas in air- or water-sensitive chemical reactions.

As molecular dinitrogen is not directly involved in human metabolism, it has to be converted into bioavailable products, namely ammonium and nitrate salts, to enable the synthesis of nitrogen-containing biomolecules essential for human life. This transformation of molecular dinitrogen into bioavailable ammonia realized by specific bacteria is called the biological nitrogen fixation. With the production of approximately 240 Mt ammonia per year[2] it significantly contributes to the world's ammonia production, and is therefore still more important than the industrial procedure performed by the Haber-Bosch process (136 Mt worldwide in 2011)[3].

Besides the importance as the essential nitrogen source for life on earth, the produced ammonium and nitrate salts are also used in the pharmaceutical industry as well as in plastic materials, colors or cooling liquids. But the most important application of ammonium salts is found with 80% in the manufacture of agricultural fertilizers. One kilogram fertilizer produces a surplus of 12 kilograms cereals or other comparable crops. Due to the increase of human population by a range of 80 million per year, the crop yield must be maximized on the existing agricultural land. Therefore, the production of fertilizers will further increase in the future.[4]

As the mechanism of biological nitrogen fixation at room temperature and under normal pressure is not yet fully elucidated, scientists are trying to model the elementary reaction steps and the whole catalytic cycle to answer fundamental questions. Additionally, as the industrial process is relatively expensive and energy consuming, alternative routes to synthesize ammonia or other nitrogen-containing products under energy saving and environmentally friendly conditions are searched.

1.1 Nitrogen cycle

Nitrogen passes through a complex cycle like all biologically relevant elements of the earth. The important steps of this cycle are illustrated in Figure 1. In the first step, the so called biological nitrogen fixation, atmospheric molecular dinitrogen is transformed into a bioavailable product. Specific bacteria, so called diazotrophic organisms, perform this reaction by assimilation and fixation of dinitrogen, and its reduction to ammonia. The subsequent nitrification characterizes the oxidation of ammonia($-$III) to nitrite($+$III) and nitrate($+$V). These products can be assimilated by plants and consequently enter the nitrogen cycle of animals and human beings, which are now capable of producing all nitrogen-containing biomolecules that are essential for life such as amino acids (proteins), nucleic acids (DNA) and porphyrin systems (hemoglobin, chlorophyll). The denitrification describes the reaction of nitrite to molecular dinitrogen and N_2O, and thus closing the nitrogen cycle.[5]
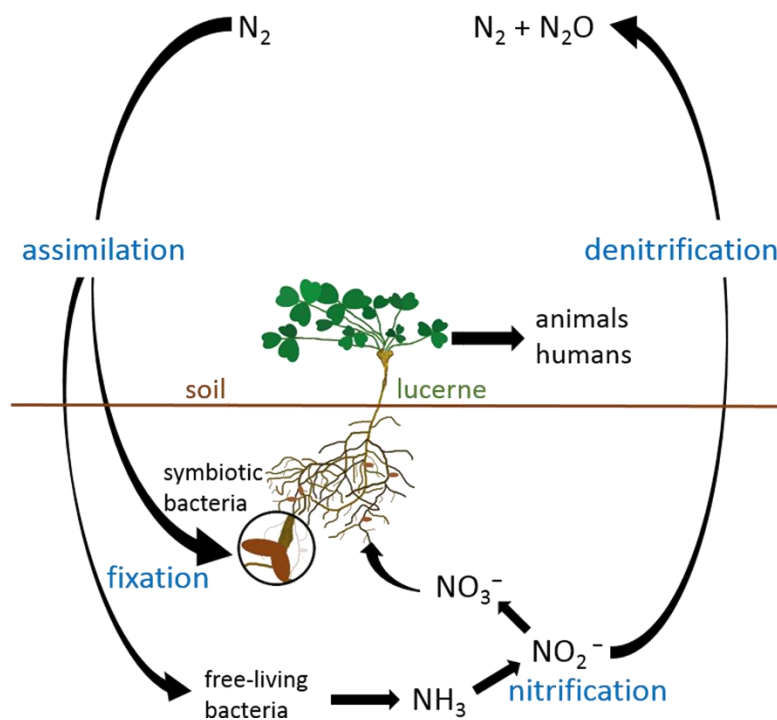

Figure 1. The Nitrogen cycle.[5]

1.2 Haber-Bosch process $-$ heterogeneous catalysis for NH_3 production

The industrial synthesis of ammonia is based on the heterogeneously catalyzed reaction between molecular dinitrogen and dihydrogen, according to the following reaction equation, and is one of the most important industrial and technological inventions of the 20th century.[6]

Reaction equation: $\qquad N_{2\,(g)} + 3H_{2\,(g)} \xrightarrow{\text{cat.}} 2NH_{3\,(g)}$
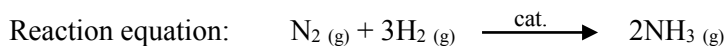
This first industrial heterogeneous catalytic system was invented by Fritz Haber on a laboratory scale in 1909, and was industrially realized by Carl Bosch at the Badische Anilin- und Soda-Fabrik (BASF) in Ludwigshafen in 1913. This iron based catalytic process is operated at high temperatures (up to 550°C) and pressures (up to 300 atm). For its invention, "the synthesis of ammonia from its elements", Haber received the Nobel Prize in Chemistry in 1918, and Bosch (together with Friedrich Bergius) "in recognition of their contributions to the invention and development of chemical high pressure methods" in 1931.[7a,7b]

With the help of Ertl's crystalline iron catalytic model surface the mechanism of heterogeneous ammonia synthesis can be understood.[8] For "his studies of chemical processes on solid surfaces" the Nobel Prize in Chemistry was awarded to Gerhard Ertl in 2007.[9] It is postulated that the reaction follows a three-step process:

(1) dissociative chemisorption of N_2 and H_2 to form N and H atoms on the iron catalyst surface, more precisely, homolytic dissociation of adsorbed N_2 and H_2 to form metal-nitrido and metal-hydride surface species;

(2) recombination of dissociated N and H to form NH followed by formation of NH_2 and NH_3 on the catalyst surface obtained by recombination with surface-bound hydrides;

(3) desorption of ammonia.

This model shows that the dissociation of adsorbed N_2 is the rate-limiting step of this reaction with an activation energy of approximately 42 kJ mol^{-1} of N_2. In this step, metal-nitrido complexes are formed consisting of triply bridging nitride atoms across surface iron atoms [$Fe_3(\mu_3-N)$]. Although the participation of electropositive alkali metals (potassium) can give a large promotional effect on that step and lower the activation barrier, high temperatures are needed to achieve an acceptable conversion rate. As ammonia synthesis proceeds under volume decrease, ammonia production is additionally favored by operating the system at high pressures (Le Chatelier's principle).

Although this industrial process consumes a lot of energy and is also responsible for the increase of the global greenhouse gas emission, it is important to point out that it achieves efficiencies of up to 70%. Surprisingly, the methane reforming process, which ensures the continuous dihydrogen production, causes ineffectiveness, whereas ammonia synthesis itself is very economical.[10] With the help of the Haber-Bosch process 136 Mt ammonia are produced per year which are mainly used for the production of artificial fertilizers. It is estimated that approximately 40% of nitrogen present in the human organism originates from ammonia synthesized by the Haber-Bosch process. Considering this fact emphasizes the great importance of this industrial process for humanity.

1.3 Nitrogenase − biological nitrogen fixation and catalytic conversion to ammonia

Biological nitrogen fixation is performed by diazotrophic organisms which are divided into two types. There are free-living diazotrophs like *Azotobacter* and the photosynthetic bacteria *Rhodopseudomonas*, and symbiotic diazotrophs like *Rhizobia* which are located at the roots of plants of the Fabaceae family (legumes, peas, beans) as shown in Figure 2.[11] The latter deliver the converted nitrogen in form of ammonium salts to the plant which itself supplies the bacteria with essential carbohydrates. This natural fertilization is well known to improve the agricultural productivity. Since 2000 years, the water fern, which forms a symbiotic relationship with cyanobacteria, is used as green manure for the cultivation of rice in China.[12]
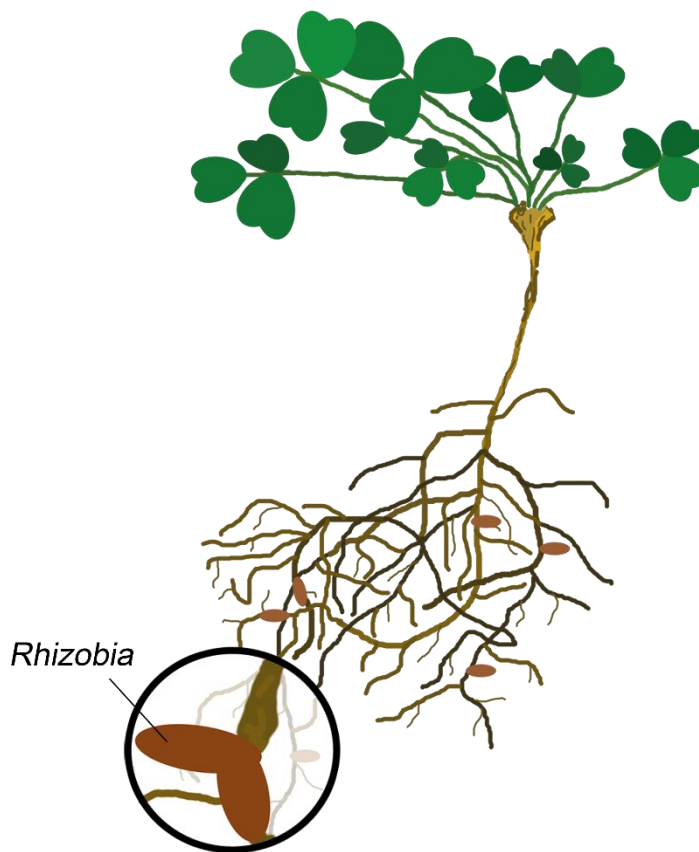

Figure 2. Schematic picture of lucerne (plant of Fabaceae family) with *Rhizobia* located at the roots.

Biological nitrogen fixation is catalyzed by the enzyme nitrogenase present in diazotrophic organisms. In this reaction atmospheric dinitrogen is reduced to bioavailable ammonia, the essential nitrogen source for plants, animals and human beings to realize the biosynthesis of nitrogen-containing biomolecules. The biological nitrogen fixation is essential for life as it supports more than one half of the human population.[13−17] Therefore, the global balance of nitrogen on Earth's biosphere relies on the capacity of diazotrophic organisms to serve the primary input of bioavailable nitrogen into the ecosystems.

The first reasonable X-ray structure of the enzyme nitrogenase, with a resolution of 2.70 Å, was obtained in 1992 (Figure 3).[18] This so called "Kim-model" showed a detailed structure of the enzyme and revealed the biggest and most complicated metal cluster present in natural enzymes so far, the FeMo-cofactor. Beside this molybdenum dependent nitrogenase carrying the FeMo-cofactor, a vanadium dependent nitrogenase with FeV-cofactor as well as an iron-only nitrogenase having a FeFe-cofactor are also present in nature but show lower efficiencies.
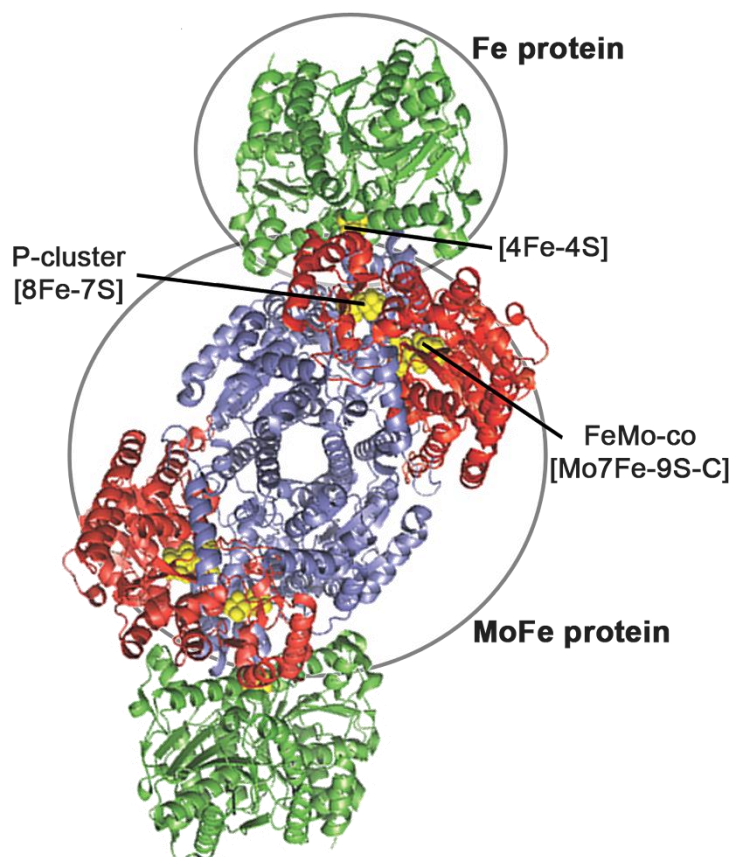

Figure 3. Structure of nitrogenase, Fe protein (green, top and bottom), MoFe protein (red and blue, middle), iron-sulfur clusters (yellow).[19]

This discovery was really impressive. Although molybdenum shows a low abundance in the Earth's crust, it represents the only transition metal of the 4d row which is essential for life. In contrast to for example iron which is only poorly available in oxidic soils due to the precipitation of iron oxides and hydroxides, molybdenum exhibits a high bioavailability attributed to the fact that oxoanionic molybdates ($Mo^{VI}O_4^{2-}$) are soluble in water. Molybdenum is present at ca. 110 nM in marine environments and is therefore the most abundant transition metal in the sea. In terrestrial environments, molybdenum concentration is estimated to a value of 50 nM.[20] Besides the presence in the molybdenum dependent nitrogenase, biologically active molybdenum is also found in other molybdoenzymes which are based on a unique tricyclic pterin, the so called molybdopterin, and catalyze oxidation reactions, for

example in the molybdenum-dependent carbon monoxide dehydrogenase (CODH) and in the sulfite oxidase.[20]

The enzyme nitrogenase consists of two structurally different and task-specific components, the Fe protein and the MoFe protein, schematically illustrated in Figure 4.
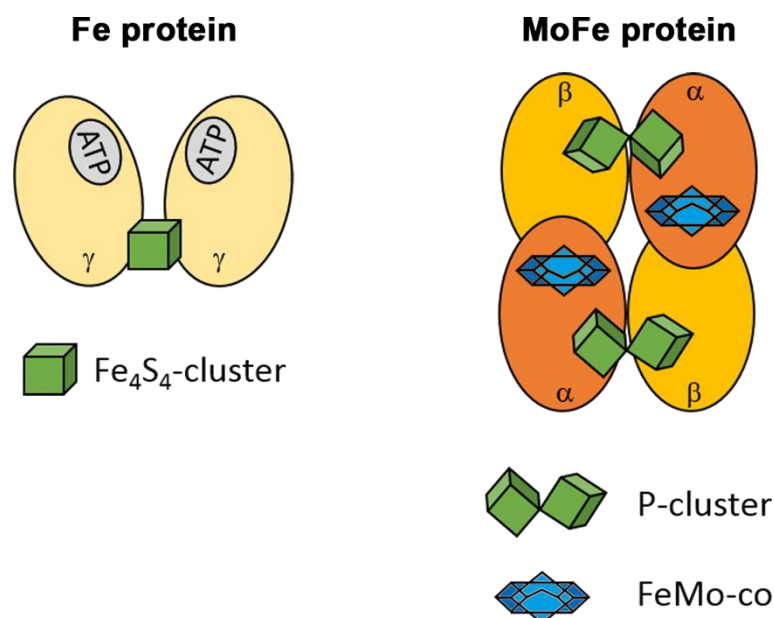

Figure 4. Schematic diagram of the **Fe protein** (left) and the **MoFe protein** (right).[12]

The **Fe protein** is called the reductase. It contains one binding region for the biochemical energy storage substance adenosine triphosphate (ATP) on each γ-unit and one iron-sulfur cluster of the type [4Fe-4S] connecting the two γ-units and working as electron transmitter. In brief, the Fe protein works as a specific ATP-dependent electron transporter.

The second component is the **MoFe protein** which comprises the actual reaction locus. It is composed of an $\alpha_2\beta_2$-tetramer, with an electron transporting P-cluster connecting the α- and β-unit, and the N_2 binding and reducing active site, the cofactor FeMo-co, localized in the α-unit. The P-cluster, a Fe_8S_7-cluster, has the shape of two Fe_4S_4 cubes sharing one sulfur atom. The FeMo-cofactor is a complex molybdenum-iron-sulfur metallocluster with the formula $MoFe_7S_9C$ (Figure 5). It consists of an inorganic Fe_6S_9 core that coordinates a central carbido ligand, as recently discovered by Einsle[21a] and by Ribbe and Neese[21b,21c], and is capped by Fe^{II} on one side and by Mo^{IV}-homocitrate on the other. Formally, it can also be seen as a Fe_4S_3-cluster and a $MoFe_3S_3$ cuban fragment bridged by three sulfido ligands and carrying a carbido ligand in the center. This metal cluster is attached to the protein via one cysteinato ligand coordinated to the Fe cap, and via one histidine coordinated to molybdenum.[22]
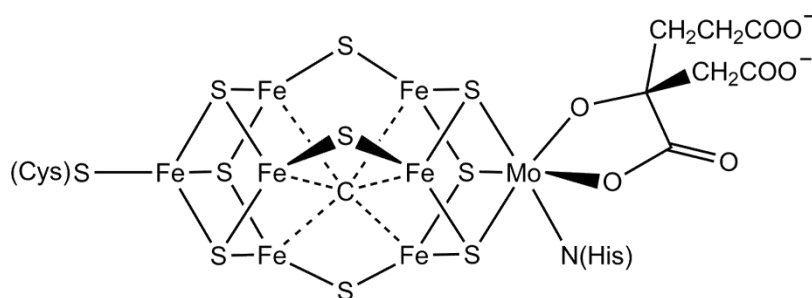
Figure 5. Molecular structure of FeMo-co.[23]

As the components of this enzyme are now known, the currently proposed reaction pathways proceeding inside the protein are described in detail in the following (view Figure 6). For the reduction of N_2 to ammonia, the protein needs electrons and protons, and of course energy. The electrons needed for the reduction of dinitrogen originate from the citrate cycle, and are transferred stepwise from reduced ferredoxin (Fd_{red}) to the Fe protein. Coordination of ATP to the Fe protein and subsequent hydrolysis to ADP + P_i effects a structural change of the γ-units resulting in the lowering of the reduction potential of the Fe_4S_4-cluster from -300 mV to -420 mV providing the energy of the reaction. This enables the electron transport to the P-cluster of the MoFe protein and subsequently to the FeMo-cofactor where the actual reduction of dinitrogen to ammonia takes place.[24]
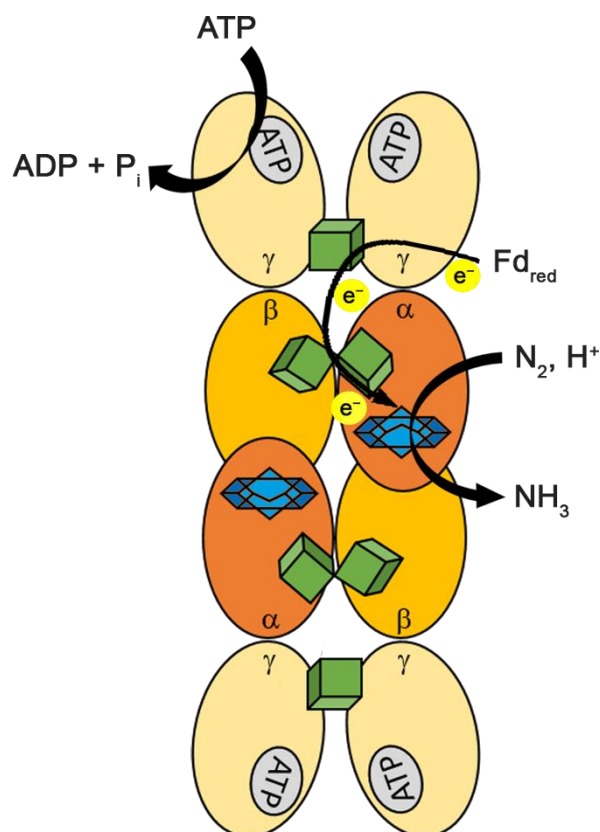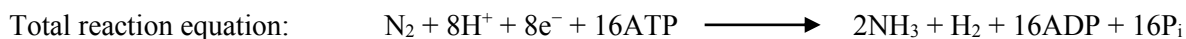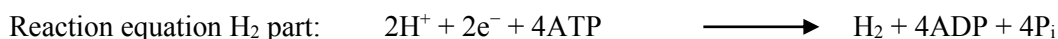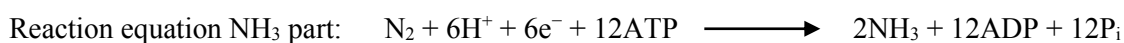

Figure 6. Schematic diagram of reaction pathways in nitrogenase.

The structure of nitrogenase obtained by X-ray single crystal analysis showed the FeMo-co in an inactive state. Up until now, the initial dinitrogen binding site as well as the catalytic mechanism is unknown. First, it was suggested that molybdenum is likely to be the locus for substrate binding and catalysis because the Mo-nitrogenase is more efficient than V- or Fe-nitrogenases. As molybdenum tolerates different oxidation states (typically from 0 to +VI), it should have the ability to stabilize several reaction intermediates. Molybdenum model complexes corroborated this hypothesis showing reasonable properties in binding of dinitrogen and performing ammonia synthesis, even catalytically.[25] On the contrary, recent studies indicate that the Fe_7S_9C core is the initial dinitrogen binding site and molybdenum functions as an electron buffer.[26−28]

In addition to the question concerning the dinitrogen binding site and the catalytic mechanism, the obligatory generation of one equivalent H_2 upon N_2 binding is one of the most puzzling aspects in nitrogenase catalysis. Besides the main reaction to ammonia, that consumes 6 electrons, 6 protons and 12 ATP, two reducing equivalents and 25% of the total energy supplied by the hydrolysis of ATP are "wasted" for the synthesis of H_2. To date, it is not exactly known why this side reaction takes place. It is proposed that only through the reductive elimination of two FeMo-co bound hydrides, leading to H_2 release, the doubly reduced metal cluster is able to bind molecular dinitrogen, as only electron rich metal centers favor N_2 coordination.[17]

Reaction equation NH_3 part: $N_2 + 6H^+ + 6e^- + 12ATP \longrightarrow 2NH_3 + 12ADP + 12P_i$

Reaction equation H_2 part: $2H^+ + 2e^- + 4ATP \longrightarrow H_2 + 4ADP + 4P_i$

Total reaction equation: $N_2 + 8H^+ + 8e^- + 16ATP \longrightarrow 2NH_3 + H_2 + 16ADP + 16P_i$

1.4 Functional Nitrogenase model systems − homogeneous ammonia synthesis

The previous section reported on the tremendous importance of industrial ammonia synthesis for the global population. Despite its efficiency, the enormous energy consumption of the Haber-Bosch process stays in contrast to the impressively efficient biological ammonia synthesis. In future, the growing population will increase the dependence on ammonia as artificial fertilizer. The dramatic rise in energy prices encourage the development of energy saving alternatives and environment-friendly processes.

Within the background of biological nitrogen fixation mediated by the enzyme nitrogenase, bioinorganic and coordination chemists have tried to design biomimetic functional model complexes that perform catalytic ammonia synthesis under ambient conditions, meaning under atmospheric pressure and at room temperature, just like the natural enzyme. With these bio-inspired model complexes information about

the mechanism of natural enzymes can be obtained as well. There are two possibilities to achieve the desired goal. On the one hand model complexes can feature perfect structural and spectroscopic similarity with the active site of the natural metalloenzyme, for example type and oxidation state of the metal, coordination geometry, chemical surrounding and redox potentials. These are called structural model complexes. On the other hand biomimetic model complexes acting as functional models are synthesized as well. They show less structural and spectroscopic alikeness, but give insights into important reaction steps in the catalytic cycle such as proton transfer, electron transfer, ligand exchange, etc. The isolation of catalytic intermediates and even the performance of catalytic reactions is possible.[29,30]

A lot of research has been done designing functional model complexes of the FeMo-cofactor, as this natural active site of the nitrogenase is a very complex system. Therefore scientists focus on binding of dinitrogen to transition metals and its reduction to ammonia, as well as on the synthesis and characterization of reaction intermediates present in catalytic ammonia synthesis.

The synthesis of transition metal dinitrogen complexes started with the pioneering work of Allen and Senoff. In 1965, they prepared the first dinitrogen complex $[Ru(N_2)(NH_3)_5]I_2$ by reduction of $RuCl_3$ with hydrazine under a dinitrogen atmosphere revealing an (η^1-N_2) end-on coordination mode.[31a,31b] Arising from these groundbreaking experiments, several strategies were pursued to realize the fixation of dinitrogen in transition metal complexes by modifying the ligand system (symmetric, non-symmetric, neutral/ionic, NHC ligands) as well as varying the type and oxidation number of transition metals.[13,32−35] In addition to the "classical" metals performing ammonia synthesis like molybdenum and iron, as they naturally occur in the enzyme nitrogenase, tungsten (Chatt)[36], ruthenium (Peters[37] and Schneider[38]), iridium (Schneider)[39], nickel (Limberg)[40] and manganese (Meyer)[41] are also used to synthesize a series of transition metal-dinitrogen and -nitrido complexes.

In the following, the focus is turned on molybdenum complexes performing dinitrogen activation and ammonia synthesis, and several intermediates of this reaction are presented as well.

1.4.1 Molybdenum phosphane complexes

In 1975, Chatt and coworkers reported, parallel to the group of Hidai, on monomeric molybdenum phosphane complexes activating dinitrogen via coordination.[42a,42b] Protolysis of the bis(dinitrogen) molybdenum(0) complex *trans*-$[Mo^0(N_2)_2(PMe_2Ph)_4]$ (**A**) (Scheme 1) at room temperature with sulfuric acid in methanol solution yielded up to 36% ammonia.[36] Other reaction intermediates appearing in ammonia synthesis could be stabilized by introducing chelating diphosphane (diphos) ligands such as dmpm [bis(dimethylphosphano)methane], depe [bis(diethylphoshano)ethane], dppe [bis(diphenylphosphano)-ethane] or dppm [bis(diphenylphosphano)methane]. The *trans*-$[Mo^0(N_2)_2(dppe)_2]$ complex (**B**) is depicted in Scheme 1.[43]

A

B
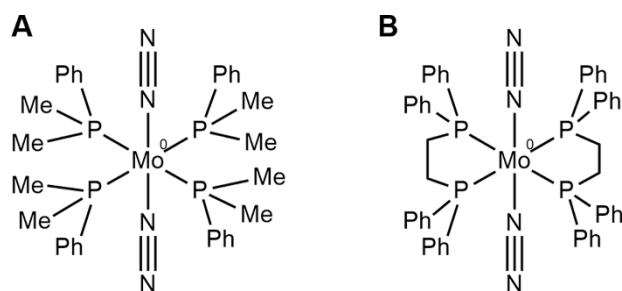
Scheme 1. Chatt's bis(dinitrogen) molybdenum(0) complexes *trans*-[Mo^0(N$_2$)$_2$(PMe$_2$Ph)$_4$] (**A**) and *trans*-[Mo^0(N$_2$)$_2$(dppe)$_2$] (**B**).

For example, protonation of one of the coordinated dinitrogen ligands in complex **B** with the acid HX gave the stable hydrazido(2−) molybdenum(III) complex [Mo^{III}X(NNH$_2$)(dppe)$_2$] with X$^-$ being the conjugate base. Based on the isolation of other reaction intermediates, a cyclic reaction mechanism for ammonia synthesis from N$_2$ was postulated (Scheme 2). The so called Chatt cycle consists of coupled electron and proton transfer steps exhibiting molybdenum intermediates in the oxidation states 0 to +IV.[44−47]

L$_2$(N$_2$)M^0—N≡N $\xrightarrow[\text{- N}_2]{\text{HX}}$ L$_2$XM^{II}—N=NH $\xrightarrow{e^\ominus / H^\oplus}$ L$_2$XM^{III}≡N—NH$_2$ $\xrightarrow{H^\oplus}$ L$_2$XM^{III}≡N—NH$_3^\oplus$

bis(dinitrogen)   diazenido   hydrazido   hydrazidium

L$_2$XM^I $\xleftarrow[\ominus\text{- NH}_4^\oplus]{H^\oplus}$ L$_2$XM^I—NH$_3$ $\xleftarrow{e^\ominus / H^\oplus}$ L$_2$XM^{II}—NH$_2$ $\xleftarrow{e^\ominus / H^\oplus}$ L$_2$XM^{III}≡NH $\xleftarrow{e^\ominus / H^\oplus}$ L$_2$XM^{IV}≡N

ammine   amido   imido   nitrido

$-X^\ominus \uparrow {+ 2N_2 \atop + e^\ominus}$

$e^\ominus / H^\oplus \downarrow {\oplus \atop -NH_4}$

L$_2$XM^{II}—N=NH =

M = Mo
L = dppe
X = conjugate base
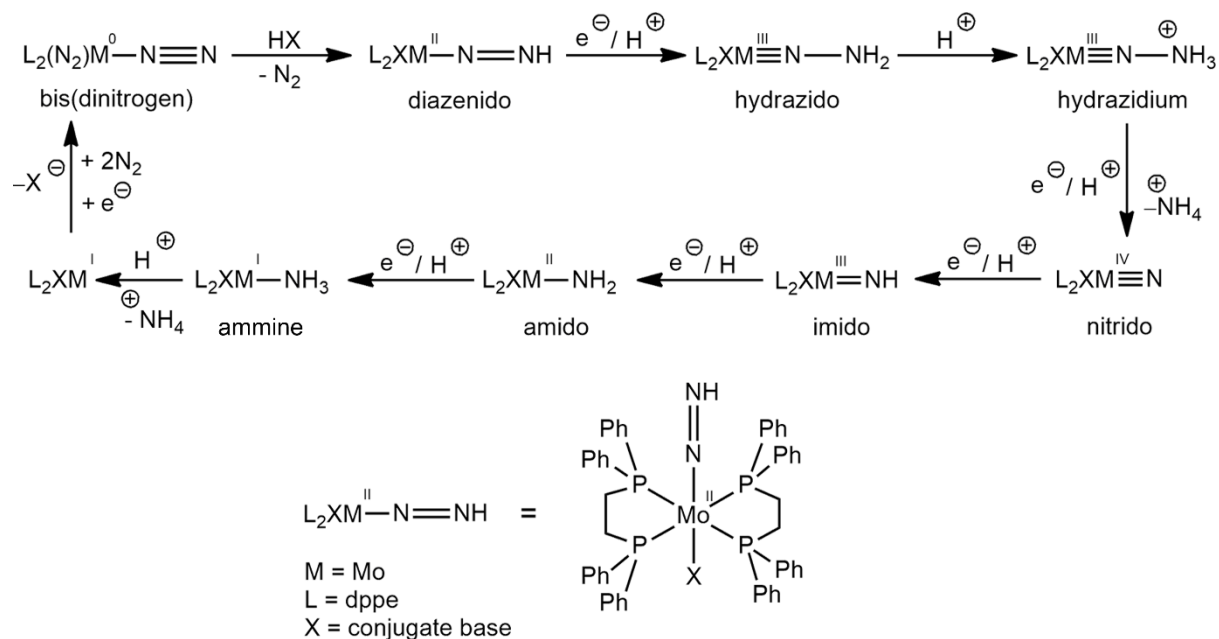
Scheme 2. Postulated reaction mechanism for N$_2$ reduction to ammonia via alternating proton and electron transfer.

In the first steps, alternating proton and electron transfer provides a reduction of the N≡N bond order, an increase of the oxidation state of molybdenum and a lowering of the oxidation state of dinitrogen. After release of the first molecule of ammonium, the nitrido(3−) molybdenum(IV) complex [Mo^{IV}X(N)(dppe)$_2$] is formed featuring with +IV the highest oxidation state for molybdenum in this cycle. In the following, proton and electron transfer leads to a lowering of the oxidation state of

molybdenum and to the release of a second molecule of ammonium. The coordination of two dinitrogen ligands including the substitution of the X^- ligand yields the starting complex **B** closing the Chatt cycle.

All these classic Chatt-type complexes show substoichiometric ammonia production upon protonation. One of the major problems of these complexes is the exchange of one dinitrogen ligand of the bis(dinitrogen) molybdenum(0) complex by the coordinating anion of the acid employed for the protonation reaction (X^-). Subsequent bimolecular disproportionation of $[Mo^IX(N_2)(diphos)_2]$ yields $[Mo^0(N_2)_2(diphos)_2]$ and $[Mo^{II}X_2(diphos)_2]$, thus leading to the loss of 50% molybdenum complex per cycle.

As the protonation of immobilized analogues $[Mo(N_2)_2(PS\text{-}diphos)(PPh_2Me)_2]$ [PS-diphos = polystyrene-$P(Ph)CH_2CH_2PPh_2$] show no formation of ammonia but hydrazine, this result corroborated that bimolecular reactions are responsible for the ammonia production in solution. Further investigations proved that the soluble hydrazido(2−) molybdenum(III) intermediate $[Mo^{III}X(NNH_2)(PR_3)_4]$ undergoes disproportionation to NH_4^+ and N_2. In contrast, when the immobilized complexes are spatially separated on the solid support, hydrazine is formed at the single metal center, whereas suppression of the bimolecular disproportionation and in consequence failure to produce ammonia is observed.[48]

Bimolecular disproportionation represents on the one hand a productive way leading to ammonia synthesis, but leads on the other hand to the loss of 50% molybdenum complex per cycle and thus prevents catalytic ammonia synthesis. Besides the latter presenting a decay pathway, the stability of these complexes is another problem. As the phosphane ligands are relatively soft donors, they have a low affinity to metal ions in higher oxidation states leading to a notable weakening of the metal-phosphorus bond, especially in the high-valent nitrido molybdenum(IV) intermediate. Both problems can be solved by the use of multidentate phosphane ligands achieving on the one hand a higher stability of the intermediates of the Chatt cycle, and on the other hand occupying the *trans* position of the dinitrogen ligand in the Mo^0 complex to avoid disproportionation reactions.[49]

This strategy has been pursued by the group of George using linear tridentate phosphane ligands of the type $Ph_2P\text{-}(CH_2)_2\text{-}E\text{-}(CH_2)_2\text{-}PPh_2$ with E = NH, NMe, S, O and PPh. Especially with the latter dpepp [bis(diphenylphosphanoethyl)phenylphosphane] ligand and bidentate phosphane coligands a series of molybdenum dinitrogen complexes has been synthesized (Scheme 3).[50]
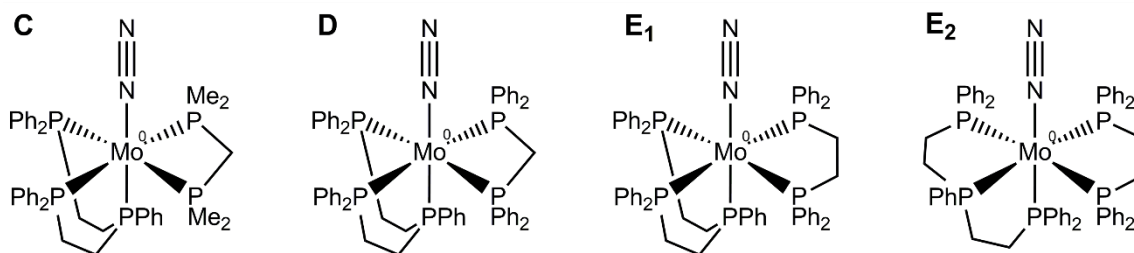
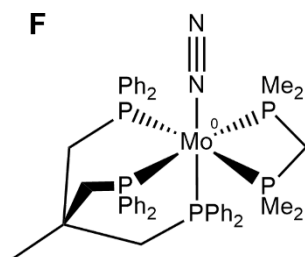Scheme 3. George's mono(dinitrogen) molybdenum(0) complexes with different pentaphosphane ligands, $[Mo^0(N_2)(dpepp)(dmpm)]$ (**C**), $[Mo^0(N_2)(dpepp)(dppm)]$ (**D**), $[Mo^0(N_2)(dpepp)(dppe)]$ (**E₁**), *Iso*-$[Mo^0(N_2)(dpepp)(dppe)]$ (**E₂**).

Protonation of [Mo(N$_2$)(dpepp)(dppm)] (**D**) by triflic acid leads to the formation of the hydrazido(2−) complex [Mo(NNH$_2$)(dpepp)(dppm)](SO$_3$CF$_3$)$_2$, and is therefore achieved under retention of the pentaphosphane ligation supporting the augmented stability of these complexes. But, treating these mono-N$_2$ complexes with excess HBr and HCl resulted in the formation of various amounts of ammonia (up to 0.44 mol per mol complex), hydrazine and N$_2$, due to decomposition of the molybdenum hydrazido complexes.[51,52]

A fundamental problem of George's complexes is the existence of two isomers as the central P donor of the tridentate ligand can either coordinate in the *trans* or in the *cis* position to the N$_2$ ligand (Scheme 3, **E$_1$** and **E$_2$**). As the IR frequencies of the N−N stretching vibrations reflect the degree of N$_2$ activation, the isomers can be assigned. Coordination of the central phosphane in the *trans* position, as shown in Scheme 3, structure **E$_1$**, reveals an N−N stretching vibration at lower frequencies than for the *cis*-complex **E$_2$**. This exhibits a stronger N$_2$ activation in **E$_1$** due to the stronger σ donor and weaker π acceptor ability of this dialkylphenylphosphane group compared to the terminal diphenylalkylphosphane groups.[53]

The introduction of the tripodal triphosphane ligand tdppme (1,1,1-tris(diphenylphosphanylmethyl)-ethane) by Tuczek and coworkers showed an improvement in the stability of mono(dinitrogen) molybdenum complexes with a pentaphosphane coordination sphere. As the tripodal ligand enforces facial coordination because of its C_3 symmetry, control over the coordination site *trans* to the dinitrogen ligand is gained. In these complexes the position *trans* to the dinitrogen ligand is always occupied by a diphenylalkylphosphane group resulting in a lower activation of N$_2$, as described earlier. Therefore, the reactivity of these complexes is strongly influenced by the bidentate coligand. Protonation of the mono(dinitrogen) molybdenum(0) complexes to the corresponding hydrazido complexes with triflic acid is only achieved by the use of dmpm [bis(dimethylphosphano)methane] as an electron donating bidentate coligand (Scheme 4, **F**).[54]


Scheme 4. Tuczek's mono(dinitrogen) molybdenum(0) complex with a tripodal triphosphane ligand and a bidentate coligand [Mo^0(N$_2$)(tdppme)(dmpm)] (**F**).

Additionally, DFT calculations were performed for these mono(dinitrogen) molybdenum(0) complexes with a pentaphosphane ligand coordination which indicated that the regeneration of the catalyst in a

cyclic reaction mode is thermally possible. Disproportionation reactions, as they occurred for the classic Chatt-type complexes associated with a 50% loss of the catalyst, are avoided by the occupation of the *trans* position of N_2. However, a catalytic reaction based on these systems has not been achieved yet.[49]

1.4.2 Molybdenum amido complexes

Besides the previously reported molybdenum(0) complexes activating dinitrogen, the chemistry of molybdenum(III) complexes bearing three anionic ligands has been developed as well. In 1995, the group of Cummins reported on the reaction between the three-coordinate molybdenum(III) complex of the structure $[Mo^{III}(N\{R\}Ar)_3]$ [R = ^tBu; Ar = 3,5-$C_6H_3Me_2$] (**G**) and molecular dinitrogen resulting in the formation of the terminal nitrido molybdenum(VI) complex $[NMo^{VI}(N\{R\}Ar)_3]$ (**H**).[55] Further investigations revealed the presence of a bimetallic reaction mechanism with $[Mo(N\{R\}Ar)_3]_2(\mu\text{-}N_2)$ as a thermally unstable but observable intermediate, which is responsible for N−N bond cleavage and the conversion into two equivalents of the nitrido molybdenum(VI) product (**H**) (Scheme 5).[56]
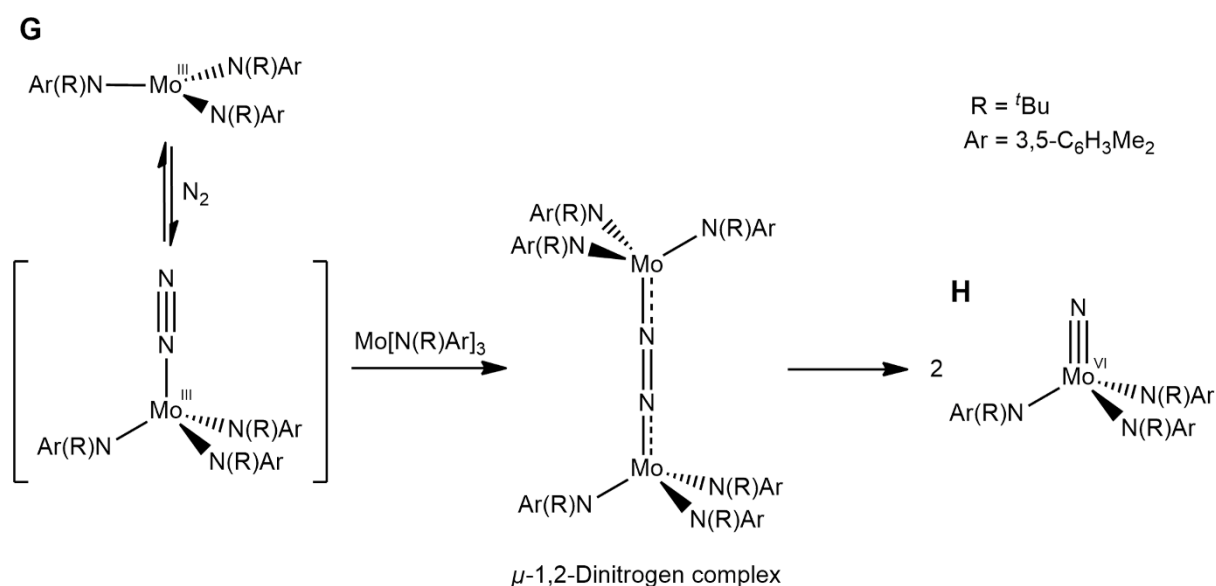
Scheme 5. Cummins' molybdenum complex with three amido ligands $[Mo^{III}(N\{R\}Ar)_3]$ (**G**) performing N_2 cleavage to provide the terminal nitrido molybdenum(VI) complex (**H**).

Based on these experiments the group of Schrock developed molybdenum complexes bearing tripodal trisanionic ligands of the type $[(ArNCH_2CH_2)_3N]^{3-}$ (= $[^{Ar}N_3N]^{3-}$) with different sterically encumbered substituents (Ar). These complexes show a trigonal bipyramidal geometry with molybdenum and the axial N_2 binding pocket protected by the aryl substituents (Scheme 6, $[(^{Ar}N_3N)Mo^{III}(N_2)]$ (**I**)). A series of high oxidation state molybdenum $[^{Ar}N_3N]$ complexes has been synthesized revealing the potential to bind and activate N_2 and stabilize the partially hydrogenated derivatives (N_2H_x).[57,58]
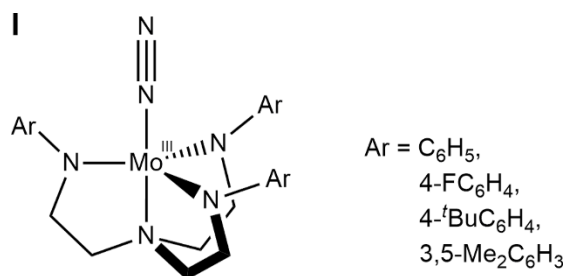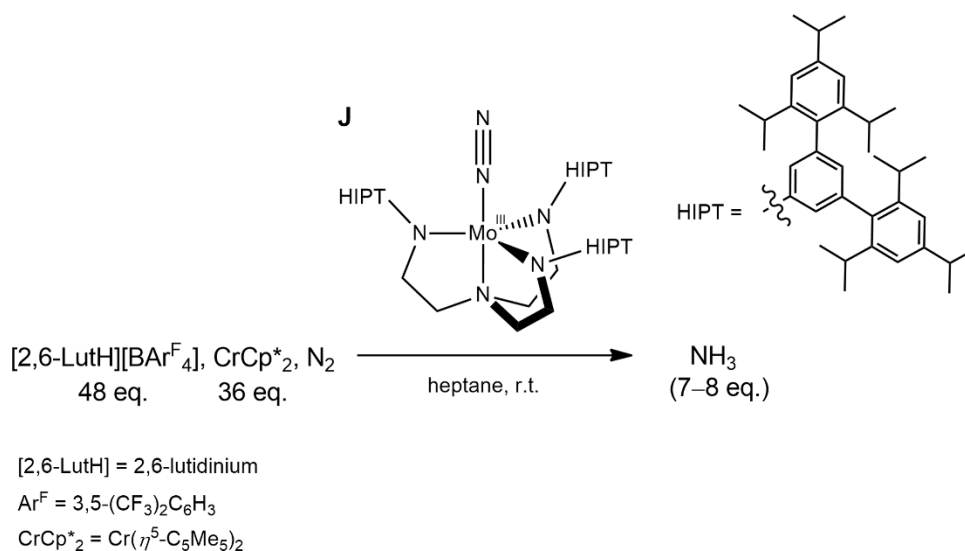
Scheme 6. Schrock's mono(dinitrogen) molybdenum(III) complex with a tripodal triamidoamine ligand $[(^{Ar}N_3N)Mo^{III}(N_2)]$ (**I**).

However, the catalytic synthesis of ammonia was not possible using relatively small substituents, for example $Ar = C_6H_5$, $4\text{-}FC_6H_4$, $4\text{-}^tBuC_6H_4$, $3,5\text{-}Me_2C_6H_3$. The bimolecular decay pathways represent the primary problem in homogeneous ammonia catalysis leading to the formation of hydrazine, dihydrogen or simply unreactive complexes. One example is the bimolecular decomposition of $[(^{Ar}N_3N)Mo^{IV}(NNH)]$ to give H_2 probably via a $[(^{Ar}N_3N)Mo^{IV}-N=N-H\cdots H-N=N-Mo^{IV}(^{Ar}N_3N)]^{\ddagger}$ transition state. Another possible side reaction due to dimerization is represented by the formation of catalytically unreactive species like the $[(^{Ar}N_3N)Mo^{III}-(\mu\text{-}N_2)-Mo^{III}(^{Ar}N_3N)]$ complex, which is subsequently reduced to $[(^{Ar}N_3N)Mo(N_2)]^-$ without splitting of the $N\equiv N$ triple bond.[59]
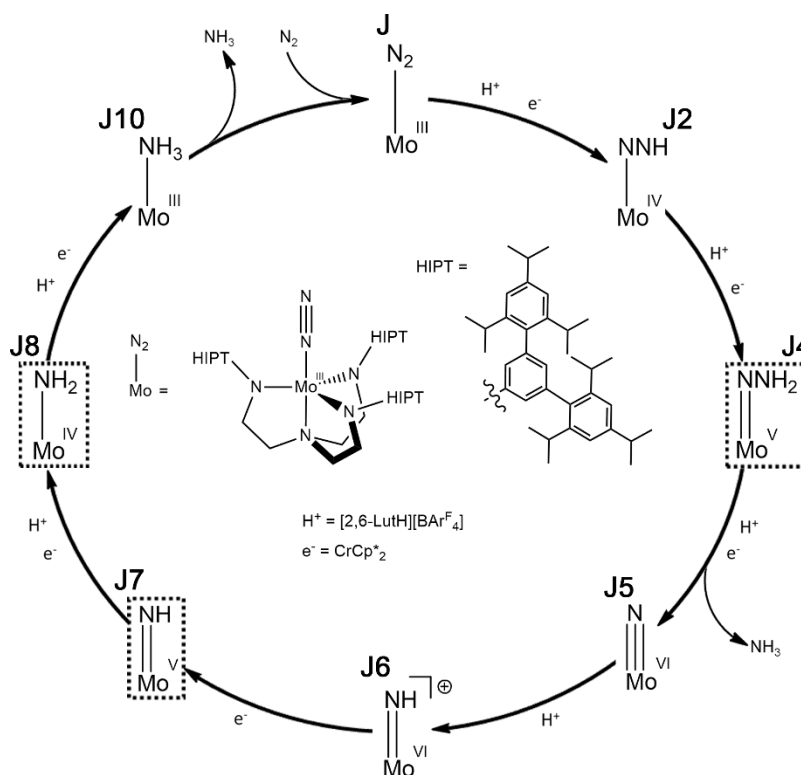
1.4.3 Catalytic ammonia synthesis

In 2002, Schrock *et al.* synthesized a $[(^{HIPT}N_3N)Mo^{III}(N_2)]$ complex (Scheme 7, **J**) with sterically encumbered hexaisopropylterphenyl (HIPT = $3,5\text{-}(2,4,6\text{-}^iPr_3C_6H_2)_2C_6H_3$) groups. Treating this complex with an excess of protons and electrons under a dinitrogen atmosphere revealed the catalytic production of ammonia. This was the first time that homogeneous catalytic ammonia synthesis starting from dinitrogen was achieved. In a classical catalytic reaction, as shown in Scheme 7, one equivalent of the catalyst (**J**), 48 eq. of the proton source [2,6-lutidinium][B(3,5-{CF$_3$}$_2$C$_6$H$_3$)$_4$] and 36 eq. of the reducing agent decamethylchromocene (CrCp*$_2$) reacted in heptane under a dinitrogen atmosphere to produce 7−8 eq. ammonia based on Mo(N$_2$).[25,60−63]

Scheme 7. Schrock's mono(dinitrogen) molybdenum(III) complex with a sterically encumbered [$^{HIPT}N_3N$]$^{3-}$ ligand [($^{HIPT}N_3N$)Mo^{III}(N$_2$)] (**J**) performing catalytic ammonia synthesis under given conditions.

Based on these experiments and the isolation of several intermediates **J**, **J2**, **J5**, **J6**, **J10** generated by strictly alternating proton and electron transfer steps, a cyclic mechanism for the reaction of dinitrogen to ammonia catalyzed by [Mo($^{HIPT}N_3N$)], with molybdenum in oxidation states from +III to +VI, was postulated (Scheme 8).[62] Additionally, DFT calculations were performed to support the validity of this mechanism.[64,65]

Scheme 8. Postulated Schrock cycle for catalytic ammonia synthesis. Proposed but not yet characterized intermediates **J4**, **J7**, **J8** are highlighted by dotted boxes.

To describe the catalytic cycle we start from the neutral paramagnetic d^3 dinitrogen molybdenum(III) complex $[(^{HIPT}N_3N)Mo^{III}(N_2)]$ (**J**) at the top of the cycle depicted in Scheme 8. Protonation and reduction lead to the diamagnetic diazenido molybdenum(IV) complex $[(^{HIPT}N_3N)Mo^{IV}(NNH)]$ (**J2**). In the following step **J2** is protonated to yield the diamagnetic hydrazido molybdenum(IV) complex $[(^{HIPT}N_3N)Mo^{IV}(NNH_2)]^+$ (**J3**). Disproportionation is observed in the following reduction step resulting in the formation of several products of the catalytic cycle, for example $[(^{HIPT}N_3N)Mo^{VI}(N)]$ (**J5**), and ammonia. In contrast, the paramagnetic intermediate $[(^{HIPT}N_3N)Mo^{V}(NNH_2)]$ (**J4**) could not be isolated yet and therefore the mechanism leading to the formation of **J5** in combination with the release of the first molecule ammonia is still unknown. The diamagnetic nitrido molybdenum(VI) complex **J5** is the only intermediate of the cycle which is relatively air-stable. Its protonation at the axial nitrido ligand yields the cationic imido molybdenum(VI) complex $[(^{HIPT}N_3N)Mo^{VI}(NH)]^+$ (**J6**). In the subsequent reduction rapid disproportionation of the initially formed imido molybdenum(V) complex **J7** into $[(^{HIPT}N_3N)Mo^{VI}(N)]$ (**J5**) and $[(^{HIPT}N_3N)Mo^{IV}(NH_2)]$ (**J8**), respectively the protonated **J8**, $[(^{HIPT}N_3N)Mo^{IV}(NH_3)]^+$ (**J9**), is observed. The diamagnetic ammine complex **J9** is reduced to the paramagnetic d^3 ammine molybdenum(III) complex $[(^{HIPT}N_3N)Mo^{III}(NH_3)]$ (**J10**). The following substitution of the axial ligand by dinitrogen liberates the second molecule of ammonia of the cycle and regenerates the starting material $[(^{HIPT}N_3N)Mo^{III}(N_2)]$ (**J**).[62]

Although the bimolecular decay pathways could be retarded due to the introduction of the bulky HIPT substituents thus making catalytic ammonia synthesis possible, the catalysis is limited to a maximum yield of 7−8 eq. ammonia. Detailed studies have identified several other side reactions and problems.

First of all, NH_3 dissociation from $[(^{HIPT}N_3N)Mo^{III}(NH_3)]$ (**J10**) followed by N_2 association leading to $[(^{HIPT}N_3N)Mo^{III}(N_2)]$ (**J**), and therefore starting a new catalytic cycle, represents a slow process due to an almost thermoneutral ligand exchange. In consequence, product inhibition takes place when NH_3 is accumulated during catalysis. The reduction of $[(^{HIPT}N_3N)Mo^{IV}(NNH_2)]^+$ (**J3**) reveals another decomposition pathway including disproportionation with unknown mechanism leading to the formation of several products of the catalytic cycle, namely $[(^{HIPT}N_3N)Mo^{VI}(N)]$ (**J5**), $[(^{HIPT}N_3N)Mo^{IV}(NNH)]$ (**J2**), $[(^{HIPT}N_3N)Mo^{III}(NH_3)]$ (**J10**) and ammonia. The intermediate $[(^{HIPT}N_3N)Mo^{V}(NH)]$ (**J7**) also disproportionates rapidly into $[(^{HIPT}N_3N)Mo^{VI}(N)]$ (**J5**) and $[(^{HIPT}N_3N)Mo^{IV}(NH_2)]$ (**J8**) involving proton and electron transfer. Another limiting factor of ammonia synthesis using these triamidoamine ligands is the protonation at one amido group of the chelate ligand facilitating its dissociation from the metal and leading to an irreversible loss of catalytic activity.[62]

In consequence, the introduction of even bulkier substituents should improve the catalytic activity of the complexes. But in contrast, choosing sterically modified substituents (Ar = 3,5-(2,4,6-$^tBu_3C_6H_2)_2C_6H_3$) resulted in a poorer activity probably due to the lower accessibility of the reaction center, especially for the proton source, favoring uncatalyzed dihydrogen formation from protons and electrons.[66]

Nevertheless, Schrock and coworkers recently reported on a new macrocyclic ligand system encapsulating the metal in a reaction pocket (Scheme 9, nitrido molybdenum(VI) complex **K**). Further work has yet to be done, but it is hoped that these complexes will show increased stability, so that the ligand is not readily lost from the metal, especially in the presence of acids and reducing agents, resulting in a sustainable catalytic activity.[67]
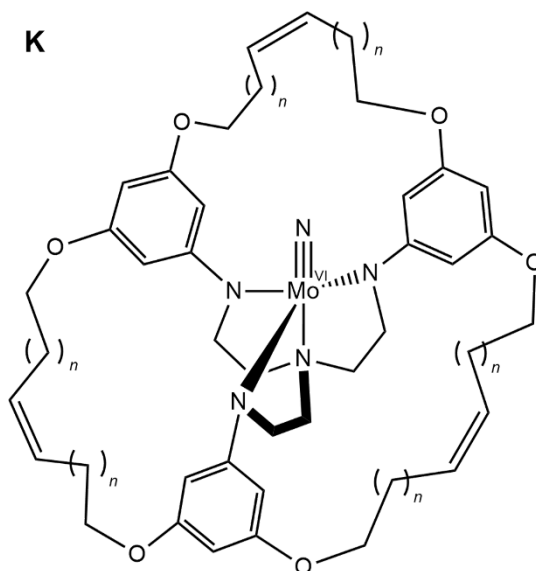
Scheme 9. Schrock's new nitrido molybdenum(VI) complex (**K**) with a macrocyclic triamidoamine ligand (n = 1, 2, 3).[67]

Another catalytically active molybdenum complex has been prepared by the group of Nishibayashi in 2011. This dinuclear molybdenum dinitrogen complex bearing PNP-type pincer ligands $[Mo(N_2)_2(PNP)]_2(\mu\text{-}N_2)$ (**L**) with PNP = 2,6-bis(di-*tert*-butyl-phosphanomethyl)pyridine was found to perform catalytic ammonia synthesis under conditions similar to Schrock's system. Treating one equivalent of the bimetallic complex with 96 eq. of the proton source [2,6-lutidinium][OSO_2CF_3] and 72 eq. of the reducing agent cobaltocene ($CoCp_2$) in toluene under N_2 atmosphere yielded approximately 12 eq. ammonia, i. e. 6 eq. per Mo (Scheme 10).[68]
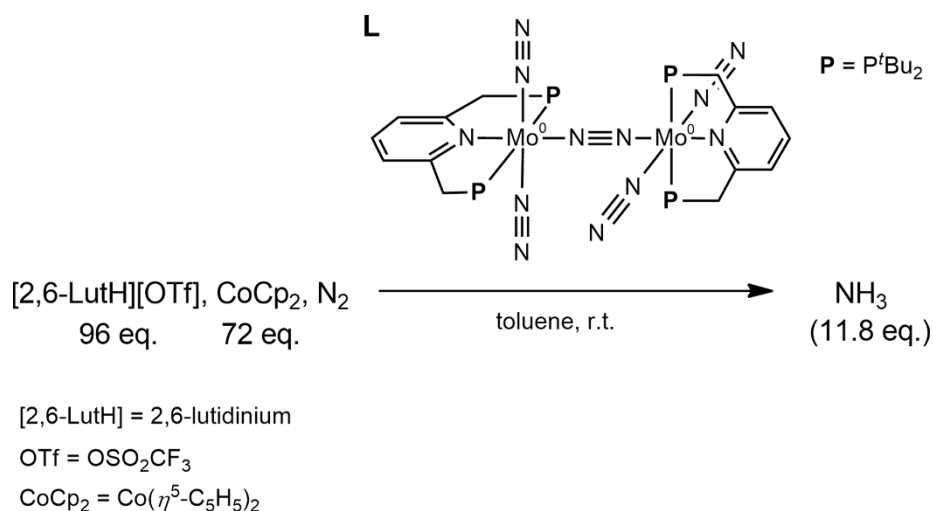
Scheme 10. Nishibayashi's dimolybdenum complex (**L**) with PNP-type ligands converting N_2 catalytically to ammonia under the given conditions.

Unlike the Schrock's catalyst, no intermediates of the catalytic cycle could be isolated in stoichiometric reactions of the catalyst neither with 2,6-lutidinium nor with cobaltocene. In a reaction of **L** with 4 eq. of the proton source $HBF_4 \cdot OEt_2$ in THF the monometallic hydrazido complex $[MoF(PNP)(NNH_2)(pyridine)][BF_4]$ was isolated and characterized, whereas the corresponding $[Mo(PNP)(NNH_2)(OTf)_2]$ complex could not be synthesized probably due to the lower coordination ability of the triflate anion resulting in a lower stability of the complex. Additionally, the dissociation of the PNP pincer ligand from the metal represents again a critical point in enabling efficient catalytic ammonia synthesis. Although the synthesis of stable intermediates failed, a reaction pathway was proposed starting with the dissociation of the dimer complex (**L**) in the presence of protons leading to the formation of the mononuclear dinitrogen complex $[Mo(PNP)N_2]$ and a protonated catalytically irrelevant complex of unknown composition. In the following it is assumed that $[Mo(PNP)N_2]$ undergoes essentially the same reaction steps as reported in the Chatt cycle (Scheme 2). But to conclude, further investigations of these complexes including the isolation of catalytically relevant intermediates are necessary to understand the mechanism of this reaction catalyzed by this PNP molybdenum complex.

In contrast to the two reports on molybdenum complexes, Peters *et al.* reported in 2012 on the catalytic conversion of dinitrogen to ammonia (6−7 eq.) using a mononuclear iron(I) complex (**M**) with a tetradentate tris(phosphano)borane ligand (Scheme 11).[69] This is the third homogeneous catalyst and the first iron based catalytic system for ammonia synthesis. Therefore it is of considerable interest focusing on the mechanism of this system in comparison to the biological nitrogen fixation mediated by the enzyme nitrogenase.

As the question of the dinitrogen coordination and reduction locus in nitrogenase is still the central element of debate, these new results confirm the capacity of a single iron center to stabilize all reaction intermediates of the catalytic cycle.
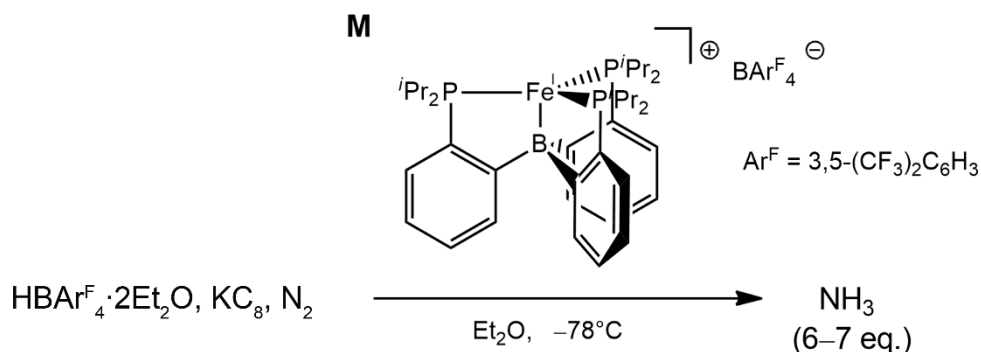
Scheme 11. Peter's mononuclear iron(I) complex (**M**) with a tris(phosphano)borane ligand converting N_2 catalytically to ammonia under the given conditions.

To conclude, three transition metal complexes are known to perform homogeneous ammonia catalysis but in all cases the yield of ammonia is lower than 8 eq. per metal center. Detailed mechanistic studies are known for the Schrock system (**J**) revealing several side reactions which are predominantly of bimolecular nature such as dimerization and disproportionation. In the past, the immobilization of catalysts has shown great potential tackling the problem of intermolecular reactions. In the following section investigations on solid phase synthesis as well as on polymer-supported biomimetic complexes are presented.

1.5 Solid phase synthesis

Historically, Merrifield[70] was the first to introduce the strategy of solid phase chemistry. He achieved to synthesize a tetrapeptide of known amino acid sequence on a solid phase. As solid support he used a polystyrene resin which was crosslinked with 1% divinylbenzene. Such three-dimensional chemically cross-linked polymer networks show special properties. Addition of solvent leads to a polymer-solvent interaction inducing a change in the polymer conformation. Specifically, the solvent uptake is accompanied by an expansion of the polymer network (swelling), whereupon the cross-linking with divinylbenzene prevents the entire dissolution of the polymer.[71] In Merrifield's experiment, the solid support was equipped with an anchor group onto which several molecules (in this case amino acids) can

be attached stepwise. Due to the immobilized reaction partner, the molecule itself which is attached can be added in excess while the unconverted reagents can be removed easily from the solid support by washing and filtration. This method leads to a nearly quantitative conversion of the immobilized reaction partners. In the last step the final oligomer or in Merrifield's case the tetrapeptide can be isolated by cleaving the product from the anchor group with the use of acids and fluoride ions (Figure 7).
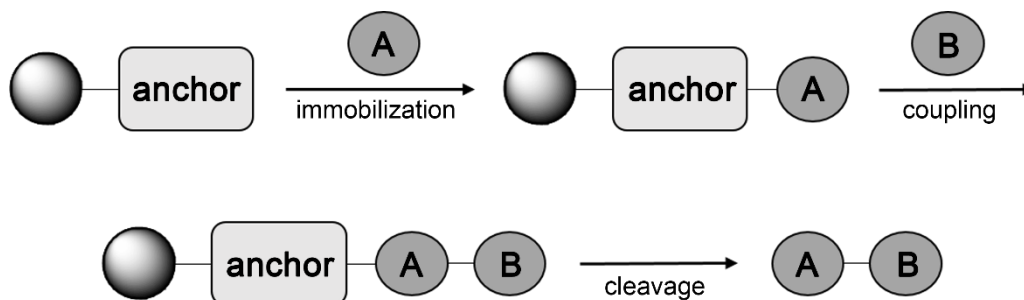
Figure 7. Principle of solid phase (peptide) synthesis.

1.5.1 Immobilized metal complexes

Although this strategy is very popular in organic chemistry[72] it is rarely used in inorganic coordination chemistry. In the last decade the immobilization of inorganic molecules onto a polymer support via formation of coordinative bonds and the synthesis of inorganic complex oligomers using solid phase synthesis strategies was established in our group. Via solid phase synthesis Heinze and Toro could synthesize trinuclear compounds consisting of molybdenum carbonyl complexes. Subsequent cleavage of the immobilized trimer with tetra-*n*-butylammonium fluoride and protonation yields the soluble trinuclear complex, which can be easily removed from the insoluble solid support by filtration (Scheme 12).[73]
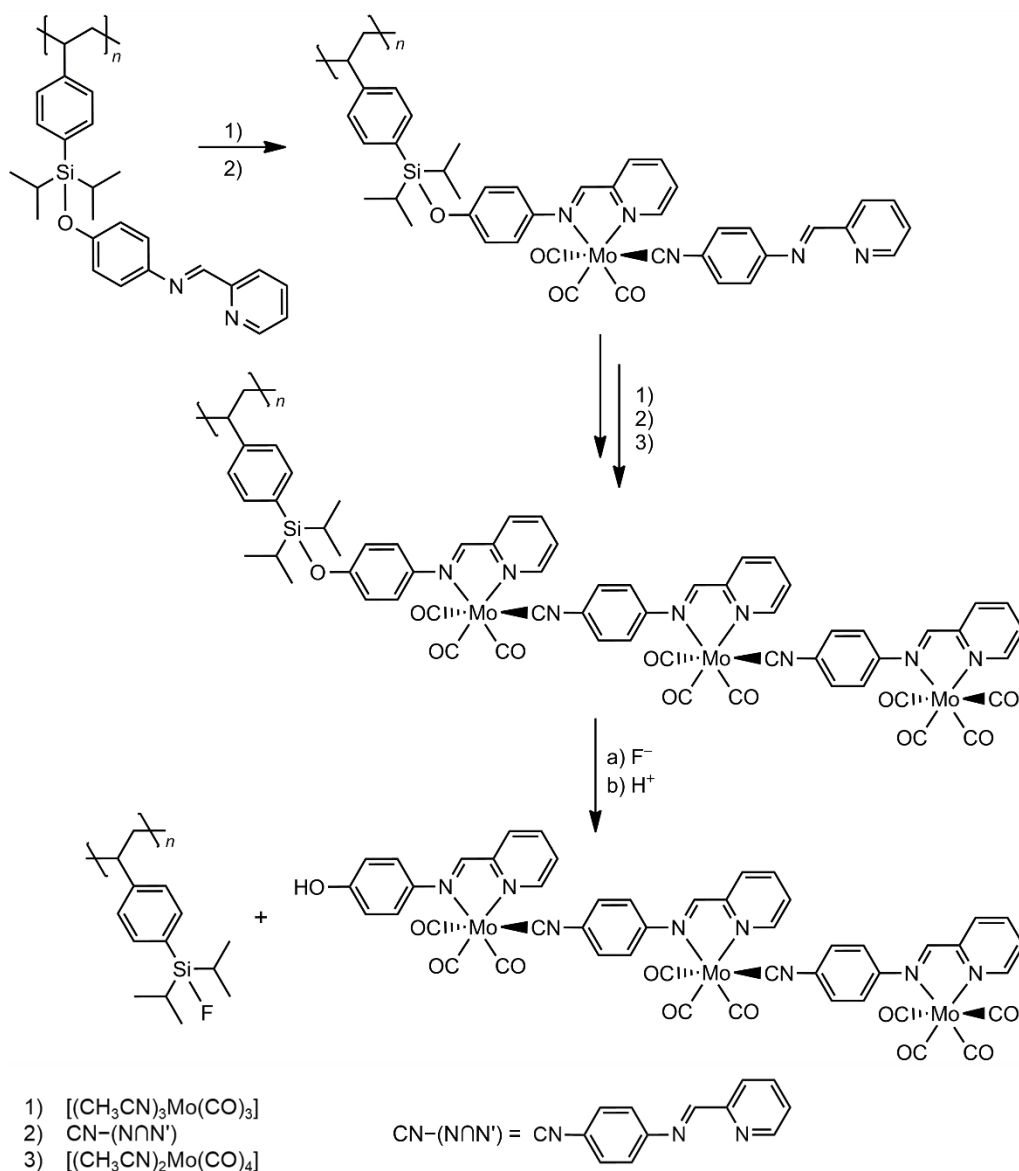
Scheme 12. Synthesis of an immobilized trinuclear molybdenum carbonyl complex and subsequent cleavage.[73]

As the synthesis of longer oligomers of the 1,1′-ferrocene amino acid (Fca) by solution methods is increasingly difficult due to the decrease in the solubility and the reactivity, Siebler and Heinze applied the technique of solid phase peptide synthesis (SPPS), analogously to the reported method from Merrifield, to successfully realize the synthesis of Fmoc-Fca$_n$-OMe oligomers with $n = 3-5$. As insoluble support Hypogel 400 PHB was used, a Hypogel resin (polystyrene/divinylbenzene grafted with PEG chains, 10 units) with a *para*-hydroxybenzyl alcohol (PHB) linker (Scheme 13).[74]
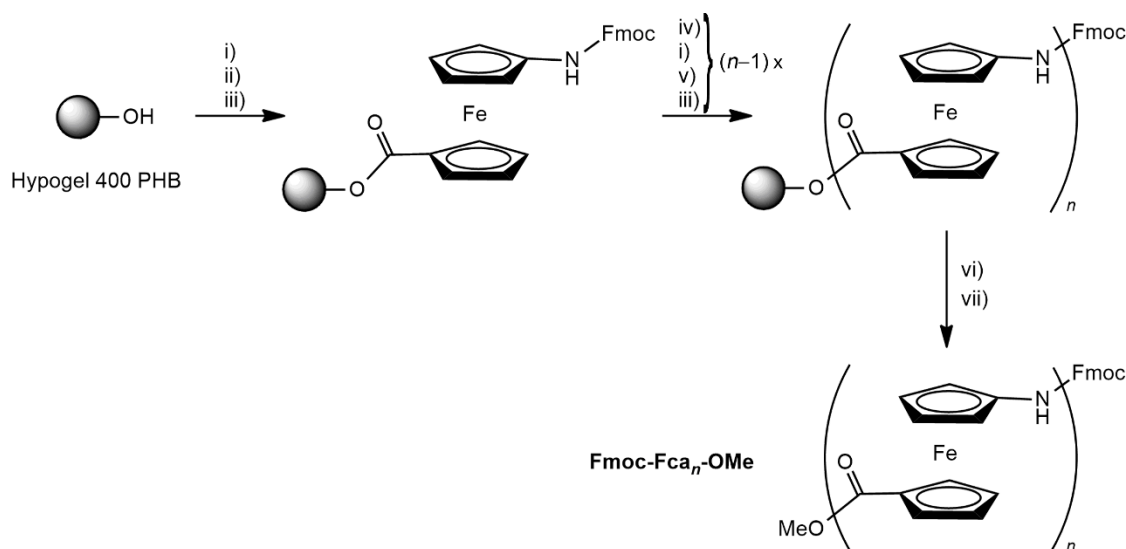
Scheme 13. SPPS of **Fmoc-Fca$_n$-OMe** (n = 3−5) from Hypogel 400 PHB. (i) **Fmoc-Fca-OH**, Ghosez's reagent (1-chloro-*N,N*,2-trimethyl-1-propenylamine), CH_2Cl_2, 1 h, 20°C. (ii) DMAP, 16 h, 20°C. (iii) acetic anhydride/pyridine (10:1), 2×30 min, 20°C. (iv) 25% piperidine/DMF, 2×30 min, 20°C. (v) 2,4,6-collidine, 16 h, 20°C. (vi) 60% TFA/CH_2Cl_2, 2 h, 20°C. (vii) diazo(trimethylsilyl)methane, toluene/MeOH (7:3), 4 h, 20°C.[74]

1.5.2 Solubility properties of cross-linked polymers

The degree of cross-linking of polystyrene with divinylbenzene influences the swelling properties of the polymer and consequently the reactivity of the immobilized molecules (steric hindrance). Moffat *et al*.[75] applied this solid phase synthesis to immobilize catalysts. In contrast to the previously reported Merrifield synthesis using the solid phase as temporary support for oligomerization reactions, the molecules (in this case the catalysts) are permanently immobilized onto the solid support. They used polyvinyl-2-pyridine, modified the cross-linking with divinylbenzene and tested the catalytic behavior of attached cobalt carbonyl complexes towards the hydroformylation of olefins. Little or no cross-linking leads to a soluble polymer, while a great deal of cross-linking leads to a very low solubility. In between, in this case with 4 to 8% divinylbenzene cross-linking, the polymer swells but does not dissolve. In this swollen state this polymer remains "solid", with the advantage of ready recovery after the reaction and the good separation of reaction products from the solid phase. But the polymer chains as well as the immobilized molecules are unfolded so that the solvent can penetrate into the polymer network and the anchored reaction centers are accessible for the reactants (Figure 8).[71] The reaction can take place in this swollen polymer just as in a comparable reaction in solution.
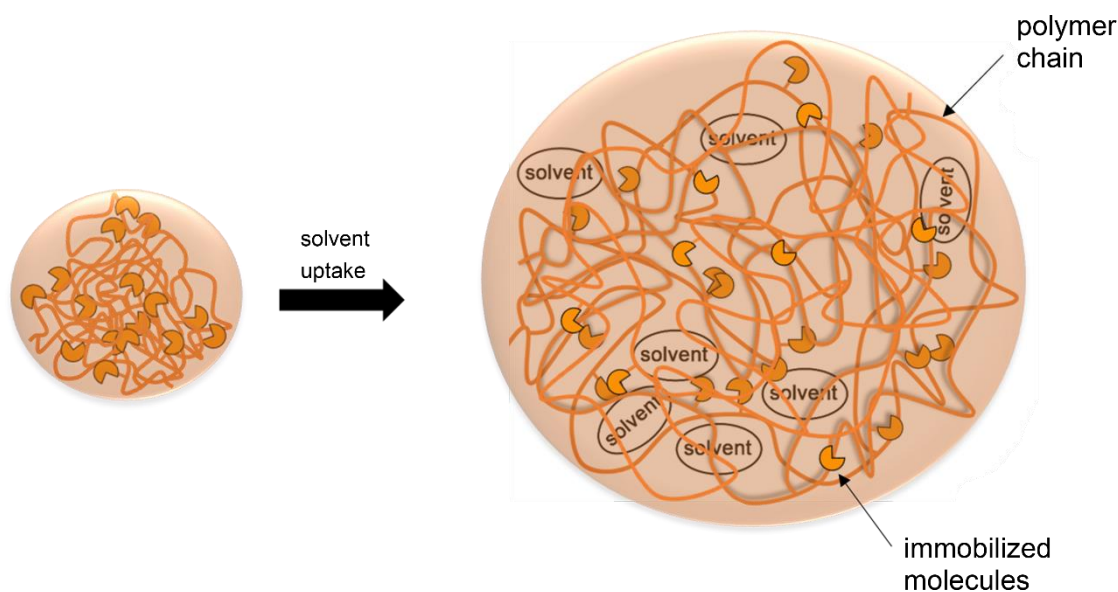
Figure 8. Schematic illustration of polymer swelling due to solvent uptake.

In contrast, in the "dry state", the so called collapsed state, the active site of the catalyst is protected against the environment, especially against oxygen and humidity. Nevertheless it is advisable to store the solid phase under inert atmosphere, if the immobilized complexes are water- or air-sensitive, because any moisture is either absorbed in the case of hygroscopic resins like polycarbonates, or adsorbed on the polymer surface in the case of non-hygroscopic resins like polystyrene.[76] When swelling the polymer in a good solvent, the water molecules can dissolve in the solvent and further react with the active site of the catalyst (and possibly destroy its activity). The collapsed state is also present when a solvent is used which is not a good swelling solvent for the solid phase. In that case neither the solvent nor the substrate can penetrate into the polymer network due to the rigidity of the polymer chains. As consequence, the substrate cannot interact with the active site of the catalyst and no product can be formed. The diffusion rates of the substrate are diminished due to a more compact network structure in the collapsed state.[77]

It is therefore possible to control the volume of the solid phase and in consequence the catalyst accessibility and the catalytic activity. The reaction progress mainly depends on the swelling degree of the solid phase in the different solvents or solvent mixtures. Good catalyst accessibility requires an expanded polymer network, thus high swelling ratios cause reactions to proceed faster than in the collapsed state.[78]

1.5.3 Immobilized biomimetic complexes and catalysts

A solid phase can also be used to immobilize catalysts.[77,79−82] Indeed, the heterogenization of homogeneous catalysts represents a special branch of this solid phase chemistry. It combines the advantages of both methods including the reactivity, activity and selectivity of homogeneous molecularly defined "single site" catalysts due to the remaining solubility while swelling the solid phase in an appropriate solvent during catalysis, and the advantages of heterogeneous catalysts which are the ready recovery and the reusability, and the easy separation of the reaction products from the solid catalyst. The prior condition to realize this heterogenization is that the soluble catalyst can be attached to a solid support without losing its defined molecular structure and surrounding ligands and therefore maintaining its catalytic activity. It involves a structurally well-characterized catalyst just as the respective homogeneous molecular catalyst. This is the advantage towards other heterogeneous catalysts used in industry, where the knowledge of reactive sites is empirical and the mechanism of the catalytic reaction is not always known. In general, it is possible that the reactivity of the catalyst is increased by immobilization, but the rigidity of the polymer-catalyst composite and the limited access to the active site can also lead to a loss of catalytic ability.[77,83]

Although the low loading of the catalyst on the solid support represents at first sight a disadvantageous fact of this type of catalyst, the advantageous change due to the immobilization is the spatial isolation of the reactive centers on the polymer chain, as they are bound at an appropriate distance, as well as the steric crowding around the catalytic centers so that they can act as single-site catalysts and show an improved catalyst stability. This so called site isolation effect, caused by the effective separation and restricted motion of the catalysts, prevents bimolecular side reactions such as disproportionation, dimerization or disadvantageous redox chemistry, as it is often relevant in homogeneous catalysis.

In 1974, Leal, Burwell, Jr. *et al*. reported on their attempts on the reversible adsorption of oxygen on silica-immobilized iron porphyrins. The formation of the monoadduct Fe-O$_2$ was observed, while the μ-oxido dimer formation (Fe^{III}-O-Fe^{III}) has been successfully suppressed due to the attachment of the iron porphyrin to the solid support.[84] Dioxido molybdenum complexes were investigated as functional oxotransferase model systems in our group.[85] Their immobilization as [Mo^{VI}O$_2$(N′N)$_2$], with (N′N) representing the deprotonated polystyrene attached ligand (Scheme 14), revealed that the formation of μ-oxido dimers (Mo^V-O-Mo^V) prevailing in homogeneous solution has been retarded.[86−88]
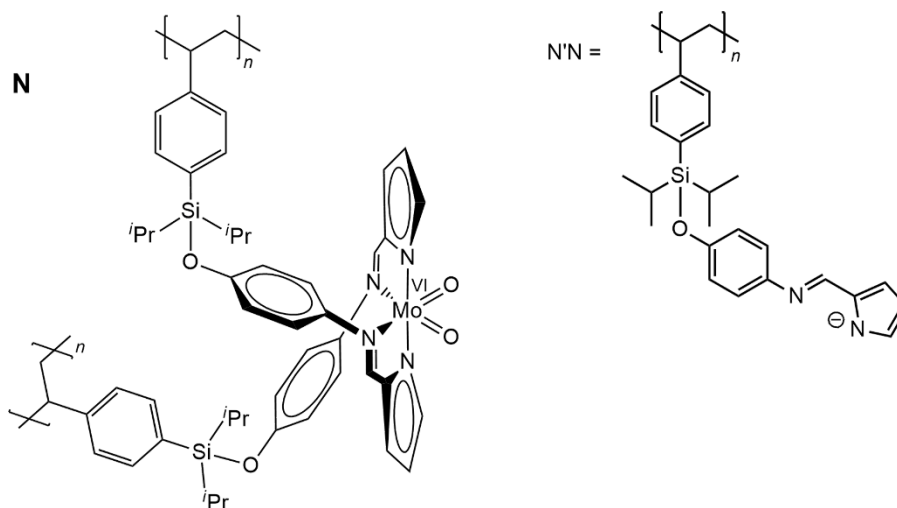
Scheme 14. Immobilized dioxido molybdenum(VI) complex [Mo^{VI}O$_2$(N′N)$_2$] (**N**) reported by Heinze and Fischer.[86]

Additionally, this immobilized dioxido molybdenum(VI) complex (**N**) shows catalytic oxygen atom transfer (OAT) to PMe$_3$ yielding OPMe$_3$ in the presence of H$_2$O and [Fe(AcC$_5$H$_4$)$_2$]$^+$ (17 turnovers). The proposed reaction mechanism of this OAT is depicted in Scheme 15. In the first step, the dioxido molybdenum(VI) complex is treated with two equivalents PMe$_3$. One equivalent is oxidized in an OAT reaction to OPMe$_3$, the second equivalent coordinates to the metal center yielding the oxido trimethylphoshane molybdenum(IV) complex (**N1**). Subsequent one-electron oxidation leads to the formation of the corresponding cationic [Mo^{V}O(PMe$_3$)(N′N)$_2$]$^+$ complex (**N2**), which undergoes a ligand exchange reaction in the presence of H$_2$O to yield the cationic oxido aqua molybdenum(V) complex (**N3**). This complex **N3** represents a proposed but not yet observed intermediate of this cycle. Deprotonation of **N3** with two equivalents of the base P$_1$-^{t}Bu provides the anionic dioxido molybdenum(V) complex (**N4**) which is oxidized in the last step to the starting complex **N** closing the catalytic cycle. Therefore this system represents a truly functional biomimetic model system for oxotransferases, in contrast to the homogeneous system which was catalytically inactive.[86]
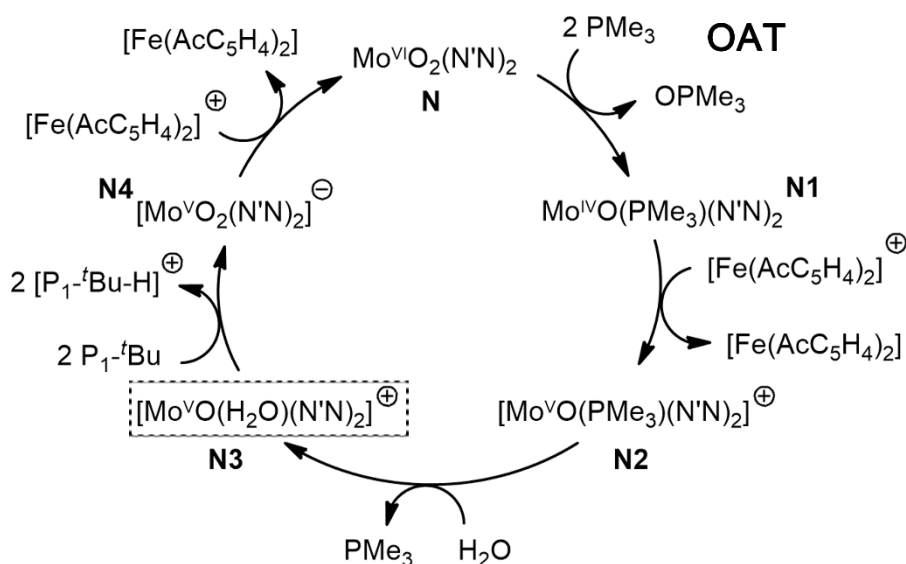
Scheme 15. Catalytic reaction mechanism proposed by Fischer and Heinze, oxygen atom transfer (OAT) to PMe$_3$ yields OPMe$_3$. Proposed but not yet observed intermediate **N3** is highlighted by a dotted box.[86]

Rational strategic principles to design new catalysts or to improve the existing ones can be employed in this special branch of immobilized homogeneous catalysts, in contrast to the classical heterogeneous catalysts. This so called "active-site engineering" and "active-site modification" comes along with the comparison of such catalysts with the well-defined active site of metalloenzymes. The aim is to mimic those active sites because in nature the most efficient catalysts and reaction pathways are realized. The key targets for bioinorganic chemists to design enzyme mimics are high catalytic activity coupled with high selectivity and the ability to work at ambient temperatures and normal pressures just like the natural enzyme. In general the enzyme mimics should be thermally and mechanically stable and capable of being regenerated when their performance diminishes due to "poisoning" of active sites.[89]

1.6 Electron Paramagnetic Resonance spectroscopy

Electron Paramagnetic Resonance (= EPR) spectroscopy is a powerful tool to investigate paramagnetic compounds in solution as well as in solid materials. This spectroscopic method is much more sensitive compared to NMR spectroscopy, so that even small amounts of a paramagnetic substance can be detected. For example, organic radicals, transition metal complexes and the active site of metalloenzymes represent such paramagnetic compounds. Information on the environment of the unpaired electron is received, like the electronic and geometric structure, the physical properties, the reactivity, or the dynamics.

1.6.1 General Aspects

Due to the relatively high linewidth of the spectra the first derivative is used for the analysis (Figure 9, bottom). The application of a magnetic field results in the separation of the degenerate energy levels of the electron spin m_S (intrinsic angular momentum), as a result of the Zeeman effect (Figure 9, top). An EPR transition, the flipping of the electron spin, is possible for $\Delta m_S = \pm 1$, resulting in the observation of $2S$ signals in the EPR spectrum. Figure 9 shows an example for one unpaired electron ($S = 1/2$).[90,91]
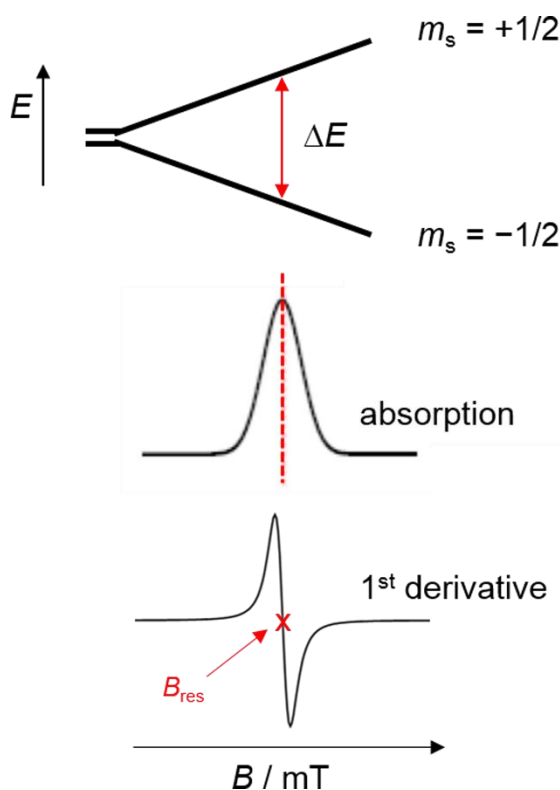
Figure 9. Example for $S = 1/2$; resonance conditions and splitting of m_S states (top), absorption spectrum (middle), first derivative of the absorption spectrum (bottom).[91]

An EPR transition occurs when the resonance conditions are complied with, as described in equation (1). For example, the energy needed for the resonance condition at a magnetic field of 300 mT (= 3000 G) lies in the range of the microwave frequency (X-band ~ 9.4 GHz).

$$\Delta E = h\,\nu = g\,\mu_B\,B \tag{1}$$

(g = g-value, μ_B = Bohr magneton, B = magnetic field)

The Landé factor, the g-value, represents a substance-specific parameter comparable to the chemical shift δ in NMR spectroscopy. The g-value for a free electron is $g_e = 2.0023$. It can be determined from EPR measurements as depicted in equation (2).[91]

$$g = h \, \nu \, / \, \mu_B \, B$$

$$= 714.5 \, \nu(\text{GHz}) \, / \, B_{\text{res}}(\text{G}) \qquad\qquad (2)$$

(ν = applied frequency in GHz, B_{res} = resonance B-field in Gauss)

In general, EPR transitions of an unpaired electron located in the SOMO (= singly occupied molecular orbital) of a paramagnetic compound occur into the HOMO (= highest occupied molecular orbital) and into the LUMO (= lowest unoccupied molecular orbital) as depicted in Figure 10.[91]
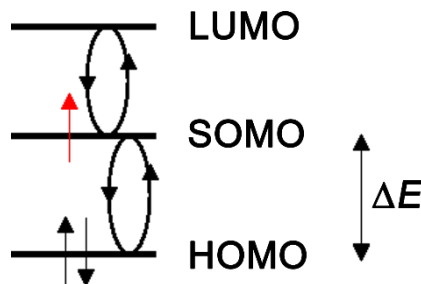

Figure 10. EPR transitions of an unpaired electron (red arrow) into the HOMO or the LUMO.[91]

These transitions can be described as a mixing or a rotation of the SOMO into the respective involved orbital, whereas the unpaired electron interacts with the orbital angular momentum via spin-orbit coupling (SOC = interaction of the spin with its orbital motion). Therefore, the g-value of an unpaired electron in a paramagnetic compound differs from a free electron g_e as defined in equation (3). The so called "g-shift" is defined as the difference $g - g_e$. Rotation of the SOMO into an empty orbital induces a magnetic field opposite to the local field resulting in $g < g_e$, whereas due to the rotation into a filled orbital a magnetic field parallel to the local one is produced ($g > g_e$).[91]

$$g = g_e \pm (a^2 \, n \, \lambda \, / \, \Delta E) \qquad\qquad (3)$$

(a^2 = covalency parameter, n = quantum mechanical coefficient,

λ = SOC constant, ΔE = energy difference between involved orbitals)

Organic radicals usually have large ΔE, as emphasized by high energy optical transitions (colorless), and small λ. In consequence, their g-values differ not much from g_e, as N- or O-based radicals feature g-values in the range of 2.003−2.006. Radical anions and cations of porphyrin amino acids have been investigated in our group corroborating these values.[92] In contrast, transition metal complexes often have small ΔE (colored), due to the splitting of the d orbitals in the ligand field, or close metal and ligand orbitals enabling charge transfer. Additionally, they have significant λ, as the SOC constant is larger for heavier elements, and therefore show g-values significantly different from g_e, ranging usually from 3 to 1. These compounds will be discussed in more detail in the next section.

Additionally, the electron spin can interact magnetically with the nucleus, more precisely with the nuclear spin (I), resulting in a coupling visible in the EPR spectrum. With this method nuclei which have a nuclear spin $I \neq 0$ and which are located in proximity to the unpaired electron can be detected. A distinction is made between hyperfine coupling, in this case the radical is located directly in an orbital of the detected nucleus, and super hyperfine coupling, where the nucleus is in close proximity to the unpaired electron. The coupling constants (A) provide more details about the radical environment as these values are nucleus-specific and depend on the distance between the unpaired electron and the nucleus, similar to coupling constants in NMR spectroscopy, and thus they are orbital-dependent, too. The resonance conditions for allowed EPR transitions are expanded by the additional selection rule $\Delta m_I = 0$. Coupling of one electron spin to n equivalent nuclei results in $2nI+1$ signals in the EPR spectrum. The relative intensities of the signals can be extracted from triangles or stick spectra, and in the special case of nuclei with $I = 1/2$ (e.g. protons) the Pascal's triangle can be used. In 2,2-diphenyl-1-picrylhydrazyl (dpph, Figure 11, right), representing an often used standard for g-value calibration in EPR spectroscopy, the unpaired electron is located at the two hydrazyl nitrogen atoms ($I(^{14}N) = 1$), with accidentally similar coupling constants, featuring a pentet in the EPR spectrum (Figure 11, bottom left), as $2 \times 2 \times 1 + 1 = 5$. The coupling constant $A(^{14}N)$ is 9.1 G and the signal intensities are 1:2:3:2:1, as expected for this paramagnetic substance (Figure 11, stick diagram top left).
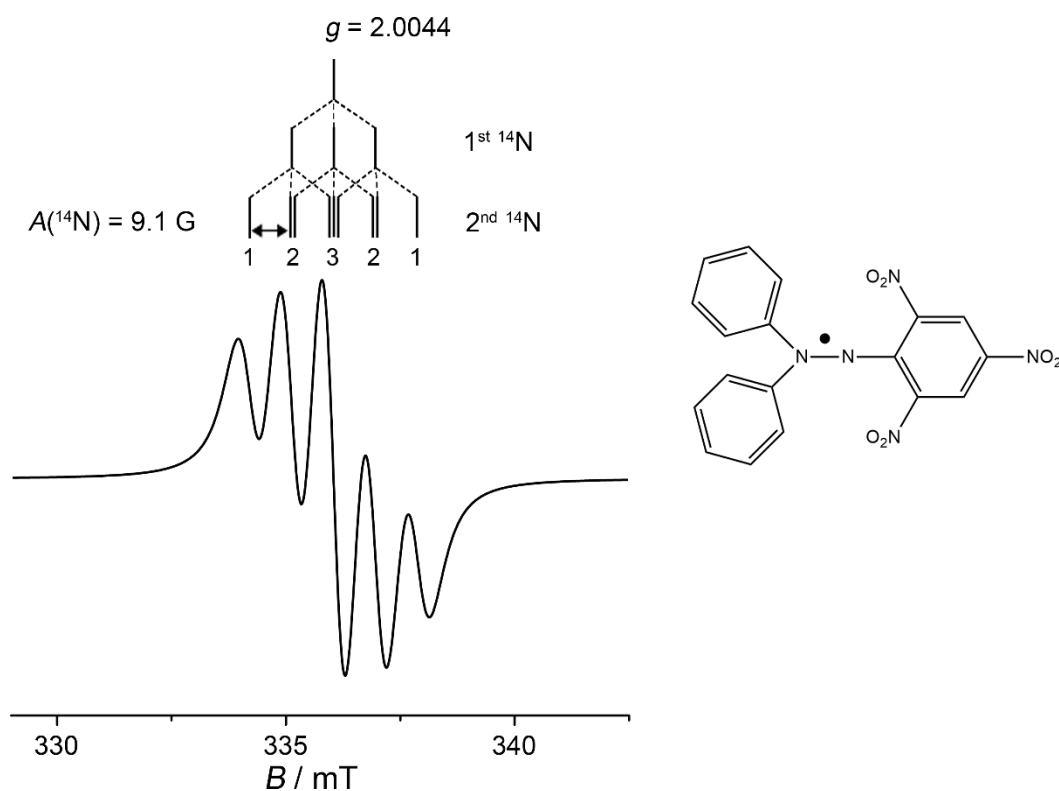

Figure 11. X-band (9.4 GHz) EPR spectrum of 2,2-diphenyl-1-picrylhydrazyl (dpph) recorded in toluene at room temperature (EPR spectrum bottom left), stick diagram showing signal intensities of the pentet (top left), molecular structure of dpph (right).

In fluid solution the molecules are tumbling rapidly on the EPR timescale. Therefore the magnetic field "observes" only the average orientation of the molecules in the solution resulting in an isotropic EPR spectrum, displayed in Figure 11, bottom left. But, as the molecules are often not spherically symmetric, they look different from different orientations. In consequence, the g- and the A-value representing tensors are dependent upon the three directions x, y, z. Measuring an EPR spectrum in a fluid solution, the magnetic field observes the average of the different g-values and A-values, the so called isotropic g- and A-value, which are defined as shown in equation (4).[90]

$$g_{iso} = (g_x + g_y + g_z) / 3 \qquad A_{iso} = (A_x + A_y + A_z) / 3 \qquad (4)$$

In contrast, measuring paramagnetic samples in frozen solution, as powder, as single crystals or embedded in a rigid matrix, in which the motion of the molecules is restricted, so called anisotropic spectra are obtained featuring different g-values (g_x, g_y, g_z) and A-values (A_x, A_y, A_z). In the following section, different anisotropic spectra are presented and explained using transition metal complexes as examples.

1.6.2 EPR spectroscopy of transition metal complexes

The g-value of transition metal complexes differs significally from g_e, as already mentioned above. On the one hand the large SOC constant is responsible, and on the other hand the relatively small energy differences between the d orbitals, ΔE, where the "rotation" or the "mixing" of the unpaired electron occurs. As there are different d orbitals present in transition metal complexes, several transitions are possible. In dependence of the geometry of the complex, different transitions can be obtained requiring different energies, corresponding to the energy differences of the involved d orbitals. In consequence, as the g-value correlates with ΔE, different values for g_x, g_y and g_z can be observed in the EPR spectrum according to the respective transitions, while measuring the paramagnetic compound as solid.

In the case of highly symmetric complexes, for example octahedral or tetrahedral complexes with only one type of ligands (O_h, T_d point group), the values for the g-tensors are equal in all three directions resulting in an isotropic EPR spectrum with $g_x = g_y = g_z$. For paramagnetic molecules with D_{4h}, C_{4v} or D_{3h} symmetry axial anisotropic spectra with $g_x = g_y \neq g_z$ are obtained, whereas complexes with C_{2v}, D_{2h} or C_1 symmetry feature rhombic anisotropic spectra with $g_x \neq g_y \neq g_z$ (Figure 12).[91]
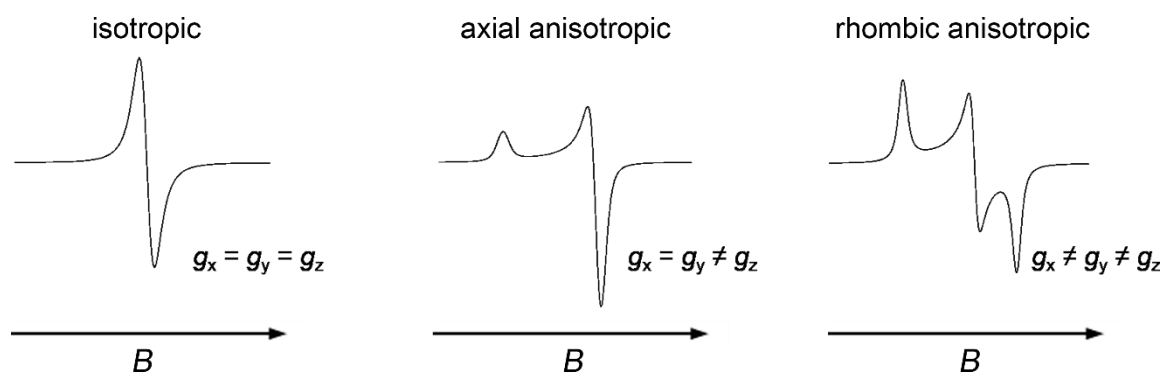
Figure 12. Isotropic (left), axial anisotropic (middle) and rhombic anisotropic (right) EPR spectra.[91]

In our group, a variety of heteroleptic bis(terpyridine)-iron(II) and -ruthenium(II) complexes, as well as a bis(terpyridine)ruthenium(II)−(bipyridine)platinum(II) complex[93] were synthesized and investigated with respect to their redox chemistry. After oxidation or reduction, the locus of the unpaired electron and the spin density distribution in the respective paramagnetic compound has been determined with the help of EPR spectroscopy. Besides the g-values, the g-anisotropy (= Δg), defined in equation (5), represents another important parameter characterizing paramagnetic compounds.[90]

$$\Delta g = g_z - g_{iso} \qquad\qquad\qquad (5)$$

For example, EPR spectra revealed that the oxidation of heteroleptic bis(terpyridine)ruthenium(II) complexes occurs at the metal center, indicated by a rhombic anisotropic spectrum with g-values and a g-anisotropy typical for ruthenium(III) centered radicals, whereas after one-electron reduction the unpaired electron is localized at the ligand denoted by a small g-shift and a small g-anisotropy.[94]

Transition metal complexes with axial anisotropic geometry will be discussed in more detail in the next two sections on the basis of copper(II) and molybdenum(V) complexes.

1.6.2.1 Copper(II) complexes

Copper(II) complexes are d^9 systems and therefore EPR active. Typical six-coordinate copper(II) complexes show Jahn−Teller elongation along the z-axis thus featuring D_{4h} symmetry. In such complexes d orbitals with z character are energetically favored and lowered in energy. Thus the unpaired electron is located in the $d_{x^2-y^2}$ orbital while all other d orbitals are occupied, resulting in $g_{x,y,z} > g_e$ indicated by the "+" sign in equation 6. Transitions are possible if the orbital hosting the unpaired electron can be transformed into another d orbital by rotation about a rotational axis. In this example the $d_{x^2-y^2}$ orbital can be transformed into the d_{xy} orbital via rotation about the z-axis. This "mixing" contributes to the magnetic field along the z-axis and therefore to g_z (equation 6) according to equation (3):

$$g_z = g_e + [a^2 \, n \, \lambda / (E_{x2-y2} - E_{xy})] \qquad\qquad (6)$$

(a^2 = covalency parameter, n = quantum mechanical coefficient,

$\lambda(Cu^{2+})_{\text{free ion value}} = 830 \text{ cm}^{-1}$)

Moreover, by rotating the d_{x2-y2} orbital along the x- and the y-axis it is transformed into the d_{yz} and d_{xz} orbital. As the latter orbitals are degenerate the energy difference between the involved orbitals is equal contributing similarly to the g-shift:

$$\Delta E = (E_{x2-y2} - E_{yz}) = (E_{x2-y2} - E_{xz})$$

$$g_x = g_y = g_e + [a^2 \, n \, \lambda / (E_{x2-y2} - E_{yz,xz})]$$

(a^2 = covalency parameter, n = quantum mechanical coefficient,

$\lambda(Cu^{2+}) = 830 \text{ cm}^{-1}$)

Figure 13 shows the splitting of the d orbitals in the ligand field of a typical six-coordinate Jahn−Teller elongated copper(II) complex and displays the respective transitions and energy differences of the involved orbitals indicating that $g_z > g_x = g_y (> g_e)$.[91]
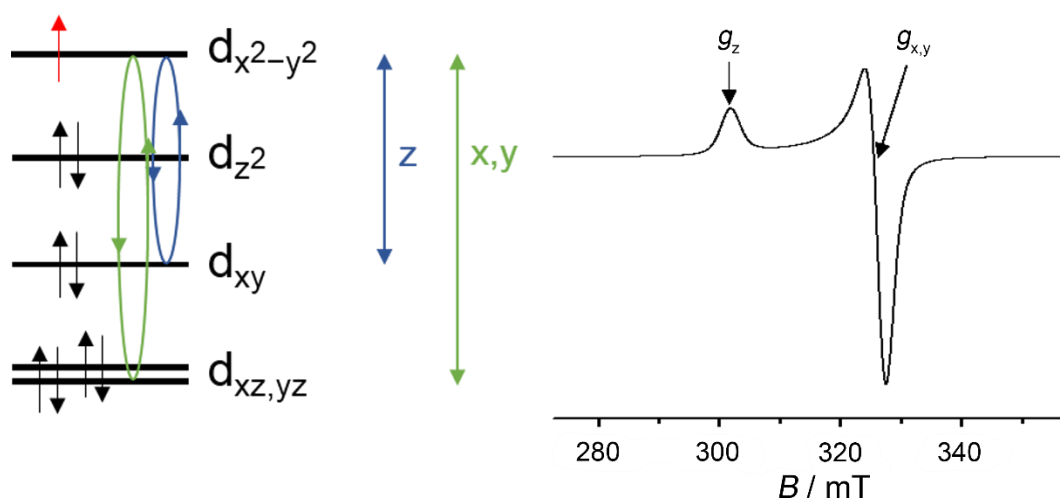

Figure 13. Ordering of d orbitals in a six-coordinate Jahn−Teller elongated copper(II) complex with D_{4h} symmetry and transitions contributing to the respective g-shift (left), and corresponding schematic axial anisotropic EPR spectrum (right).[91]

The EPR spectrum, exemplified in Figure 14, shows an axial anisotropic system, as well as hyperfine coupling featuring four signals, due to the nuclear spin of the two copper isotopes $I(^{63/65}Cu) = 3/2$, with ^{63}Cu and ^{65}Cu having a natural abundance of 100%. These two isotopes have similar gyromagnetic ratios and thus feature similar hyperfine coupling constants $A(^{63/65}Cu)$.[95] The hyperfine coupling constant in the z-direction, parallel to the magnetic field, is usually larger than the corresponding values in the x- and y-directions, which are therefore rarely resolved in the X-band spectra. In order to obtain the $A_{x,y}$-values, measurements can be performed at higher frequencies, for example using Q-band EPR

spectroscopy (34 GHz). Another possibility is the calculation of the $A_{x,y}$-values according to equation (4), if A_{iso} is known from isotropic measurements.
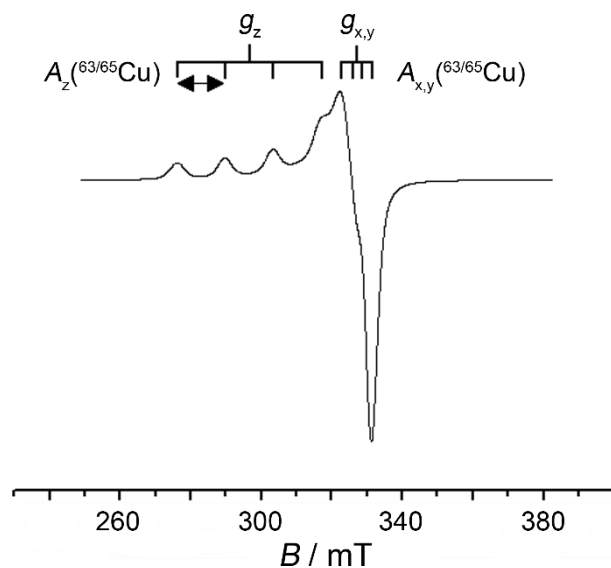
Figure 14. Axial anisotropic X-band spectrum of a copper(II) complex with hyperfine coupling $A(^{63/65}\mathrm{Cu})$.

On the contrary, in Jahn−Teller compressed copper(II) complexes the unpaired electron is located in the d_{z^2} orbital. Rotation along the z-axis affords no transformation of the d_{z^2} orbital, and the unpaired electron behaves like a free electron with $g_z \approx g_e$, whereas the rotation along the x- or the y-axis provides a transformation into the d_{yz} or the d_{xz} orbital, respectively. In this case the g-values obtained are arranged in the order: $g_x = g_y > g_z$ ($\approx g_e$). The corresponding schematic EPR spectrum is displayed in Figure 15.[91]

Figure 15. Ordering of d orbitals in a six-coordinate Jahn−Teller compressed copper(II) complex (left) and corresponding axial anisotropic spectrum (right).[91]

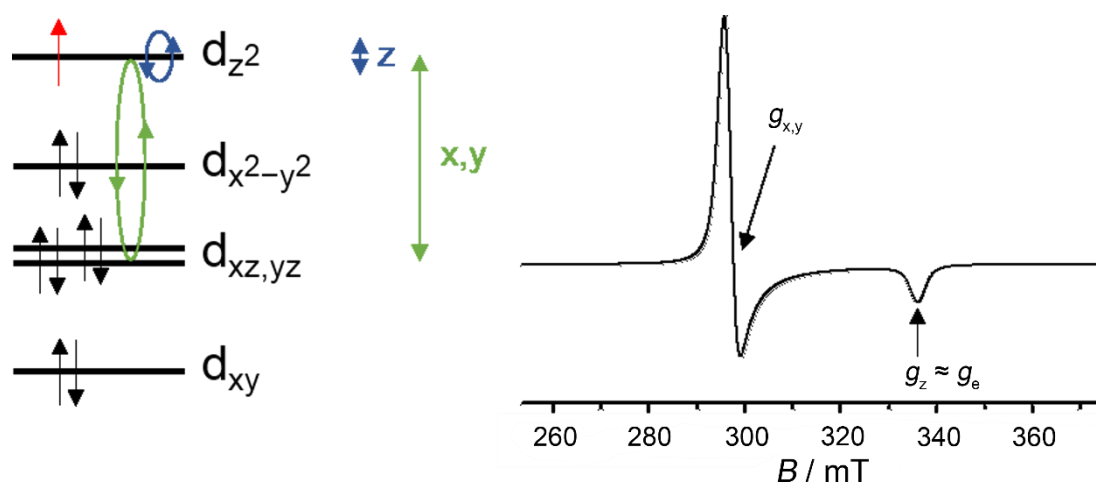The pattern of the EPR spectrum is therefore a useful tool for identifying the SOMO. The "magic pentagon" displayed in Figure 16 summarizes the contributions of all orbital rotations to the respective g-values. The values in blue color represent the quantum mechanical coefficient n (see equation (3)).[91]
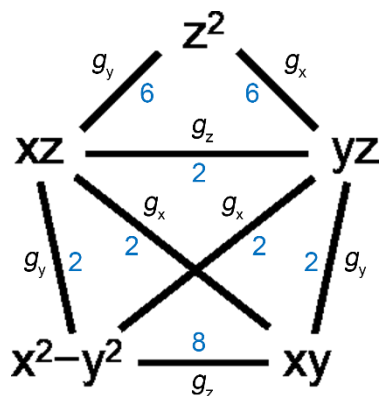

Figure 16. "Magic pentagon", the quantum mechanical coefficients n are given in blue.[91]

1.6.2.2 Molybdenum(V) complexes

Molybdenum(V) complexes representing d^1 systems are EPR active as well. In such mononuclear six-coordinate complexes with lower symmetry (e.g. D_{4h}) the unpaired electron is located in the energetically lowest d_{xy} orbital while all other d orbitals are empty, resulting in $g < g_e$ indicated by the "−" sign in equation (7). Transitions are possible due to rotation into the next energetically higher lying orbitals. In this example rotations of the d_{xy} orbital along the x- and the y-axes lead to the d_{xz} and the d_{yz} orbitals, which are degenerate, whereas rotation along the z-axis transforms the d_{xy} orbital into the d_{x2-y2} orbital. According to the energy differences between the respective orbitals the following g-values are observed:

$$g_x = g_y = g_e - [a^2\, n\, \lambda\, / \, (E_{xz,yz} - E_{xy})] \qquad \text{with } n = 2$$
$$g_z = g_e - [a^2\, n\, \lambda\, / \, (E_{x2-y2} - E_{xy})] \qquad \text{with } n = 8 \qquad (7)$$

$g_z < g_x = g_y\ (< g_e)$

(a^2 = covalency parameter, n = quantum mechanical coefficient (see Figure 16),

$\lambda(Mo^{5+})_{\text{free ion value}} = 1030\ \text{cm}^{-1}$)

Figure 17 shows the arrangement of the d orbitals in the ligand field and an exemplified axial anisotropic EPR spectrum typical for such molybdenum(V) complexes.[91]
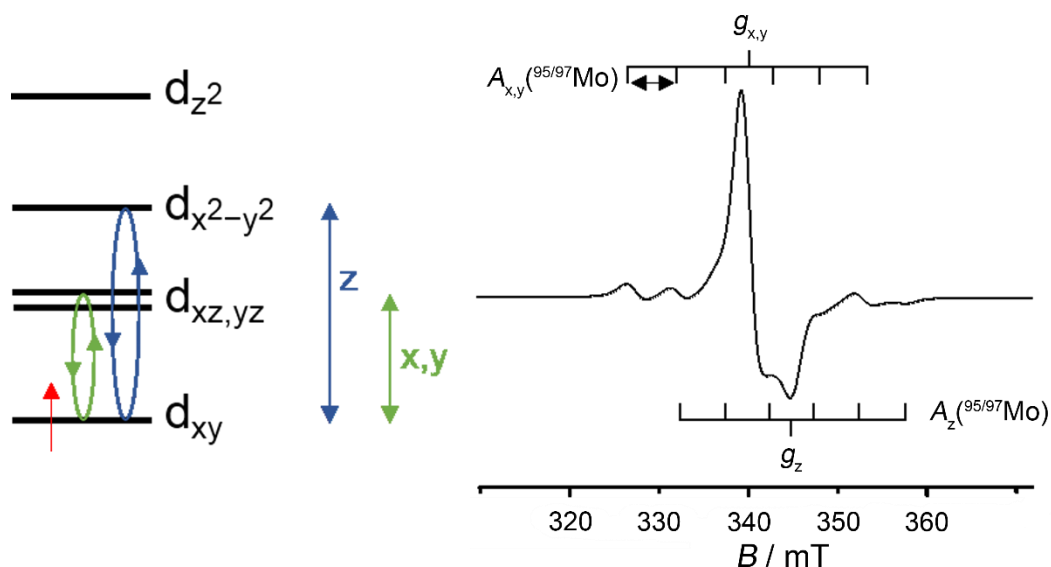
Figure 17. Axial ligand field for d^1 complexes (left) and axial anisotropic spectrum (right) with hyperfine coupling $A_{x,y}(^{95/97}Mo)$ and $A_z(^{95/97}Mo)$.[91]

Due to the hyperfine coupling to the nuclear spin of the ^{95}Mo and the ^{97}Mo isotopes with $I(^{95/97}Mo) = 5/2$ the g-values split into six signals with the respective direction dependent hyperfine coupling constants $A_{x,y,z}(^{95/97}Mo)$, which are similar for these two isotopes because of the similar gyromagnetic ratios.[95] As the natural abundance of these two isotopes is only 25% and as the remaining isotopes (75%) have no nuclear spin, $I(^{92/94/96/98/100}Mo) = 0$, the hyperfine coupling pattern in anisotropic spectra is often poorly resolved, additionally g- and A-tensors are not coincident, and thus hard to interpret. On the contrary, isotropic EPR measurements in fluid solution feature one main signal, a singlet for the 75% molybdenum isotopes with $I = 0$, as well as the six hyperfine coupling lines (satellites) corresponding to the remaining 25% molybdenum isotopes possessing $I = 5/2$, and thus showing smaller intensities of 4% each relative to the $I = 0$ resonance (Figure 18).
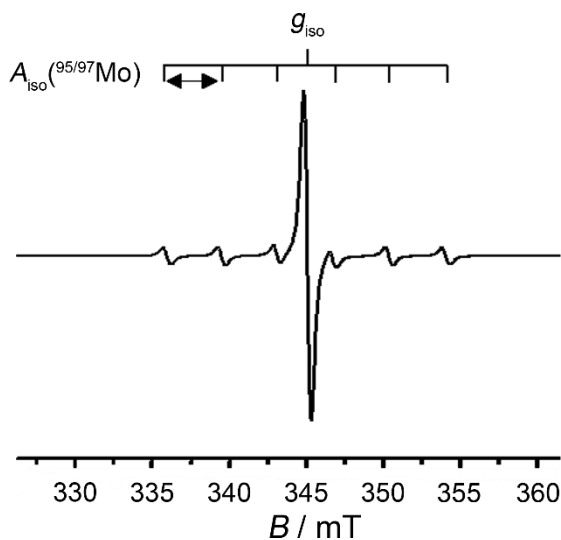

Figure 18. Typical isotropic EPR spectrum of a molybdenum(V) complex recorded in solution with g_{iso} and hyperfine coupling $A_{iso}(^{95/97}Mo)$.

Additionally to the hyperfine coupling, EPR spectra can also feature super hyperfine coupling as depicted in Figure 19. In this example of our group, an imido phosphane molybdenum(V) complex, the unpaired electron is located at the metal center and interacts with the molybdenum nucleus. Thus the spectrum shows the typical hyperfine satellite coupling pattern as depicted in Figure 18. But, as spin density is also located at the phosphane ligand, the unpaired electron interacts with the nuclear spin of phosphorus $I(^{31}P) = 1/2$ (natural abundance 100%). Due to this super hyperfine coupling each signal, the satellites as well as the main signal, splits into a doublet with a coupling constant $A_{iso}(^{31}P)$.[85]
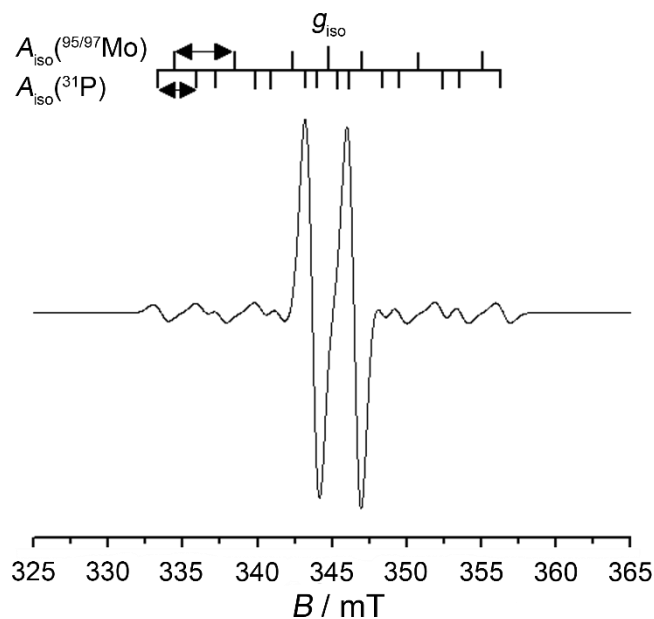
Figure 19. Isotropic EPR spectrum of a molybdenum(V) phosphane complex featuring hyperfine coupling $A_{iso}(^{95/97}Mo)$ and super hyperfine coupling $A_{iso}(^{31}P)$.[85]

To conclude, EPR spectroscopy provides a valuable method to investigate paramagnetic compounds both in solution and in the solid state according to their geometry, electronic structure, spin density and spin localization, physical properties, dynamics (performing temperature-dependent measurements), as well as with respect to their reactivity.

REFERENCES

[1]   E. Riedel, *Anorganische Chemie*, Walter de Gruyter GmbH & Co. KG, 6. Auflage, Berlin, New York, **2004**, 458.

[2]   W. Kaim, B. Schwederski, *Bioanorganische Chemie*, Teubner Verlag, 4. Auflage, Wiesbaden, **2005**, 231−241.

[3]   United States Geological Survey, *Mineral Commodity Summaries*, January **2012**.

[4]   a) www.ammoniaksynthese.de. Retrieved Aug. 31, 2009.

        b) https://web.archive.org/web/20071221132707/http://www.ammoniaksynthese.de/e0.html. Retrieved Mar. 05, 2014.

        c) http://www.basf.com/group/corporate/site-ludwigshafen/de_DE/function/conversions:/ publish/content/about-basf/worldwide/europe/Ludwigshafen/Education/Lernen_mit_der_ BASF/ammoniaksynthese/data/Ammoniaksynthese.pdf. Retrieved Apr. 15, 2014.

[5]   http://www.chemiedidaktik.ipn.uni-kiel.de/1992_umweltbelastung/dueng2.htm. Retrieved Apr. 16, 2014.

[6]   V. Smil, *Nature* **1999**, *400,* 415.

[7]   a) "Fritz Haber - Facts". *Nobelprize.org.* Nobel Media AB 2013. Retrieved Feb. 25, 2014. <http://www.nobelprize.org/nobel_prizes/chemistry/laureates/1918/haber-facts.html>.

        b) "The Nobel Prize in Chemistry 1931". *Nobelprize.org.* Nobel Media AB 2013. Retrieved Jun. 11, 2014. <http://www.nobelprize.org/nobel_prizes/chemistry/laureates/1931/>.

[8]   G. Ertl, *Angew. Chem*. **2008**, *120*, 3578−3590; *Angew. Chem. Int. Ed*. **2008**, *47*, 3524−3535.

[9]   "The Nobel Prize in Chemistry 2007". *Nobelprize.org.* Nobel Media AB 2013. Retrieved Feb. 25, 2014. <http://www.nobelprize.org/nobel_prizes/chemistry/laureates/2007/>.

[10]   R. Schloegl, *Angew. Chem*. **2003**, *115*, 2050−2055; *Angew. Chem. Int. Ed*. **2003**, *42*, 2004−2008.

[11]   J. Erfkamp, A. Müller, *Chemie in unserer Zeit* **1990**, *6*, 267−279.

[12]   K. Schneider, A. Müller, *Forschung an der Universität Bielefeld* **1999**, *20*, 43−49.

[13]   H.-P. Jia, E. A. Quadrelli, *Chem. Soc. Rev*. **2014**, *43*, 547−564.

[14]   J. B. Howard, D. C. Rees, *Chem. Rev*. **1996**, *96*, 2965−2982.

[15]   B. K. Burgess, D. J. Lowe, *Chem. Rev*. **1996**, *96*, 2983−3001.

[16]   B. M. Hoffman, D. R. Dean, L. C. Seefeldt, *Acc. Chem. Res*. **2009**, *42*, 609−619.

[17]   B. M. Hoffman, D. Lukoyanov, D. R. Dean, L. C. Seefeldt, *Acc. Chem. Res*. **2013**, *46*, 587−595.

[18]   a) J. Kim, D. C. Rees, *Science* **1992**, *257*, 1677–1682.

        b) M. K. Chan, J. Kim, D. C. Rees, *Science* **1993**, *260*, 792–794.

[19]   http://bcs.whfreeman.com/ichem4e/content/cat_020/moleculeshtml/ch26f45.html. Retrieved Mar. 05, 2014.

[20]   J. A. Hernandez, S. J. George, L. M. Rubio, *Biochemistry* **2009**, *48*, 9711−9721.

[21]   a) T. Spatzal, M. Aksoyoglu, L. Zhang, S. L. A. Andrade, E. Schleicher, S. Weber, D. C. Rees, O. Einsle, *Science* **2011**, *334*, 940.

        b) K. M. Lancaster, M. Roemelt, P. Ettenhuber, Y. Hu, M. W. Ribbe, F. Neese, U. Bergmann, S. DeBeer, *Science* **2011**, *334*, 974−977.

c) K. M. Lancaster, Y. Hu, U. Bergmann, M. W. Ribbe, S. DeBeer, *J. Am. Chem. Soc.* **2013**, *135*, 610−612.

[22] A. Müller, E. Krahn, *Angew. Chem.* **1995**, *107*, 1172−1179; *Angew. Chem. Int. Ed. Engl.* **1995**, *34*, 1071−1078.

[23] K. C. MacLeod, P. L. Holland, *Nat. Chem.* **2013**, *5*, 559−565.

[24] J. B. Howard, D. C. Rees, *Proc. Natl. Acad. Sci. USA* **2006**, 103, 17088−17093.

[25] D. V. Yandulov, R. R. Schrock, *Science* **2003**, *301*, 76−78.

[26] L. C. Seefeldt, B. M. Hoffman, D. R. Dean, *Annu. Rev. Biochem.* **2009**, *78*, 701−722.

[27] R. R. Eady, *Chem. Rev.* **1996**, *96*, 3013−3030.

[28] L. C. Seefeldt, I. G. Dance, D. R. Dean, *Biochemistry* **2004**, *43*, 1401−1409.

[29] K. Heinze, "Solid Phases as Protective Environments for Biomimetic Catalysts" in *Molecular Catalysts: Structure and Functional Design* (Eds.: L. H. Gade, P. Hofmann), Wiley-VCH, Weinheim, **2014**, 423−452.

[30] W. Kaim, B. Schwederski, *Bioanorganische Chemie*, Teubner Verlag, 4. Auflage, Wiesbaden, **2005**, 39.

[31] a) A. D. Allen, C. V. Senoff, *Chem. Commun.* **1965**, 621−622.

b) A. D. Allen, F. Bottomley, R. O. Harris, V. P. Reinsalu, C. V. Senoff, *J. Am. Chem. Soc.* **1967**, *89*, 5595−5599.

[32] S. Hinrichsen, H. Broda, C. Gradert, L. Söncksen, F. Tuczek, *Annu. Rep. Prog. Chem., Sect. A: Inorg. Chem.* **2012**, *108*, 17−47.

[33] M. D. Fryzuk, *Chem. Commun.* **2013**, *49*, 4866−4868.

[34] H.-J. Himmel, M. Reiher, *Angew. Chem.* **2006**, *118*, 6412−6437; *Angew. Chem. Int. Ed.* **2006**, *45*, 6264−6288.

[35] B. A. MacKay, M. D. Fryzuk, *Chem. Rev.* **2004**, *104*, 385−401.

[36] J. Chatt, A. J. Pearman, R. L. Richards, *Nature* **1975**, *253*, 39−40.

[37] A. Takaoka, L. C. H. Gerber, J. C. Peters, *Angew. Chem.* **2010**, *122*, 4182−4185; *Angew. Chem. Int. Ed.* **2010**, *49*, 4088−4091.

[38] B. Askevold, J. T. Nieto, S. Tussupbayev, M. Diefenbach, E. Herdtweck, M. C. Holthausen, S. Schneider, *Nat. Chem.* **2011**, *3*, 532−537.

[39] M. G. Scheibel, B. Askevold, F. W. Heinemann, E. J. Reijerse, B. de Bruin, S. Schneider, *Nat. Chem.* **2012**, *4*, 552−558.

[40] S. Pfirrmann, S. Yao, B. Ziemer, R. Stösser, M. Driess, C. Limberg, *Organometallics* **2009**, *28*, 6855−6860.

[41] H. Kropp, A. E. King, M. M. Khusniyarov, F. W. Heinemann, K. M. Lancaster, S. DeBeer, E. Bill, K. Meyer, *J. Am. Chem. Soc.* **2012**, *134*, 15538−15544.

[42] a) M. Hidai, Y. Mizobe, Y. Uchida, *J. Am. Chem. Soc.* **1976**, *88*, 7824−7825.

b) M. Hidai, *Coord. Chem. Rev.* **1999**, *185−186*, 99−108.

[43] J. Chatt, J. R. Dilworth, R. L. Richards, *Chem. Rev.* **1978**, *78*, 589−625.

[44] J. Chatt, A. J. Pearman, R. L. Richards, *J. Chem. Soc., Dalton Trans.* **1978**, 1766−1776.

[45] C. J. Pickett, J. Talarmin, *Nature* **1985**, *317*, 652−653.

[46] N. Lehnert, F. Tuczek, *Inorg. Chem.* **1999**, *38*, 1659−1670.

[47]   N. Lehnert, F. Tuczek, *Inorg. Chem.* **1999**, *38*, 1671−1682.

[48]   T. A. George, B. B. Kaul, *Inorg. Chem.* **1990**, *29*, 4969−4974.

[49]   H. Broda, S. Hinrichsen, F. Tuczek, *Coord. Chem. Rev.* **2013**, *257*, 587−598.

[50]   J. A. Baumann, T. A. George, *J. Am. Chem. Soc.* **1980**, *102*, 6153−6154.

[51]   T. A. George and R. C. Tisdale, *J. Am. Chem. Soc.* **1985**, *107*, 5157−5159.

[52]   T. A. George, L. Ma, S. N. Shailh, R. C. Tisdale, J. Zubieta, *Inorg. Chem.* **1990**, *29*, 4789−4796.

[53]   K. Klatt, G. Stephan, G. Peters, F. Tuczek, *Inorg. Chem.* **2008**, *47*, 6541−6550.

[54]   J. Krahmer, H. Broda, C. Näther, G. Peters, W. Thimm, F. Tuczek, *Eur. J. Inorg. Chem.* **2011**, *28*, 4377−4386.

[55]   C. E. Laplaza, C. C. Cummins, *Science* **1995**, *268*, 861−863.

[56]   C. E. Laplaza, M. J. A. Johnson, J. C. Peters, A. L. Odom, E. Kim, C. C. Cummins, G. N. George, I. J. Pickering, *J. Am. Chem. Soc.* **1996**, *118*, 8623−8638.

[57]   M. Kol, R. R. Schrock, R. Kempe, W. M. Davis, *J. Am. Chem. Soc.* **1994**, *116*, 4382−4390.

[58]   G. E. Greco, R. R. Schrock, *Inorg. Chem.* **2001**, *40*, 3861−3878.

[59]   W. W. Weare, R. R. Schrock, A. S. Hock, P. Müller, *Inorg. Chem.* **2006**, *45*, 9185−9196.

[60]   D. V. Yandulov, R. R. Schrock, *J. Am. Chem. Soc.* **2002**, *124*, 6252−6253.

[61]   D. V. Yandulov, R. R. Schrock, A. L. Rheingold, C. Ceccarelli, W. M. Davis, *Inorg. Chem.* **2003**, *42*, 796−813.

[62]   D. V. Yandulov, R. R. Schrock, *Inorg. Chem.* **2005**, *44*, 1103−1117.

[63]   W. W. Weare, X. Dai, M. J. Byrnes, J. M. Chin, R. R. Schrock, P. Müller, *Proc. Natl. Acad. Sci. USA* **2006**, *103*, 17099−17106.

[64]   F. Studt, F. Tuczek, *Angew. Chem.* **2005**, *117*, 5783−5787; *Angew. Chem. Int. Ed.* **2005**, *44*, 5639−5642.

[65]   S. Schenk, B. Le Guennic, B. Kirchner, M. Reiher, *Inorg. Chem.* **2008**, *47*, 3634−3650.

[66]   V. Ritleng, D. V. Yandulov, W. W. Weare, R. R. Schrock, A. S. Hock, W. M. Davis, *J. Am. Chem. Soc.* **2004**, *126*, 6150−6163.

[67]   M. F. Cain, W. P. Forrest, Jr., D. V. Peryshkov, R. R. Schrock, P. Müller, *J. Am. Chem. Soc.* **2013**, *135*, 15338−15341.

[68]   K. Arashiba, Y. Miyake, Y. Nishibayashi, *Nat. Chem.* **2011**, *3*, 120−125.

[69]   J. S. Anderson, J. Rittle, J. C. Peters, *Nature* **2013**, 501, 84−88.

[70]   R. B. Merrifield, *J. Am. Chem. Soc.* **1963**, *85*, 2149−2154.

[71]   M. D. Lechner, K. Gehrke, E. H. Nordmeier, *Makromolekulare Chemie*, Birkhäuser Verlag, 4. Auflage, Basel, Boston, Berlin, **2010**, pages 24, 232, 233.

[72]   J. S. Früchtel, G. Jung, *Angew. Chem.* **1996**, *108*, 19−46; *Angew. Chem. Int. Ed. Engl.* **1996**, *35*, 17−42.

[73]   K. Heinze, J. D. B. Toro, *Angew. Chem.* **2003**, *115*, 4671−4674; *Angew. Chem. Int. Ed.* **2003**, *42*, 4533−4536.

[74]   D. Siebler, C. Förster, K. Heinze, *Dalton Trans.* **2011**, *40*, 3558−3575.

[75]   A. J. Moffat, *J. Catal.* **1970**, *18*, 193−199.

[76] http://www.ptonline.com/knowledgecenter/Plastics-Drying/Resin-Types/Hygroscopic-VS-Non-Hygroscopic-Resins. Retrieved Apr. 16, 2014.

[77] J. C. Bailar, Jr., "Heterogenizing" Homogeneous Catalysts in *Catalysis Reviews: Science and Engineering*, **1974**, *10*, 17−36.

[78] A. Döring, W. Birnbaum, D. Kuckling, *Chem. Soc. Rev.* **2013**, *42*, 7391−7420.

[79] D. Xuereb, J. Dzierzak, R. Raja, "Biomimetic Single-Site Heterogeneous Catalysts: Design Strategies and Catalytic Potential" in *Catalysis by Metal Complexes 33: Heterogenized Homogeneous Catalysts for Fine Chemicals Production,* (Eds.: P. Barbaro, F. Ligiari), Springer, Dordrecht, **2010**, chapter 2.

[80] J. M. Notenstein, A. Katz, *Chem. Eur. J.* **2006**, *12*, 3954−3965.

[81] L. L. Welbes, A. S. Borovik, *Acc. Chem. Res.* **2005**, *38*, 765−774.

[82] D. E. De Vos, I. F. J. Vankelecom, P. A. Jacobs (Eds.), *Chiral Catalyst Immobilization and Recycling*, Wiley-VCH, Weinheim, **2007**.

[83] M. Heitbaum, F. Glorius, I. Escher, *Angew. Chem.* **2006**, *118*, 4850−4881; *Angew. Chem. Int. Ed.* **2006**, *45*, 4732−4762.

[84] O. Leal, D. L. Anderson, R. G. Bowman, F. Basolo, R. L. Burwell, Jr., *J. Am. Chem. Soc.* **1975**, *97*, 5125−5129.

[85] K. Hüttinger, C. Förster, T. Bund, D. Hinderberger, K. Heinze, *Inorg. Chem.* **2012**, 51, 4180−4192.

[86] K. Heinze, A. Fischer, *Eur. J. Inorg. Chem.* **2007**, 1020−1026.

[87] K. Heinze, A. Fischer, *Eur. J. Inorg. Chem.* **2010**, 1939−1947.

[88] K. Heinze, G. Marano, A. Fischer, *J. Inorg. Biochem.* **2008**, *102*, 1199−1211.

[89] J. M. Thomas, R. Raja, D. W. Lewis, *Angew. Chem.* **2005**, *117*, 6614−6641; *Angew. Chem. Int. Ed.* **2005**, *44*, 6456−6482.

[90] G. Jeschke, *Einführung in die ESR-Spektroskopie*, Vorlesungsskript, Universität Konstanz, **2007**.

[91] D. Collison, The EPSRC UK National Electron Paramagnetic Resonance Service at the University of Manchester, *Introductory Workshop on the Theory and Practice of EPR spectroscopy*, lecture notes, **2013** and references reported therein.

[92] J. Melomedov, A. Wünsche von Leupoldt, M. Meister, F. Laquai, K. Heinze, *Dalton. Trans.* **2013**, *42*, 9727−9739.

[93] J. Dietrich, A. Wünsche von Leupoldt, M. Grabolle, U. Resch-Genger, K. Heinze, *Eur. J. Inorg. Chem.* **2013**, 3009−3019.

[94] A. Breivogel, M. Meister, C. Förster, F. Laquai, K. Heinze, *Chem. Eur. J.* **2013**, *19*, 13745−13760.

[95] http://pse.science-and-fun.de/pages/molybdaen.php. Retrieved May 27, 2014.

2. AIM OF WORK

The objective of this work is to combine the advantages of heterogeneous and homogeneous catalysis synthesizing a polystyrene-supported Schrock-type molybdenum complex with a monodentate N_xH_y ligand, which serves as starting material to investigate the mechanism of ammonia synthesis according to the literature known Schrock cycle. Due to the site isolation of the reaction centers on the solid support and the polystyrene backbone acting as protective environment, side reactions of bimolecular nature should be suppressed. Thus it is expected to realize the isolation of new intermediates of the proposed catalytic cycle, which are unstable in Schrock's homogeneous catalytic system. Especially, the analysis of immobilized molybdenum(V) complexes with the help of EPR spectroscopy is the main focus of this work.

A further important aim is the investigation of this immobilized complex concerning its ability to produce ammonia in the presence of a proton source and an electron source based on the methods reported by Schrock *et al*. Therefore, different reaction conditions can be applied to optimize the yield of ammonia obtained from this reaction, and to determine whether this heterogeneous process is catalytic or not.

Additionally to these molybdenum compounds, another emphasis is placed on the studies of copper(II) complexes featuring temperature-dependent Jahn−Teller dynamics. These effects should be observed and analyzed by means of EPR spectroscopy.

3. RESULTS AND DISCUSSION

In the following section the results of this work are presented as a collection of manuscripts and publications.

The first manuscript deals with the preparation of tetrachlorido molybdenum(IV) and trichlorido nitrido molybdenum(VI) precursor complexes from molybdenum(V) pentachloride according to literature known methods. These compounds were implemented in a subsequent complex synthesis using a sterically unencumbered tripodal triamidoamine ligand and different bases. The successful preparation of the chlorido molybdenum(IV) complex is reported as well as a new reaction pathway leading to the nitrido molybdenum(VI) complex, a stable intermediate of the Schrock cycle, in a single reaction step. This reaction represents a new way to enter the Schrock cycle.

The second chapter presents the publication on "Proton and Electron Transfer to a Polymer-Supported Nitrido Molybdenum(VI) Complex". The X-ray data reported therein were analyzed by ████████ ████. ██████████, research associate in the group of █████████████ (Johannes Gutenberg University of Mainz), was responsible for the ICP-MS measurements. In this paper, which was published in the *European Journal of Inorganic Chemistry*, the synthesis of the nitrido molybdenum(VI) complex is described in detail as well as the successful application of this reaction procedure to solid phase chemistry. The polymer-supported nitrido molybdenum(VI) complex was prepared using a polymer-anchored triamidoamine ligand. The reactivity of both complexes, the soluble and the polymer-immobilized nitrido molybdenum(VI) complexes, towards protons and electrons was investigated as these reactions are relevant to the final steps in the Schrock cycle leading to ammonia release. In the first step the soluble and the polymer-confined nitrido molybdenum(VI) complexes are protonated at the nitrido ligand to form the corresponding imido complexes. One-electron reduction of the soluble imido molybdenum(VI) complex is irreversible, probably due to bimolecular side reactions such as disproportionation, dimerization or disadvantageous redox chemistry. However, single-electron transfer to the polymer-anchored imido complex by cobaltocene gave the imido molybdenum(V) complex, which is sufficiently stable for spectroscopic characterization. In contrast to the soluble analogue, bimolecular reactions are suppressed due to the immobilization of the complexes onto the solid support. The electron paramagnetic resonance (EPR) spectra of the immobilized d^1 complex and its *N*-deuterated congener reveal spin density on the molybdenum center and the axial imido ligand corroborating the successful synthesis of this intermediate of the Schrock cycle.

Further investigations on polymer-supported nitrido molybdenum(VI) complexes with respect to ammonia release in the presence of a proton and an electron source are presented in the third chapter. ICP-MS measurements reported therein were performed and analyzed by ███████████, research associate in the group of ████████████████ (Johannes Gutenberg University of Mainz). The amount of released ammonia was studied and optimized by applying different reaction conditions (solvents). Additionally, EPR spectra of immobilized nitrato copper(II) complexes were recorded at different temperatures in different solvents providing information about the effective isolation of immobilized complexes. The experiments revealed the strong dependence of the reactivity and the accessibility of immobilized reaction centers on the type of solvent. This is an important aspect for the optimization of ammonia release from the immobilized nitrido molybdenum(VI) complexes.

In the last section, the publication on the "Effect of Chelate Ring Expansion on Jahn−Teller Distortion and Jahn−Teller Dynamics in Copper(II) Complexes" is presented. My contributions to this work, which was published in *Inorganic Chemistry*, included the performance and analysis of electrochemical experiments and the recording and simulation of the variable temperature X-band CW EPR spectra. The synthesis of all reported copper(II) complexes was performed by ████████████. ███████████, research associate in the group of █████████████████ (Max Planck Institute for Polymer Research), was responsible for the measurements and simulations of pulsed X-band EPR spectra, and ████████████████ and ██████████████████ analyzed the X-ray data. The copper(II) complex *mer*-$[Cu^{II}(ddpd)_2](BF_4)_2$ containing the tridentate ddpd ligand, which coordinates in a meridional fashion, was investigated at different temperatures. In the solid state at low temperatures ($T < 100$ K) the complex cations localize in Jahn–Teller elongated polyhedra featuring the longest Cu–N bond pointing in the molecular x or y directions whereby the z axis is constrained by the tridentate ddpd ligand. Increasing the temperature results in dynamically averaged (fluxional) polyhedra in the molecular x and y directions, which were observed by multifrequency variable temperature EPR measurements and by variable temperature X-ray diffraction studies.

Contents:

3.1 [(^{xyl}N$_3$N)Mo^{IV}Cl] and [(^{xyl}N$_3$N)Mo^{VI}N] Complexes as Entrance into the Schrock Cycle −
Preparation of suitable precursors

Anica Wünsche von Leupoldt, Katja Heinze

3.2 Proton and Electron Transfer to a Polymer-Supported Nitrido Molybdenum(VI) Complex

Anica Wünsche von Leupoldt, Christoph Förster, Tobias J. Fiedler, Nicolas H. Bings, Katja Heinze

Published in: *Eur. J. Inorg. Chem.* **2013**, *36*, 6079−6090.

[DOI:10.1002/ejic.201301156]

http://onlinelibrary.wiley.com/doi/10.1002/ejic.201301156/pdf

3.3 Reactivity of a Polymer-Supported Nitrido Molybdenum(VI) Complex towards Protons and Electrons

Anica Wünsche von Leupoldt, Dorothée Iffland, Nicolas H. Bings, Katja Heinze

3.4 Effect of Chelate Ring Expansion on Jahn−Teller Distortion and Jahn−Teller Dynamics in Copper(II) Complexes

Katharina Mack, Anica Wünsche von Leupoldt, Christoph Förster, Maria Ezhevskaya, Dariush Hinderberger, Karl W. Klinkhammer, Katja Heinze

Published in: *Inorg. Chem.* **2012**, *51*, 7851−7858.

[DOI:10.1021/ic300929g]

http://pubs.acs.org/doi/ipdf/10.1021/ic300929g

3.1 $[(^{xyl}N_3N)Mo^{IV}Cl]$ and $[(^{xyl}N_3N)Mo^{VI}N]$ Complexes

       as Entrance into the Schrock Cycle – Preparation of suitable precursors

*Anica Wünsche von Leupoldt, Katja Heinze*

ABSTRACT

The reliable synthesis of stable molybdenum complex precursors are important steps as these are used as starting materials for the preparation of molybdenum complexes relevant to the Schrock cycle for NH_3 formation. The tetrachlorido molybdenum(IV) precursor with labile CH_3CN ligands, $[Mo^{IV}Cl_4(CH_3CN)_2]$ (**II**), as well as the trichlorido nitrido molybdenum(VI) acetonitrile precursor complex, $[Mo^{VI}Cl_3N(CH_3CN)]_4$ (**III**), have been prepared according to literature known methods. Subsequent complexation reactions to give $[(^{xyl}N_3N)Mo^{IV}Cl]$ (**IV**) and $[(^{xyl}N_3N)Mo^{VI}N]$ (**5**) using the ligand 2,2′,2″-tris(3,5-dimethylphenylamino)triethylamine $[^{xyl}N_3N]H_3$ and different bases have been investigated by paramagnetic ^1H NMR spectroscopy. In the case of the chlorido molybdenum(IV) complex **IV** the use of $LiN(SiMe_3)_2$ was successful, whereas the synthesis of the nitrido molybdenum(VI) complex **5** was achieved using the base $LiNMe_2$.

1. INTRODUCTION

The studies of catalytic ammonia synthesis from dinitrogen using model complexes is of enormous interest. Scientists try to understand the mechanism of this complex reaction and search for new compounds, homogeneous transition-metal catalysts, which perform the activation of dinitrogen and its reduction to ammonia under ambient conditions.

In 2003 Schrock *et al.* reported on a molybdenum complex, with a sterically encumbered tripodal ligand, 2,2′,2″-tris(hexaisopropylterphenyl)triethylamide $[^{HIPT}N_3N]^{3-}$, which is capable to activate dinitrogen, and they were able to isolate a dinitrogen molybdenum(III) complex, $[(^{HIPT}N_3N)Mo^{III}(N_2)]$.[1] This performs catalytic ammonia production from N_2 at room temperature yielding 7−8 equivalents, based on $Mo(N_2)$, corresponding to four turnovers. Besides the observation of catalytic activity, the reaction mechanism including the isolation of several intermediates of the catalytic cycle has been studied. These experiments and additional DFT calculations[2,3] allowed to postulate the so called Schrock cycle depicted in Scheme 1. Several precursor complexes were used as starting material for the respective complex synthesis by Schrock *et al.* The complex $[(^{HIPT}N_3N)Mo^{IV}Cl]$ is of considerable interest as it

represents the basic starting compound for several N_xH_y containing complexes involved in the Schrock cycle. Especially the dinitrogen fixation realized by $[(^{HIPT}N_3N)Mo^{IV}Cl]$, under dinitrogen atmosphere in the presence of strong reducing agents such as magnesium[1], sodium amalgam[5] or sodium naphthalenide[6] is an important step yielding the complex $[(^{HIPT}N_3N)Mo^{II}(N_2)]^-$. Subsequent one electron oxidation with a Zn^{2+} salt leads to the formation of the neutral complex $[(^{HIPT}N_3N)Mo^{III}(N_2)]$ indicating the starting point of ammonia synthesis from molecular dinitrogen (Scheme 1, top).[1,4,7]

Scheme 1. Overview of the Schrock cycle (proposed intermediates given in dotted boxes) with common entries $[LMo^{III}(N_2)]$ (top) and $[LMo^{VI}N]$ (down right), with $L = (^{HIPT}N_3N)$, highlighted by grey boxes.[7]

Concerning the synthesis of $[(^{HIPT}N_3N)Mo^{IV}Cl]$ several routes are conceivable as illustrated in Scheme 2. In the first route **A** the precursor complex $Mo^{IV}Cl_4(THF)_2$ is converted into the desired complex $[(^{HIPT}N_3N)Mo^{IV}Cl]$ by substitution of THF and chlorido ligands by the ligand $[^{HIPT}N_3N]H_3$ in the presence of the base lithium hexamethyldisilazane, $LiN(SiMe_3)_2$.[1] Another reaction pathway is depicted by route **B** involving the precursor $Mo^{IV}(NMe_2)_4$, carrying the intrinsic base dimethylamide, which reacts with $[^{HIPT}N_3N]H_3$ to yield the complex $[(^{HIPT}N_3N)Mo^{IV}(NMe_2)]$ in a first step. Subsequent

treatment with 2,6-lutidinium chloride leads to the formation of [(^{HIPT}N$_3$N)Mo^{IV}Cl] by substitution of dimethylamide by chloride.[8]
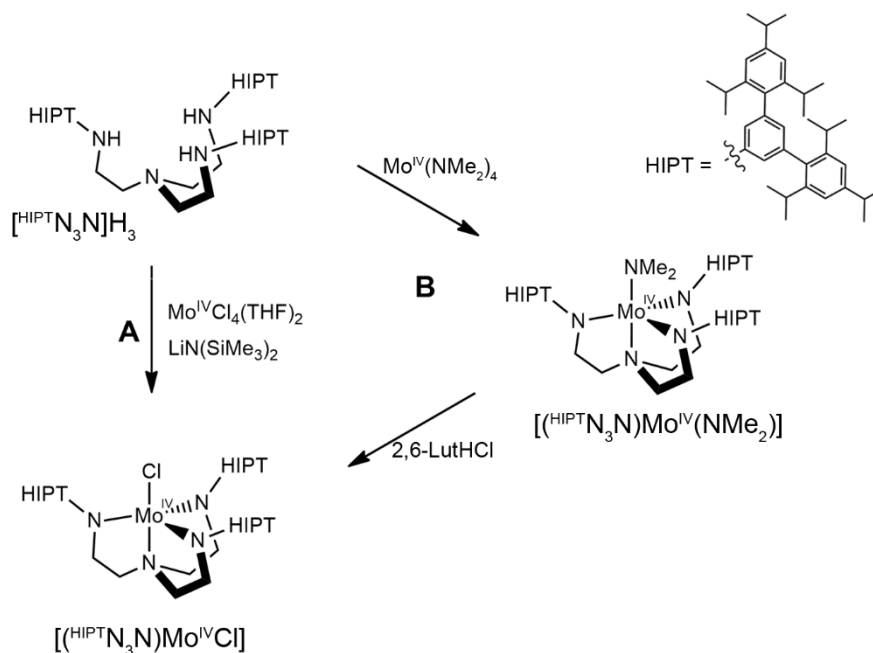
Scheme 2. Synthesis of [(^{HIPT}N$_3$N)Mo^{IV}Cl] starting from [^{HIPT}N$_3$N]H$_3$, route **A** (left), route **B** (right).

In addition the complex [(^{HIPT}N$_3$N)Mo^{IV}Cl] is used as starting material for the preparation of the nitrido molybdenum(VI) complex [(^{HIPT}N$_3$N)Mo^{VI}N], whereby NaN$_3$ or (Me$_3$Si)N$_3$ are employed as nitrogen sources and oxidants (Scheme 3, route **C**).[1] Starting from this stable nitrido molybdenum(VI) complex, representing another possible entry opportunity into the catalytic circle, the second half of the Schrock cycle leading to the formation of the second molecule of ammonia can be examined. In the last years Schrock *et al.* developed an alternative reaction pathway for the synthesis of such nitrido molybdenum(VI) complexes displayed in Scheme 3 (route **D**) involving a nitrido molybdenum(VI) precursor with an internal amido base, Mo^{VI}N(NMe$_2$)$_3$.
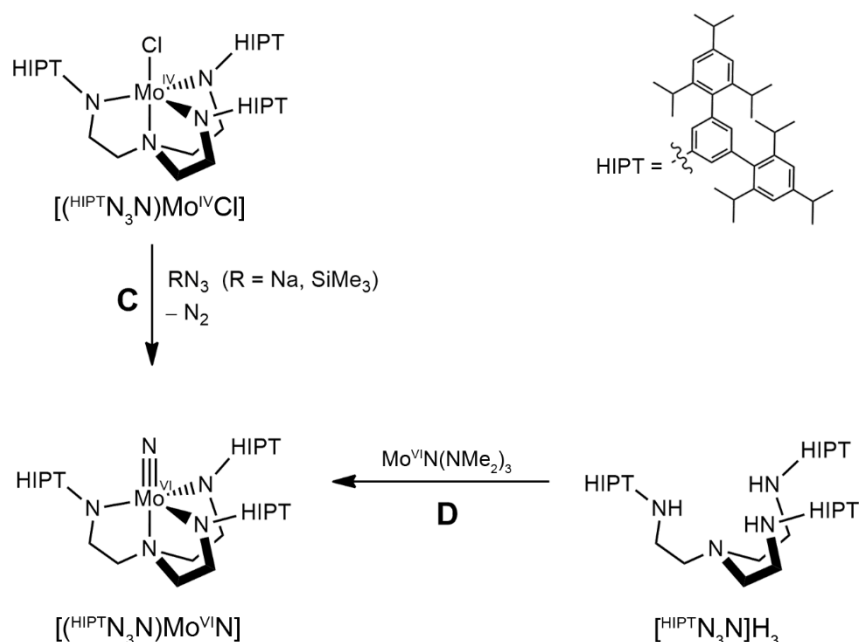
Scheme 3. Synthesis of [(^{HIPT}N$_3$N)Mo^{VI}N] starting from [(^{HIPT}N$_3$N)Mo^{IV}Cl] (route **C**, left), using the precursor Mo^{VI}N(NMe$_2$)$_3$ (route **D**, right).

Although route **D** has been established in Schrock's group and has been applied for new triamidoamide nitrido molybdenum(VI) complexes[9], the multi-step synthesis of the required precursor[10,11] depicted in Scheme 4 presents a serious disadvantage.
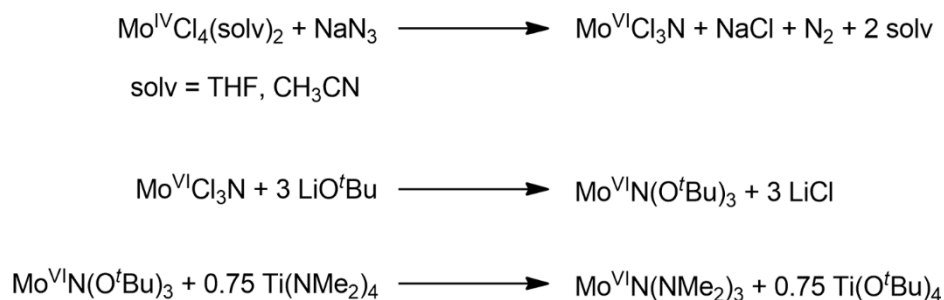

Scheme 4. Multi-step synthesis of Mo^{VI}N(NMe$_2$)$_3$.

Our attempts to synthesize the literature known molybdenum precursor compounds, Mo^{IV}(NMe$_2$)$_4$[12], Mo^{IV}Cl$_4$(CH$_3$CN)$_2$[13] and [Mo^{VI}Cl$_3$N(CH$_3$CN)]$_4$[14] are reported here, as well as the corresponding chlorido molybdenum(IV) and nitrido molybdenum(VI) complexes, [(^{xyl}N$_3$N)Mo^{IV}Cl][8] and [(^{xyl}N$_3$N)Mo^{VI}N], and a novel pathway to enter the Schrock cycle.
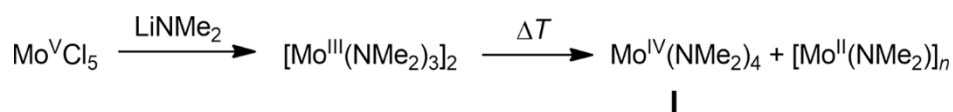
2. RESULTS AND DISCUSSION

The synthesis of the different literature known molybdenum precursor complexes (**I−III**) is depicted in Scheme 5. Starting from these precursors we tried to synthesize the respective molybdenum triamidoamide complexes, the literature known chlorido molybdenum complex (**IV**) and the novel nitrido molybdenum complex (**5**), using different reaction conditions. As a tripodal ligand the sterically less encumbered triamidoamine ligand 2,2′,2″-tris(3,5-dimethylphenylamino)triethylamine $[^{xyl}N_3N]H_3$ was chosen.[15]
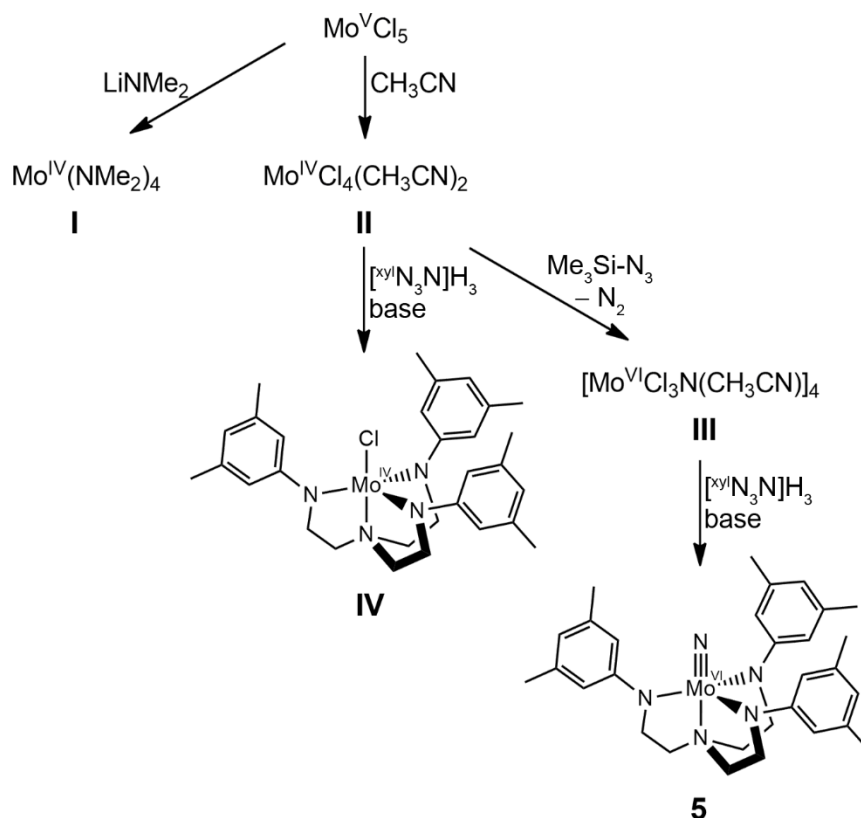
Scheme 5. Synthesis of molybdenum precursor complexes **I**, **II**, **III** and the corresponding complexes **IV** and **5**.

The synthesis of $Mo^{IV}(NMe_2)_4$ (**I**) was performed according to Chisholm *et al.*[12] Molybdenum(V) pentachloride was added slowly in small portions through a short glass bridge to a mixture of lithium dimethylamide in THF and petroleum ether (40−60°C) at 0°C. Addition of solid $MoCl_5$ has been carried out carefully to avoid overheating of the reaction mixture. However, in our attempt, we observed that the solvent warmed up and evaporated. In consequence the evaporated tetrahydrofuran condensed in the flask containing the solid $MoCl_5$ forming clumps which got stuck inside the connecting glass tube. Therefore, it took several hours to add all molybdenum pentachloride and to complete the reaction. Subsequent evaporation of the solvent under reduced pressure left a brown solid in the reaction flask indicating the presence of initially formed dimer di[tris(dimethylamido)molybdenum(III)]. Heating the

brown residue in the reaction flask initiates the disproportionation of the Mo^{III} dimer into polymeric dimethylamido molybdenum(II) and the desired purple colored product **I** as illustrated in Scheme 6.[12]

$$Mo^VCl_5 \xrightarrow{\text{LiNMe}_2} [Mo^{III}(NMe_2)_3]_2 \xrightarrow{\Delta T} Mo^{IV}(NMe_2)_4 + [Mo^{II}(NMe_2)]_n$$

$$\textbf{I}$$

Scheme 6. Reaction pathways for the synthesis of **I**.

During removal of the last traces of solvent under reduced pressure traces of the purple product already appeared in the liquid nitrogen trap indicating the success of the reaction. The liquid nitrogen cold trap was changed, and the sublimation of the low melting product **I** was continued the next day. However, all attempts to isolate the purple solid requiring separation from $[Mo^{III}(NMe_2)_3]_2$ and $[Mo^{II}(NMe_2)]_n$ were unsuccessful. As this reaction is known to give only low yields (roughly 10%) it is conceivable that the product **I** decomposed completely overnight via reaction with air and moisture. Possibly, the flask was not sealed tightly. The ^1H NMR spectrum (Figure 1) of the brown residue in the reaction flask recorded in C_6D_6 shows no signal of the product **I**, expected at $\delta = 3.27$ ppm[16], but corroborates the hydrolytic decomposition yielding dimethylamine ($\delta = 3.44, 2.20$ ppm). Additionally, it reveals that the solvent THF ($\delta = 3.58, 1.42$ ppm) was not completely removed under reduced pressure. As there was no evidence for a successful preparation of **I**, the brown residue was not further investigated.
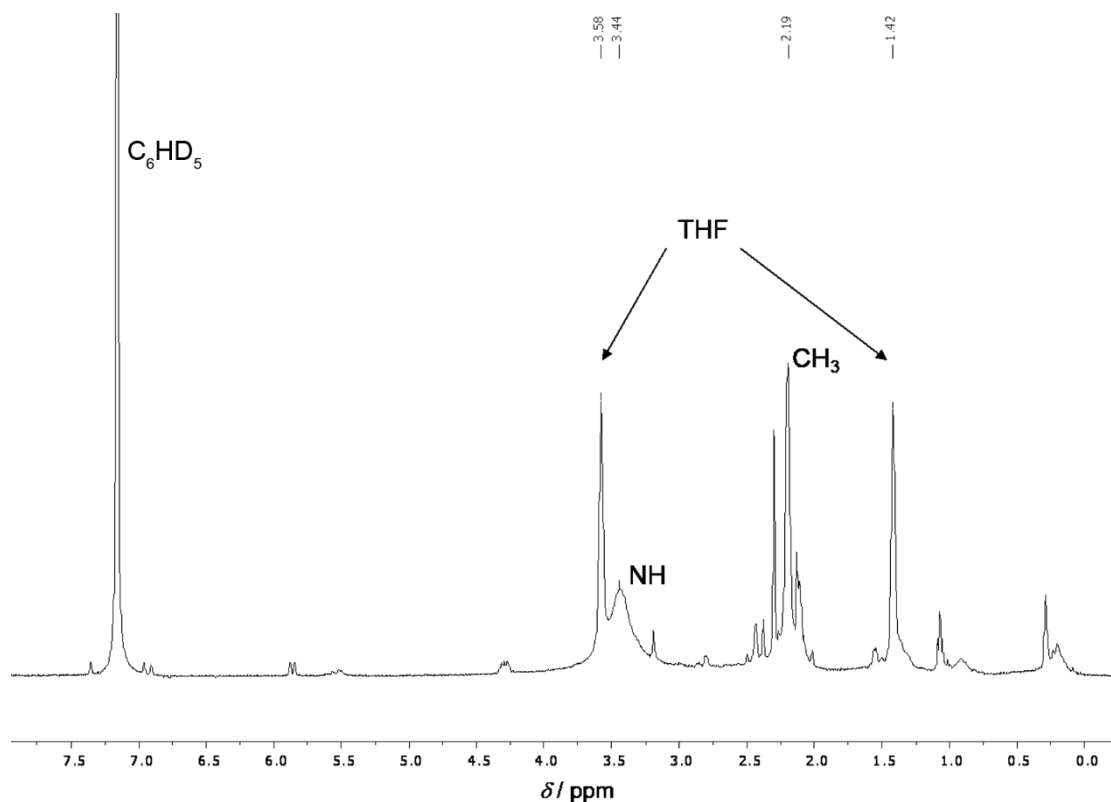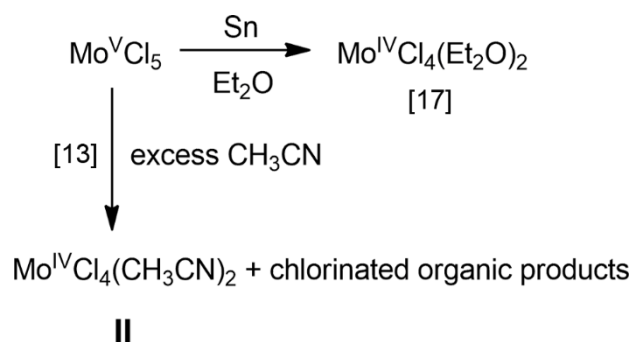

Figure 1. ^1H NMR spectrum of the brown residue from the reaction of $MoCl_5$ with $LiNMe_2$ in C_6D_6.

For future work, it might be advisable to continue the sublimation right after the evaporation of the solvents. In addition, in the literature known method a petroleum ether mixture with a boiling point range of 35−75°C was used for the synthesis. This could hinder the evaporation of the solvent and therefore facilitate the addition of the solid $MoCl_5$. As an alternative, Kuiper *et al.* reported on a method to synthesize the precursor **I** using $MoCl_4(OEt_2)_2$ and $LiNMe_2$ in 25% yield.[16]

For the synthesis of $Mo^{IV}Cl_4(solv)_2$ two pathways are reported in the literature and displayed in Scheme 7. The reduction of Mo^VCl_5 with tin in diethylether according to Poli *et al.*[17] yields the tetrachlorido bis(diethylether) molybdenum(IV) complex. As this reaction includes the complicated separation of the product from the residual tin using a medium size cannula, the synthesis route involving acetonitrile as solvent as well as reducing agent leading to the formation of $Mo^{IV}Cl_4(CH_3CN)_2$ (**II**) was preferred. Here we describe this reaction according to the method published by Dilworth and Richards.[13]

$$Mo^VCl_5 \xrightarrow[\text{Et}_2\text{O}]{\text{Sn}} Mo^{IV}Cl_4(Et_2O)_2 \quad [17]$$

$$[13] \downarrow \text{excess } CH_3CN$$

$$Mo^{IV}Cl_4(CH_3CN)_2 + \text{chlorinated organic products}$$

II

Scheme 7. Reaction pathways for the synthesis of tetrachlorido molybdenum(IV) complexes.

Molybdenum(V) pentachloride was added as solid in small portions to acetonitrile at 0°C. Precipitation of the orange-brown product $Mo^{IV}Cl_4(CH_3CN)_2$ (**II**) was completed after standing overnight and subsequent concentration of the suspension under reduced pressure. The product was purified by washing with small amounts of acetonitrile and dried under reduced pressure giving a yield of 91%. As this molybdenum(IV) precursor is moisture sensitive and not very stable over a long time, probably due to the loss of the acetonitrile ligands, it is advisable to use this compound in the next reaction shortly after its preparation.

Complexation to form the chlorido molybdenum(IV) complex **IV** using precursor **II** and $[^{xyl}N_3N]H_3$ was performed under basic conditions. This reaction depicted in Scheme 8 was examined using two different bases, namely a) lithium hexamethyldisilazane and b) lithium dimethylamide.
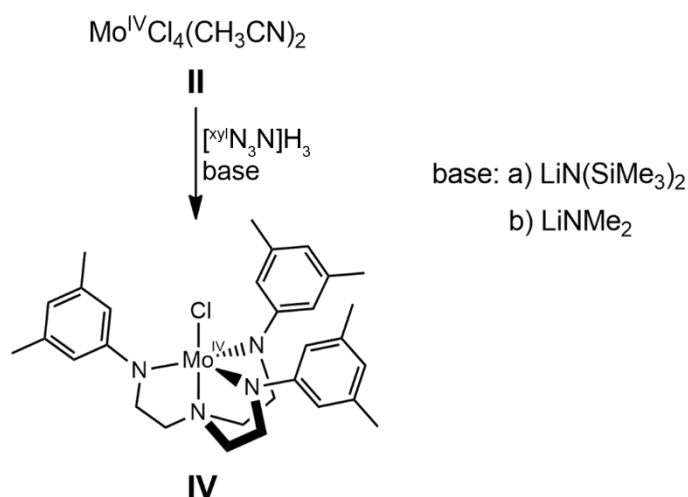
Scheme 8. Synthesis of **IV** using a) LiN(SiMe$_3$)$_2$ and b) LiNMe$_2$ as base.

The first reaction denoted with a) was performed according to the literature known method reported by Schrock *et al*. for the HIPT substituted chelate.[1] After dissolving [^{xyl}N$_3$N]H$_3$ in THF the tetrachlorido molybdenum(IV) precursor **II** was added as solid resulting in a color change from yellow to red-brown indicating the successful formation of the triaminoamine adduct complex. The reaction mixture was stirred for an additional hour, then 3.5 equivalents LiN(SiMe$_3$)$_2$ were added. Further work-up as reported in the experimental section yielded a red powder attributed to **IV**. Additionally, an analogous reaction was carried out *in situ* in an NMR tube revealing the formation of two paramagnetic products. The ^{1}H NMR spectrum displayed in Figure 2 shows with δ = 9.41 (H^o), −15.22 (CH$_2$), −75.62 (CH$_2$) ppm the expected signals of the desired chlorido molybdenum(IV) complex **IV**. Especially the high field shifted signals from the CH$_2$ groups of the tripodal ligand are characteristic for this paramagnetic molybdenum(IV) complex, a d^2 high spin system with two unpaired electrons.[1] These two methylene proton resonances could not be clearly assigned to the CH$_2$NMo and the CH$_2$N protons, as the two-dimensional NMR experiments provided no valuable data and thus no insight into the proton assignment. The other proton signals corresponding to the complex cannot be assigned because they are located between 8 and 0 ppm thus obscured by the resonances of the uncoordinated ligand [^{xyl}N$_3$N]H$_3$. Furthermore, the ^{1}H NMR resonances at −18.72 (CH$_2$) and −57.77 (CH$_2$) ppm indicate the presence of a second paramagnetic molybdenum(IV) complex, probably the hexamethyldisilazanido molybdenum(IV) complex [(^{xyl}N$_3$N)Mo^{IV}(N{SiMe$_3$}$_2$)], as the bis(trimethylsilyl)amide anion is known to substitute Cl$^-$ ligands in molybdenum complexes.[18] Therefore LiN(SiMe$_3$)$_2$ represents not only the base in this reaction and stoichiometrically forms LiCl, but it can also act as a good ligand.
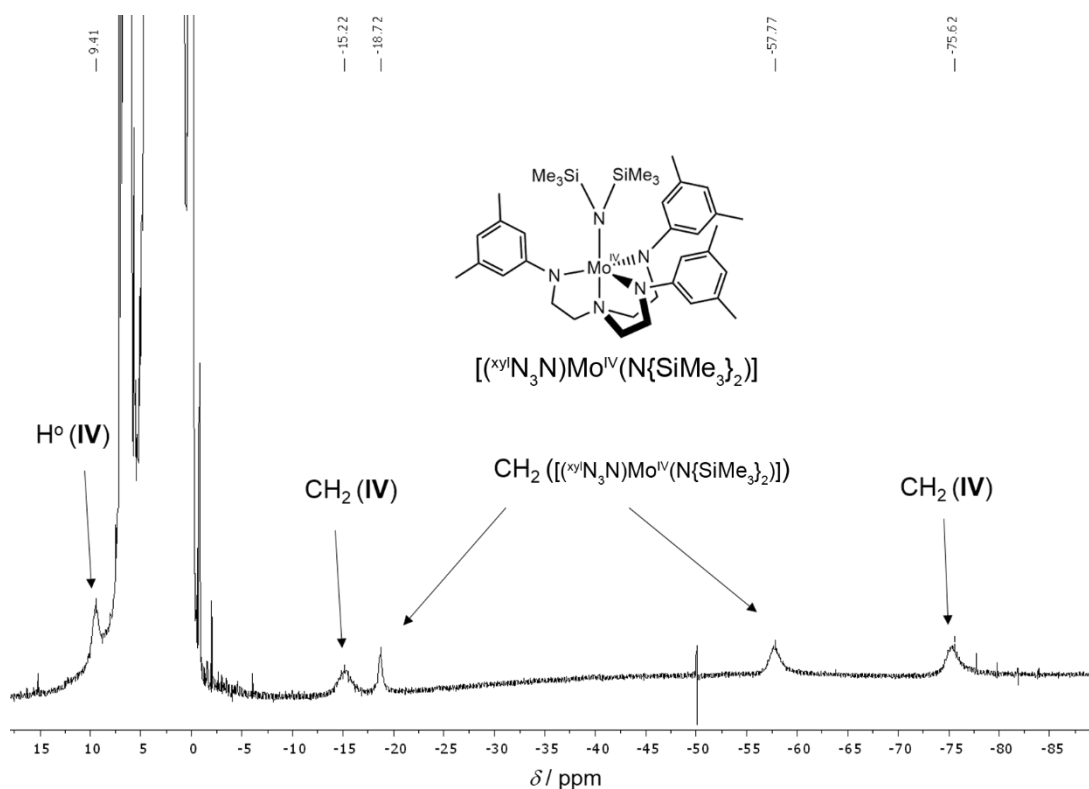
Figure 2. ^{1}H NMR spectrum of the *in situ* reaction between [^{xyl}N$_3$N]H$_3$ and Mo^{IV}Cl$_4$(CH$_3$CN)$_2$ in presence of LiN(SiMe$_3$)$_2$ in [D$_8$]THF.

An alternative route b) using LiNMe$_2$ as base was investigated in a second *in situ* reaction. [^{xyl}N$_3$N]H$_3$ was dissolved in [D$_8$]THF in the NMR tube and the tetrachlorido molybdenum(IV) precursor **II** was added as a solid resulting in a color change from yellow to red-brown due to the formation of the adduct complex. After 20 minutes 3.5 equivalents LiNMe$_2$ were added. The ^{1}H NMR spectrum displayed in Figure 3 shows no evidence for the successful formation of the complex **IV**.
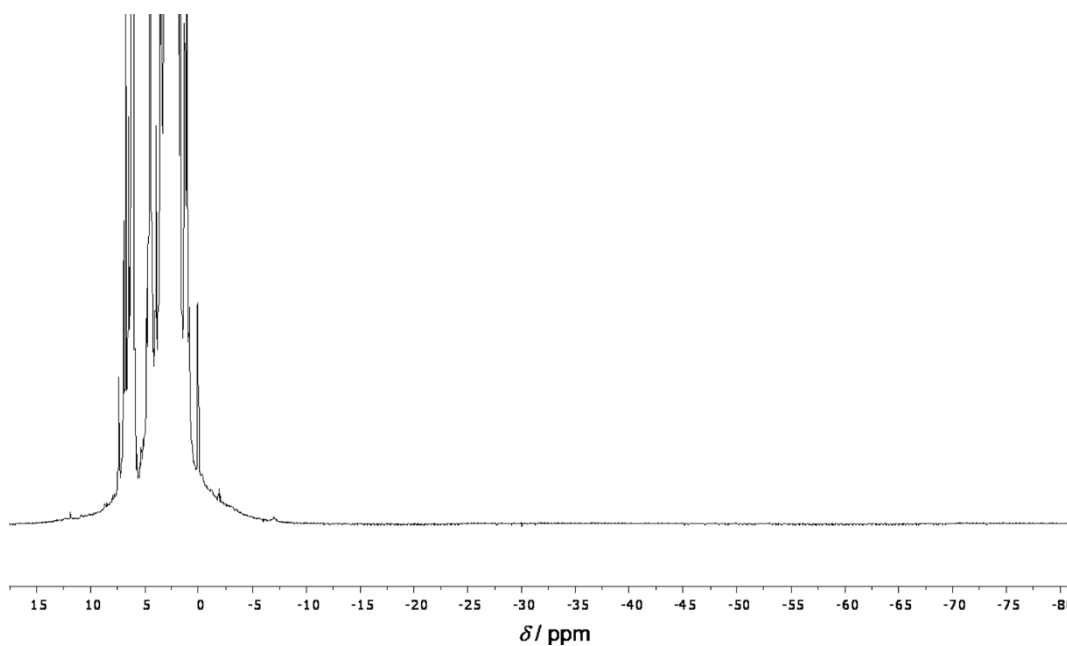

Figure 3. ^{1}H NMR spectrum of the *in situ* reaction between [^{xyl}N$_3$N]H$_3$ and Mo^{IV}Cl$_4$(CH$_3$CN)$_2$ in presence of LiNMe$_2$ in [D$_8$]THF.

In the ^{1}H NMR spectrum shown in Figure 3 the typical high field shifted proton signals of the methylene groups of the ligand backbone are absent, whereas the proton signals showing the highest intensity belong to the uncoordinated ligand [$^{xyl}N_3N$]H_3 as depicted in Figure 4. For this reaction it is advisable to use more than 3.5 equivalents of the base because dimethylamide is a good ligand as well. Therefore the formation of several products is possible including the desired complex **IV**, the complex [($^{xyl}N_3N$)Mo^{IV}(NMe$_2$)], the precursor Mo^{IV}(NMe$_2$)$_4$ and the deprotonated ligand. In this *in situ* reaction here, none of these products can be clearly assigned to the resonances appearing in the ^{1}H NMR spectrum (Figure 4).
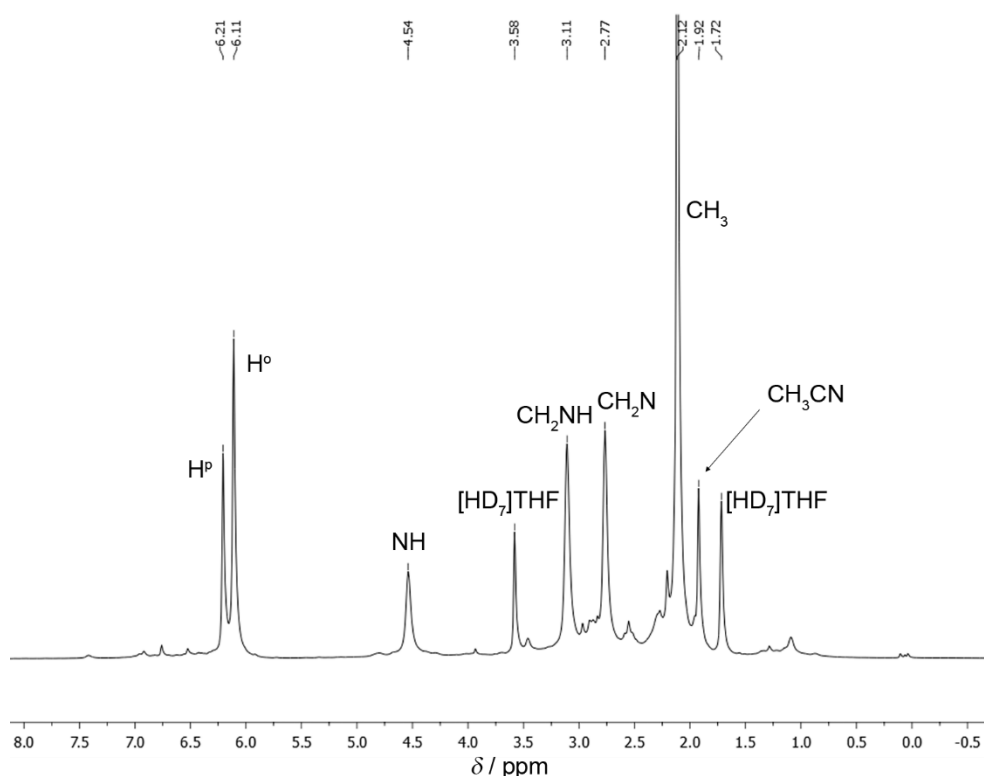

Figure 4. ^{1}H NMR spectrum of the *in situ* reaction between [$^{xyl}N_3N$]H_3 and Mo^{IV}Cl$_4$(CH$_3$CN)$_2$ in presence of LiNMe$_2$ in [D$_8$]THF (range of −0.5 to 8.0 ppm). The proton resonances of [$^{xyl}N_3N$]H_3, acetonitrile and [HD$_7$]THF are assigned.

To conclude, complexation of precursor **II** and [$^{xyl}N_3N$]H_3 to form the the chlorido molybdenum(IV) complex **IV** is achieved using the base lithium hexamethyldisilazane, as proven by ^{1}H NMR spectroscopy. In the future, this successful reaction pathway should be preffered, although the ^{1}H NMR spectrum also shows the presence of a second paramagnetic molybdenum(IV) complex.

The synthesis of trichlorido nitrido molybdenum(VI) precursor complexes is typically realized by treating the tetrachlorido molybdenum(IV) precursor with an azide such as sodium azide or trimethylsilyl azide according to published methods.[14,19] The synthesis of $[Mo^{VI}Cl_3N(CH_3CN)]_4$ (**III**) according to Dehnicke *et al.*[14] is displayed in Scheme 9.
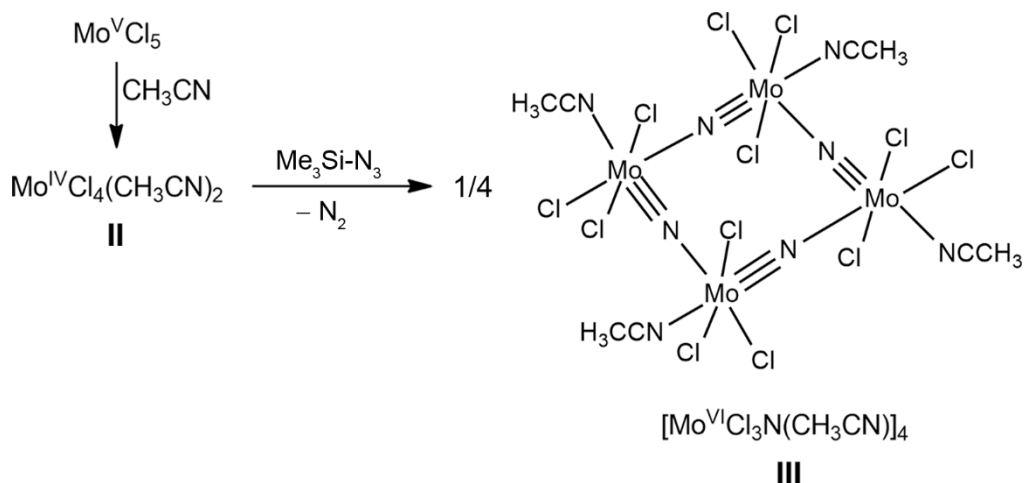
Scheme 9. Synthesis of **III** and molecular structure according to references [11] and [14].

Starting from Mo^VCl_5 the tetrachlorido molybdenum(IV) precursor (**II**) was synthesized as described above. Addition of trimethylsilyl azide to this precursor dissolved in dichloromethane resulted in the evolution of gaseous N_2 and the formation of the red product **III**. The infrared spectrum of the isolated compound recorded in nujol shows the expected absorption band for the Mo≡N stretching vibration at 1035 cm^{-1} and the bands for coordinated acetonitrile at 2303 and 2276 cm^{-1} comparable to the reported bands in the literature (2301, 2274 and 1037 cm^{-1})[14] confirming the success of this reaction (Figure 5).
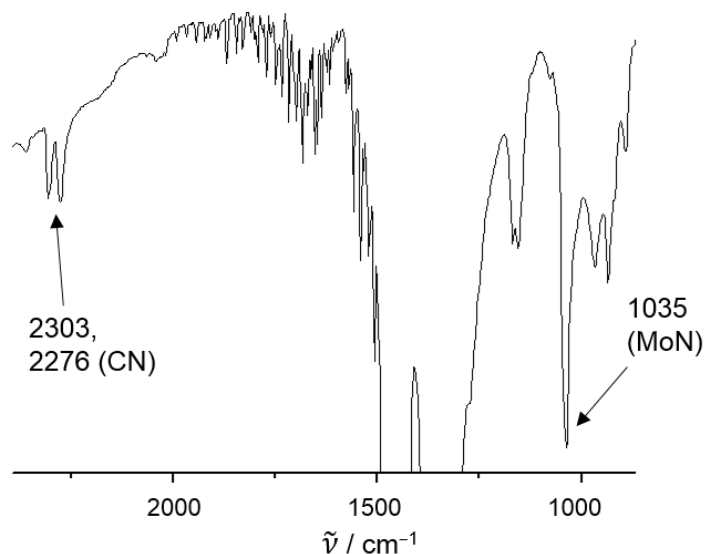

Figure 5. IR spectrum of **III** in nujol, characteristic bands are assigned.

All these molybdenum(IV) and (VI) precursor complexes presented here should not be stored over a long period of time, even under an inert atmosphere. They should be prepared freshly, and it is advisable to proceed with the next reaction shortly after.

The nitrido molybdenum(VI) complex (**5**) is accessible via a simplified reaction consisting of only one step (Scheme 10). This route involving the ligand [^{xyl}N$_3$N]H$_3$, the trichlorido nitrido molybdenum(VI) precursor (**III**) and LiNMe$_2$ as base was established in this work and is already published.[15]
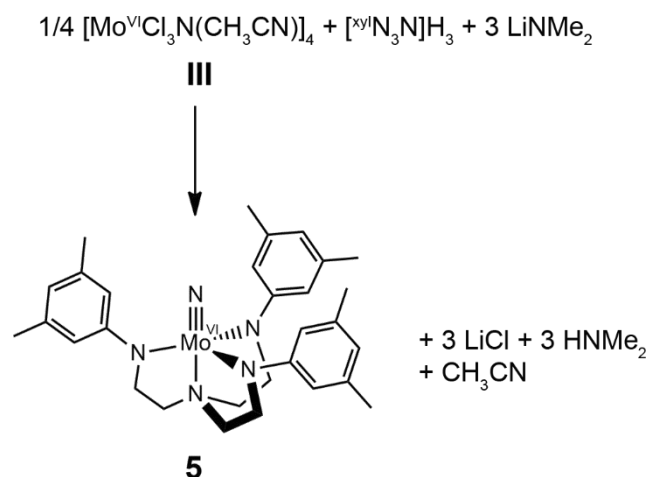
Scheme 10. One-step synthesis of **5**.

With this complex **5** representing a stable intermediate of the Schrock cycle as illustrated in Scheme 1 a new way to enter the Schrock cycle was found. This one-step reaction procedure has the advantage to be applicable to solid phase chemistry. Thus we could synthesize an immobilized nitrido molybdenum(VI) complex analogously to the soluble complex **5** using a polymer-supported tripodal ligand. Starting from these nitrido complexes the initial steps of the second half of the Schrock cycle including protonation and reduction were investigated and the results were published in [15].

3. CONCLUSIONS

We have prepared the tetrachlorido molybdenum(IV) (**II**) and the trichlorido nitrido molybdenum(VI) (**III**) precursor complexes. These starting materials were implemented in a subsequent complex synthesis using the ligand 2,2′,2″-tris(3,5-dimethylphenylamino)triethylamine [^{xyl}N$_3$N]H$_3$. The successful synthesis of the chlorido molybdenum(IV) complex (**IV**) was achieved by using lithium hexamethyldisilazane as base as shown by ^{1}H NMR spectroscopy. A new reaction pathway, consisting of only a single step, was established for the synthesis of the nitrido molybdenum(VI) complex (**5**) which represents a stable intermediate of the Schrock cycle. The reaction procedure and the analytical data for **5** are reported in literature [15].

4. EXPERIMENTAL SECTION

General considerations: All reactions were performed under inert atmosphere (Schlenk techniques, glove box). THF was distilled from potassium, diethylether, petroleum ether b.p. 40−60° and toluene from sodium, and dichloromethane from CaH$_2$. The ligand 2,2′,2″-tris(3,5-dimethylphenylamino)triethylamine [^{xyl}N$_3$N]H$_3$ and the nitrido molybdenum(VI) complex **5** were synthesized according to the published procedures.[15] All chemicals were obtained from commercial suppliers and used without further purification. IR spectra were recorded on a BioRad Excalibur FTS 3100 spectrometer using nujol and potassium bromide disks. NMR spectra were recorded on a Bruker Avance DRX 400 spectrometer at 400.31 MHz (^{1}H). All resonances are reported in ppm *versus* the solvent signal as internal standard [D$_8$]THF (^{1}H: δ = 1.72, 3.58 ppm); C$_6$D$_6$ (^{1}H: δ = 7.20 ppm).

Reaction of MoCl$_5$ with LiNMe$_2$: According to reference [12] lithium dimethylamide (4.25 mg, 83.3 mmol) was diluted in 56 mL petroleum ether and 34 mL THF. Molybdenum(V) pentachloride (4.5 mg, 16.5 mmol) was added in portions under stirring at 0°C. The color of reaction solution turned red. After completion of MoCl$_5$ addition the reaction was stirred overnight at 25°C and afterwards heated under reflux (60°C) for 1.5 h. The product was filtered to remove the lithium salts and subsequently the solvent was evaporated under reduced pressure leaving a brown residue. During removal of the last traces of the solvent a purple solid indicating the product Mo(NMe$_2$)$_4$ appeared in the liquid nitrogen cold trap. At this stage the evaporation was stopped. The liquid nitrogen trap was changed and the sublimation of the brown residue in the flask was continued by raising the temperature up to 70°C under reduced pressure but isolation of the product failed. ^{1}H NMR (C$_6$D$_6$): δ = 3.44 (NH), 2.20 (CH$_3$) ppm corresponding to dimethylamine, HNMe$_2$.

Synthesis of MoCl₄(CH₃CN)₂ (II): According to reference [13] molybdenum(V) pentachloride (2.0 g, 7.3 mmol) was added over a period of 45 min to acetonitrile (10 mL, 190 mmol) at 0°C. The orange-brown product precipitated and the suspension was stirred for additional 2 h. After standing over night at room temperature the suspension was concentrated under reduced pressure followed by washing of the precipitate with acetonitrile (2×5 mL). The orange-brown product was dried under reduced pressure yielding 2.15 g (6.41 mmol, 91.7%) [MoCl₄(CH₃CN)₂].

Reaction of MoCl₄(CH₃CN)₂ with [ˣʸˡN₃N]H₃ using LiN(SiMe₃)₂: [ˣʸˡN₃N]H₃ (138 mg, 0.30 mmol) was dissolved in 10 mL THF and MoCl₄(CH₃CN)₂ (**II**) (100 mg, 0.31 mmol) was added as a solid resulting in the formation of a dark brown solution. After stirring for 1 h at 25°C solid LiN(SiMe₃)₂ (175 mg, 3.49 mmol) was added according to reference [1] and the red-brown solution was stirred for an additional hour. After standing overnight the solvent was removed under reduced pressure and the residue was dried at 60°C under reduced pressure. THF (5 mL) were added to the solid and the flask was stored at −20°C. After two weeks a red powder precipitated. An analogous reaction was performed *in situ* in an NMR tube with [D₈]THF revealing the formation of the product **IV**, together with a second product, with the following proton signals similar to published data[1]: ¹H NMR ([D₈]THF): δ = 9.41 (br s, Hᵒ), −15.22 (br s, CH₂), −75.62 (br s, CH₂) ppm.

Reaction of MoCl₄(CH₃CN)₂ with [ˣʸˡN₃N]H₃ using LiNMe₂: The reaction was carried out *in situ* in an NMR tube. [ˣʸˡN₃N]H₃ (28,6 mg, 0.062 mmol) was dissolved in [D₈]THF (0.5 mL) and MoCl₄(CH₃CN)₂ (**II**) (20 mg, 0.062 mmol) was added as a solid resulting in the formation of a dark brown solution. After 20 min solid LiNMe₂ (11.2 mg, 0.22 mmol) was added and the mixture was analyzed using ¹H NMR spectroscopy revealing that the desired product **IV** was not formed, even after several days.

Synthesis of [MoCl₃N(CH₃CN)]₄ (III): According to reference [14] the tetrachlorido molybdenum(IV) acetonitrile complex [MoCl₄(CH₃CN)₂] (**II**) (800 mg, 2.5 mmol) was suspended in dichloromethane (20 mL) and trimethylsilylazide (280 mg, 0.32 mL, 2.43 mmol) was added slowly. Evolution of N₂ is observed. The solution was stirred overnight at 25°C, filtered and washed with dichloromethane (3×10 mL). The filtrate was concentrated under reduced pressure resulting in the precipitation of a red water sensitive solid (454 mg, 1.41 mmol, 58.12%). IR (Nujol): $\tilde{\nu}$ = 2303 (w, CN), 2276 (w, CN), 1035 (m, MoN) cm⁻¹. The IR data match literature values.[14]

REFERENCES

[1]   D. V. Yandulov, R. R. Schrock, A. L. Rheingold, C. Ceccarelli, W. M. Davis, *Inorg. Chem.* **2003**, *42*, 796−813.

[2]   F. Studt, F. Tuczek, *Angew. Chem.* **2005**, *117*, 5783–5787; *Angew. Chem. Int. Ed.* **2005**, *44*, 5639–5642.

[3]   S. Schenk, B. Le Guennic, B. Kirchner, M. Reiher, *Inorg. Chem.* **2008**, *47*, 3634–3650.

[4]   D. V. Yandulov, R. R. Schrock, *Science* **2003**, *301*, 76–78.

[5]   W. W. Weare, R. R. Schrock, A. S. Hock, P. Müller, *Inorg. Chem.* **2006**, *45*, 9185–9196.

[6]   G. E. Greco, R. R. Schrock, *Inorg. Chem.* **2001**, *40*, 3861–3878.

[7]   D. V. Yandulov, R. R. Schrock, *Inorg. Chem.* **2005**, *44*, 1103−1117.

[8]   G. E. Greco, R. R. Schrock, *Inorg. Chem.* **2001**, *40*, 3850–3860.

[9]   M. F. Cain, W. P. Forrest, Jr., D. V. Peryshkov, R. R. Schrock, P. Müller, *J. Am. Chem. Soc.* **2013**, *135*, 15338–15341.

[10]   M. J. A. Johnson, P. M. Lee, A. L. Odom, W. M. Davis, C. C. Cummins, *Angew. Chem. Int. Ed. Engl.* **1997**, *36*, 87–91.

[11]   D. M.-T. Chan, M. H. Chisholm, K. Folting, J. C. Huffman, N. S. Marchant, *Inorg. Chem.* **1986**, *25*, 4170–4174.

[12]   D. C. Bradley, M. H. Chisholm, *J. Chem. Soc. (A)* **1971**, 2741−2744.

[13]   J. R. Dilworth, R. L. Richards, *Inorg. Synth.* **1990**, *28*, 33−37.

[14]   E. Gauch, A. Hagenbach, J. Strähle, A. Dietrich, B. Neumüller, K. Dehnicke, *Z. Anorg. Allg. Chem.* **2000**, *626*, 489−493.

[15]   A. Wünsche von Leupoldt, C. Förster, T. J. Fiedler, N. H. Bings, K. Heinze, *Eur. J. Inorg. Chem.* **2013**, *36*, 6079−6090.

[16]   D. S. Kuiper, P. T. Wolczanski, E. B. Lobkovsky, T. R. Cundari, *Inorg. Chem.* **2008**, *47*, 10542–10553.

[17]   F. Stoffelbach, D. Saurenz, R. Poli, *Eur. J. Inorg. Chem.* **2001**, 2699–2703.

[18]   J. Heppekausen, R. Stade, R. Goddard, A. Fürstner, *J. Am. Chem. Soc.* **2010**, *132*, 11045–11057.

[19]   K. Seyferth, R. Taube, *J. Organomet. Chem.* **1982**, *229*, C19–C23.

3.2   Proton and Electron Transfer to a Polymer-
         Supported Nitrido Molybdenum(VI) Complex

Anica Wünsche von Leupoldt[a], Christoph Förster[a],

Tobias J. Fiedler[a], Nicolas H. Bings[a], and Katja Heinze[a]*
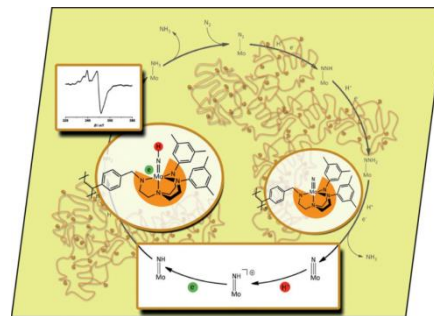
COVER PICTURE

Dedicated to Professor Werner Uhl on the occasion of his 60th birthday

[a] Institute of Inorganic Chemistry and Analytical Chemistry, Johannes Gutenberg University of Mainz, Duesbergweg 10−14, 55128 Mainz, Germany

E-mail: katja.heinze@uni-mainz.de; http://www.ak-heinze.chemie.uni-mainz.de/

ABSTRACT

The protonation and reduction of nitrido and imido complexes are important steps during the reduction of dinitrogen to NH$_3$ mediated by transition-metal complexes. A polymer- immobilized analogue (**P-2**) of the Schrock–Yandulov nitrido molybdenum(VI) complex has been prepared from a sterically unencumbered polymer-anchored triamidoamine ligand (**P-1**) and [MoCl$_3$N(CH$_3$CN)]$_4$ as an "MoN" source. The polymer-confined nitrido complex has been protonated by [2,6-lutH][Al{OC(CF$_3$)$_3$}$_4$] (2,6-lut = 2,6-lutidine) at the nitride ligand to form the corresponding imido complex **P-3**, as shown by a variety of spectroscopic techniques and DFT calculations. Specifically, the NH stretching vibration of **P-3** and the ND stretching vibration of the *N*-deuterated analogue **P-3^D** as well as the vibrations of the counterion are particularly useful for unambiguous characterization. Single-electron transfer to the supported molybdenum(VI) complexes **P-3**/**P-3^D** by cobaltocene as one-electron reductant gave the imido molybdenum(V) congeners **P-4**/**P-4^D** as shown by diffuse reflectance UV/Vis (DR-UV/Vis) and IR spectroscopy in combination with DFT calculations. The electron paramagnetic resonance (EPR) spectra of the immobilized d^1 complex **P-4** and its deuterated isotopomer **P-4^D** reveal spin density on the molybdenum center and the imido ligand. For comparison of their spectroscopic and reactivity properties, the analogous soluble ligand **1** and its nitrido (**2**) and imido (**3**) complexes have also been synthesized. Compounds **1** and **2** were also characterized by single-crystal X-ray diffraction.
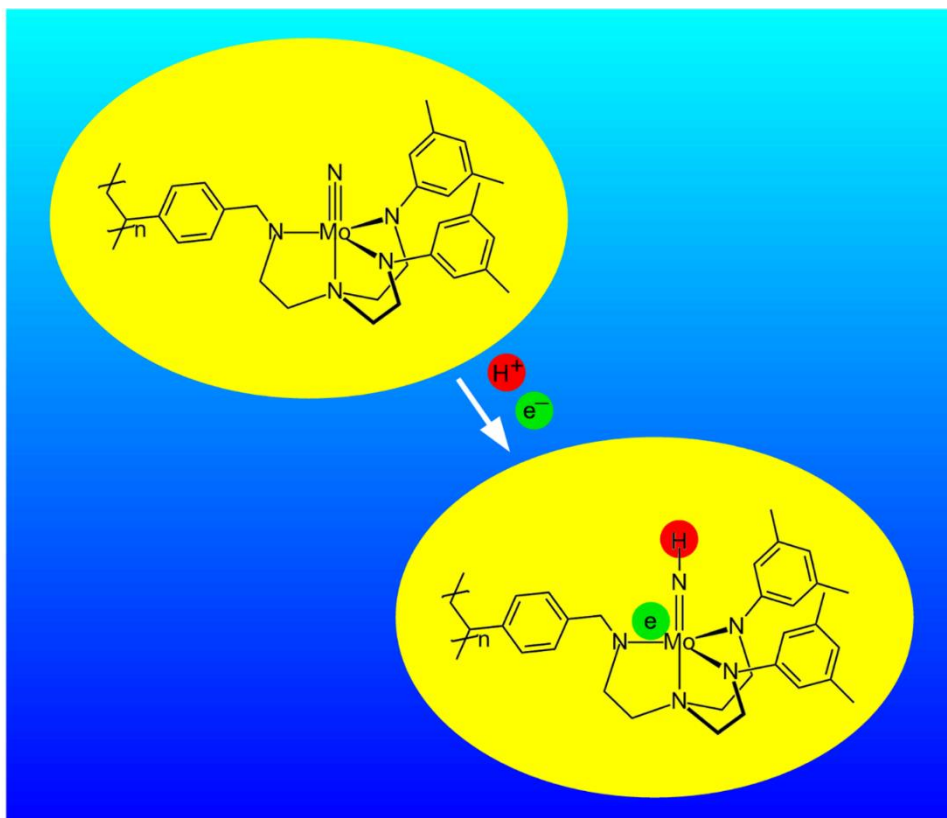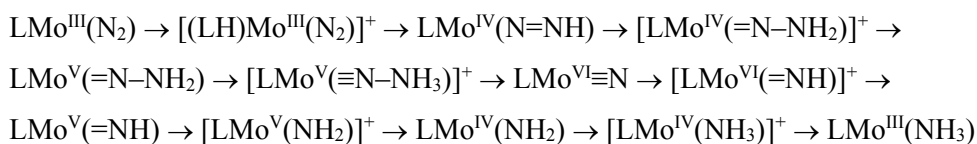
1. INTRODUCTION

The mechanism of biological nitrogen fixation by Mo-dependent nitrogenases is of considerable interest because of its fundamental and application aspects. The tremendous complexity of dinitrogen activation at metal centers, which involves sixfold protonation and reduction and N–N cleavage to finally produce ammonia via a wealth of intermediates, presents a huge challenge to bioinorganic chemists wishing to model these elementary reaction steps and finally the whole catalytic cycle.[1–8] The exact binding site of N_2 at the FeMo cofactor of nitrogenase is still a matter of debate (iron sulfur cluster periphery vs. molybdenum center),[2,3,9,10] and model systems featuring iron, molybdenum, and many other transition-metals have been investigated with respect to N_2 binding and activation.[2] Molybdenum complexes in particular have been very successful models for single N_2 activation steps.[1,3–5,7,8] Even full catalytic cycles with molybdenum have been devised by Schrock et al. with triamidoamine π-donor ligands (Scheme 1, **A**)[11] and by Nishibayashi et al. with PNP-type pincer ligands (Scheme 1, **B**).[12]
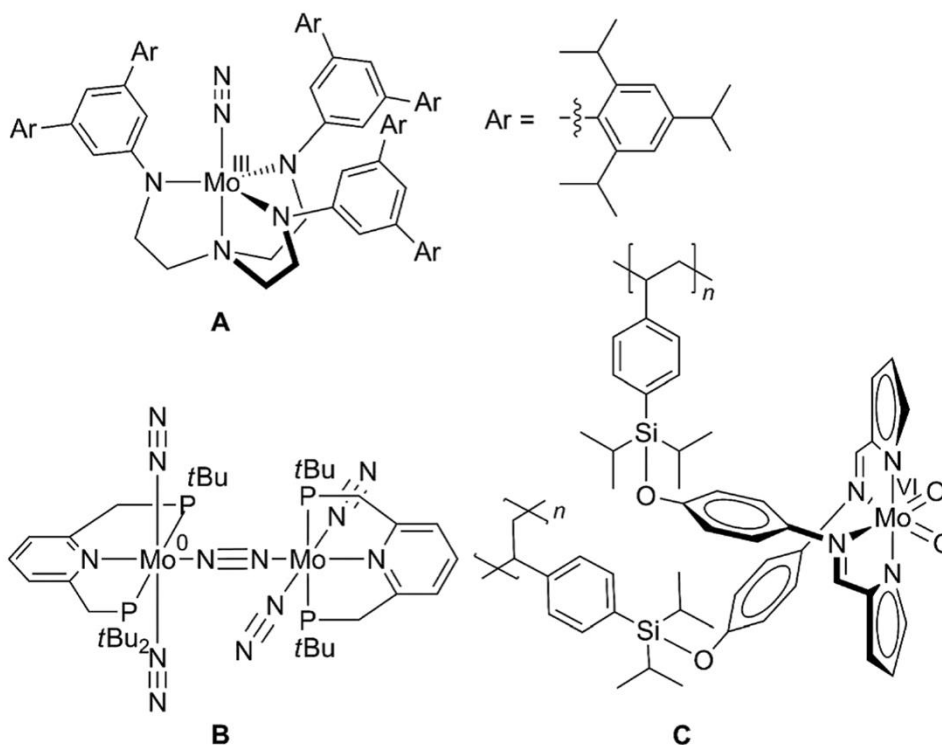
Scheme 1. Schrock's dinitrogen molybdenum(III) complex LMo(N$_2$) with a sterically encumbered triamidoamine ligand (**A**), Nishibayashi's dinuclear PNP-type molybdenum(0) complex (**B**), and Heinze's immobilized dioxido molybdenum(VI) complex (**C**).

Complexes of the type *trans*-Mo^0(N$_2$)$_2$L$_4$ (L = phosphane) were investigated by Chatt, and they produce ammonia upon protonation with mineral acids,[1,2,13] whereas the analogous polymer-immobilized complexes[14] (characterized by the IR signature of end-on-coordinated N$_2$ ligands and gel-phase ^{31}P NMR spectroscopy)[15,16] fail to release ammonia. This inability has been ascribed to intermediate molybdenum(III) hydrazido(2–) complexes Mo^{III}X(NNH$_2$)L$_4$, which undergo disproportionation to NH$_4^+$ and N$_2$ in solution. Owing to site isolation of the immobilized complexes, bimolecular disproportionation is suppressed, and consequently NH$_4^+$ cannot form.

The most thoroughly studied functional system is certainly the Schrock–Yandulov cycle, which starts from the dinitrogen molybdenum(III) complex LMo^{III}(N$_2$) **A** [Scheme 1, L = tris(hexaisopropyl-terphenyl)triamidoamine] or the nitrido molybdenum(VI) complex LMo^{VI}N. In the last decade, many intermediates of the N$_2$ reduction cycle have been isolated and characterized.[3–5,11] The cycle is believed to include the following intermediates generated by strictly alternating proton- and electron-transfer steps.

LMo^{III}(N$_2$) $\rightarrow$ [(LH)Mo^{III}(N$_2$)]$^+$ $\rightarrow$ LMo^{IV}(N=NH) $\rightarrow$ [LMo^{IV}(=N–NH$_2$)]$^+$ $\rightarrow$

LMo^V(=N–NH$_2$) $\rightarrow$ [LMo^V($\equiv$N–NH$_3$)]$^+$ $\rightarrow$ LMo^{VI}$\equiv$N $\rightarrow$ [LMo^{VI}(=NH)]$^+$ $\rightarrow$

LMo^V(=NH) $\rightarrow$ [LMo^V(NH$_2$)]$^+$ $\rightarrow$ LMo^{IV}(NH$_2$) $\rightarrow$ [LMo^{IV}(NH$_3$)]$^+$ $\rightarrow$ LMo^{III}(NH$_3$)

Detailed studies have identified several bottlenecks of this cycle: (1) One problem is the slow NH_3/N_2 ligand substitution $LMo^{III}(NH_3) \rightarrow LMo^{III}(N_2)$, which seems to be an almost thermoneutral associative ligand exchange and, thus, leads to product inhibition of the catalyst, especially if NH_3 accumulates.[3] (2) Unreactive N_2-bridged dimers LMo^{III}–$(\mu$-$N_2)$–$Mo^{III}L$ are formed if the aryl substituent at the triamidoamine ligand is too small.[17,18] This dinuclear μ-N_2 complex is reduced to $[LMo(N_2)]^-$ without splitting of the N≡N triple bond. (3) A complex disproportionation with an unknown mechanism is operative in the preparation of the hydrazido(2–) complex LMo^VNNH_2 from $[LMo^{VI}NNH_2]^+$ by reduction to give $LMo^{VI}N$, $LMo^{IV}(NNH)$, $LMo^{III}(NH_3)$, and ammonia, probably by bimolecular steps and, thus, by an abiological process. (4) A hydrogenase shunt, especially with less bulky hybrid ligands, leads to decomposition of $LMo^{IV}(NNH)$ to give H_2. At present it is unknown if the mechanism is uni- or bimolecular in molybdenum.[19] One possibility could be a rapid bimolecular decomposition via an $[LMo^{IV}$–N=N–H$\cdots$H–N=N–$Mo^{IV}L]^‡$ transition state.[19] (5) The LMo^VNH intermediates disproportionate into $LMo^{VI}N$ and $LMo^{IV}(NH_2)$, especially with $[LMo^{VI}(NH)]^+$ as the proton transfer agent, at low acid concentrations, possibly according to the following equations.[20]

$[LMo(NH)]^+ + LMo(NH) \rightarrow LMoN + [LMo(NH_2)]^+$

$[LMo(NH)]^+ + LMo(NH_2) \rightarrow LMoN + [LMo(NH_3)]^+$
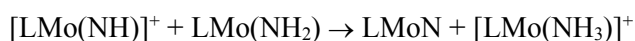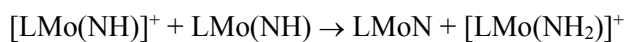
At least some of these challenges could in principle be tackled by immobilization of the active species onto a solid support.[21–25] For example, bimolecular decay pathways such as disproportionation, the formation of inert μ-N_2 complexes, or the hydrogenase shunt could be retarded by site isolation of the reactive complexes. The formation of μ-oxido dimers of iron porphyrinato complexes has already been successfully suppressed by immobilization onto a surface.[26] For oxido molybdenum(V) complexes, we were able to retard μ-oxido dimer formation (from disproportionation and condensation reactions) by anchoring the reactive species onto a polymeric support (Scheme 1, **C**).[27] The immobilized complexes **C** can sustain a biomimetic catalytic cycle reminiscent of that of molybdenum oxotransferases, which includes oxygen-atom transfer and two proton-coupled electron-transfer steps. Furthermore, relevant intermediates in the oxidation states IV, V, and VI have been characterized.[27–30]

We report here our attempts to immobilize nitrido molybdenum(VI) complexes relevant to the second half of the Schrock–Yandulov cycle onto a solid polymer support. In addition, we describe their reactivity towards protons and electrons. These reactions are especially relevant to the final steps in the Schrock cycle that ultimately lead to ammonia release from nitrido complexes.

2. RESULTS AND DISCUSSION

As described above, we decided to immobilize a 2,2′-bis(3,5-dimethylphenylamino)-2″-(benzylamino)triethylamine ligand onto a polystyrene/1% divinylbenzene copolymer to produce polymeric support **P-1** to prevent complex deactivation by intermolecular reactions. In comparison to the sterically highly demanding Schrock system,[3–5] the immobilized ligand is less bulky and does not

protect the active site by itself. The polymer-supported nitrido molybdenum(VI) complex **P-2** shall be protected by the site isolation effect rather than the steric demand of the tripodal ligand. For comparison, we also describe the synthesis and properties of a related soluble ligand **1** and its nitrido molybdenum(VI) complex **2** (Scheme 2).
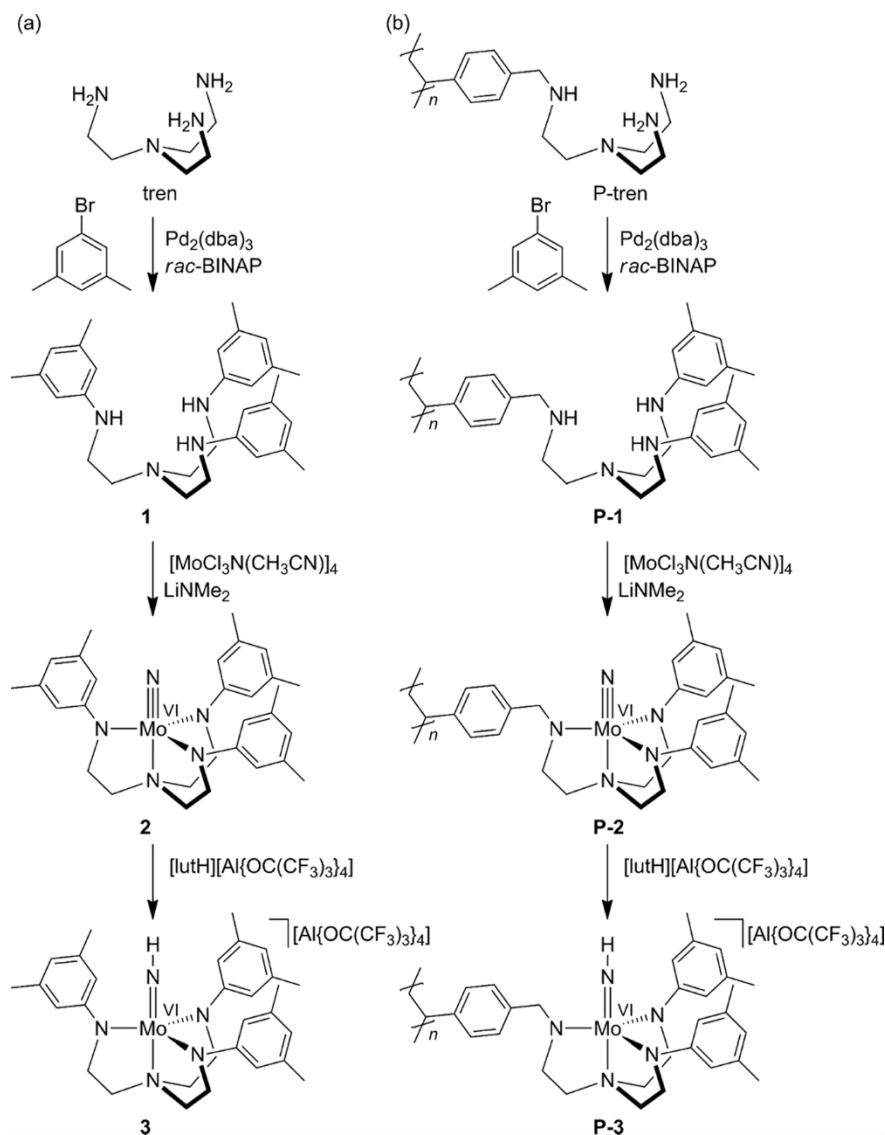
Scheme 2. (a) Synthesis of soluble ligands and complexes (**1**, **2**, **3**) and (b) their polymer-supported congeners (**P-1**, **P-2**, **P-3**); dba = dibenzylideneacetone, BINAP = 2,2′-bis(diphenylphosphanyl)-1,1′-binaphthyl; lut = 2,6-lutidine.

Synthesis and Characterization of Soluble Reference Compounds 1–3

The symmetrical ligand 2,2′,2″-tris(3,5-dimethylphenylamino)triethylamine (**1**) is readily synthesized from tris(2-aminoethyl)amine [tren, $N(CH_2CH_2NH_2)_3$] by using 5-bromo-m-xylene in a palladium-catalyzed Buchwald–Hartwig amination according to the method reported by Schrock et al. (Scheme 2a).[31,32] Overarylation products can be removed by chromatography. The ^{1}H NMR spectrum of **1** fully conforms to the reported data,[31,32] and the ^{13}C NMR, ^{15}N NMR, and IR spectroscopic data, as well as

the mass spectrometric data and elemental analysis agree with the formula. In the solid state, two absorptions corresponding to NH stretching vibrations are detected for **1** at $\tilde{v}$ = 3390 and 3340 cm^{-1}; this suggests the presence of hydrogen bonds in the solid state. In tetrahydrofuran (THF) solution, these bands collapse into a single band at 3365 cm^{-1}, which shows that the hydrogen bonds are intramolecular in nature.

X-ray quality crystals of **1** (monoclinic, $P2_1/n$) were obtained by recrystallization from petroleum ether (b.p. 40–60 °C). The structural analysis of **1** reveals nearly (noncrystallographic) threefold symmetry with three consecutive intramolecular NH$\cdots$N hydrogen bonds (N$\cdots$N distances 3.4–3.6 Å; Table 1, Figure 1a and b) that ensure a high pre-organization, similar to the expected tripodal coordination of **1** to a metal center. The previously reported crystallographically characterized 2,2′,2″-tris(arylamino)triethylamines [aryl = 2,6-C$_6$H$_3$(CH$_3$)$_2$,[33] 2-(CH$_2$-4-C$_6$H$_4$NO$_2$)C$_6$H$_4$,[34] 2-(CH$_2$-4-C$_6$H$_4$CF$_3$)C$_6$H$_4$,[34] and quinoline][35] feature *ortho* substituents at their aryl groups, which enables a tripodal shape but prevents intramolecular hydrogen bonds between the secondary amines. Thus, the N$\cdots$N distances are much longer in these ligands (3.8–5.6 Å), which demonstrates that the xylyl substituents employed in **1** are sterically much less demanding. DFT [B3LYP level of theory, LANL2DZ basis set, polarizable continuum model (PCM) for THF] optimization of ligand **1** yields a similar geometry, although the structure is more symmetric (Figure 1c and d, Table 1). This is also reflected in the NH stretching vibration pattern of optimized **1** with $\tilde{v}$ = 3449/3448 cm^{-1} (vs, ~e symmetry) and 3440 cm^{-1} (w, ~a$_1$ symmetry; energy scaled by 0.9614).[36]

Table 1. Hydrogen-bond distances [Å] and angles [°] in ligand **1** and its ammonium salt [**1**-H$_3$][Cl][CoCl$_4$] derived from X-ray diffraction analysis and for models of **1** and **P-1** derived from DFT calculations.

	D–H	H$\cdots$A	D$\cdots$A	D–H$\cdots$A	
1[a]	0.78	2.98	3.63	142.8	N25–H25$\cdots$N14
	0.92	2.51	3.43	174.8	N14–H14$\cdots$N3
	0.87	2.53	3.39	171.8	N3–H3$\cdots$N25
[**1**-H$_3$][Cl] [CoCl$_4$][a]	0.90	2.28	3.16	164.7	N2-H2A$\cdots$Cl2
	0.90	2.26	3.16	177.5	N2-H2B$\cdots$Cl3[b]
1[c]	1.02	2.52	3.52	167.2	N1-H1$\cdots$N2
	1.02	2.53	3.53	167.5	N2-H2$\cdots$N3
	1.02	2.53	3.53	167.3	N3-H3$\cdots$N1
P-1[c]	1.02	3.26	4.03	133.0	N1-H1$\cdots$N2
	1.02	2.54	3.55	171.3	N2-H2$\cdots$N3
	1.03	2.09	3.12	174.2	N3-H3$\cdots$N1

[a] X-ray data. [b] Symmetry code: –z + 1, x – 1/2, –y + ½. [c] DFT data (B3LYP, LANL2DZ, PCM THF).

Metalation and deprotonation of **1** to give nitrido complex **2** is successfully achieved by two different routes, namely, the two-step procedure of Schrock with MoCl$_4$(thf)$_2$[37–39]/Li[N(SiMe$_3$)$_2$], subsequent chloride substitution with (Me$_3$Si)N$_3$ and thermal N$_2$ elimination[40,41] or more conveniently by

employing [MoCl$_3$N(CH$_3$CN)]$_4$[42,43] to give a red adduct complex and LiNMe$_2$ to deprotonate the ligand and induce chloride abstraction (Scheme 2a). In both cases, the air-stable nitrido complex **2** is obtained as a yellow powder. Complex **2** is characterized by ^{1}H, ^{13}C, and N–H-correlation NMR, IR and UV/Vis spectroscopy. The ^{1}H, ^{13}C, and ^{15}N resonances of **1** are characteristically shifted to lower field upon deprotonation and metalation (except for those of N$_{amido}$ and C$_{meta}$, which shift to higher field; see Exp. Sect.). The position of the low-energy π–π* transitions of the ligand at ca. 297 and 256 nm are hardly affected except for some broadening in that of **2** (Figure S1, Supporting Information). However, amido-to-molybdenum charge-transfer absorptions at ca. 347 and 516 nm are discernible in **2** (Figure S1). The IR absorption of the characteristic Mo≡N stretching vibration of **2** is detected as a complex pattern at ca. 1094 and 1024 cm^{-1}. Complex **2** crystallized from toluene in the space group $P2_1/c$ (Figure 2a). The Mo≡N distance is 1.666(2) Å, and the Mo···N$_{amine}$ distance is 2.410(2) Å. The DFT model of **2** calculates the Mo≡N distance as 1.701 Å (Figure 2b), which is slightly longer than the calculations of Reiher et al. for LMoN (1.680 Å)[45a] and the results of the single-crystal X-ray diffraction analysis of LMoN (1.652 Å).[41] The Mo···N$_{amine}$ distance of **2** is calculated as 2.468 Å, which is slightly shorter than that calculated by Reiher et al. for LMoN (2.533 Å)[45a] but slightly longer than the results of X-ray analyses of LMoN (2.395 Å)[41] and **2**.
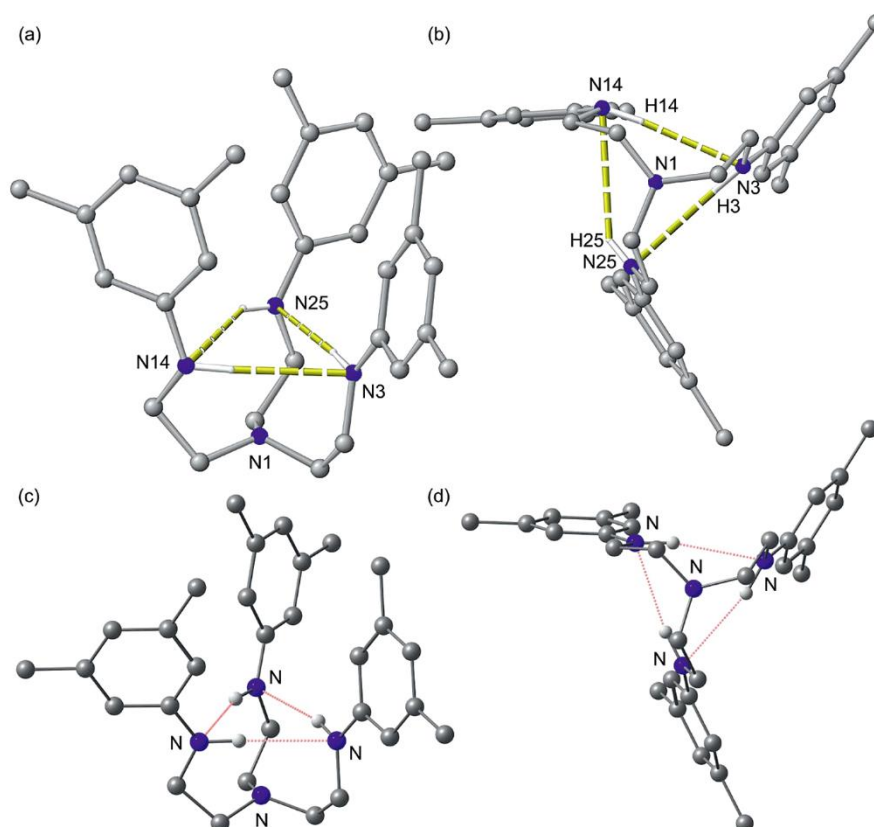

Figure 1. Molecular crystal structure of **1**; (a) side view, (b) top view. Molecular structure optimized by DFT (B3LYP, LANL2DZ, PCM THF); (c) side view, (d) top view. CH hydrogen atoms omitted.

Similar to the experimental results, the DFT model of **2** predicts that the Mo≡N stretching vibration is coupled to ligand backbone modes, and three intense bands are found at 1043, 1040, and 1039 cm^{-1} (scaled by 0.9614).[36] The Kohn–Sham frontier molecular orbitals consist of amido-ligand-centered highest occupied molecular orbitals (HOMOs) and MoN-centered lowest unoccupied molecular orbitals (LUMOs; Figure S2a), which allow for amido-to-MoN charge-transfer transitions.
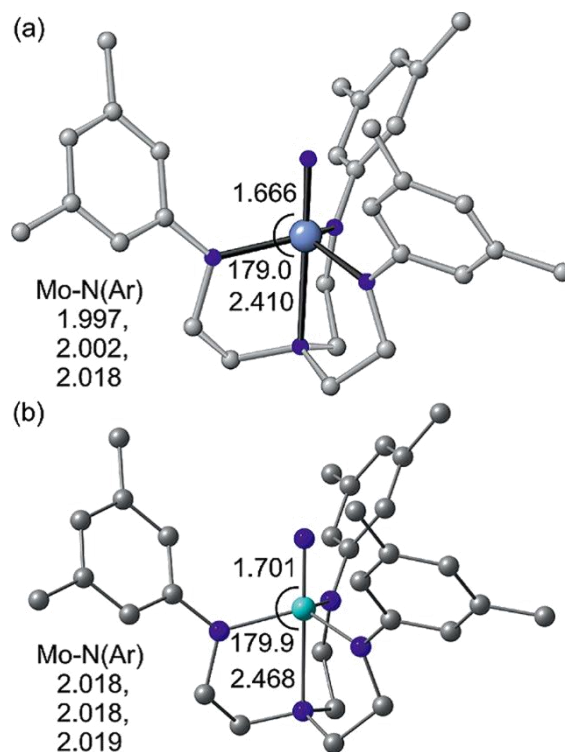

Figure 2. (a) Molecular crystal structure of **2**. (b) DFT model of **2** (B3LYP, LANL2DZ, PCM THF). Selected distances [Å] and angles [°] are shown.

In the cyclic voltammogram, **2** is irreversibly reduced at –3.5 V vs. ferrocene/ferrocenium in THF with [nBu$_4$N][B(C$_6$F$_5$)$_4$] as the supporting electrolyte. A follow-up transformation, possibly dimerization, is indicated by an oxidative wave at –2.9 V in the reverse scan. The sterically protected Schrock nitrido complex LMoN is reversibly reduced to the anion [LMoN]$^-$ at –2.68 V vs. ferrocene/ferrocenium in fluorobenzene with [nBu$_4$N][PF$_6$] as the electrolyte.[46] The lower potential of **2** might be due to the more electron-donating xylyl ligand. The reduction potentials of LMoN and **2** are much lower than those of the typical reductants employed for N$_2$ reduction in the Schrock catalytic cycle.[44] However, protonation before reduction helps to adjust the reduction potentials.[45a]

As shown experimentally[20] and theoretically[45] for the Schrock system, the nitrido ligand is the most basic site, and protonation of the tripodal amido ligand is less favorable.[45a] Hence, the nitrido complex **2** was treated with 1 equiv. [2,6-lutH][Al{OC(CF$_3$)$_3$}$_4$][40,56] (2,6-lut = 2,6-lutidine) to give the cationic green imido molybdenum(VI) complex **3** (Scheme 2a). Owing to the higher basicity of **1** than that of the Schrock ligand, some decomposition also occurs to produce the protonated tripod ligand **1** (ca. 70% by NMR) and unidentified Mo species. The imido complex **3** is characterized in situ by its characteristic

^{1}H NMR NH resonance at δ = 6.33 ppm and ^{15}N NMR NH resonance at δ = 425 ppm {heteronuclear multiple quantum correlation (HMQC), [D$_8$]THF}, which are similar to those of the sterically protected Schrock analogue [LMoNH][+] [δ(^{1}H) = 6.60 ppm; δ(^{15}N) = 427.7 ppm in C$_6$D$_6$].[41] The absorptions in the UV/Vis spectrum of **3** are very similar to those of **2**, except for a shift of the charge-transfer bands to higher energy (314 and 376 nm; Figure S1). The NH stretching mode of **3** is observed at 3278 cm^{–1} in the IR spectrum. The low energy of this band relative to that of the sterically highly protected Schrock derivative [LMoNH][+] (3341 cm^{–1}) points to some NH···X interaction in **3**, for example, **3**·thf or **3**·lut.[41] The DFT model of **3** predicts an elongation of the Mo=N distance, a concomitant shortening of the Mo···N$_{amine}$ distance owing to the weaker *trans* influence of the imido ligand, and a nearly linear Mo=N–H unit (Figure 3), which is in full accordance with the experimental and theoretical data.[20,45a] The NH stretching vibration of **3** (without explicit coordination of a hydrogen atom acceptor) is calculated by DFT at 3430 cm^{–1} (scaled by 0.9614)[36]. Again, the HOMOs are centered on the tripodal amido ligand, and the LUMOs are localized on the MoNH unit (Figure S2b).
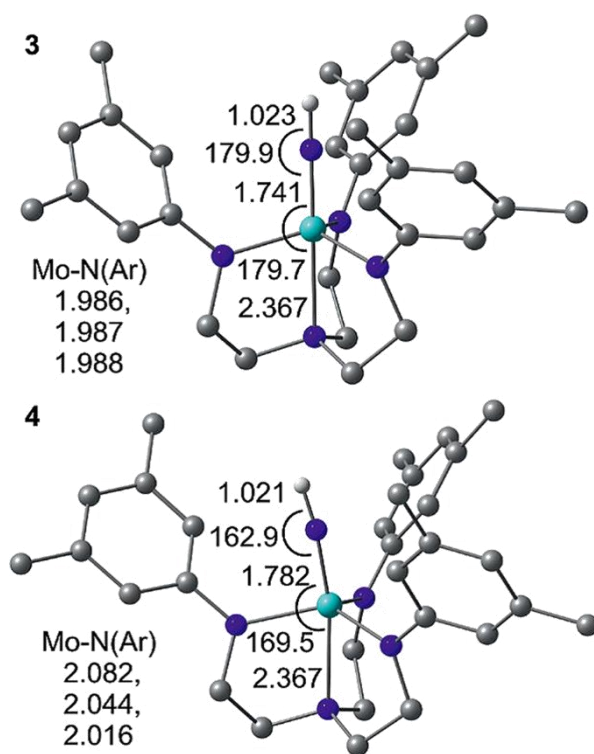

Figure 3. DFT models of **3** and **4** (B3LYP, LANL2DZ, PCM THF). Selected distances [Å] and angles [°] are shown.

Similar to the Schrock derivative $[LMoNH]^+$ ($E_p = -1.26$ V in fluorobenzene),[46] the cationic complex **3** (prepared in situ) is only irreversibly reduced in the cyclic voltammogram to the corresponding neutral Mo^VNH species **4** $\{E_p \approx -1.85$ V in THF/$[nBu_4N][B(C_6F_5)_4]\}$. This is possibly caused by subsequent proton- and electron-transfer reactions between the initially generated Mo^VNH species to give $Mo^{VI}N$ and $Mo^{IV}NH_2$ complexes.[20] Thus, we were unable to unambiguously characterize soluble **4** by electron paramagnetic resonance (EPR) or IR spectroscopy. Attempts to generate a kinetically more stable version of **4** by employing the site isolation effect by polymer immobilization are described below.

Synthesis and Characterization of Polymer-Supported Systems P-1 to P-4

The immobilized ligand **P-1** was prepared from commercially available immobilized P-tren (Iris Biotech GmbH) by a Buchwald–Hartwig amination similar to that used in the synthesis of the soluble ligand **1** from tren (Scheme 2b). The functionalized polymer **P-1** is characterized by a (negative) Kaiser test (Supporting Information, Figure S3),[47,48] which proves that all primary amines have been arylated under the applied optimized reaction conditions. The IR spectrum of **P-1** shows a broad absorption band derived from NH stretching vibrations at $\tilde{\nu} \approx 3350$ cm^{-1}, which is substantially different from those of P-tren (ca. 3425, 3370, and 3300 cm^{-1}) but at comparable energy to those of **1**. This indicates that there are intramolecular hydrogen bonds in the immobilized ligand. Harmonic frequency calculations on a DFT-optimized model of **P-1** (Figure 4) yielded three absorptions for the NH stretches at $\tilde{\nu} = 3421$, 3375, and 3213 cm^{-1} (scaled by 0.9614)[36] with that of the hydrogen bond to the benzyl-substituted nitrogen atom N3H3···N1 much stronger than the other ones owing to the higher basicity of N1. Furthermore, the amine N1 atom is a less potent hydrogen atom donor, and the N1H1···N2 distance clearly falls outside the range of hydrogen bonding distances (Table 1). Therefore, the tripodal cavity in **P-1** is more distorted than that in **1** owing to the differently substituted nitrogen donor atoms (Figures 1 and 4, Table 1).
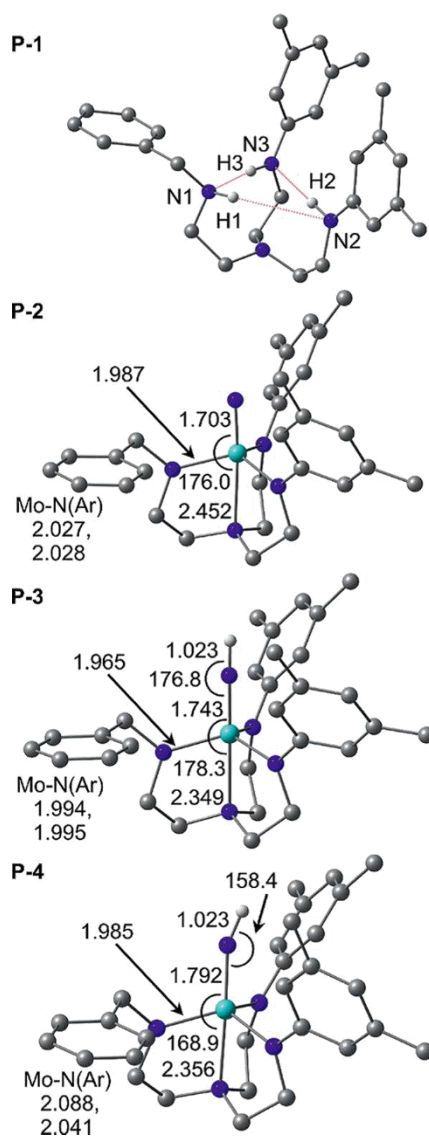
Figure 4. DFT models of **P-1**, **P-2**, **P-3**, and **P-4** (B3LYP, LANL2DZ, PCM THF).

The immobilized arylamines of **P-1** shift the absorption edge of the polymer into the visible spectral region (Figure 5). As further proof for the correct ligand formation on the polymeric support, we introduced Cu^{II} as an optical probe and EPR label[49–51] by treating **P-1** with $Cu(ClO_4)_2 \cdot 6H_2O$ and $Cu(NO_3)_2 \cdot 3H_2O$. Indeed, both Cu^{II}-loaded resins **P-5a** and **P-5b** feature the green color of the immobilized Cu^{II} complex and give broad absorptions between $\lambda_{max} = 700$ and 900 nm in the diffuse reflectance UV/Vis (DR-UV/Vis) spectra (Figure 5) similar to those of comparable copper(II) complexes.[52] The perchlorate and nitrate counterions are detected by their characteristic stretching vibrations at 1105 and 1384 cm^{-1}, respectively. The amount of immobilized copper in **P-5b** matches the expected value as measured by inductively coupled plasma MS (ICP-MS; 0.46 mmol g^{-1}).[53] In the EPR spectrum (77 K) of **P-5a**, resonances at $g_{1,2,3} = 2.020$, 2.139, and 2.231 with characteristic hyperfine coupling to $^{63/65}Cu$ nuclei of $A_{1,2,3} = 15$, 30, and 160 G are observed (Figure 6). The EPR spectrum of **P-5b** is less well resolved ($g_{1,2,3} = 2.058$, 2.134, and 2.250; $A_{1,2,3} = 40$, 20, and 170 G), but it is characteristic

of Cu^{II} coordination. These values are similar to the data reported for comparable copper(II) complexes with substituted tren ligands[52,54] under dilute conditions. This suggests that tridentate coordination sites are indeed available on the matrix for metal-ion coordination and that the coordination sites are magnetically isolated.
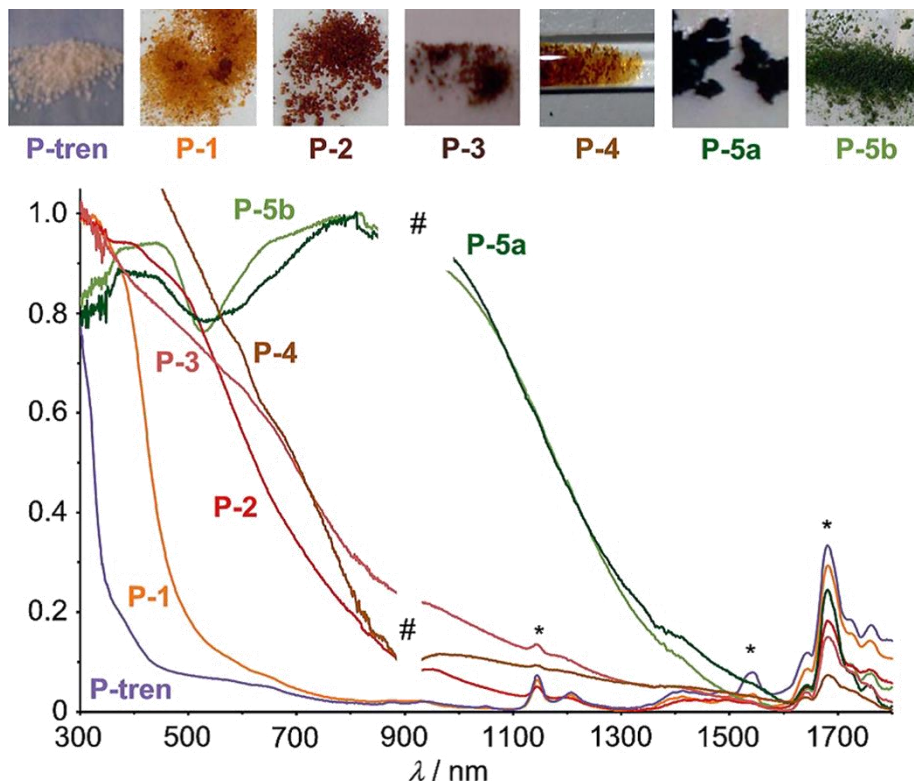

Figure 5. DR-UV/Vis spectra and photographs of P-tren, **P-1**, **P-2**, **P-3**, **P-4**, **P-5a**, and **P-5b** (* denotes overtones of CH and NH stretching vibrations of the polymer backbone; # denotes spikes and noises cause by the switch of detector of the spectrometer).
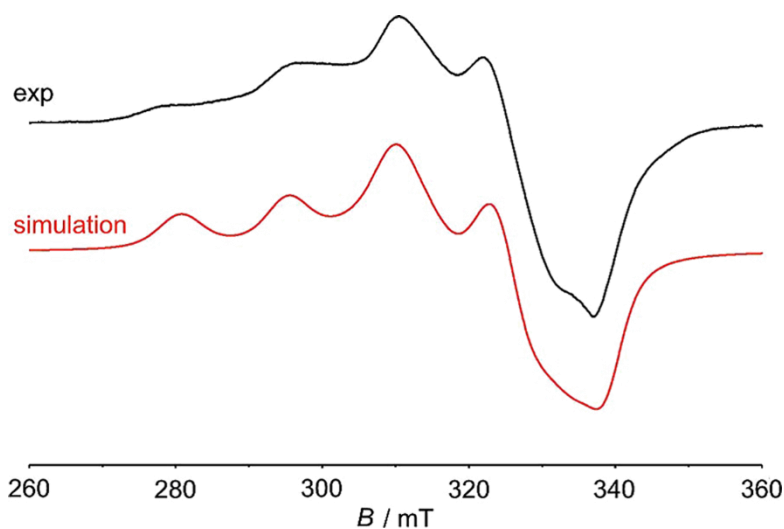

Figure 6. Experimental and simulated X-band EPR spectra of **P-5a** (solid, 77 K, 9.4 GHz).

The immobilized nitrido molybdenum(VI) complex is obtained by treating the supported ligand **P-1** with [MoCl$_3$N(CH$_3$CN)]$_4$[42,43] and LiNMe$_2$ as base (Scheme 2b). The resulting orange-red polymer **P-2** was characterized by DR-UV/Vis spectroscopy (Figure 5). The absorption edge of **P-2** is shifted bathochromically relative to that of **P-1** owing the ligand-to-metal charge-transfer bands of the immobilized molybdenum(VI) complex (Figure 5). The IR spectrum of **P-2** (difference spectrum "**P-2** minus **P-1**") shows the presence of weak absorption bands at $\tilde{v}$ = 1053 and 1028 cm^{-1} assignable to MoN stretching vibrations. The calculated Mo≡N distance of the DFT model (B3LYP, LANL2DZ, PCM THF) of **P-2** is slightly longer than that of **2** owing to the stronger electron-donating effect of the N$_{benzyl}$ donor. This is also reflected in the shorter Mo–N$_{benzyl}$ distance and the diminished *trans* influence of Mo≡N (shorter Mo···N$_{amine}$ distance; Figures 2 and 4). The DFT calculation on **P-2** predicts absorptions for Mo≡N stretching vibrations coupled to ligand backbone deformations at $\tilde{v}$ = 1045, 1035, and 1030 cm^{-1} (scaled by 0.9614)[36], which correspond to the experimentally observed absorption pattern in the Mo≡N region. The amount of immobilized molybdenum in **P-2** was estimated by hydrolytic release (HNO$_3$, H$_2$O) and ICP-MS quantification as 0.32 mmol g^{-1} polymer.[53] The amount of NH$_3$ released from **P-2** by acidic hydrolysis (by HCl in a H$_2$O/dioxane/benzene/ethanol mixture), measured as ammonium ions by ^{1}H NMR spectroscopy of the characteristic 1:1:1 triplet at δ = 7.46 ppm with $^1J_{14N,H}$ = 50Hz[55] (relative to toluene as internal standard; 0.32 mmol g–1 polymer), perfectly agrees with the amount of molybdenum and corroborates the 1:1 molybdenum/nitrido stoichiometry. The tren ligand **1** (and by analogy **P-1**) itself is stable in the presence of acid and does not form ammonia. In fact, the threefold protonated conjugate acid of **1** has been crystallized as [**1**-H$_3$][Cl][CoCl$_4$] (Figure 7; cubic, $P2_1$3). The [**1**-H$_3$]$^{3+}$ ion features crystallographic C_3 symmetry. Interestingly, the chloride ion Cl2 is coordinated by the triammonium ion through three hydrogen bonds in the trigonal binding pocket, whereas the tetrachloridocobaltate(II) ions are attached to the NH groups pointing to the outside of the trigonal cavity. The cavity formed by the triammonium ion of **1** is rather open as compared to that of the neutral ligand **1** (Figure 1) or metal complexes derived from triamido amine ligands.

Careful equimolar protonation of **P-2** with [2,6-lutH][Al{OC(CF$_3$)$_3$}$_4$][56] yielded a red-brown polymer **P-3**, which was characterized by IR spectroscopy (difference spectrum "**P-3** minus **P-2**"). The IR spectrum shows a new weak absorption at ca. 3315 cm^{-1} (NH stretching vibration) and several absorptions assignable to the aluminato counterion,[56] which overlap with possible Mo=N absorptions (possibly buried under the 975 cm^{-1} anion band; see Exp. Sect.). The DR-UV/Vis spectrum of **P-3** reveals a slightly shifted absorption edge relative to that of **P-2** (Figure 5). The amount of 2,6-lutidine generated by the acid/base reaction was quantified by ^{1}H NMR spectroscopy with toluene as an internal standard and corroborates quantitative proton transfer from 2,6-lutidinium to the nitrido complex. Deuteration of **P-2** with [2,6-lutD][Al{OC(CF$_3$)$_3$}$_4$] gives the corresponding *N*-deuterated derivative **P-3D**, which shows the expected ND vibration at ca. 2337 cm^{-1}, this further corroborating the successful acid/base reaction. The DFT model of **P-3** predicts three Mo=N vibrations coupled to ligand backbone

vibrations at 948, 963, and 966 cm^{-1} and the NH stretching vibration at 3426 cm^{-1} (all scaled by 0.9614)[36]. As expected, the d^0 Mo^{VI} complex **P-3** is EPR-silent at 77 K.
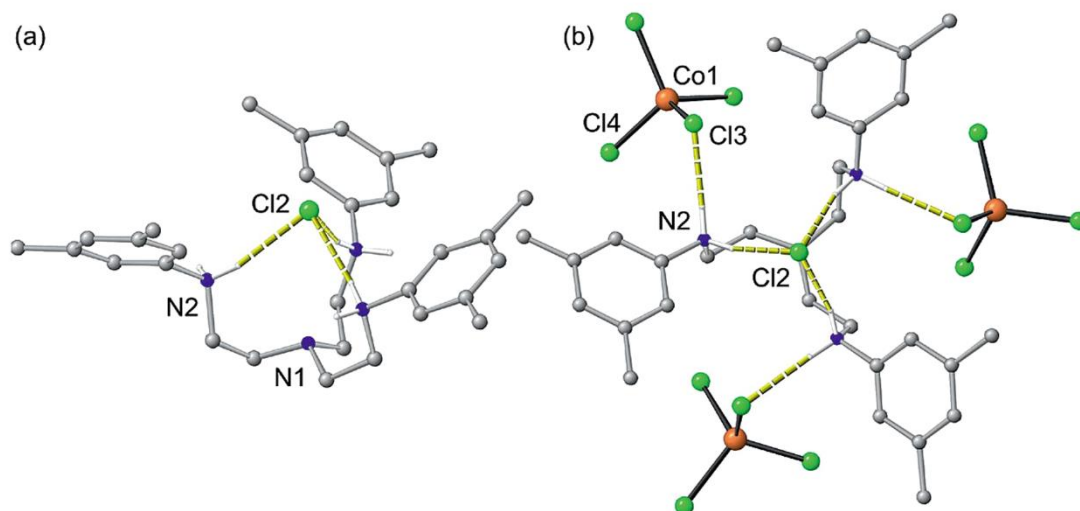

Figure 7. Molecular crystal structure of [**1**-H$_3$][Cl][CoCl$_4$]. (a) Side view of the {[**1**-H$_3$][Cl]}$^{2+}$ unit, (b) top view with the attached [CoCl$_4$]$^{2-}$ ions showing the threefold symmetry (CH hydrogen atoms omitted).

The treatment of the immobilized cationic imido molybdenum(VI) complex **P-3** with the one-electron reductant cobaltocene ($E = -1.33$ mV vs. FcH/FcH$^+$ in CH$_2$Cl$_2$)[57] yields the corresponding soluble diamagnetic cobaltocenium ion (characterized and quantified by ^{1}H NMR spectroscopy; $\delta = 5.04$ ppm with toluene as internal standard) and a polymer-anchored molybdenum(V) species **P-4**, which was characterized by IR, DR-UV/Vis, and EPR spectroscopy.[27,58] The NH stretching vibration of **P-4** is not clearly observed and neither is the corresponding ND stretch of the isotopomer **P-4D**, which might be because of their lower intensity compared to those of **P-3**/**P-3D**. The absorption bands associated with the aluminato counterion are basically absent in **P-4**, which suggests that it is a neutral immobilized complex. In the DR-UV/Vis spectrum, the absorption edge of **P-4** is only weakly affected with respect to that of **P-3**.

In contrast to diamagnetic **P-3**, the cobaltocene-treated polymer **P-4** is EPR-active. The EPR spectrum of **P-4** at 77 K displays a slightly rhombic feature at $g_{1,2,3} = 1.9020, 1.9290, 1.9890$. The $g < 2.0$ resonance is characteristic of a d^1 Mo^V complex (Figure 8b).[27,58] Hyperfine coupling to ^{1}H or ^{14}N nuclei is not clearly resolved but is required for a sufficiently acceptable simulation of the shape of the lower g signal [$A_{1,2,3}$(^{1}H) = 1, 8, 8G; $A_{1,2,3}$(^{14}N) = 1, 4, 4G]. The presence of coupling to ^{1}H nuclei is evident by comparison of the EPR spectrum of **P-4** with that of the isotopomer **P-4D** (Figure 8b), which has a smaller line width in the low g region as expected for smaller A(^{2}H) coupling constants. The slightly rhombic g tensor points to some distortion of the (pseudo)trigonal symmetry; this is also reflected in the DFT model of **P-4**, which features a bent imido ligand with a Mo=N–H angle of 158° (Figure 4). At the moment, it is unclear if this distortion arises from the inherent lower symmetry of the immobilized tripod

ligand or from a possible Jahn–Teller distortion of a nearly C_3-symmetric d^1 molybdenum(V) complex. As a similar distortion is found for the DFT model of **4** (Figure 3), a Jahn–Teller effect might be operative in **P-4**.
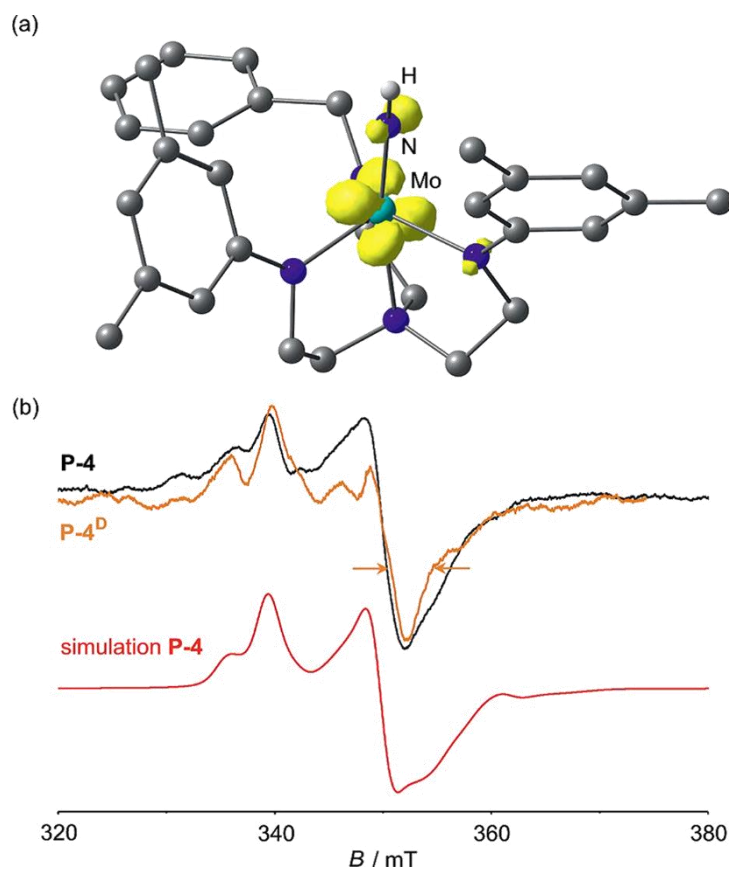

Figure 8. (a) Spin density (isosurface 0.02 a.u.) calculated for the DFT model of **P-4** and (b) X-band EPR spectra of **P-4** and **P-4^D** (solid, 77 K, 9.4 GHz) and simulation.

The DFT model of **P-4** predicts Mo=N stretching vibrations coupled to ligand backbone vibrations at 834, 841, 842, and 847 cm^{-1}; the NH stretch is calculated at 3404 cm^{-1} (all scaled by 0.9614)[36] with a 74% lower intensity than that of **P-3**, which explains why we were unable to experimentally observe the NH/ND mode in the polymer. Single-point DFT/PCM/GIAO calculations of the optimized structure (B3LYP, LANL2DZ, PCM THF) with the EPR-II basis[59] set for C, H, N and the WTBS basis set for Mo[60,61] yielded values for the g tensor of $g_{1,2,3} = 1.8218, 1.9458, 1.9816$. The isotropic hyperfine coupling constants to ^{14}N and ^{1}H were calculated as $A(^{14}N) = 3.9$ G and $A(^1H) = 7.5$ G, which is also reflected by the delocalization of the spin density onto the molybdenum center, the nitrogen atom of the monodentate amido ligand, and to a smaller extent one amido nitrogen atom of the tripod ligand (Figure 8a). Thus, the paramagnetic matrix-confined molybdenum(V) imido complex **P-4** is stable enough for spectroscopic characterization, in contrast to its soluble analogue, which is prone to further (bimolecular) reactivity.

3. CONCLUSIONS

We have prepared a polymer-immobilized analogue (**P-2**) of the Schrock–Yandulov nitrido molybdenum(VI) complex LMoN by using a sterically unencumbered polymer-anchored triamidoamine ligand **P-1** and [MoCl₃N(CH₃CN)]₄ as the "MoN" source. The analogous soluble ligand **1** and its nitrido complex **2** have been synthesized for comparison. The soluble and immobilized nitrido complexes are protonated at the nitrido ligand to the corresponding imido complexes **3** and **P-3**, respectively, as shown by a variety of spectroscopic techniques. One-electron reduction of the soluble complex **3** is irreversible, probably because of bimolecular proton/electron transfer reactions. However, the polymer-anchored imido molybdenum(VI) complexes **P-3**/**P-3$^\mathbf{D}$** can be reduced to their imido molybdenum(V) congeners **P-4**/**P-4$^\mathbf{D}$** as shown by DR-UV/Vis, IR, and EPR spectroscopy in combination with DFT calculations. In the future, we aim to characterize more intermediates relevant to the Schrock–Yandulov cycle anchored on a polymer support. The results of these efforts will be reported in due course.

4. EXPERIMENTAL SECTION

General considerations: All reactions were performed under an inert gas (Schlenk techniques, glove box). For the solid-phase reactions a flask with a nitrogen inlet and a coarse-porosity fritted glass filter that allows addition and removal of reagents and solvents without exposure of the resin to the atmosphere was used.[62] THF was distilled from potassium, and petroleum ether (b.p. 40–60°C) and toluene were distilled from sodium. Tris(2-aminoethyl)amine resin (1% divinyl benzene, 100–200 mesh, 0.6–1.0 mmol g⁻¹) was obtained from IRIS Biotech GmbH (Germany). Other chemicals were obtained from commercial suppliers and used without further purification. Compound **1**,[31,32] [MoCl₃N(CH₃CN)]₄,[42,43] MoCl₄(thf)₂,[37,39] and Li[Al{OC(CF₃)₃}₄][56] were synthesized as reported. IR spectra were recorded on a BioRad Excalibur FTS 3000 spectrometer with samples in THF in KBr cells, cesium iodide disks, or potassium bromide disks. The UV/Vis spectra of sample solutions in 1.0 cm cells (Hellma, suprasil) wre recorded with a Varian Cary 5000 spectrometer. The solid-phase spectra were recorded by using this spectrometer equipped with a Praying Mantis diffuse reflectance Accessory. Field desorption (FD) mass spectra were recorded with a Finnigan MAT90 FD spectrometer. ESI mass spectra were recorded with a Micromass Q-TOF-Ultima spectrometer. NMR spectra were recorded with a Bruker Avance DRX 400 spectrometer at 400.31 (^{1}H), 100.66 (^{13}C{^{1}H}), 367.67 (^{19}F), and 40.56 MHz (^{15}N). All resonances are reported in ppm relative to the solvent signal as an internal standard {[D₈]THF (^{1}H: δ = 1.72, 3.58 ppm; ^{13}C: δ = 25.5, 67.7 ppm); C₆D₆ (^{1}H: δ = 7.20 ppm; ^{13}C: δ = 128.0 ppm)} or to external CFCl₃ (^{19}F: δ = 0 ppm) and external CH₃NO₂ (90% in CDCl₃; ^{15}N: δ = 380.23 ppm). The ^{15}N NMR data are reported relative to liquid NH₃ as reference (δ = 0 ppm). Electrochemical experiments were performed with a BioLogic SP-50 voltammetric analyzer with platinum wire working and counter electrodes and a 0.01 M Ag/AgNO₃ reference electrode. Scan rates were 20–50 mV s⁻¹ for cyclic

voltammetry experiments and 10 mV s^{-1} for square-wave voltammetry experiments with 0.1 M [nBu$_4$N][B(C$_6$F$_5$)$_4$] as supporting electrolyte in THF. Potentials are given relative to the ferrocene/ferrocenium couple. X-band continuous wave (CW) EPR spectra were measured with a Miniscope MS 300 (Magnettech GmbH, Germany) spectrometer. The *g*-values are referenced to external Mn^{2+} in ZnS (*g* = 2.118, 2.066, 2.027, 1.986, 1.946, 1.906). Simulations were performed with the EasySpin program package.[63] Elemental analyses were performed by the microanalytical laboratory of the chemical institutes of the University of Mainz. ICP-MS measurements (Mo, Cu) were performed with an HP 4500 instrument by using external calibration.

Density Functional Calculations: Calculations were performed with the Gaussian09/DFT[64] series of programs. The B3LYP formulation of density functional theory was used with the LANL2DZ basis set. To include solvent effects, the integral equation formalism polarizable continuum model (IEFPCM, THF) was employed. No symmetry constraints were imposed on the molecules. All structures were characterized as minima by frequency analysis (N_{imag} = 0), except for **3**, which shows low-energy imaginary frequencies for methyl rotations of the mesityl substituents. In GIAO calculations, the EPR-II basis set[59] was employed for C, H, and N, and the WTBS basis set was employed for Mo.[60,61]

X-ray Structure Determinations: The intensity data were collected with a STOE IPDS 2T diffractometer with Mo-K_α radiation (λ = 0.71073 Å) and corrected for absorption and other effects. The diffraction frames were integrated by using the SAINT package, and most were corrected for absorption with MULABS.[65,66] The structures were solved by direct methods and refined by the full-matrix method based on F^2 by using the SHELXTL software package.[67,68] All non-hydrogen atoms were refined anisotropically, and the positions of all hydrogen atoms were generated with appropriate geometric constraints and allowed to ride on their respective parent carbon atoms with fixed isotropic thermal parameters. CCDC-930315 (for **1**), -934080 (for [**1**-H$_3$][Cl][CoCl$_4$]), and 959158 (for **2**) contain the supplementary crystallographic data for this paper. These data can be obtained free of charge from The Cambridge Crystallographic Data Centre via www.ccdc.cam.ac.uk/data_request/cif.

1: C$_{30}$H$_{42}$N$_4$ (458.68); *T* = 193(2) K; 0.60 × 0.60 × 0.40 mm; monoclinic, $P2_1/n$ (No. 14); *a* = 15.5119(9) Å; *b* = 10.8753(5) Å; *c* = 16.4685(10) Å; β = 99.360(5)°; *V* = 2741.2(3) Å^3; Z = 4; density = 1.111 Mg m^{-3}; absorption coefficient 0.066 mm^{-1}; *F*(000) = 1000; θ range for data collection = 3.13–28.80°; limiting indices: $-18 \le h \le 20$, $-13 \le k \le 14$, $-22 \le l \le 22$; reflections collected/unique = 17984/7056 [*R*(int) = 0.0348]; completeness to θ = 28.80°: 98.7%; absorption correction: semi-empirical from equivalents; max./min. transmission = 0.9742/0.9617; data/restraints/parameters = 7056/0/314; goodness-of-fit on F^2 = 1.050; final *R* indices [*I* > 2σ(*I*)]: R_1 = 0.0480, wR_2 = 0.1330; *R* indices (all data): R_1 = 0.0684, wR_2 = 0.1533; extinction coefficient = 0.020(2); largest diff. peak/hole = 0.219/–0.194 eÅ^{-3}.

[1-H₃][Cl][CoCl₄]: $C_{30}H_{45}Cl_5CoN_4$ (697.89); T = 173(2) K; 0.26 × 0.24 × 0.21 mm; cubic, $P2_13$ (No. 198); a = 15.3039(2) Å; V = 3584.32(8) Å³; Z = 4; density = 1.293 Mg m⁻³; absorption coefficient = 0.876 mm⁻¹; $F(000)$ = 1460; θ range for data collection = 1.88–27.90°; limiting indices: $-20 \leq h \leq 20$, $-20 \leq k \leq 20$, $-20 \leq l \leq 20$; reflections collected/unique = 88109/2886 [R(int) = 0.0691]; completeness to θ = 27.90°: 100%; absorption correction: semi-empirical from equivalents; max./min. transmission = 0.832/0.796; data/restraints/parameters = 2886/0/127; goodness-of-fit on F^2 = 1.052; final R indices [$I > 2\sigma(I)$]: R_1 = 0.0300, wR_2 = 0.0815; R indices (all data): R_1 = 0.0355, wR_2 = 0.0836; absolute structure parameter = –0.013(18); largest diff. peak/hole = 0.666/–0.233 eÅ⁻³.

2: $C_{30}H_{39}MoN_5$ (565.60); T = 173(2) K; 0.23 × 0.04 × 0.03 mm; monoclinic, $P2_1$/c (No. 14); a = 11.4616(11) Å; b = 27.237(3) Å; c = 9.9571(10) Å; β = 115.729(6)°; V = 2800.3(5) Å³; Z = 4; density = 1.342 Mg m⁻³; absorption coefficient = 0.495 mm⁻¹; $F(000)$ = 1184; θ range for data collection = 2.39–28.10°; limiting indices: $-15 \leq h \leq 15$, $-35 \leq k \leq 31$, $-13 \leq l \leq 12$; reflections collected/unique = 20915/6769 [R(int) = 0.0758]; completeness to θ = 28.10°: 99.1%; absorption correction: semi-empirical from equivalents; max./min. transmission = 0.9853/0.8946; data/restraints/parameters = 6769/0/331; goodness-of-fit on F^2 = 0.891; final R indices [$I > 2\sigma(I)$]: R_1 = 0.0400, wR_2 = 0.0697; R indices (all data): R_1 = 0.0705, wR_2 = 0.0764; largest diff. peak/hole = 0.584/–0.694 eÅ⁻³.

[2,6-LutD]Cl: [2,6-LutH]Cl (100 mg, 0.69 mmol) was dissolved in D_2O (0.5 mL, 99.97% D), and the mixture was stirred at room temperature for 12 h. The solvent was removed under reduced pressure, and the colorless powder was washed several times with THF and dried under reduced pressure. Yield 79.5 mg (0.55 mmol, 80%). MS (ESI+): m/z (%) = 109.1 (100) $[C_7H_8DN]^+$. ¹H NMR ([D₈]THF): δ = 8.20 (t, ³$J_{H,H}$ = 7.8 Hz, 1 H, H$_p$), 7.59 (d, ³$J_{H,H}$ = 7.8 Hz, 2 H, H$_m$), 2.82 (s, 6 H, CH₃) ppm.

[2,6-LutH][Al{OC(CF₃)₃}₄]: [2,6-LutH]Cl (100 mg, 0.69 mmol) and Li[Al{OC(CF₃)₃}₄][56] (673.5 mg, 0.69 mmol) were dissolved in CH_2Cl_2 (30 ml), and the mixture was stirred at room temperature for 12 h. After filtration of the mixture through Celite, the filtrate was dried under reduced pressure. Yield 630 mg (0.59 mmol, 85%). ¹H NMR (CD₂Cl₂): δ = 16.38 (br. s, 1 H, NH), 8.16 (t, ³$J_{H,H}$ = 8.0 Hz, 1 H, H$_p$), 7.50 (d, ³$J_{H,H}$ = 8.0 Hz, 2 H, H$_m$), 2.91 (s, 6 H, CH₃) ppm. ¹³C{¹H} NMR (CD₂Cl₂): δ = 154.2 (s, C$_o$), 145.6 (C$_p$), 125.3 (s, C$_m$), 121.7 (q, ¹$J_{C,F}$ = 293 Hz, CF₃), 19.6 (s, CH₃) ppm. ¹⁹F NMR (CD₂Cl₂): δ = –76.1 (s, CF₃) ppm. MS (ESI+): m/z (%) = 108.6 (100) $[C_7H_9N]^+$. MS (ESI–): m/z (%) = 966.9 (100) $[Al\{OC(CF_3)_3\}_4]^-$.

[2,6-LutD][Al{OC(CF₃)₃}₄]: [2,6-LutD][Al{OC(CF₃)₃}₄] was prepared analogously to [2,6-LutH][Al{OC(CF₃)₃}₄] from [2,6-lutD]-Cl. ¹H-NMR ([D₈]THF): δ = 16.39 (br. s, 0.4 H, NH), 8.26 (t, ³$J_{H,H}$ = 7.6 Hz, 1 H, H$_p$), 7.62 (d, ³$J_{H,H}$ = 7.6 Hz, 2 H, H$_m$), 2.82 (s, 6 H, CH₃) ppm; corresponding to 60% D. ¹⁹F NMR ([D₈]THF): δ = –78.1 (s, CF₃) ppm. MS (ESI+): m/z (%) = 109.1 (96) $[C_7H_8DN]^+$.

Ligand 1: Ligand **1** was prepared according to ref.[31,32] ¹H NMR ([D₈]THF): δ = 6.21 (s, 3 H, H$_p$), 6.11 (s, 6 H, H$_o$), 4.57 (t, 3 H, ³$J_{H,H}$ = 5.0 Hz, NH), 3.11 (td, 6 H, ³$J_{H,H}$ = 5.0 Hz, ³$J_{H,H}$ = 6.0 Hz, CH₂NH),

2.77 (t, 6 H, $^3J_{H,H}$ = 6.0 Hz, CH$_2$N), 2.12 (s, 18 H, CH$_3$) ppm. ^{13}C{^{1}H} NMR ([D$_8$]THF): δ = 149.7 (s, C$_i$), 138.4 (s, C$_m$), 119.0 (s, C$_p$), 111.4 (s, C$_o$), 54.2 (s, CH$_2$N), 42.5 (s, CH$_2$NH), 21.5 (s, CH$_3$) ppm. ^{15}N NMR (HMBC, [D$_8$]THF): δ = 26 (N), 62 (NH) ppm. MS (FD): m/z (%) = 458.5 (100) [M]$^+$. IR (KBr): $\tilde{\nu}$ = 3390 (m, NH), 3340 (s, NH), 3012 (m, CH), 2941 (m, CH), 2842 (s, CH), 1607 (vs, CC), 1517 (s), 1473 (s), 1340 (s, CN), 1193 (s, CN), 1060 (m, CN), 817 (s), 690 (m) cm^{-1}. UV/Vis (THF): λ (ε) = 252 (29925), 299 (6565 M^{-1} cm^{-1}) nm. C$_{30}$H$_{42}$N$_4$ (458.69): calcd. C 78.56, H 9.23, N 12.21; found C 78.40, H 9.09, N 12.21. Single crystals suitable for X-ray analysis were obtained by recrystallization from petroleum ether (b.p. 40–60°C).

Complex 2. Method A: The chlorido complex was prepared from **1** and MoCl$_4$(thf)$_2$ with Li[N(SiMe$_3$)$_2$] as base in THF, similarly to the procedure described by Schrock.[32] To the chlorido complex (100 mg, 0.22 mmol) dissolved in toluene/THF (10:1, 11 ml) was added Me$_3$SiN$_3$ (130 mg, 1.1 mmol), and the mixture was heated to 90°C for 12 h. The volatiles were removed under reduced pressure at 90–100°C. The resulting yellow-brown solid was dissolved in petroleum ether (b.p. 40–60°C; 50 mL), and the mixture was filtered through Celite. The filtrate was dried under reduced pressure to yield a yellow powder. Yield 50 mg (0.088 mmol, 36%).

Method B: Compound **1** (100 mg, 0.22 mmol) and [MoCl$_3$N(CH$_3$CN)]$_4$ (105 mg, 0.09 mmol) were dissolved in THF (20 mL). The reaction mixture turned dark red and was stirred for 20 min. The addition of solid LiNMe$_2$ (54 mg, 0.88 mmol) resulted in an immediate color change to purple. The solution was heated to 50°C to remove the volatile NHMe$_2$. The color changed to red-brown, and toluene (10 mL) was added. The mixture was stirred at 60°C for 12 h, during which LiCl precipitated. All solvents and residual traces of LiNMe$_2$ were removed under reduced pressure at 50–90°C. The solid residue was dissolved in toluene (20 mL), and the solution was filtered through Celite. The solvent was removed under reduced pressure to yield a yellow powder. After recrystallization from toluene at room temperature, yellow crystals suitable for X-ray diffraction analysis were obtained. Yield 40 mg (0.07 mmol, 32%). ^{1}H NMR ([D$_8$]THF): δ = 7.11 (s, 6 H, H$_o$), 6.51 (s, 3 H, H$_p$), 3.89 (br. t, 6 H, CH$_2$NMo), 3.01 (br. t, 6 H, CH$_2$N), 2.19 (s, 18 H, CH$_3$) ppm. ^{13}C{^{1}H} NMR ([D$_8$]THF): δ = 161.7 (s, C$_i$), 137.1 (s, C$_m$), 124.3 (s, C$_p$), 119.7 (s, C$_o$), 57.4 (s, CH$_2$N), 51.3 (s, CH$_2$NMo), 21.5 (s, CH$_3$) ppm. ^{15}N NMR (HMBC, [D$_8$]THF): δ = 41 (N$_{amine}$), 44 (N$_{amido}$) ppm; N$_{nitrido}$ not observed in the HMBC experiment. IR (CsI): $\tilde{\nu}$ = 1094 (m, MoN), 1024 (m, MoN) cm^{-1}. UV/Vis (THF): λ (ε) = 259 (10910), 298 (7350), 347 (2470), 516 (1810 M^{-1} cm^{-1}) nm. CV (THF): E_p(red) = –3.5 V (irr.); E_p(ox, reverse scan) = –2.9 V. C$_{30}$H$_{39}$MoN$_5$ (565.61): calcd. C 63.71, H 6.95, N 12.38; found C 62.64, H 7.33, N 13.38.

Complex 3: Compound **2** (20 mg, 0.035 mmol) was dissolved in benzene (5 mL), and solid [2,6-lutH][Al{OC(CF$_3$)$_3$}$_4$] (37 mg, 0.035 mmol) was added. The solution immediately changed from yellow-brown to green. This treatment leads to complex **3** in addition to some decomposition giving ligand **1** according to NMR and IR spectroscopy and unidentified Mo species. ^{1}H NMR (C$_6$D$_6$): δ = 7.38 (s, 6 H, H$_o$), 6.67 (s, 1 H, NH), 6.56 (s, 3 H, H$_p$), 3.56 (t, $^3J_{H,H}$ = 5 Hz, 6 H, CH$_2$NMo), 2.24 (br. t, 6 H, CH$_2$N), 2.14 (s, 18 H, CH$_3$). ^{1}H NMR ([D$_8$]THF): δ = 6.81 (s, 6 H, H$_o$), 6.65 (s, 1 H, NH), 6.33 (s, 3 H,

H_p), 4.40 (t, $^3J_{H,H}$ = 5 Hz, 6 H, CH$_2$NMo), 3.63 (t, $^3J_{H,H}$ = 5 Hz, 6 H, CH$_2$N), 2.19 (s, 18 H, CH$_3$). ^{13}C{^{1}H} NMR (C$_6$D$_6$): δ = 161.5 (s, C$_i$), 137.4 (s, C$_m$), 125.1 (s, C$_p$), 119.5 (s, C$_o$), 56.5 (s, CH$_2$N), 50.7 (s, CH$_2$NMo), 21.6 (s, CH$_3$) ppm. ^{15}N NMR (HMBC, C$_6$D$_6$): δ = 42 (N$_{amine}$), 226 (N$_{amido}$) ppm (MoNH not observed under these conditions). ^{15}N NMR (HMBC, [D$_8$]THF): δ = 80 (N$_{amine}$), 245 (N$_{amido}$) ppm (MoNH not observed under these conditions). ^{15}N NMR (HMQC, [D$_8$]THF): δ = 425 (MoNH) ppm. IR (THF): $\tilde{\nu}$ = 3278 (NH) cm^{-1}. IR (CsI): $\tilde{\nu}$ = 1278 [m, Al{OC(CF$_3$)$_3$}$_4^-$], 1242 [m, Al{OC(CF$_3$)$_3$}$_4^-$], 1222 [m, Al{OC(CF$_3$)$_3$}$_4^-$], 976 [s, Al{OC(CF$_3$)$_3$}$_4^-$], 728 [s, Al{OC(CF$_3$)$_3$}$_4^-$] cm^{-1}. UV/Vis (THF): λ = 261, 296, 314, 376 nm. CV (THF): E_p = −1.85 V (irr.).

Anchored Complex P-1: The palladium catalyst was preformed: *rac*-BINAP (0.05 g, 0.09 mmol) was dissolved in toluene (5 mL) at 70°C, and solid Pd$_2$(dba)$_3$ (0.03 g, 0.03 mmol) was added. The mixture was heated to 60°C for 2 h and then filtered through Celite. Tris(2-aminoethyl)amine resin (0.62 mmol g^{-1}, as analyzed by nitrogen content, 5 g, 3.1 mmol) was swollen in toluene (25 mL). To this suspension was added sodium *tert*-butoxide (0.84 g, 8.8 mmol), 1-bromo-3,5-dimethylbenzene (1.17 g, 6.3 mmol), and the catalyst solution. The orange-red suspension was stirred slowly at 85–95°C for 48 h. The suspension was cooldes to room temperature, and the resin was collected by filtration and washed several times with toluene (50 mL), THF (50 mL), and ethanol (50 mL) to remove excess reagents and formed NaBr. Finally, the resin was washed three times with diethyl ether (75 mL) and dried under reduced pressure. To monitor the success of the arylation, a portion of the resin was treated with ninhydrin. The absence of a blue color indicated the absence of primary amines. IR (CsI): $\tilde{\nu}$ = 3350 (br, NH) cm^{-1}. Elemental analysis found 2.84% N, which corresponds to 0.51 mmol ligand/g (based on the assumption of only monoarylated amines).

Anchored Complex P-2: Polymer **P-1** (500 mg, 0.25 mmol) was swollen in toluene/THF (10:1, 55 mL), and [MoCl$_3$N(CH$_3$CN)]$_4$ (120 mg, 0.10 mmol) in THF (5 mL) was added. The resin turned light red and was stirred at room temperature for 1 h. Solid LiNMe$_2$ (51 mg, 1 mmol) was added, and the suspension was heated to 70–80°C for 4 d, which resulted in the formation of a dark red resin and some white LiCl precipitate on the flask wall. The resin was washed several times with THF (50 mL) until the solutions were colorless. Finally, the red resin was washed three times with diethyl ether (3×30 mL) and dried under reduced pressure at 50–100°C. IR (CsI, difference spectrum): $\tilde{\nu}$ = 1053 (m, Mo≡N), 1028 (m, Mo≡N) cm^{-1}. Elemental analysis found 3.14% N, which corresponds to 0.45 mmol complex/g (based on the assumption of only monoarylated amines and quantitative complexation). Mo release by ICP-MS: 0.326(1) mmol g^{-1}; thus, not all sites are available for complexation with molybdenum. NH$_3$ release by ^{1}H NMR: 0.32 mmol g^{-1} {as NH$_4$Cl; ^{1}H NMR ([D$_6$]DMSO/C$_6$D$_6$/HCl in 1,4-dioxane): δ = 7.46 ppm (t, $^1J_{14N,H}$ = 50 Hz); integrated against toluene as internal standard; ^{15}N NMR: δ = 23 ppm (d, $^1J_{15N,H}$ = 70 Hz)}.

Anchored Complex P-3: Compound **P-2** (15 mg, 4.5 μmol) was swollen in THF (1 mL), and [2,6-lutH][Al{OC(CF$_3$)$_3$}$_4$] (4.3 mg, 4.0 μmol) dissolved in THF (1 mL) was added. The suspension was

stirred at room temperature for 2 h. The solution was removed with a syringe, and the red polymer was washed twice with THF (2×3 mL). The combined solutions were concentrated under reduced pressure, and all volatiles were trapped in HCl/dioxane (77 K) to determine the amount of generated 2,6-lutidine by ^{1}H NMR spectroscopy. The generated 2,6-lutidine was measured as [2,6-lutH]Cl in [D$_6$]DMSO with toluene as internal standard: 4.2 μmol (quantitative within error). IR (CsI): $\tilde{\nu}$ = 3315 (w, br., NH), 1278 [m, Al{OC(CF$_3$)$_3$}$_4^-$], 1242 [m, Al{OC(CF$_3$)$_3$}$_4^-$], 1221 [m, Al{OC(CF$_3$)$_3$}$_4^-$], 975 [s, Al{OC(CF$_3$)$_3$}$_4^-$], 728 [s, Al{OC(CF$_3$)$_3$}$_4^-$] cm^{-1}. EPR (THF, 77 K): silent.

Anchored Complex P-3^D: P-3^D was synthesized analogously to **P-3** from **P-2** (15 mg, 4.5 μmol) and [2,6-lutD][Al{OC(CF$_3$)$_3$}$_4$] (4.3 mg, 4.0 μmol; ca. 60% deuterated). IR (CsI): $\tilde{\nu}$ = 2337 (w, br., ND), 1277 [m, Al{OC(CF$_3$)$_3$}$_4^-$], 1240 [m, Al{OC(CF$_3$)$_3$}$_4^-$], 1224 [m, Al{OC(CF$_3$)$_3$}$_4^-$], 976 [s, Al{OC(CF$_3$)$_3$}$_4^-$], 727 [s, Al{OC(CF$_3$)$_3$}$_4^-$] cm^{-1}.

Anchored Complex P-4: Compound **P-3** (10 mg, 2.5 μmol) was swollen in THF, and solid Cp$_2$Co (0.45 mg, 2.4 μmol) was added. The solution turned from purple to brown indicating oxidation of Cp$_2$Co to [Cp$_2$Co]$^+$. After 1 h the supernatant solution was removed by syringe and the red-brown polymer was dried under reduced pressure. EPR (THF, 77 K): $g_{1,2,3}$ = 1.9890, 1.9290, 1.9020; A(^{1}H) = 1, 8, 8 G; A(^{14}N) = 1, 4, 4 G; A($^{95/97}$Mo) = 32, 52, 55 G. Amount of formed [Cp$_2$Co]$^+$ by ^{1}H NMR referenced against toluene as internal standard: 2.5 μmol (quantitative within error). IR (CsI): absorption bands of the counterion are absent.

Anchored Complex P-4^D: P-4^D was synthesized analogously to **P-4** from **P-3^D** (10 mg, 2.5 μmol) and Cp$_2$Co (0.45 mg, 2.4 μmol). EPR (THF, 77 K): $g_{1,2,3}$ = 1.9870, 1.9290, 1.9040; A(^{2}H) = 0, 1.2, 1.2 G; A(^{14}N) = 1, 4, 4 G; A($^{95/97}$Mo) = 31, 51, 52 G. IR (CsI): absorption bands of the counterion are absent.

Anchored Complex P-5a: A procedure according to ref.[54] was adopted to prepare a [Cu(NCCH$_3$)(tren)](ClO$_4$)$_2$ complex. Cu(ClO$_4$)$_2$·6H$_2$O (20 mg, 0.054 mmol) was dissolved in dry THF (1 mL) in a Schlenk flask to give a blue solution, which was transferred to another Schlenk flask containing the yellow resin **P-1** (100 mg, 0.05 mmol) swollen in dry CH$_2$Cl$_2$. The color of the resin immediately changed to light green. All solvents were removed under reduced pressure, and CH$_2$Cl$_2$ was added. After 5 min, NEt$_3$ (25 μL diluted in 1 mL of CH$_2$Cl$_2$) was added, and the mixture was stirred for 20 min to give a dark green resin. The resin was washed several times with water and CH$_2$Cl$_2$ and dried in vacuo. The dark green resin was washed several times with dry acetonitrile (30 mL) until the washing solutions were colorless and then again dried in vacuo. IR (CsI): $\tilde{\nu}$ = 3259 (br. m, NH), 2163 (m, CN), 1105 (s, ClO$_4^-$) cm^{-1}. DR-UV/Vis: $\lambda \approx$ 800 nm. EPR (CH$_2$Cl$_2$, 295 K): g = 2.0350, 2.1340, 2.2280; A($^{63/65}$Cu) = 12, 28, 150 G. EPR (solid, 295 K): g = 2.0280, 2.1400, 2.2280; A($^{63/65}$Cu) = 15, 30, 159 G. EPR (CH$_2$Cl$_2$, 77 K): g = 2.0250, 2.1350, 2.2290; A($^{63/65}$Cu) = 15, 30, 157 G. EPR (solid, 77 K): g = 2.0200, 2.1390, 2.2310; A($^{63/65}$Cu) = 15, 30, 160 G. Immobilized [Cu(NCCH$_3$)(tren)](ClO$_4$)$_2$ (0.43 mmol g^{-1}): calcd. N 3.04; found N 2.97.

Anchored Complex P-5b: $Cu(NO_3)_2 \cdot 3H_2O$ (12 mg, 0.05 mmol) was dissolved in THF (2 mL) to produce a turquoise solution. The yellow resin **P-1** (100 mg, 0.05 mmol ligand) was added to the solution, and the color of the resin immediately changed to green. The mixture was stirred for 20 min, and the resin was washed several times with THF (30 mL) until the washing solutions were colorless. The residue was dried in vacuo to afford **P-5b** as a green powder. IR (CsI): $\tilde{\nu}$ = 3222 (w, NH), 1384 (s, NO_3^-) cm^{-1}. DR-UV/Vis: $\lambda \approx 800$ nm. EPR (THF, 295 K): g = 2.0510, 2.1390, 2.2440; $A(^{63/65}Cu)$ = 28, 22, 160 G. EPR (solid, 295 K): g = 2.0520, 2.1390, 2.2440; $A(^{63/65}Cu)$ = 33, 23, 160 G. EPR (THF, 77 K): g = 2.0450, 2.1330, 2.2250; $A(^{63/65}Cu)$ = 35, 22, 170 G. EPR (solid, 77 K): g = 2.0510, 2.1390, 2.2440; $A(^{63/65}Cu)$ = 28, 22, 160 G. Immobilized [Cu(tren)(NO_3)](NO_3) (0.46 mmol g^{-1}): calcd. N 3.84; found N 3.95. Cu release by ICP-MS: 0.461(1) mmol g^{-1} (calcd. 0.46 mmol g^{-1}).

Supporting Information (for this article is available on the WWW under http://dx.doi.org/10.1002/ejic.201301156): UV/Vis spectra of **1**, **2**, and **3**; frontier molecular orbitals of **2** and **3**; Kaiser tests of P-tren and **P-1**; Cartesian coordinates of DFT-optimized geometries of **1**–**4** and **P-1** to **P-4** models (B3LYP, LANL2DZ, IEFPCM THF).

REFERENCES

[1]   H. Broda, S. Hinrichsen, F. Tuczek, *Coord. Chem. Rev.* **2013**, *257*, 587–598.

[2]   S. Hinrichsen, H. Broda, C. Gradert, L. Söncksen, F. Tuczek, *Annu. Rep. Prog. Chem., Sect. A: Inorg. Chem.* **2012**, *108*, 17–47.

[3]   R. R. Schrock, *Angew. Chem.* **2008**, *120*, 5594–5605; *Angew. Chem. Int. Ed.* **2008**, *47*, 5512–5522.

[4]   W. W. Weare, X. Dai, M. J. Byrnes, J. M. Chin, R. R. Schrock, P. Müller, *Proc. Natl. Acad. Sci. USA* **2006**, *103*, 17099–17106.

[5]   R. R. Schrock, *Acc. Chem. Res.* **2005**, *38*, 955–962.

[6]   B. A. MacKay, M. D. Fryzuk, *Chem. Rev.* **2004**, *104*, 385–401.

[7]   M. Hidai, *Coord. Chem. Rev.* **1999**, *185–186*, 99–108.

[8]   J. Chatt, J. R. Dilworth, R. L. Richards, *Chem. Rev.* **1978**, *78*, 589–625.

[9]   a) B. M. Hoffman, D. R. Dean, L. C. Seefeldt, *Acc. Chem. Res.* **2009**, *42*, 609–619; b) L. C. Seefeldt, B. M. Hoffman, D. R. Dean, *Annu. Rev. Biochem.* **2009**, *78*, 701–722.

[10]   J. B. Howard, D. C. Rees, *Proc. Natl. Acad. Sci. USA* **2006**, *103*, 17088–17093.

[11]   D. V. Yandulov, R. R. Schrock, *Science* **2003**, *301*, 76–78.

[12]   K. Arashiba, Y. Miyake and Y. Nishibayashi, *Nat. Chem.* **2011**, *3*, 120–125.

[13]   J. Chatt, A. J. Pearman, R. L. Richards, *Nature* **1975**, *253*, 39–40.

[14]   T. A. George, B. B. Kaul, *Inorg. Chem.* **1990**, *29*, 4969–4974.

[15]   K. Heinze, *Chem. Eur. J.* **2001**, *7*, 2922–2932.

[16]   M. S. Robillard, J. S. Leith, G. A. van der Marel, J. H. van Boom, J. Reedijk, *Eur. J. Inorg. Chem.* **2003**, 1529–1532.

[17]   M. Kol, R. R. Schrock, R. Kempe, W. M. Davis, *J. Am. Chem. Soc.* **1994**, *116*, 4382–4390.

[18]   G. E. Greco, R. R. Schrock, *Inorg. Chem.* **2001**, *40*, 3861–3878.

[19]   W. W. Weare, R. R. Schrock, A. S. Hock, P. Müller, *Inorg. Chem.* **2006**, *45*, 9185–9196.

[20]   D. V. Yandulov, R. R. Schrock, *Inorg. Chem.* **2005**, *44*, 1103–1117.

[21]   D. Xuereb, J. Dzierzak, R. Raja, "Biomimetic Single-Site Heterogeneous Catalysts: Design Strategies and Catalytic Potential" in *Catalysis by Metal Complexes 33: Heterogenized Homogeneous Catalysts for Fine Chemicals Production,* (Eds.: P. Barbaro, F. Ligiari), Springer, Dordrecht, **2010**, chapter 2.

[22]   J. M. Notenstein, A. Katz, *Chem. Eur. J.* **2006**, *12*, 3954–3965.

[23]   J. M. Thomas, R. Raja, D. W. Lewis, *Angew. Chem.* **2005**, *117*, 6614–6641; *Angew. Chem. Int. Ed.* **2005**, *44*, 6456–6482.

[24]   L. L. Welbes, A. S. Borovik, *Acc. Chem. Res.* **2005**, *38*, 765–774.

[25]   D. E. De Vos, I. F. J. Vankelecom, P. A. Jacobs (Eds.), *Chiral Catalyst Immobilization and Recycling*, Wiley-VCH, Weinheim, **2007**.

[26]   O. Leal, D. L. Anderson, R. G. Bowman, F. Basolo, R. L. Burwell Jr., *J. Am. Chem. Soc.* **1975**, *97*, 5125–5129.

[27]   K. Heinze, A. Fischer, *Eur. J. Inorg. Chem.* **2007**, 1020–1026.

[28]   K. Heinze, A. Fischer, *Eur. J. Inorg. Chem.* **2010**, 1939–1947.

[29]   K. Hüttinger, C. Förster, T. Bund, D. Hinderberger, K. Heinze, *Inorg. Chem.* **2012**, 51, 4180–4192.

[30]   K. Heinze, G. Marano, A. Fischer, *J. Inorg. Biochem.* **2008**, *102*, 1199–1211.

[31]   G. E. Greco, A. I. Popa, R. R. Schrock, *Organometallics* **1998**, *17*, 5591–5593.

[32]   G. E. Greco, R. R. Schrock, *Inorg. Chem.* **2001**, *40*, 3850–3860.

[33]   Y. S. Moroz, M. K. Takase, P. Müller, E. V. Rybak-Akimova, *Acta Crystallogr., Sect. E* **2011**, *67*, o3421.

[34]   A. Almesåker, J. L. Scott, L. Spiccia, C. R. Strauss, *Tetrahedron Lett.* **2009**, *50*, 1847–1850.

[35]   A. Pramanik, G. Das, *Tetrahedron* **2009**, *65*, 2196–2200.

[36]   W. Koch, M. C. Holthausen, *A Chemist's Guide to Density Functional Theory*, Wiley-VCH, Weinheim, **2001**.

[37]   F. Stoffelbach, D. Saurenz, R. Poli, *Eur. J. Inorg. Chem.* **2001**, 2699–2703.

[38]   J. Dilworth, R. L. Richards, *Inorg. Synth.* **1990**, *28*, 33–37.

[39] E. A. Allen, B. J. Brisdon, G. W. A. Fowles, *J. Chem. Soc.* **1964**, 4531–4534.

[40] D. V. Yandulov, R. R. Schrock, *J. Am. Chem. Soc.* **2002**, *124*, 6252–6253.

[41] D. V. Yandulov, R. R. Schrock, A. L. Rheingold, C. Ceccarelli, W. M. Davis, *Inorg. Chem.* **2003**, *42*, 796–813.

[42] E. Gauch, A. Hagenbach, J. Strähle, A. Dietrich, B. Neumüller, K. Dehnicke, *Z. Anorg. Allg. Chem.* **2000**, *626*, 489–493.

[43] K. Seyferth, R. Taube, *J. Organomet. Chem.* **1982**, *229*, C19–C23.

[44] V. Ritleng, D. V. Yandulov, W. W. Weare, R. R. Schrock, A. S. Hock, W. M. Davis, *J. Am. Chem. Soc.* **2004**, *126*, 6150–6163.

[45] a) S. Schenk, B. Le Guennic, B. Kirchner, M. Reiher, *Inorg. Chem.* **2008**, *47*, 3634–3650; b) F. Studt, F. Tuczek, *Angew. Chem.* **2005**, *117*, 5783–5787; *Angew. Chem. Int. Ed.* **2005**, *44*, 5639–5642.

[46] T. Munisamy, R. R. Schrock, *Dalton Trans.* **2012**, *41*, 130–137.

[47] E. Kaiser, R. L. Colescott, C. D. Bossinger, P. I. Cook, *Anal. Biochem.* **1970**, *34*, 595–598.

[48] V. K. Sarin, S. B. H. Kent, J. P. Tam, R. B. Merrifield, *Anal. Biochem.* **1981**, *117* 147–157.

[49] K. Heinze, A. Reinhart, *Inorg. Chem.* **2006**, *45*, 2695–2703.

[50] E. Hübner, G. Türkoglu, M. Wolf, U. Zenneck, N. Burzlaff, *Eur. J. Inorg. Chem.* **2008**, 1226–1235.

[51] A. Schiller, R. Scopelliti, M. Benmelouka, K. Severin, *Inorg. Chem.* **2005**, *44*, 6482–6492.

[52] A. Almesåker, P. Gamez, J. L. Scott, S. J. Teat, J. Reedijk, L. Spiccia, *Eur. J. Inorg. Chem.* **2010**, 5394–5400.

[53] a) R. S. Houk, V. A. Fassel, G. D. Flesch, A. L. Gray, E. Taylor, *Anal. Chem.* **1980**, *52*, 2283–2289; b) N. H. Bings, A. Bogaerts, J. A. C. Broekaert, *Anal. Chem.* **2013**, *85*, 670–704.

[54] G. Izzet, B. Douziech, T. Prangé, A. Tomas, I. Jabin, Y. Le Mest, O. Reinaud, *Proc. Natl. Acad. Sci. USA* **2005**, *102*, 6831–6836.

[55] J. K. M. Sanders, B. K. Hunter, C. J. Jameson, G. Romeo, *Chem. Phys. Lett.* **1988**, *143*, 471–476.

[56] I. Krossing, A. Reisinger, *Eur. J. Inorg. Chem.* **2005**, 1979–1989.

[57] N. G. Connelly, W. E. Geiger, *Chem. Rev.* **1996**, *96*, 877–910.

[58] J. Topich, *Inorg. Chem.* **1982**, *21*, 2079–2082.

[59] V. Barone in *Recent Advances in Computational Methods Part 1* (Ed.: D. P. Chong), World Scientific, Singapore, **1995**.

[60] a) S. Huzinaga, B. Miguel, *Chem. Phys. Lett.* **1990**, *175*, 289–291; b) S. Huzinaga, B. Klobukowski, *Chem. Phys. Lett.* **1993**, *212*, 260–264.

[61] The WTBS basis set was obtained from the Extensible Computational Chemistry Environment Basis Set Database, Version 02/02/06, as developed and distributed by the Molecular Science Computing Facility, Environmental and Molecular Sciences Laboratory, which is part of the

Pacific Northwest Laboratory, P.O. Box 999, Richland, WA 99352 and funded by the U.S. Department of Energy. The Pacific Northwest Laboratory is a multiprogram laboratory operated by Battelle Memorial Institute of the U.S. Department of Energy under Contract DE-AC06–76RLO.

[62]   a) K. Heinze, *Chem. Eur. J.* **2001**, *7*, 2922–2932; b) K. Heinze, J. D. Bueno Toro, *Angew. Chem.* **2003**, *115*, 4671–4674; *Angew. Chem. Int. Ed.* **2003**, *42*, 4533–4536; c) K. Heinze, V. Jacob, C. Feige, *Eur. J. Inorg. Chem.* **2004**, 2053–2061; d) K. Heinze, J. D. Bueno Toro, *Eur. J. Inorg. Chem.* **2004**, 3498–3507.

[63]   S. Stoll, A. Schweiger, *J. Magn. Reson.* **2006**, *178*, 42–55.

[64]   M. J. Frisch, G. W. Trucks, H. B. Schlegel, G. E. Scuseria, M. A. Robb, J. R. Cheeseman, G. Scalmani, V. Barone, B. Mennucci, G. A. Petersson, H. Nakatsuji, M. Caricato, X. Li, H. P. Hratchian, A. F. Izmaylov, J. Bloino, G. Zheng, J. L. Sonnenberg, M. Hada, M. Ehara, K. Toyota, R. Fukuda, J. Hasegawa, M. Ishida, T. Nakajima, Y. Honda, O. Kitao, H. Nakai, T. Vreven, J. A. Montgomery, Jr., J. E. Peralta, F. Ogliaro, M. Bearpark, J. J. Heyd, E. Brothers, K. N. Kudin, V. N. Staroverov, R. Kobayashi, J. Normand, K. Raghavachari, A. Rendell, J. C. Burant, S. S. Iyengar, J. Tomasi, M. Cossi, N. Rega, J. M. Millam, M. Klene, J. E. Knox, J. B. Cross, V. Bakken, C. Adamo, J. Jaramillo, R. Gomperts, R. E. Stratmann, O. Yazyev, A. J. Austin, R. Cammi, C. Pomelli, J. W. Ochterski, R. L. Martin, K. Morokuma, V. G. Zakrzewski, G. A. Voth, P. Salvador, J. J. Dannenberg, S. Dapprich, A. D. Daniels, O. Farkas, J. B. Foresman, J. V. Ortiz, J. Cioslowski, D. J. Fox, *Gaussian 09*, Revision A.02, Gaussian, Inc., Wallingford CT, **2009**.

[65]   *SMART Data Collection and SAINT-Plus Data Processing Software for the SMART System*, various versions, Bruker Analytical X-Ray Instruments Inc., Madison, **2000**.

[66]   B. Blessing, *Acta Crystallogr., Sect. A* **1995**, *51*, 33–38.

[67]   G. M. Sheldrick, *SHELXTL*, version 5.1, Bruker AXS, Madison, **1998**.

[68]   G. M. Sheldrick, *SHELXL-97*, University of Göttingen, **1997**.

3.3 Reactivity of a Polymer-Supported Nitrido Molybdenum(VI) Complex towards Protons and Electrons

Anica Wünsche von Leupoldt, Dorothée Iffland, Nicolas H. Bings, Katja Heinze

ABSTRACT

The publication from A. Wünsche von Leupoldt, C. Förster, T. J. Fiedler, N. H. Bings and K. Heinze, which appeared in the *European Journal of Inorganic Chemistry*, reported on the proton and electron transfer to a polymer-supported nitrido molybdenum(VI) complex (**P-2**) leading to a stable imido molybdenum(V) complex, an intermediate of the Schrock cycle. These results showed the potential of this immobilized complex towards NH$_3$ generation, which is investigated in this work. An alternative pathway to give a polymer-anchored triamidoamine ligand **P-1'** using an Ullmann-type coupling reaction is presented. Polymer **P-1'** features the same spectroscopic properties (IR, DR-UV/Vis) as the previously reported functionalized solid phase **P-1**, but shows a lower ligand loading. On the basis of this new starting material **P-1'** the polymer-supported nitrido molybdenum(VI) complex (**P-2'**) has been prepared from [Mo^{VI}Cl$_3$N(CH$_3$CN)]$_4$ as "MoN" source. The spectroscopic properties (IR, DR-UV/Vis) of **P-2'** are in accordance to the previously reported immobilized nitrido molybdenum(VI) complex **P-2**. The loading of **P-2'** is with 0.14 mmol molybdenum g^{-1} polymer lower than reported on **P-2** (0.32 mmol g^{-1}). For reasons of characterization, the immobilized copper(II) complexes **P-5a'** and **P-5b'** have been prepared as well by treating **P-1'** with Cu(ClO$_4$)$_2$·6H$_2$O and Cu(NO$_3$)$_2$·3H$_2$O, respectively. Both polymers **P-5a'** and **P-5b'** feature the same spectroscopic properties (IR, DR-UV/Vis, EPR) but also a lower loading compared to the previously reported immobilized copper(II) complexes **P-5a** and **P-5b** from **P-1**. Electron paramagnetic resonance (X-band EPR) spectra of the immobilized nitrato copper(II) complexes **P-5b** have been recorded at different temperatures in different solvents. With the help of this spectroscopic method the degree of swelling of the cross-linked solid phase and the mobility of the immobilized complexes has been assessed giving important clues about the spatial isolation, the reactivity and the accessibility of the immobilized reaction centers. These features are important aspects in view of the formation of ammonia from the immobilized nitrido molybdenum(VI) complexes **P-2** and **P-2'**. The swelling properties of the cross-linked polymer determine the reaction conditions concerning the choice of solvent. Additionally, the use of compatible acids/conjugate bases systems and appropriate electron donors reveal challenges for successful catalytic ammonia synthesis. Thus, polymers **P-2** and **P-2'** have been investigated with respect to ammonia synthesis in the presence of protons, [2,6-lutH][Al(OC{CF$_3$}$_3$)$_4$] (2,6-lutH = 2,6-lutidinium), and electrons, CoCp*$_2$ (Cp* = {η^5-C$_5$Me$_5$}). With the application of different reaction conditions the yield of generated ammonia has been optimized to a

maximum of one equivalent per "MoN" unit. Hence, no catalytic activity of the immobilized nitrido molybdenum(VI) complexes **P-2** and **P-2'** is observed. The lack of turnover is likely due to irreversible 2,6-lutidine coordination to the metal center.

1. INTRODUCTION

The invention of new catalysts, especially homogeneous catalysts, for ammonia synthesis from N_2 is of considerable interest as scientists try to find novel compounds performing the catalytical reduction of molecular dinitrogen under ambient conditions just as the natural enzyme nitrogenase. This stays in contrast to the industrial process invented by Haber and Bosch, which requires high temperatures and high pressures and thus represents a very energy consuming method.[1,2]

To date three model complexes exist achieving homogeneous catalytic ammonia formation at ambient temperature under dinitrogen atmosphere (Scheme 1). Two of these complexes are molybdenum based complexes, namely Mo^{III} complex **A** synthesized by Schrock et al.[3–6] using a triamidoamine ligand with sterically encumbered hexaisopropylterphenyl (= HIPT) substituents and Mo^0 complex **B** prepared by Nishibayashi et al.[7] using PNP-type pincer ligands. The third complex **C** reported by Peters et al.[8] is an Fe^I based compound with a tris(phosphano)borane ligand, and represents the first mononuclear iron complex showing catalytic activity towards N_2.
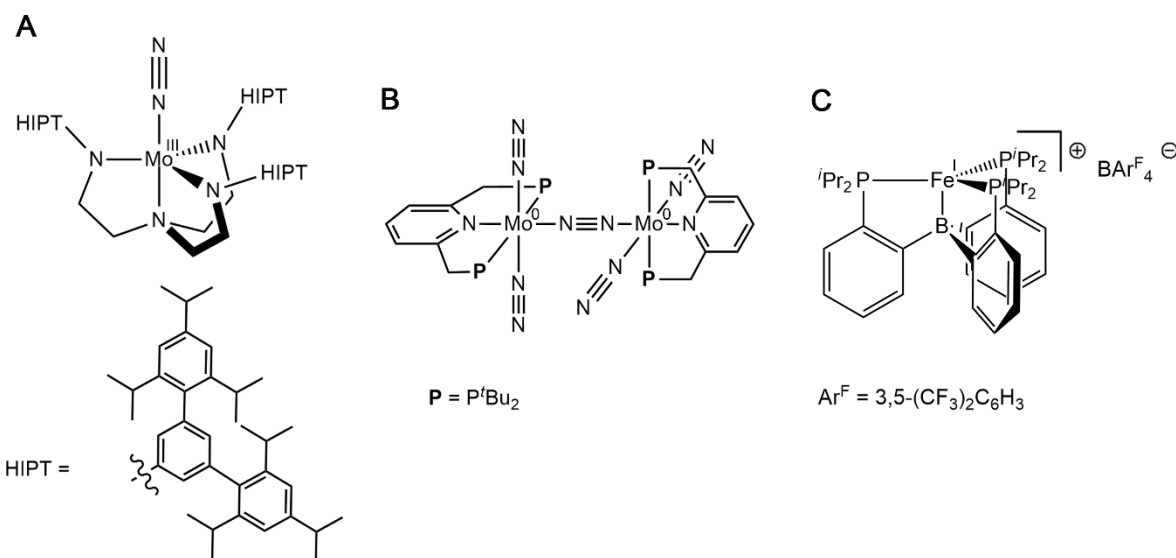
Scheme 1. Complexes achieving homogeneous catalytic ammonia synthesis.

In the Schrock system catalytic ammonia formation was only achieved by installing three sterically encumbered HIPT substituents on the chelate ligand which suppress bimolecular decay pathways. The Schrock−Yandulov catalytic cycle represents the most thoroughly studied system including the isolation

and characterization of at least eight relevant intermediates up to now. The catalytic reactivity was investigated starting from the dinitrogen molybdenum(III) complex [(^{HIPT}N$_3$N)Mo^{III}(N$_2$)] (**A**) or the nitrido molybdenum(VI) complex [(^{HIPT}N$_3$N)Mo^{VI}N] (**I**). Performing a typical catalytic reaction, heptane was added to one equivalent of the catalyst and 48 eq. of the proton source [2,6-lutH][B(3,5-{CF$_3$}$_2$C$_6$H$_3$)$_4$]. Then 36 eq. of the reducing agent decamethylchromocene CrCp*$_2$ dissolved in heptane were added dropwise to the mixture over a period of one hour. With this procedure the formation of H$_2$, depicted in Scheme 2, equation (1), is largely suppressed because the available amount of the proton source is small, due to its poor solubility in heptane.[3]

$$2,6\text{-LutH}^{\oplus} + CrCp*_2 \longrightarrow {}^1/_2 H_2 + 2,6\text{-Lut} + CrCp*_2^{\oplus} \qquad (1)$$
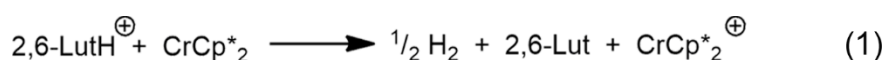
Scheme 2. Formation of H$_2$ by proton reduction with CrCp*$_2$.

The local concentration of the soluble molybdenum complex is always higher and therefore it is more likely that the protons and electrons react with the molybdenum complex. In the following Scheme 3 showing the equations (2)−(5) the proposed mechanism for the protonation and reduction of the nitrido molybdenum(VI) complex [(^{HIPT}N$_3$N)Mo^{VI}N] (**I**) leading to the final release of ammonia is described in more detail. Especially complexes (**II**) and (**III**) representing proposed intermediates of this reaction could not be isolated by the group of Schrock so far. After three protonation and reduction steps the ammine molybdenum(III) complex [(^{HIPT}N$_3$N)Mo^{III}(NH$_3$)] (**IV**) is formed. As depicted in Scheme 3, equation (5), this complex undergoes a reversible ligand exchange reaction with N$_2$ leading to the dinitrogen molybdenum(III) complex [(^{HIPT}N$_3$N)Mo^{III}(N$_2$)] (**A**) and liberating ammonia.[6,9,10]

$$[(^{HIPT}N_3N)Mo^{VI}N] + H^{\oplus} + e^{\ominus} \longrightarrow [(^{HIPT}N_3N)Mo^{V}(NH)] \qquad (2)$$
$$\textbf{I} \qquad\qquad\qquad\qquad\qquad\qquad \textbf{II}$$

$$[(^{HIPT}N_3N)Mo^{V}(NH)] + H^{\oplus} + e^{\ominus} \longrightarrow [(^{HIPT}N_3N)Mo^{IV}(NH_2)] \qquad (3)$$
$$\textbf{II} \qquad\qquad\qquad\qquad\qquad\qquad \textbf{III}$$

$$[(^{HIPT}N_3N)Mo^{IV}(NH_2)] + H^{\oplus} + e^{\ominus} \longrightarrow [(^{HIPT}N_3N)Mo^{III}(NH_3)] \qquad (4)$$
$$\textbf{III} \qquad\qquad\qquad\qquad\qquad\qquad \textbf{IV}$$

$$[(^{HIPT}N_3N)Mo^{III}(NH_3)] + N_2 \rightleftharpoons [(^{HIPT}N_3N)Mo^{III}(N_2)] + NH_3 \qquad (5)$$
$$\textbf{IV} \qquad\qquad\qquad\qquad\qquad\qquad \textbf{A}$$

$$[(^{HIPT}N_3N)Mo^{III}(N_2)] + H^{\oplus} + e^{\ominus} \longrightarrow [(^{HIPT}N_3N)Mo^{IV}(NNH)] \qquad (6)$$
$$\textbf{A} \qquad\qquad\qquad\qquad\qquad\qquad \textbf{V}$$

$$[(^{HIPT}N_3N)Mo^{IV}(NNH)] + H^{\oplus} + e^{\ominus} \longrightarrow [(^{HIPT}N_3N)Mo^{V}(NNH_2)] \qquad (7)$$
$$\textbf{V} \qquad\qquad\qquad\qquad\qquad\qquad \textbf{VI}$$
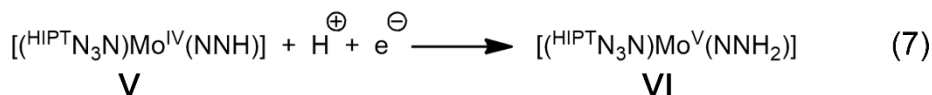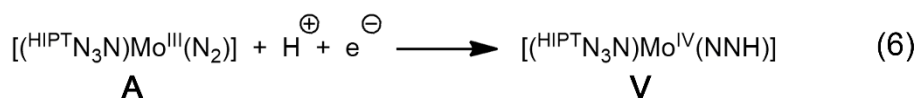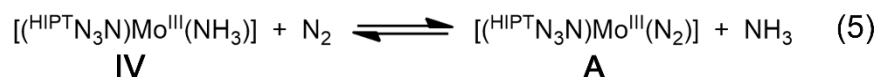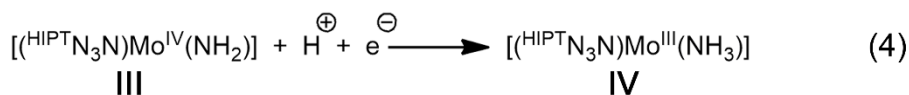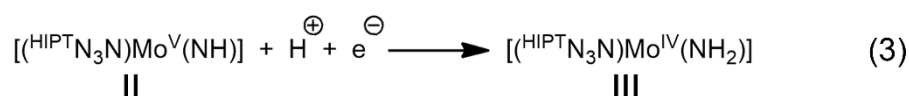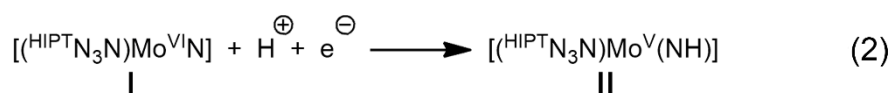
Scheme 3. Reaction equations describing the stepwise protonation and reduction of [(^{HIPT}N$_3$N)Mo^{VI}N] (**I**).

According to the stepwise reactions depicted in Scheme 3 the release of ammonia, starting from the nitrido molybdenum(VI) complex [LMoN] (**I**) with L = (^{HIPT}N$_3$N), is expected to proceed as shown in Figure 1, when idealized quantitative reactions and the absence of proton and electron exchange between the molybdenum complexes are assumed. This assumption cannot be made for homogeneous systems in solution, but may be valid for polymer-supported complexes due to the site isolation effect. After the first step, the addition of one equivalent of the proton source and the reducing agent, the imido molybdenum(V) complex [LMo(NH)] (**II**) is generated and no ammonia is released. The second H$^+$/e$^-$ step yields the amido molybdenum(IV) complex [LMo(NH$_2$)] (**III**) and still no ammonia release should be observed. After addition of the third equivalent H$^+$/e$^-$ the ammine molybdenum(III) complex [LMo(NH$_3$)] (**IV**) is formed. At this stage it is expected that ammonia is liberated enabling its detection. The dinitrogen molybdenum(III) complex [LMo(N$_2$)] (**A**) is formed as a result of ligand exchange starting a reaction cycle from **A**. The following H$^+$/e$^-$ steps proceed via the diazenido molybdenum(IV) complex [LMo(NNH)] (**V**) and the hydrazido molybdenum(V) complex [LMo(NNH$_2$)] (**VI**) resulting again in the release of ammonia after three steps yielding complex **I**.[6]
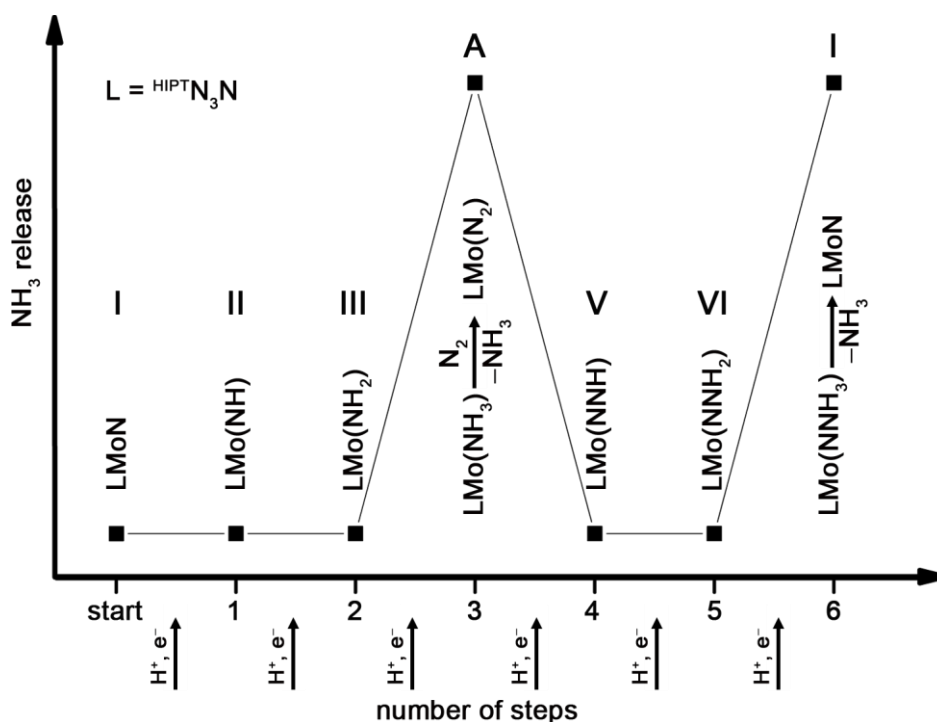
Figure 1. Cycle of alternating addition of protons and electrons to **I** resulting in NH$_3$ release at every third step.

With the application of the reported optimized reaction conditions, the Schrock group was able to obtain 7−8 eq. NH$_3$ starting from one equivalent [(^{HIPT}N$_3$N)Mo^{III}(N$_2$)] (**A**). Starting from one equivalent [(^{HIPT}N$_3$N)Mo^{VI}N] (**I**) they were able to generate 6−7 eq. NH$_3$, i. e. one equivalent less in comparison to

the previous experiment. Hence, the catalysis is limited to a maximum of four turn overs (TON = 4). Thus other side reactions are present leading to an inactivation of the catalyst and low catalytic efficiency. Bimolecular reactions such as disproportionation initialized by proton transfer are the main side reactions observed for this system. As an example the proton-assisted disproportionation of intermediate **II**, [($^{HIPT}N_3N$)Mo^V(NH)], into [($^{HIPT}N_3N$)Mo^{VI}N] (**I**) and [($^{HIPT}N_3N$)Mo^{IV}(NH$_2$)] (**III**) is shown in Scheme 4.[6] These reactions do not represent side reactions leading to an inactivation of the catalyst, as all products are part of the catalytic cycle, but show a reason for a lowering of catalytic efficiency. Additionally, these bimolecular reactions prevent the successful isolation of reaction intermediates.

$$[(^{HIPT}N_3N)Mo^{VI}N] + H^{\oplus} \longrightarrow [(^{HIPT}N_3N)Mo^{VI}(NH)]^{\oplus}$$
$$\mathbf{I}$$

$$[(^{HIPT}N_3N)Mo^{VI}(NH)]^{\oplus} + [(^{HIPT}N_3N)Mo^{V}(NH)] \longrightarrow [(^{HIPT}N_3N)Mo^{VI}N] + [(^{HIPT}N_3N)Mo^{V}(NH_2)]^{\oplus}$$
$$\mathbf{II} \qquad\qquad\qquad\qquad\qquad\qquad \mathbf{I}$$

$$[(^{HIPT}N_3N)Mo^{V}(NH_2)]^{\oplus} + [(^{HIPT}N_3N)Mo^{V}(NH)] \longrightarrow [(^{HIPT}N_3N)Mo^{VI}(NH)]^{\oplus} + [(^{HIPT}N_3N)Mo^{IV}(NH_2)]$$
$$\mathbf{II} \qquad\qquad\qquad\qquad\qquad\qquad\qquad\qquad \mathbf{III}$$
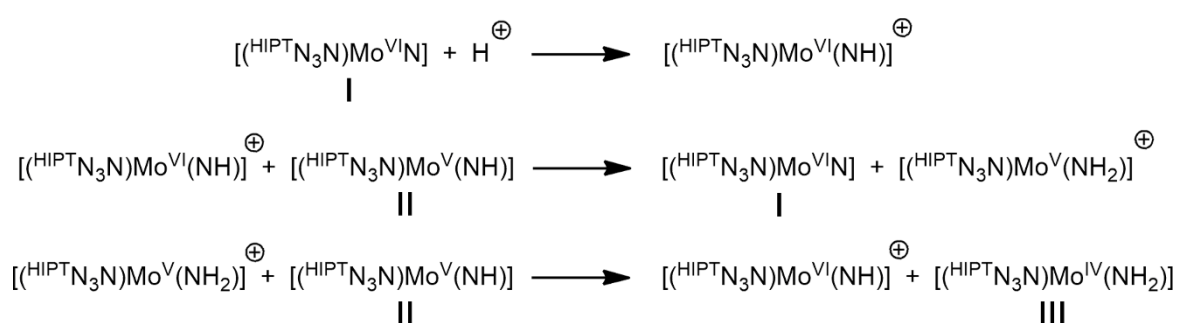
Scheme 4. Proton-assisted disproportionation of [($^{HIPT}N_3N$)Mo^V(NH)] (**II**) as an example for bimolecular side reactions.

Furthermore, protonation of the triamidoamine ligand backbone at the amido group facilitates chelate ligand dissociation from the metal and finally leads to decomposition of the catalyst, especially at high 2,6-lutidinium concentrations. Coordination of the corresponding base 2,6-lutidine at the axial position of the molybdenum(III) complex leading to formation of catalytically unreactive [($^{HIPT}N_3N$)Mo^{III}(2,6-lut)] complex (**VII**) represents an additional relevant pathway to the loss of catalytic activity, as 2,6-lutidine cannot be substituted by N$_2$ (Scheme 5).[6]

$$[(^{HIPT}N_3N)Mo^{III}(NH_3)] + 2,6\text{-Lut} \rightleftharpoons [(^{HIPT}N_3N)Mo^{III}(2,6\text{-lut})] + NH_3 \qquad (8)$$
$$\mathbf{IV} \qquad\qquad\qquad\qquad\qquad\qquad \mathbf{VII}$$

$$[(^{HIPT}N_3N)Mo^{III}(N_2)] + 2,6\text{-Lut} \rightleftharpoons [(^{HIPT}N_3N)Mo^{III}(2,6\text{-lut})] + N_2 \qquad (9)$$
$$\mathbf{A} \qquad\qquad\qquad\qquad\qquad\qquad \mathbf{VII}$$
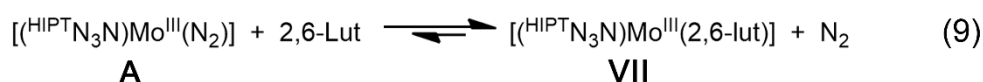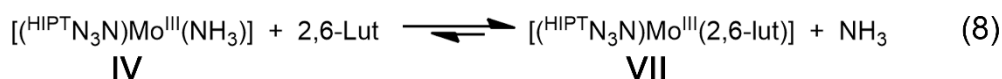
Scheme 5. Formation of [($^{HIPT}N_3N$)Mo^{III}(2,6-lut)] (**VII**) from **IV** or **A**.

In the Schrock system 2,6-lutidine can coordinate to molybdenum(IV) leading to a paramagnetic (d^2), cationic [(^{HIPT}N$_3$N)Mo^{IV}(2,6-lut)]$^+$ complex (**VIII**).[6] Subsequent reduction of **VIII** with CrCp*$_2$ under dinitrogen atmosphere yields the dinitrogen molybdenum(III) complex **A** and free 2,6-lutidine as shown in Scheme 6, equation (10). In the sterically demanding Schrock system N$_2$ is competitive for binding to molybdenum(III). The initially formed neutral d^3 lowspin [(^{HIPT}N$_3$N)Mo^{III}(2,6-lut)] complex (**VII**) readily loses 2,6-lutidine due to steric aspects and coordinates the significantly smaller N$_2$ ligand. In consequence, 2,6-lutidine is unlikely to bind strongly to molybdenum(III) in the Schrock system, and thus dinitrogen coordination to molybdenum(III) is sterically favored during a catalytic reaction.[6,11]

$$[(^{HIPT}N_3N)Mo^{IV}(2\text{,}6\text{-lut})]^{\oplus} + N_2 \xrightarrow[-\ CrCp^*_2{}^{\oplus}]{CrCp^*_2} [(^{HIPT}N_3N)Mo^{III}(N_2)] + 2\text{,}6\text{-Lut} \qquad (10)$$

$$\textbf{VIII} \hspace{10cm} \textbf{A}$$
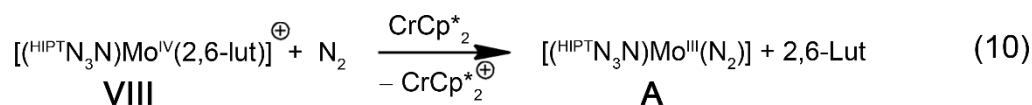
Scheme 6. Formation of **A** from [(^{HIPT}N$_3$N)Mo^{IV}(2,6-lut)]$^+$ (**VIII**).

Especially, complex deactivation of the [(^{HIPT}N$_3$N)Mo^V(NH)] intermediate (**II**) via bimolecular pathways (Scheme 4) could be essentially avoided by immobilization of the Schrock−Yandulov-type nitrido molybdenum(VI) complex (**P-2**) using a polymer-anchored triamidoamine ligand (**P-1**). Protonation at the nitrido **P-2** ligand yielded the corresponding imido molybdenum(VI) complex (**P-3**) which could be reduced to its imido molybdenum(V) congener (**P-4**). These reactions are compiled in Scheme 7.[12]

P-1

P-2

P-3

P-4
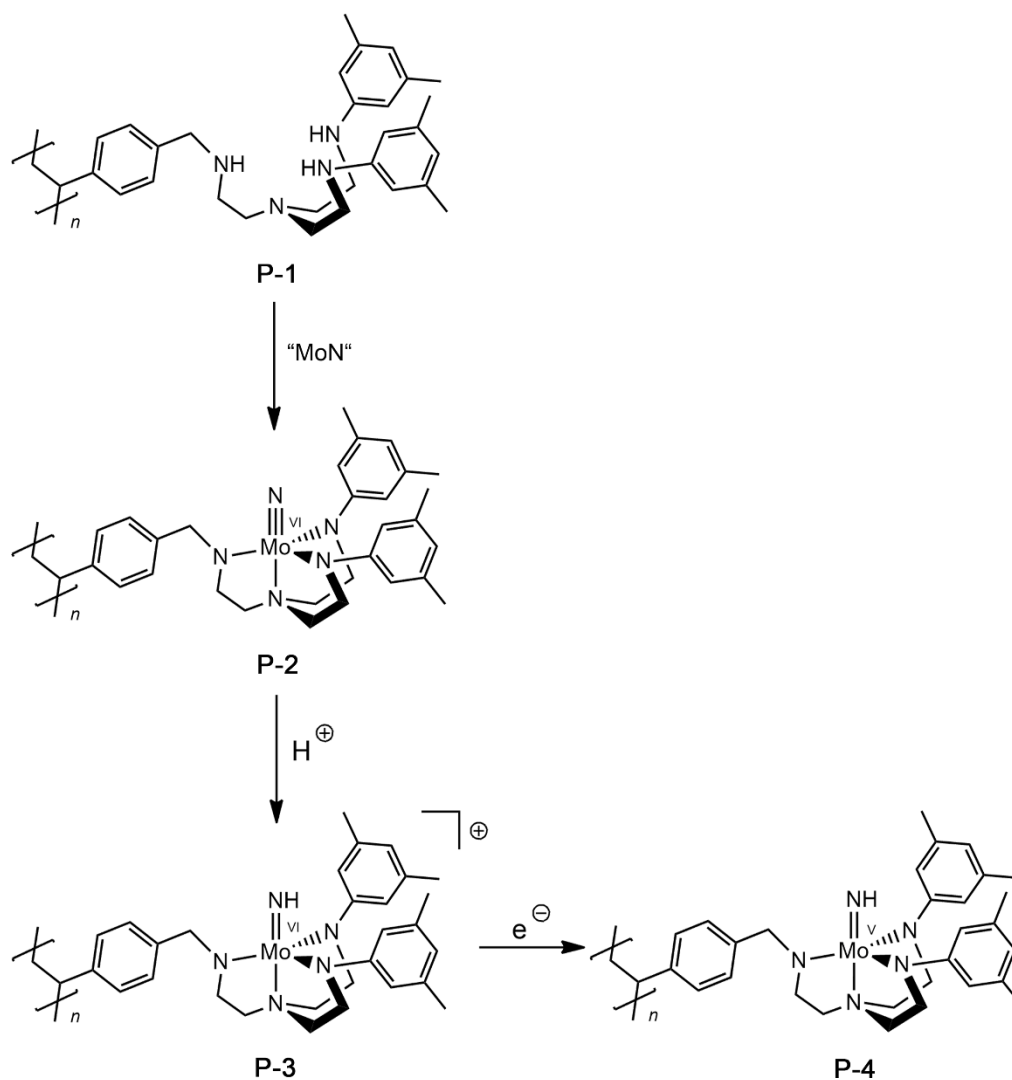
Scheme 7. Reaction pathway for the synthesis of **P-2**, **P-3** and **P-4**.[12]

On the basis of our previous successful synthesis and characterization of the immobilized imido molybdenum(V) complex **P-4**, we report here our attempts to investigate the potential activity of immobilized nitrido molybdenum(VI) complexes **P-2** with respect to ammonia formation via consecutive protonation and reduction steps according to Figure 1. Therefore the reactivity of the polymer-supported complexes is studied under various reaction conditions. In addition, the swelling properties of the solid phase, playing a decisive role in the accessibility of immobilized complexes, are investigated by EPR spectroscopy of polymer-supported copper(II) complexes in different solvents. In this work, an alternative synthesis of the immobilized triamidoamine ligand **P-1** is described as well.

2. RESULTS AND DISCUSSION

Synthesis and Characterization of Polymer-Supported Ligands and Complexes P-1', P-2', P-5a' and P-5b'

In addition to the previously reported palladium-catalyzed Buchwald-Hartwig amination of the tripodal ligand P-tren, immobilized onto a polystyrene/1% divinylbenzene copolymer, yielding the polymer-supported 2,2′-bis(3,5-dimethylphenylamino)-2″-benzylamino)triethylamine ligand **P-1**, we describe an alternative route to give polymeric support **P-1'**, which is structurally identical to **P-1**.[12] The immobilized ligand **P-1'** was prepared from commercially available immobilized P-tren (Iris Biotech GmbH) by using 5-bromo-*m*-xylene in a copper-catalyzed Ullmann-type coupling reaction according to the method published by Buchwald (Scheme 8).[12] We modified the reaction conditions for the solid phase synthesis using toluene as solvent instead of DMF. For comparison and proof, we successfully synthesized the soluble symmetric ligand 2,2′,2″-tris(3,5-dimethylphenylamino)triethylamine (**1'**) using this copper-catalyzed coupling in DMF. The spectroscopic data of the product fully conform to the previously reported data.[12]
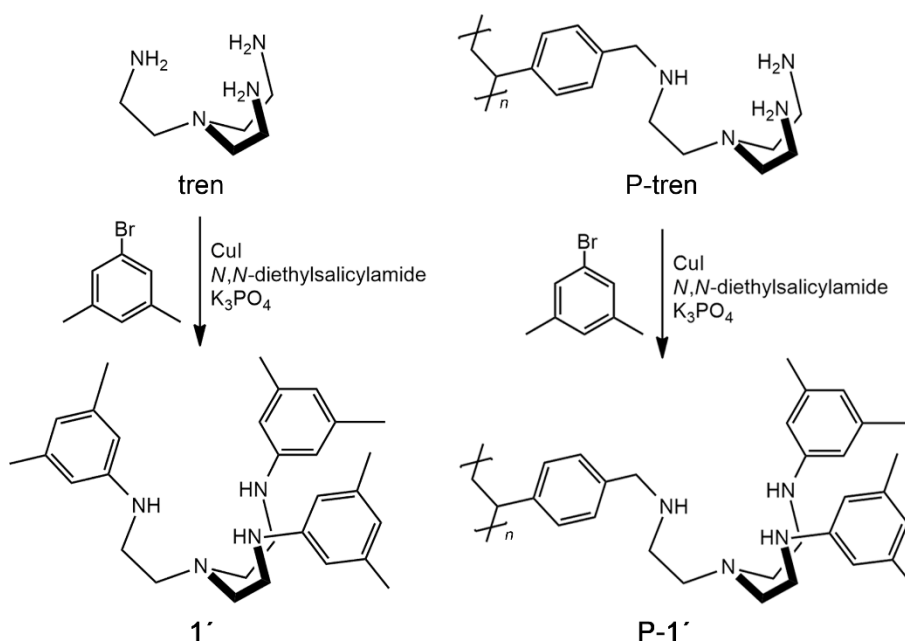
Scheme 8. Synthesis of ligand **1'** and polymer-supported ligand **P-1'** via copper-catalyzed Ullmann-type coupling.

The functionalized yellow polymer **P-1'** is characterized by a (negative) Kaiser test, a ninhydrin-based test for primary amines,[14,15] proving the arylation of all primary amines of P-tren (Figure 2).

P-1´

Figure 2. Photographs of the yellow polymer **P-1'** (left) and negative Kaiser test of **P-1'** (right).

With an NH vibration band at about 3350 cm^{-1} in the IR spectrum and with a bathochromic shift of the absorption band in the diffuse reflectance UV/Vis (DR-UV/Vis) spectrum (Figure 5, bottom) the spectroscopic properties of **P-1'** conform to the previously reported immobilized ligand **P-1** which was prepared by Buchwald-Hartwig amination. The loading of the solid support measured by elemental analysis amounts 2.06% N. That value corresponds to 0.37 mmol ligand g^{-1}, based on the assumption of only monoarylated amines, revealing a lower degree of loading compared to **P-1** (0.52 mmol ligand g^{-1})[12].

As further proof of the correct ligand formation on the solid phase, Cu^{II} was introduced as an optical probe and EPR label[16,17,18] by treating **P-1'** with Cu(ClO$_4$)$_2$·6H$_2$O or Cu(NO$_3$)$_2$·3H$_2$O, respectively, according to Scheme 9.

solv = solvent (CH$_3$CN, THF, CH$_2$Cl$_2$)
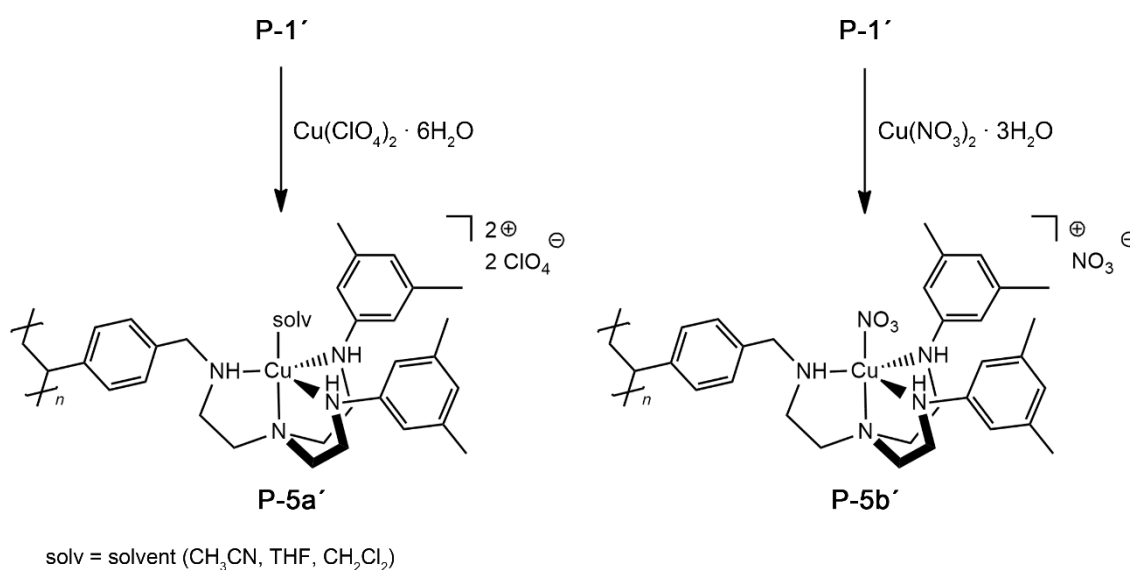
Scheme 9. Synthesis of immobilized copper(II) complexes **P-5a'** and **P-5b'**.

Both resins [Cu(tren)(solvent)](ClO$_4$)$_2$ **P-5a'** and [Cu(tren)(NO$_3$)](NO$_3$) **P-5b'** feature the characteristic green color of Cu^{II} tren complexes and show a broad absorption around 700 nm in the normalized DR-UV/Vis spectra similar to the previously reported copper(II) complexes **P-5a** and **P-5b** (Figure 3).[12]
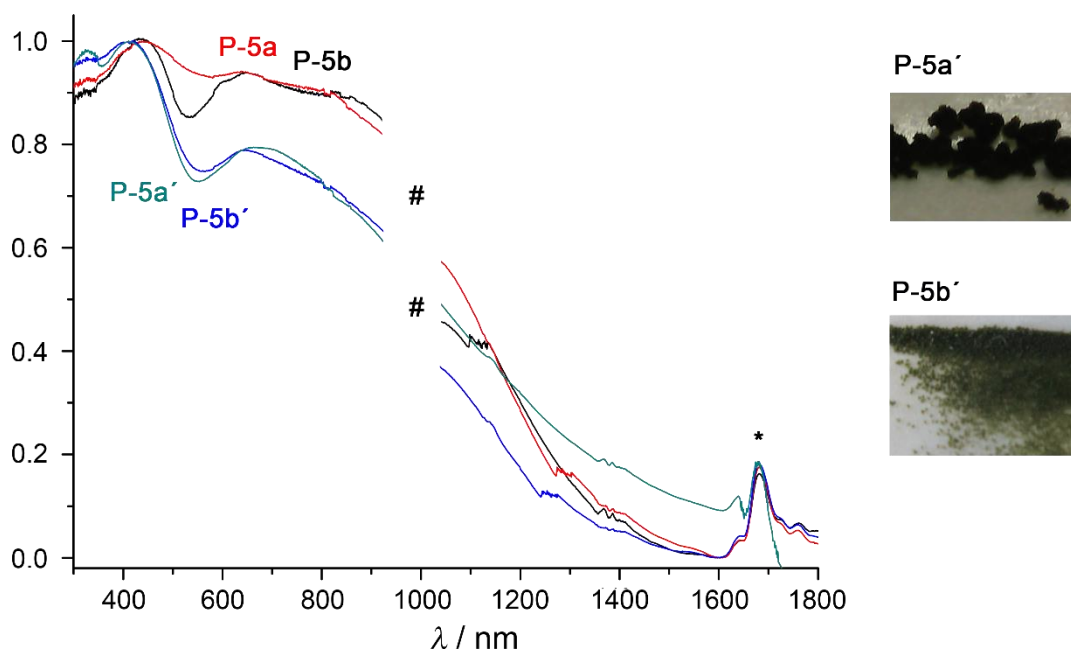
Figure 3. Comparison of DR-UV/Vis measurements (left) of **P-5a**, **P-5b**, **P-5a'**, **P-5b'** (* denotes overtones of CH and NH stretching vibrations of the polymer backbone; # denotes spikes and noise cause by the switch of detector of the spectrometer), photographs of **P-5a'** and **P-5b'** (right).

The spectra in Figure 3 show lower intensities of the copper-based absorption (700 nm) of **P-5a'** and **P-5b'** in comparison the respective absorption of **P-5a** and **P-5b**. This result is in accordance to a smaller amount of copper immobilized onto the here reported polymeric support, as expected due to the lower ligand loading of **P-1'**. The elemental analysis of **P-5a'** (N 2.22 = 0.31 mmol g^{-1}) matches approximately the expected theoretical value (N 2.31 = 0.33 mmol g^{-1}) as well as the amount of immobilized copper measured by inductively coupled plasma MS[19,20] (ICP-MS; 0.30 mmol g^{-1}) corroborating the lower loading of the solid phase compared to the corresponding **P-5a** (N 2.97 = 0.43 mmol g^{-1})[12]. In the IR spectra of **P-5a'** and **P-5b'** the characteristic stretching vibrations of the perchlorate and nitrate counterions are detected at 1102 and 1360 cm^{-1}, respectively.

The EPR spectrum of solid **P-5a'** recorded at 295 K shows resonances at $g_{1,2,3}$ = 2.025, 2.125, 2.228 with characteristic hyperfine coupling to $^{63/65}$Cu nuclei of $A_{1,2,3}$ = 12, 28, 158 G (Figure 4, left). In the less well resolved EPR spectrum of solid **P-5b'** measured at 77 K g-values of $g_{1,2,3}$ = 2.045, 2.133, 2.240 are observed with hyperfine coupling $A_{1,2,3}$($^{63/65}$Cu) = 33, 15, 170 G (Figure 4, right). As expected the EPR measurements fully agree with the data reported for **P-5a** and **P-5b**, as well as with other copper(II) complexes with tripodal N-ligands, corroborating the formation of trigonal bipyramidal metal complexes.[12,21,22]
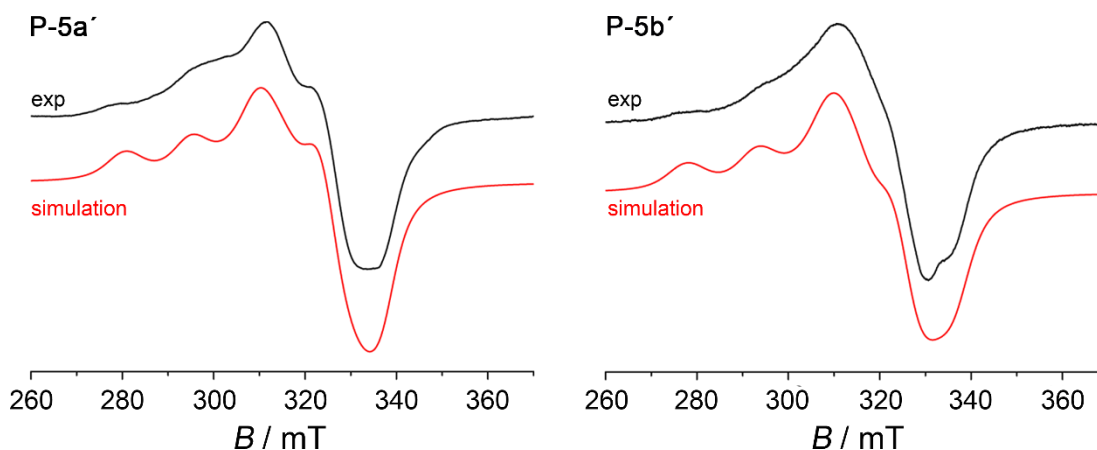
Figure 4. Experimental and simulated X-band EPR spectra of **P-5a'** (left; solid, 295 K, 9.4 GHz) and **P-5b'** (right; solid, 77 K, 9.4 GHz).

The immobilized nitrido molybdenum(VI) complex (**P-2'**) is obtained by treating the supported ligand **P-1'** with [Mo^{VI}Cl$_3$N(CH$_3$CN)]$_4$[23] as "MoN" source under basic conditions (LiNMe$_2$) as depicted in Scheme 10 analogously to the published method.[12]
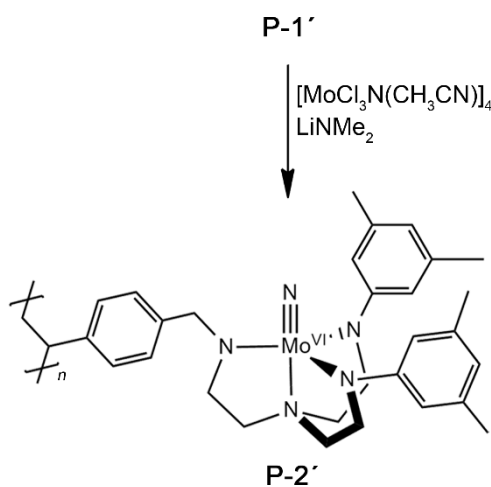
Scheme 10. Synthesis of immobilized nitrido molybdenum(VI) complex **P-2'**.

The resulting red polymer **P-2'** (Figure 5, top right) was characterized by IR spectroscopy (Figure 5, top left, difference spectrum " **P-2'** − **P-1'** ") showing vibrations at 1070 and 1029 cm^{-1} characteristic for the Mo≡N stretching vibration coupled to ligand backbone vibrations in trisamidoamine complexes, and by DR-UV/Vis spectroscopy (Figure 5, bottom) matching to the spectroscopic data reported for the immobilized complex **P-2**.[12]
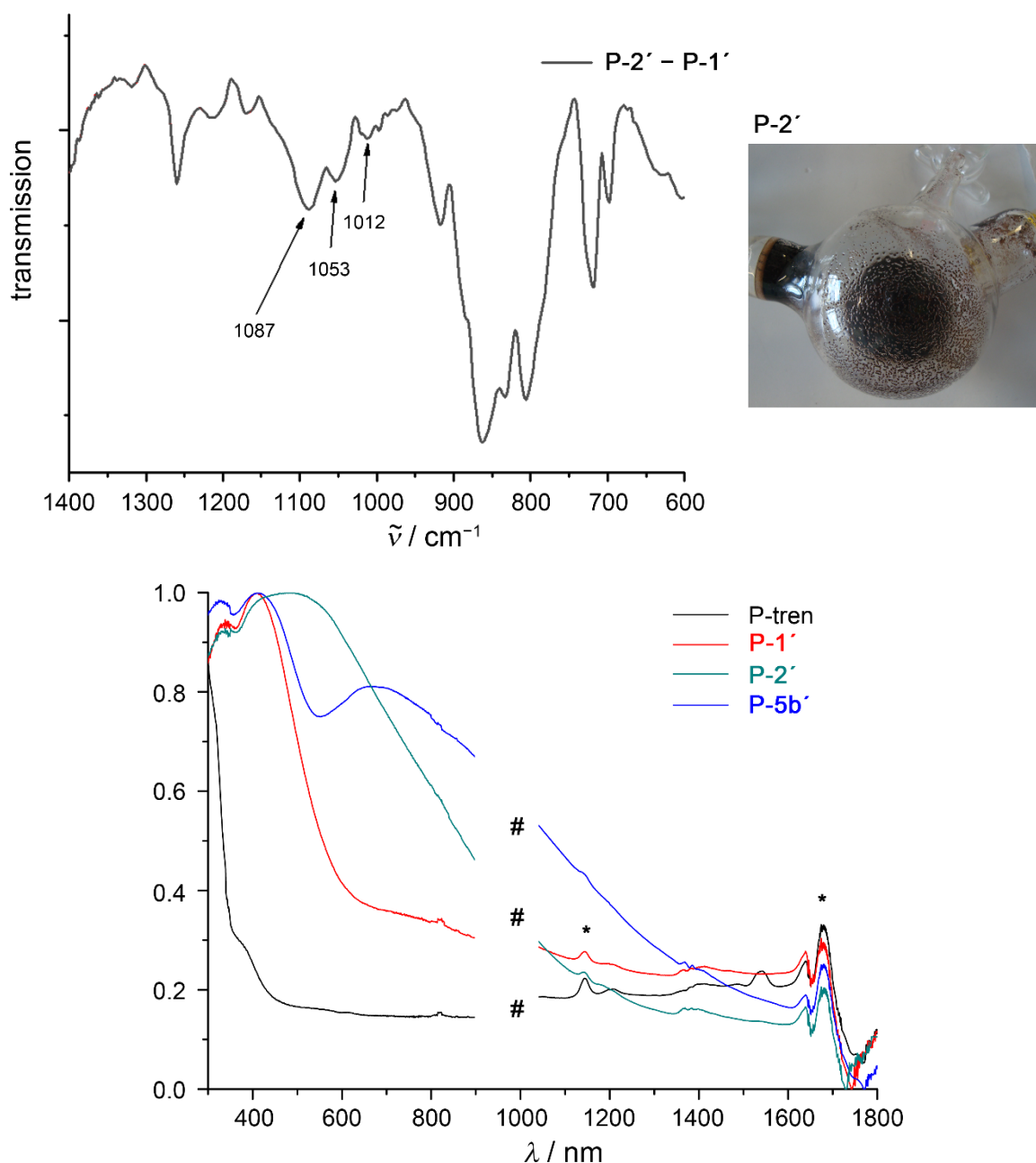
Figure 5. Difference IR spectrum of " **P-2' − P-1'** " (top left), DR-UV/Vis spectra (bottom) of P-tren, **P-1'**, **P-2'**, **P-5b'** (* denotes overtones of CH and NH stretching vibrations of the polymer backbone; # denotes spikes and noise cause by the switch of detector of the spectrometer) and photograph (top right) of **P-2'**.

The amount of immobilized molybdenum and the corresponding amount of ammonia released from the nitrido molybdenum(VI) complex was estimated after acidic hydrolysis (HCl, dioxane, H_2O) of **P-2'** and subsequent removal of the solvents from the acidic washing solution. The residue was investigated by ICP-MS quantification (in HNO_3) revealing the amount of molybdenum (0.140 ± 0.01 mmol g^{-1} polymer), and by ^1H NMR spectroscopy (in [D_6]DMSO) revealing the amount of ammonia (0.135 ± 0.01 mmol g^{-1} polymer) measured as NH_4^+ ions (1:1:1 triplet at $\delta = 7.46$ ppm with $^1J_{14N,H} = 50Hz^{[24]}$) relative to toluene as internal standard. This result corroborates the 1:1

molybdenum:nitrido stoichiometry. As expected, the loading of the solid support (0.14 mmol g^{-1} polymer) is lower compared to **P-2** (0.32 mmol g^{-1} polymer).[12] The amount of immobilized molybdenum in **P-2'** is also lower compared to the amount of immobilized copper in **P-5a'** (0.30 mmol g^{-1} polymer). Due to a partly overarylation of the immobilized amine ligands to give tertiary amines, molybdenum coordination to the immobilized chelate ligand is partly prevented explaining the lower loading.

Investigation of Polymer-Supported Copper(II) Complexes P-5a and P-5b by EPR spectroscopy

Previous studies on immobilized paramagnetic compounds have shown the great potential of EPR spectroscopy to investigate the mobility of immobilized complexes and the swelling properties of polymeric supports in different solvents and under different conditions.[16,25] For example, polymer-supported copper (II) complexes were investigated in our group with respect to the coordination geometry, mobility and reactivity in the dry and solvent-swollen state using EPR spectroscopy.[16] The swelling properties of solid phases are of considerable interest as it influences the accessibility of the immobilized reaction centers and in consequence the required reaction time, as observed for nitroxide radicals immobilized on brush polymers.[26] This information is relevant to the investigation of the reactivity or the potential catalytic activity of the immobilized nitrido molybdenum(VI) complexes **P-2** and **P-2'**, which will be discussed in the next section.

Thus we recorded EPR spectra of immobilized copper(II) complexes **P-5a** and **P-5b** at different temperatures (room temperature and 77 K) and different states (solid/collapsed and solvent-swollen polymer). The spectra reveal information concerning the rigidity of the immobilized complexes and the swelling of the solid support. In all cases the EPR spectra show anisotropic signal patterns leading to the conclusion that the copper(II) complexes are rigidly coupled to the solid support. Even the EPR spectra of solvent-swollen polymer samples, for example **P-5a** in CH$_2$Cl$_2$, measured at 295 K are anisotropic albeit with a smaller g-anisotropy (g-anisotropy = $g_3 - g_{iso}$ = 0.0957) and a smaller copper hyperfine coupling constant (A_3($^{63/65}$Cu) = 150 G) as well as a smaller peak-to-peak distance (55.8 mT) than the other spectra. Hence the degree of swelling of the polymer support affects the translational and rotational freedom of the immobilized complexes.[27] Despite the swelling of the solid phase, these measurements show that the rotation of the complexes is restricted and the tumbling rate is small due to the short bridge between the ligand and the polymer explaining the anisotropy of the spectra (Figure 6).
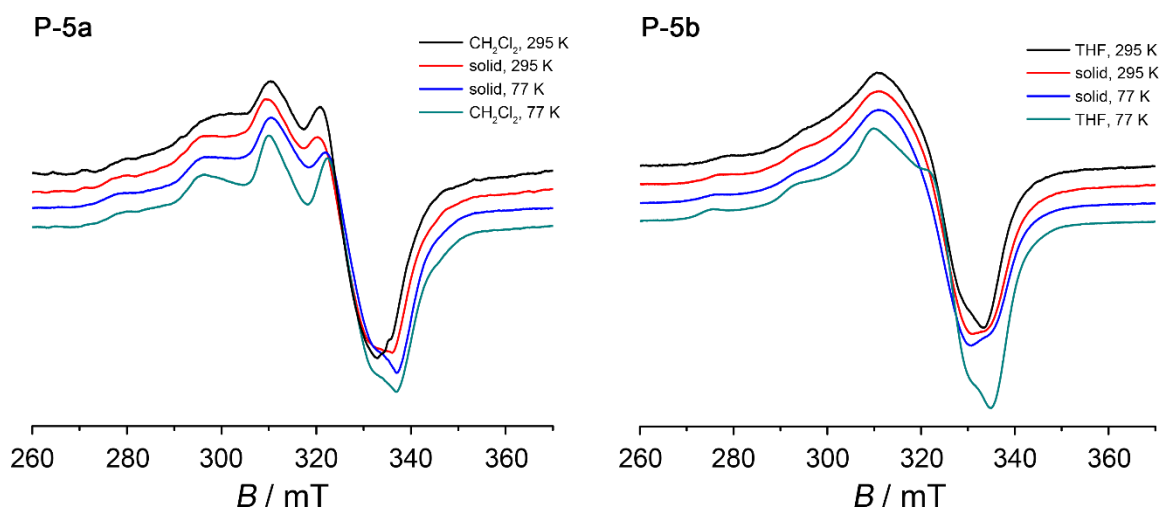
Figure 6. Experimental X-band EPR spectra of **P-5a** (left) and **P-5b** (right) at 295 K and at 77 K as solid and solvent-swollen samples revealing the rigidity of immobilized copper(II) complexes.

In contrast, immobilized copper(II) complexes prepared from Anja Reinhart in our group, with one acetylacetonato ligand and connected by a dipyrromethene ligand to an insoluble Wang resin (polystyrene-bound-4-benzyloxybenzyl alcohol; 0.6−1.0 mmol g^{-1}; 1% divinyl benzene), showed almost isotropic EPR spectra at 295 K in the THF-swollen state.[16] This result can be ascribed to a better mobility of the complexes due to a longer distance between the chelate ligand and the polymer backbone, 18 bonds compared to 6 bonds in **P-5a**, and more flexible σ-bonds in between.

In comparison to the swollen samples measured in frozen solution, the EPR spectra of collapsed polymer samples (solid) measured at 295 K and at 77 K show different *g*-values as well as broadening of the hyperfine coupling lines especially in the g_3 component (Figure 6, red and blue lines). In contrast, EPR spectra of molecular nitrato copper(II) complexes with bulky *para*-nitrobenzylphenyl substituted (*p*-NO$_2$BP) triamidoamine ligand [Cu(*p*-NO$_2$BP)$_3$trenNO$_3$](NO$_3$)[21] measured as a powder, show nearly isotropic spectra (*g*-anisotropy ≈ 0) without observable hyperfine coupling due to strong *intermolecular* spin-spin interactions. This reveals that the copper(II) complexes are not magnetically isolated in the solid state at all. The EPR spectra recorded for **P-5a** and **P-5b** reveal that the immobilized copper(II) complexes are sufficiently separated from each other to show hyperfine coupling to $^{63/65}$Cu, as this has also been observed by Hübner, Burzlaff *et al*. for immobilized copper(II) complexes connected by an *N,N,O* scorpionato linker to the solid support.[17] The observed hyperfine coupling is in accordance with magnetically isolated copper(II) centers on the solid phase without the possibility of spin-spin interactions.[17] However, the copper(II) complexes are not perfectly separated or magnetically diluted so that dipole-dipole interactions are still present resulting in line broadening of the spectra. As these interactions are distance-dependent the effect of line broadening can be used to determine the distance

between spin labels.[28,29] Thus spin labels like nitroxides are often introduced into biological systems, for example into proteins, to receive information about the geometric structure of this system.[30]

In the low temperature spectrum of collapsed **P-5b** (Figure 6, right) a slightly better resolution is achieved as well as an increased peak-to-peak distance (59.4 mT) compared to the 295 K spectrum (57.2 mT). This can be ascribed to the reduction of the dipole-dipole interactions and the freezing-in of the rotation or vibration of the immobilized complexes at lower temperatures, as the latter contributes to line broadening and decrease of the peak-to-peak distance.[29]

EPR spectra of **P-5b** were recorded in different solvents and solvent mixtures, namely THF, CH_2Cl_2/THF, CH_2Cl_2/THF/toluene and CH_2Cl_2/toluene, at 77 K. The spectra, depicted in Figure 7, visualize the effect of site isolation according to the respective swelling properties in the solvents and the capability for solvent uptake of the polymer.[31,32] The solid phase shows reasonable swelling in solvents like tetrahydrofuran and dichloromethane.[33] Thus the EPR spectra recorded in those solutions show a relatively small linewidth, which is typical for isolated copper(II) complexes in frozen solution (Figure 7, black and red line).
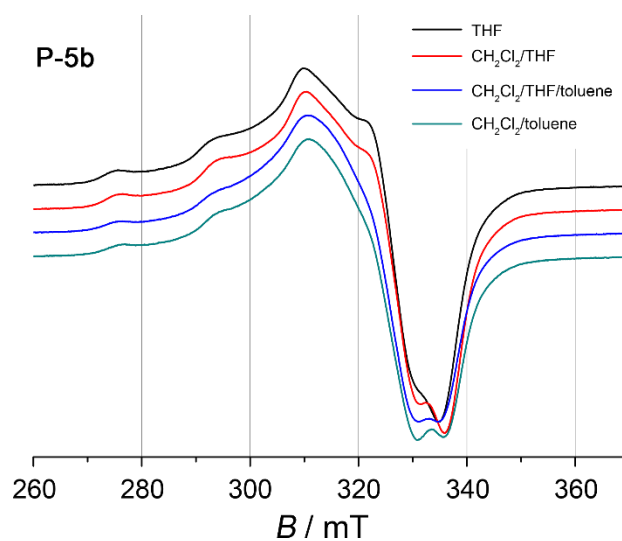
Figure 7. Experimental X-band EPR spectra of **P-5b** at 77 K swollen in different solvent mixtures.

Under these conditions the copper(II) centers are spatially separated from each other and shielded by solvent molecules as illustrated in Figure 8. In consequence of this magnetic dilution the average distance between the spin centers is increased leading to the suppression of intermolecular dipole-dipole interactions, as reported on other immobilized copper(II) complexes and polymer embedded radical-metal systems.[17,34]
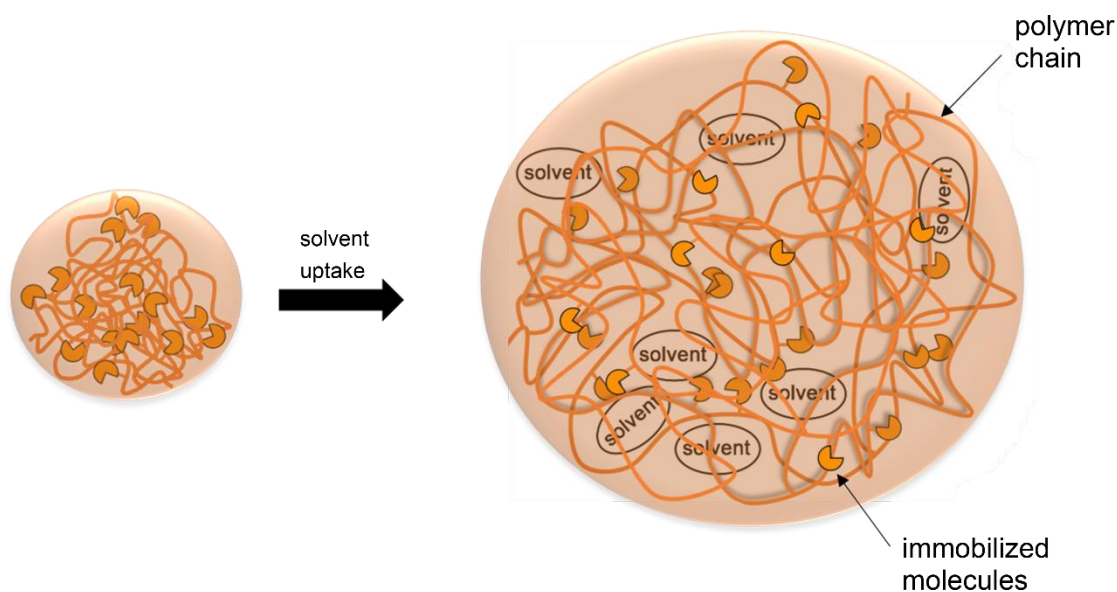
Figure 8. Model of the polymer swelling due to solvent uptake resulting in increased separation of active sites (site isolation effect).

Swelling the Cu^{II} polymer samples in toluene/solvent mixtures results again in a broadening of the EPR resonances as the polymer swells less in toluene than in THF (Figure 7, blue and green line).[33] This effect of line broadening is therefore attributed to marginally increased dipole-dipole interactions between the copper(II) centers in toluene. Additional spin-spin interactions between the copper(II) centers and the toluene molecules can also contribute to line broadening due to unresolved proton coupling. In contrast to the EPR measurements of the collapsed polymers at 77 K (see Figure 9) only a broadening of the spectra is observed but no change in the g-values or in the peak-to-peak distance (60.3 mT) corroborating that the copper(II) complexes are still well separated on the polymer support (Figure 7).

In contrast, recording EPR spectra of **P-5b** in petroleum ether at 77 K spectra matching that of the dry, unswollen solid phase are obtained (Figure 9, blue and green line). This effect is ascribed to the very poor swelling of the solid phase in this solvent.[33] Therefore it behaves like a dry polymer featuring a lower peak-to-peak distance (59.4 mT) due to dipole-dipole interactions of the immobilized copper(II) complexes.

P-5b
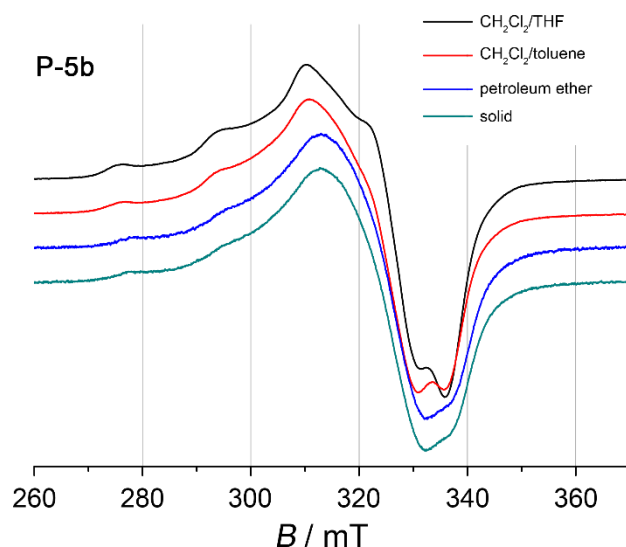
Figure 9. Experimental X-band EPR spectra of **P-5b** at 77 K swollen in different solvent mixtures and in the dried state.

To corroborate this hypothesis the room temperature EPR spectra of **P-5b** in THF and petroleum ether were compared. The resulting spectrum of the THF sample (Figure 10, red line) shows with 54.3 mT a smaller peak-to-peak distance compared to 56.9 mT for the petroleum ether sample (Figure 10, black line). As expected, the immobilized copper(II) complexes are more flexible in THF due to an improved swelling and the related increase of the volume of the polymer (see Figure 8).[31] In accordance to the low temperature EPR experiment (Figure 9), the spectra in Figure 10 confirm that the petroleum ether-swollen polymer behaves nearly like the collapsed solid phase (Figure 10, blue line). The spectra reveal only marginally different peak-to-peak distances (57.2 mT for the dried polymer) corroborating again that petroleum ether is a very poor swelling agent for this polystyrene solid phase.[33]

P-5b
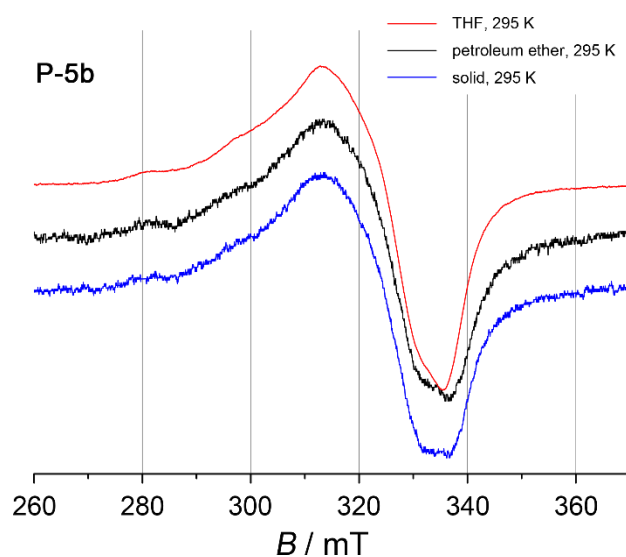
Figure 10. Experimental X-band EPR spectra of **P-5b** at 295 K swollen in different solvents and in the dried state.

It has to be mentioned that this study is only possible for copper(II) polymer **P-5b** because no solvent coordinates to copper(II) as NO_3^- is a non-exchanging axial ligand under these conditions. In contrast it is expected that the immobilized perchlorate copper(II) complexes **P-5a** coordinate solvent molecules as ligands resulting in a change of the EPR spectrum, as known for perchlorate copper(II) complexes with a calix[6]arene functionalized tren ligand [Cu(calix[6]tren)(solvent)](ClO_4)_2 (solvent = water, acetonitrile, dimethylformamide, ethanol).[22]

To conclude, spatial separation of the immobilized copper(II) complexes is achieved, due to solvent uptake and swelling of the cross-linked polymer. This can be monitored by EPR spectroscopy in different solvents at different temperatures. The polystyrene solid phase shows a good swelling behavior in THF, CH_2Cl_2 and toluene, whereas in saturated hydrocarbons like petroleum ether it behaves like a dry, collapsed polymer. These results are in accordance to the reports on comparable resins[32,33] and provide important information concerning the dependence of accessibility and reactivity of active sites from the type of solvent.[26]

Investigations on the Reactivity of P-2 and P-2'

As the previous experiments on proton and electron transfer to a polymer-supported nitrido molybdenum(VI) complex showed the successful stabilization of intermediates of the Schrock cycle,[12] the immobilized nitrido molybdenum(VI) complexes were studied in terms of NH_3 release upon treatment with protons and electrons. Different reaction conditions to improve the yield of ammonia were employed in a series of experiments using molybdenum(VI) complexes **P-2** and **P-2'**.

In the "Schrock catalysis" the catalytic activity was investigated starting from the dinitrogen molybdenum(III) complex $[(^{HIPT}N_3N)Mo^{III}(N_2)]$ (**A**) or the nitrido molybdenum(VI) complex $[(^{HIPT}N_3N)Mo^{VI}N]$ (**I**) under optimized conditions. One equivalent of the catalyst and 48 eq. of [2,6-lutH][B(3,5-{CF_3}_2C_6H_3)_4] were dissolved in heptane and 36 eq. of Cr{η^5-C_5Me_5}_2 dissolved in heptane were added dropwise to the mixture. The reaction starting from **A** as catalyst is shown in Scheme 11 a). After stirring the mixture for additional 20 minutes, the headspace containing NH_3 was transferred under reduced pressure into a liquid nitrogen-cooled HCl/dioxane flask. In this step 75% of the total ammonia could be isolated. The solid residue in the flask was treated with MeOH/THF/NaO^{t}Bu transforming the remaining dissolved 25% ammonia to gaseous NH_3 which was again transferred into the HCl/dioxane trap ensuring the detection of all produced ammonia. The cooled flask was allowed to warm to room temperature while NH_4Cl was formed. After removing the solvent and excess acid, the total amount of ammonia collected in the trap as NH_4Cl was determined by the indophenol method.[35] The application of this procedure led to the catalytic synthesis of 7−8 eq. NH_3 starting from one equivalent

[(^{HIPT}N$_3$N)Mo^{III}(N$_2$)] (**A**), and 6−7 eq. NH$_3$ starting from one equivalent [(^{HIPT}N$_3$N)Mo^{VI}N] (**I**). With the use of heptane as solvent the formation of H$_2$, from the direct reaction of the proton and the electron source shown in equation (1), is suppressed as discussed before. The local concentration of the molybdenum complex is always higher and therefore it is more likely that the proton source and the electron source react with the molybdenum complex.[6]

a)

$$[2,6\text{-LutH}][\text{BAr}^F{}_4], \text{CrCp}^*{}_2, \text{N}_2 \xrightarrow[\text{heptane, r.t.}]{\text{\LARGE A}} \text{NH}_3$$

        48 eq.   36 eq.   (7–8 eq.)

b)

$$[2,6\text{-LutH}][\text{Al}(\text{OR}^F)_4], \text{CoCp}^*{}_2, \text{N}_2 \xrightarrow[\text{solvent, r.t.}]{\text{\textbf{P-2 / P-2$'$}}} \text{NH}_3$$

[2,6-LutH] = 2,6-lutidinium
Ar^F = 3,5-(CF$_3$)$_2$C$_6$H$_3$
OR^F = OC(CF$_3$)$_3$
Cp* = η^5-C$_5$Me$_5$
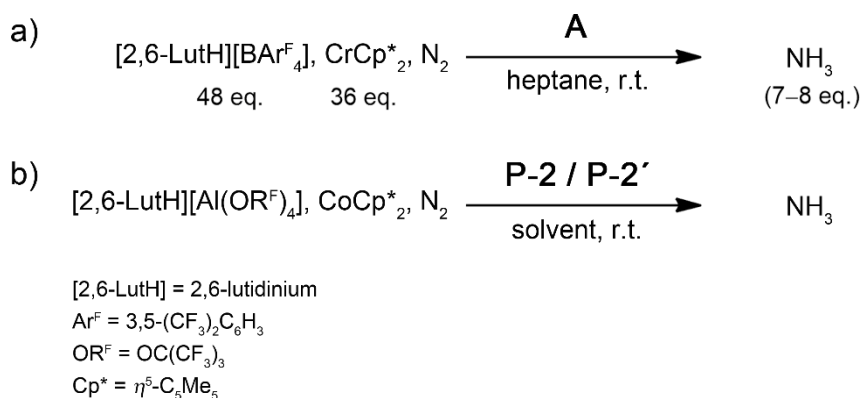
Scheme 11. a) "Schrock catalysis", catalytic ammonia synthesis performed in heptane under ambient conditions; b) conditions used in this study.

In the following, the studies on the formation of ammonia by treating **P-2** and **P-2'** with protons and electrons are presented using the conditions depicted in Scheme 11 b). The amount of employed starting materials and the yield of ammonia are given in equivalents (eq.) with respect to "MoN". One equivalent of the polymer-supported nitrido molybdenum(VI) complex **P-2** was weighed in a solid phase flask together with 5.8 eq. of [2,6-lutH][Al(OC{CF$_3$}$_3$)$_4$], and 4.6 eq. of the reducing agent CoCp*$_2$ with $E_{1/2} = -1.84$ V vs. Fc/Fc$^+$[6] compared to $E_{1/2} = -1.47$ V vs. Fc/Fc$^+$ for CrCp*$_2$[6]. Petroleum ether, which slowly dissolves the proton source, was added as solvent under a dinitrogen atmosphere. After two days the gas phase was transferred under reduced pressure into a liquid nitrogen-cooled HCl/dioxane flask. Besides NH$_3$, the corresponding base 2,6-lutidine generated in proton transfer reactions is removed under reduced pressure as well, and also collected in the HCl/dioxane flask giving 2,6-lutidinium chloride. After warming to room temperature the volatiles in the trap (solvent and excess HCl) were removed under reduced pressure and the remaining solid NH$_4$Cl and 2,6-lutidinium chloride were analyzed via ^{1}H NMR spectroscopy in [D$_6$]DMSO. No significant amounts of NH$_4^+$ ions were detected as depicted in Figure 11. This can be explained by the fact that the solid phase shows no swelling in petroleum ether (vide supra). The solid phase rather acts as a protective environment, as the catalytic centers are essentially inaccessible, and thus almost no ammonia evolved under these reaction conditions. Reaction between the proton source and the electron source is however possible leading to the formation of dihydrogen and 2,6-lutidine (not quantified in this step).
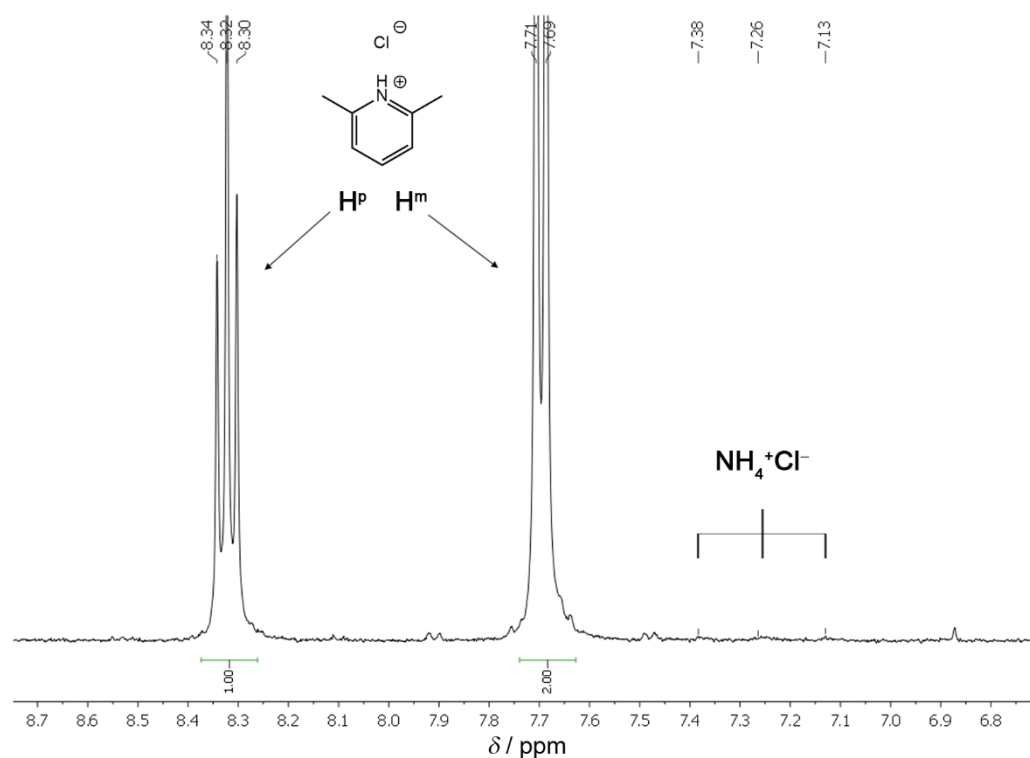
Figure 11. ^{1}H NMR spectrum in [D$_6$]DMSO of the volatiles trapped in HCl/dioxane after treatment of immobilized **P-2** with protons and electrons in petroleum ether.

By subsequent acidic hydrolysis (THF/H$_2$O/HCl) of the reaction mixture the immobilized nitrido molybdenum(VI) complexes are qualitatively hydrolyzed to release ammonia. Under these conditions ammonium chloride is formed, as well as 2,6-lutidinium chloride from the remaining proton source in the reaction mixture. Both salts are quantified by ^{1}H NMR spectroscopy in [D$_6$]DMSO (Figure 12).
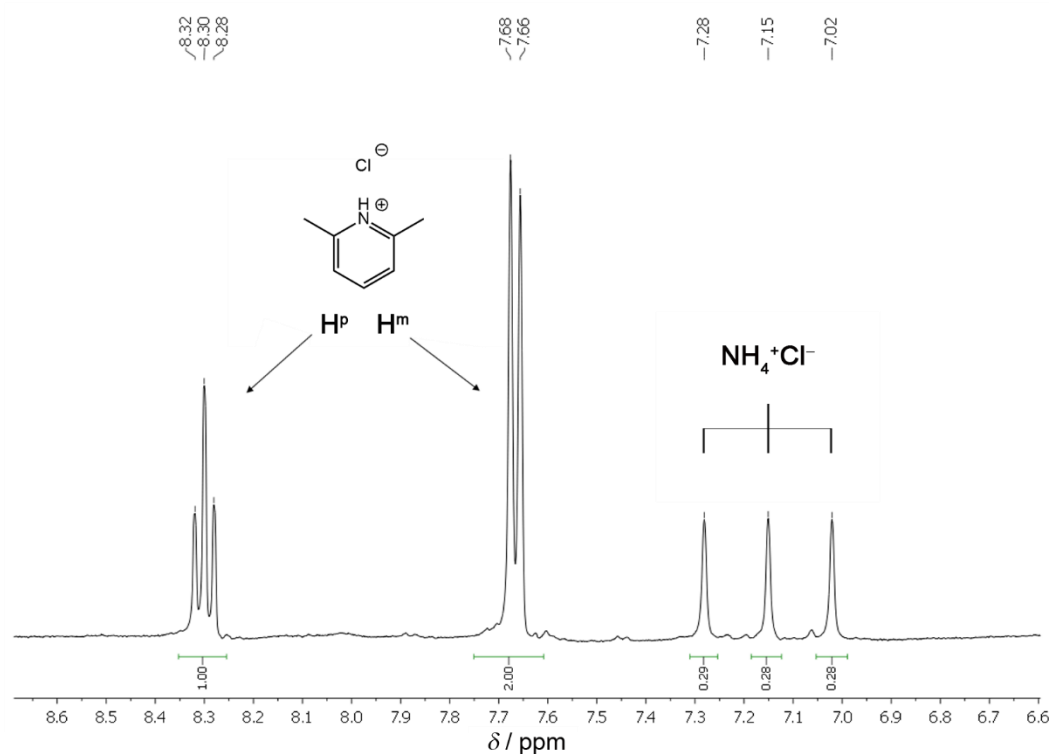
Figure 12. ^{1}H NMR spectrum in [D$_6$]DMSO after acidic hydrolysis (THF, H$_2$O, HCl) of the reaction mixture containing **P-2**, 2,6-lutH$^+$ and CoCp*$_2$.

Integration of the ^{1}H NMR signals and quantification relative to toluene as internal standard revealed 0.97 eq. ammonium chloride (nearly quantitative) and 4.44 eq. 2,6-lutidinium chloride (77%) to be present after acidic hydrolysis (Figure 13).

These results lead to the conclusion that only 1.36 eq. of the proton source (5.8 eq. − 4.44 eq.) are consumed in the first reaction step using petroleum ether (see Figure 11). Thus the normally fast reaction between the proton source and the electron source is retarded due to the poor solubility of [2,6-lutH][Al(OC{CF$_3$}$_3$)$_4$] in petroleum ether but it is still possible to some extent (23%). In fact this reaction is faster than the reaction with **P-2** due to the very poor swelling of **P-2** in petroleum ether.
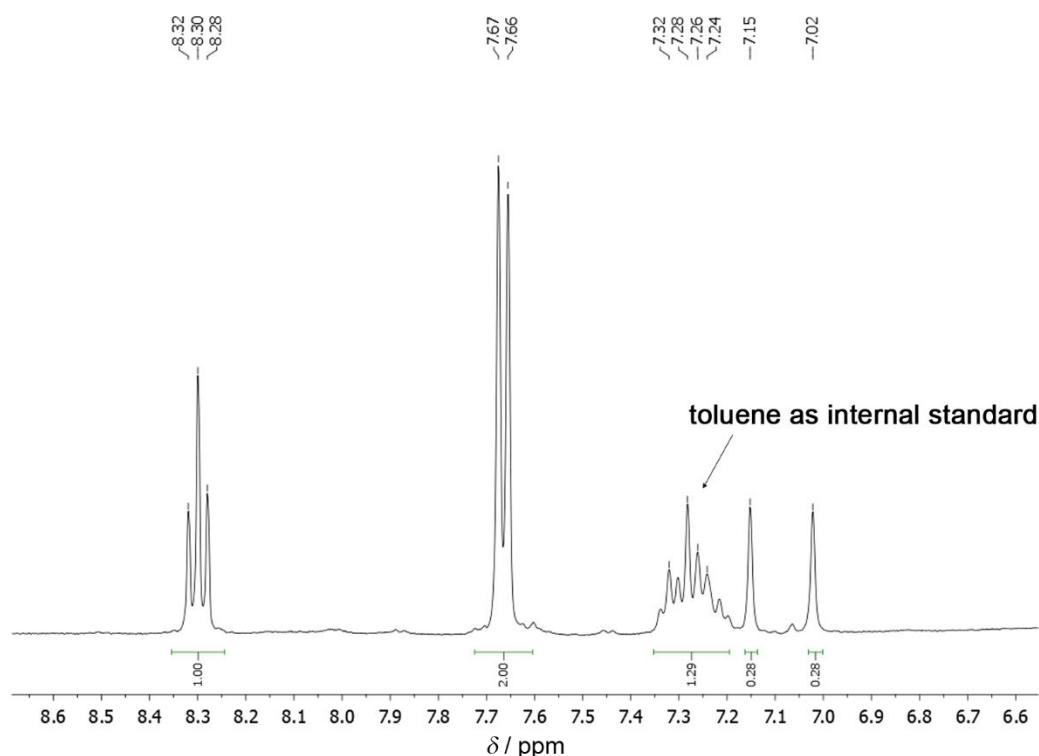
Figure 13. ^{1}H NMR spectrum in [D$_6$]DMSO; quantification of NH$_4$Cl with toluene as internal standard.

In consequence of these results, benzene was chosen as solvent representing a better swelling agent for the solid phase and therefore improving the accessibility of the reaction centers. One equivalent of **P-2** was weighed in a solid phase flask together with 8.7 eq. of [2,6-lutH][Al(OC{CF$_3$}$_3$)$_4$], and 8.1 eq. of the reducing agent CoCp*$_2$ was weighed as solid on the other side of the glass filter of the solid phase flask. Benzene was added as solvent under a dinitrogen atmosphere. The proton source is fairly soluble in benzene ensuring the protonation of the nitrido molybdenum(VI) complexes immobilized on the solid support. The solid phase flask is oriented in such manner that the glass filter and the solid CoCp*$_2$ are not in contact with the solvent. Gently shaking of the flask leads the solvent to pass the glass filter dissolving a small amount of the reducing agent which is then added to the reaction mixture. Repeating

this procedure results in the addition of CoCp*$_2$ sort of dropwise. However, a problem appears under these conditions: While the solvent passes the glass filter, the dissolved proton source readily reacts with CoCp*$_2$ generating H$_2$. Nevertheless, the reaction was continued for 2 h and then all volatiles were transferred under reduced pressure into a liquid nitrogen-cooled HCl/dioxane flask. Quantification of ammonia isolated in the trap as NH$_4$Cl via ^{1}H NMR spectroscopy reveals 0.14 eq. NH$_4^+$, whereas the integration of the 2,6-lutidinium signals in the ^{1}H NMR spectrum indicates with 7.32 eq. a higher consumption by H$_2$ formation (Figure 14).
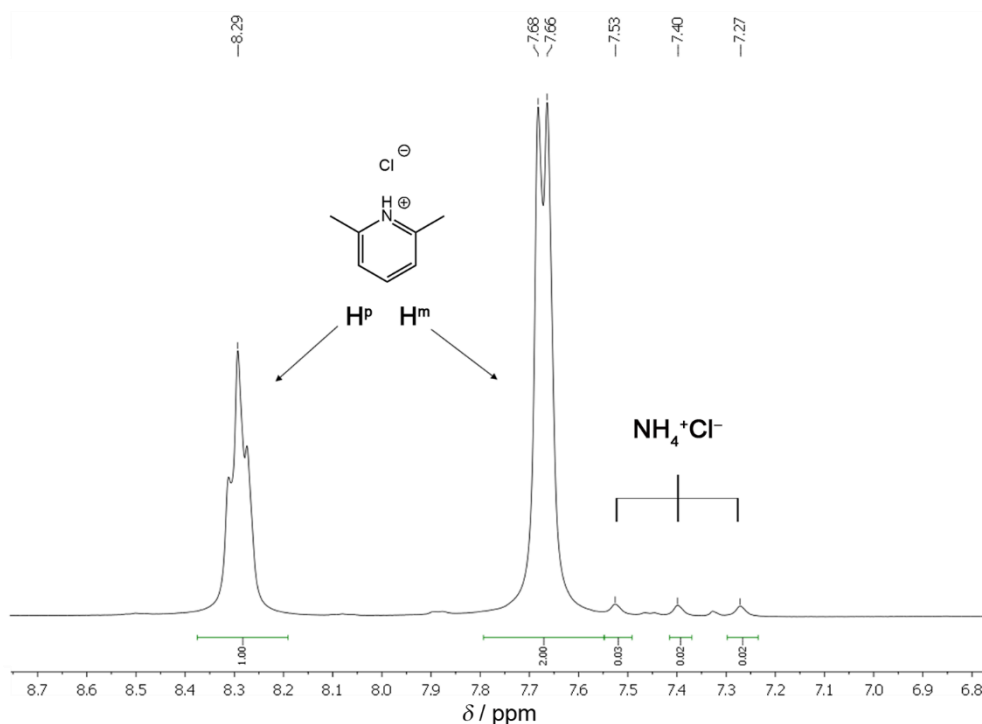
Figure 14. ^{1}H NMR spectrum in [D$_6$]DMSO of the volatiles trapped in HCl/dioxane.

By extracting the solid residue in the reaction flask with THF and collecting the liquid phase in HCl ammonium chloride and 2,6-lutidinium chloride have been isolated. Under the assumption of isolating the remaining 1.38 equivalents of the proton source in this step, and integrating the proton signals in the ^{1}H NMR spectrum relative to 2,6-lutidinium, as depicted in Figure 15, it is proposed that another crop ammonium (0.08 eq.) was extracted in this step.
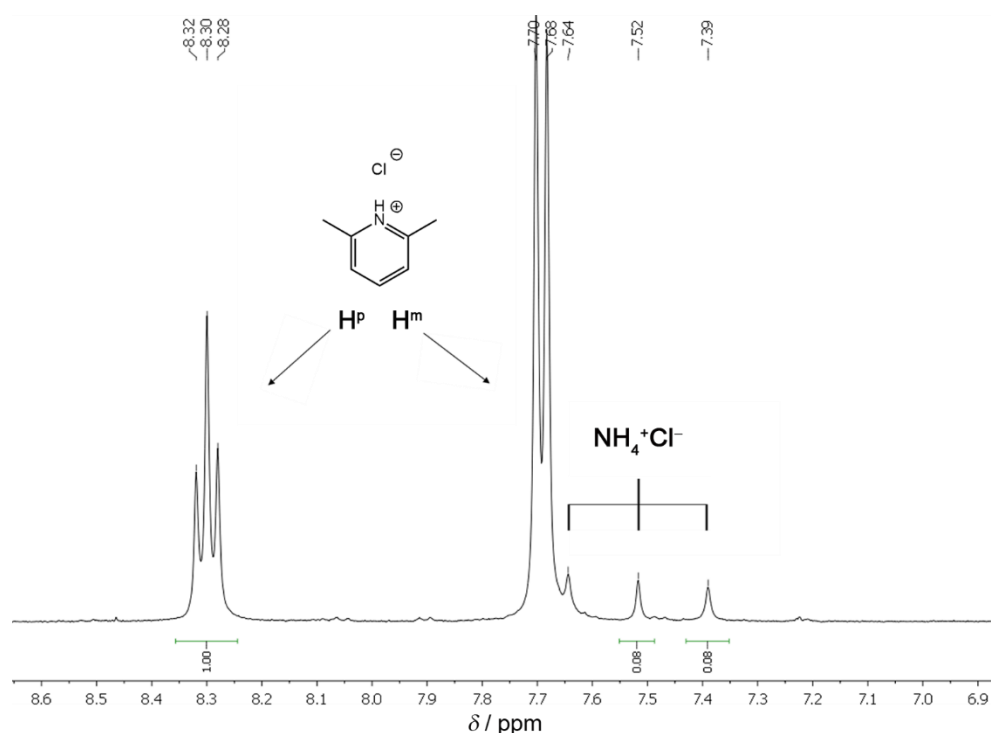
Figure 15. ^{1}H NMR spectrum in [D$_6$]DMSO of the washing solution.

This result reveals that protonation of generated ammonia by 2,6-lutH$^+$ to yield ammonium, as shown in equation (11), Scheme 12, is possible in benzene leading to a total amount of NH$_3$ + NH$_4^+$ of 0.22 eq. based on "MoN" in the NH$_3$/NH$_4^+$ ratio of 1.75:1.
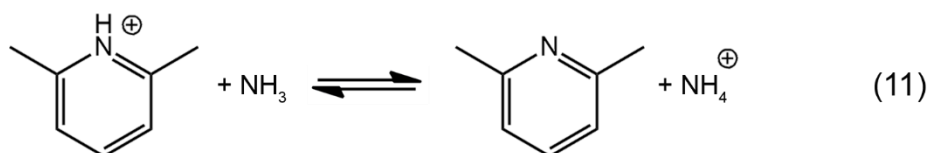
Scheme 12. Acid/base equilibrium of 2,6-lutidinium and ammonia.

These reaction settings show that ammonia release from immobilized nitrido molybdenum(VI) complexes is realized in benzene (22% yield) and that only 8.5%[*1] of the proton source are consumed for ammonia release meaning that the side reaction involving dihydrogen formation is still preferred. In the following table the results of the first and the second experiment are summarized (Table 1).

[*1] = (3×NH$_3$ gas phase + 4×NH$_4^+$ liquid phase) / total 2,6-lutidinium consumption

experiment	solvent	NH$_3$ gas phase	2,6-lut gas phase	NH$_4^+$ washing solution	2,6-lutH$^+$ washing solution	total yield NH$_3$ + NH$_4^+$
1	petroleum ether	-----	23%	not determined	not determined	-----
2	benzene	14%	84%	8%	16%	22%

Table 1. Isolated NH$_3$, NH$_4^+$, 2,6-lut and 2,6-lutH$^+$ in the respective experiment using different solvents.

In consequence, the extent of the protonation of generated NH$_3$ by [2,6-lutH][Al(OC{CF$_3$}$_3$)$_4$] to the corresponding ammonium salt, which remains in the reaction flask, is dependent on the reaction solvent (Scheme 12). In the case of using polar solvents the proton source is dissolved at high concentration shifting the equilibrium to the right (Scheme 12). The protonation of immobilized nitrido molybdenum(VI) with [2,6-lutH][Al(OC{CF$_3$}$_3$)$_4$] in THF revealed only traces (< 0.013 eq. based on "MoN") of ammonia in the gas phase. According to the pK_a value of 2,6-lutidinium (pK_a = 6.75 in aqueous solution)[36] compared to the pK_a value of ammonium (pK_a = 9.25)[37] 2,6-lutidine is present and can be transferred under reduced pressure, whereas ammonium remains as salt in the reaction flask.

Under conditions of the "Schrock catalysis" this is a minor problem due to the use of heptane and the poor solubility of [2,6-lutH][B(3,5-{CF$_3$}$_2$C$_6$H$_3$)$_4$] in this unpolar solvent. Thus the low H$^+$ concentration in solution has a smaller effect on the protonation of ammonia (>75% gaseous ammonia)[38]. The different solvent employed (benzene) favors the presence of ammonium instead of NH$_3$. As good swelling solvents for the solid phase have to be used (benzene), which are also fairly good solvents for the proton source as well as for the electron source, an excess of 2,6-lutH$^+$ is present in the solution. This leads to protonation of ammonia to NH$_4^+$. To determine the total amount of generated ammonia there are two possibilities. One the one hand, the solid residue in the reaction flask can be worked up under basic conditions similar to the "Schrock conditions" to determine the total amount of generated ammonia via the gas phase. On the other hand, the solid phase can be extracted with THF, a good solvent for ammonium salts, and the combined extracts can be acidified to yield NH$_4^+$. As all salts are easily extracted from the solid phase suspension, the latter method is preferred. Furthermore, this method leaves the immobilized molybdenum complexes intact. In contrast, the basic workup using methanol and potassium *tert*-butanolate results not only in the formation of gaseous ammonia, but also in a decomposition of the molybdenum catalyst as usually observed for these complexes in the presence of protic solvents (see hydrolysis experiments for molybdenum release).

Hence good swelling solvents for the solid phase have to be used, which are simultaneously good solvents for the proton source and the reducing agent. This favors the fast formation of dihydrogen. The

next reaction was hence performed using smaller amounts of [2,6-lutH][Al(OC{CF$_3$}$_3$)$_4$] and CoCp*$_2$. Therefore one equivalent of **P-2'** was weighed together with 6.6 eq. [2,6-lutH][Al(OC{CF$_3$}$_3$)$_4$] and 6.6 eq. CoCp*$_2$ in a Schlenk flask, and a toluene/THF mixture (10:5 mL) was added under dinitrogen. After 24 h the volatiles were transferred under reduced pressure and collected in the liquid nitrogen cooled HCl/dioxane trap. After warming to room temperature the volatiles (NH$_3$, 2,6-lutidine) in the trap were removed under reduced pressure and the remaining solid was analyzed via ^{1}H NMR spectroscopy. 0.084 eq. ammonium chloride and 5.19 eq. 2,6-lutidinium chloride (79%) were produced. After addition of fresh solvent (toluene/THF 10:5 mL) the reaction mixture was stirred for 27 h and the volatiles were transferred into an HCl/dioxane flask. Quantification of the collected volatiles yielded 0.095 eq. ammonium chloride and 0.97 eq. 2,6-lutidinium chloride. At least 29%[*2] of the protons are spent for the formation of ammonia and only 71% for the formation of H$_2$ in this step. As NH$_4$$^+$ has not been determined in this experiment the total yield of ammonia should be even higher.

After this second reaction, 93% of the proton source are consumed and therefore another 0.71 eq. [2,6-lutH][Al(OC{CF$_3$}$_3$)$_4$] and 0.75 eq. CoCp*$_2$ were added to the reaction mixture as well as 10 mL toluene and 5 mL THF. Stirring for 48 h and collecting the volatiles in an HCl/dioxane flask revealed another 0.022 eq. of ammonium chloride and 0.58 eq. 2,6-lutidinium chloride corresponding to the consumption of at least 11%[*2] of the proton source for ammonia production. As the consumption of the proton source reached again overall 92% another 1.45 eq. [2,6-lutH][Al(OC{CF$_3$}$_3$)$_4$], 1.5 eq. CoCp*$_2$ and toluene/THF (10:5) were added. The reaction mixture was stirred for 24 h and then the volatiles were transferred under reduced pressure. The ^{1}H NMR spectrum revealed 0.029 eq. ammonium chloride and 1.56 eq. 2,6-lutidinium chloride. An overview of the amount of isolated NH$_4$Cl and 2,6-lutidinium chloride in every single reaction step is given in Table 2.

number of steps	NH$_3$ (gas phase)	2,6-lut (gas phase)	efficiency[*2] (minimum)
1	0.084 eq.	5.19 eq.	5%
2	0.095 eq.	0.97 eq.	29%
3 (addition of 0.67 eq. 2,6-LutH$^+$)	0.022 eq.	0.58 eq.	11%
4 (addition of 1.3 eq. 2,6-LutH$^+$)	0.029 eq.	1.56 eq.	6%

Table 2. Amount of NH$_3$ and 2,6-lut isolated in each step using toluene/THF (2:1), and efficiency of proton consumption for NH$_3$ production.

[*2] $= 3 \times$ NH$_3$ $_{\text{gas phase}}$ / 2,6-lut $_{\text{gas phase}}$

Lowering the concentration of protons and electrons in the reaction flask yields smaller amounts of ammonia regarding the single steps, but increases the efficiency of proton consumption for ammonia release per step (up to 29% in the second step). Over these four steps 0.23 eq. ammonia (23%) have been released and isolated selectively in the gas phase, whereas the proton source consumption was nearly quantitative (95%, 8.30 eq.) as expected. These results are summarized in Figure 16.

Protonation of ammonia can take place under these reaction conditions. To determine the total amount of ammonia generated over the four reaction steps, the solid residue in the reaction flask was dissolved in THF and the washing solutions were collected in an HCl containing flask. Via ^{1}H NMR spectroscopy 0.150 eq. NH$_4$Cl have been determined after quantification with toluene.

Figure 16. Sum of released ammonia and consumed 2,6-lutH$^+$, transferred as volatiles and trapped in HCl/dioxane.

In total, 0.38 eq. (38%) ammonia were generated in this third experiment with 23% isolated in the gas phase as NH$_3$ and 15% in the washing solution as NH$_4^+$ leading to a NH$_3$/NH$_4^+$ ratio of 1.53:1. In the following table the results are compared with the previous experiment (Table 3). Increasing the polarity of the solvent results in the augmented protonation of ammonia leading to a lower NH$_3$/NH$_4^+$ ratio.

experiment	solvent	NH$_3$ gas phase	2,6-lut gas phase	NH$_4^+$ washing solution	2,6-lutH$^+$ washing solution	total yield NH$_3$ + NH$_4^+$
2	benzene	14%	84%	8%	16%	22%
3	toluene/THF 2:1	23%	95%	15%	5%	38%

Table 3. Comparison of isolated ammonia in experiments 2 and 3.

In a further experiment the effect of protonation without reduction of the immobilized nitrido molybdenum(VI) complexes was investigated. Therefore, 1.4 equivalents [2,6-lutH][Al(OC{CF$_3$}$_3$)$_4$] dissolved in THF were added to one equivalent of **P-2'** and the amount of ammonia and ammonium isolated in the gas and in the liquid phase was determined, respectively. The results are given in Table 4.

number of steps	NH$_3$ gas phase	NH$_4^+$ washing solution	sum of isolated NH$_3$ + NH$_4^+$
1	0.013 eq.	0.045 eq.	0.058 eq.
2	0.0 eq.	0.050 eq.	0.108 eq.
3	0.0 eq.	0.066 eq.	0.174 eq.

Table 4. Amount of isolated ammonia in the gas and in the liquid phase in each step using THF as solvent, and the total yield calculated as the sum over the steps.

In the first step 0.013 eq. ammonia has been isolated in the gas phase and 0.045 eq. ammonium in the liquid phase giving an NH$_3$/NH$_4^+$ ratio of 1:3.5. This result corroborates that in the presence of 2,6-lutidinium ammonia is protonated to ammonium which is retained in the liquid phase (equation (11), Scheme 12). In contrast to the previous protonation and reduction experiment, only traces of ammonia have been isolated in the gas phase over the three protonation steps and also the total amount of ammonia released by protonation is smaller. Thus the release of ammonia due to protonation of immobilized nitrido molybdenum(VI) is possible to some extent, whereby the molybdenum product is unclear, but it is much more efficient adding the proton and the electron source (see Table 2 and 3).

To reduce dihydrogen formation the next experiment was performed with one equivalent **P-2'**, adding first 1.4 eq. of the proton source in THF and after 3 h 1.4 eq. of the reducing agent in THF/toluene (2:1) under dinitrogen. After addition of all components, the mixture was stirred for additional 3 h. The volatiles were then transferred under reduced pressure and collected in a liquid nitrogen-cooled

HCl/dioxane flask. The reaction mixture was extracted with THF (3×5 mL) and the combined solutions were collected in an HCl/THF flask. After this step, all ammonia and ammonium evolved in the reaction is trapped in HCl and removed out of the reaction flask, as well as 2,6-lutidine, 2,6-lutidinium and the remaining salts accumulated during the reaction, for example $[CoCp*_2][Al(OC\{CF_3\}_3)_4]$.

Pursuing this strategy the immobilized nitrido molybdenum complexes should be protonated, allowing for their subsequent reduction. Whereas the dihydrogen formation occurring from the fast reaction of the proton source with the reducing agent (equation (1), Scheme 2) is suppressed, because at the point of $CoCp*_2$ addition most protons from the 2,6-lutidinium salt are already consumed by **P-2'**, dihydrogen formation is still possible to some extent as shown in Scheme 13, equation (12), in accordance with equation (1).[3]

$$H^{\oplus} + NH_3 \rightleftharpoons NH_4^{\oplus}$$

$$H^{\oplus} + CoCp*_2 \longrightarrow {}^1/_2\,H_2 + CoCp*_2^{\oplus} \qquad (12)$$

Scheme 13. Reaction equations leading to dihydrogen formation.

This procedure was repeated 17 times, collecting the gas phase and the washing solution separately and analyzing both by ^1H NMR spectroscopy (Table 5). The total amount of ammonium chloride isolated in each step is shown graphically in Figure 17 and the error bars represent estimated errors arising from quantification with toluene as internal standard in the ^1H NMR spectra.

Figure 17. Total amount of isolated NH_4Cl per "MoN" with error bars for each reaction step.

number of steps	NH$_3$ gas phase (eq.)	estimated error (eq.)	NH$_4^+$ liquid phase (eq.)	estimated error (eq.)	total yield NH$_3$ + NH$_4$Cl (eq.)	estimated error (eq.)
1	0.044	0.0003	0.135	0.0005	0.178	0.0008
2	0.023	0.0004	0.113	0.0005	0.314	0.0017
3	0.023	0.0019	0.129	0.0010	0.466	0.0045
4	0.030	0.0016	0.105	0.0019	0.600	0.0080
5	0.003	0.0027	0.054	0.0009	0.657	0.0116
6	0.001	0.0013	0.023	0.0007	0.681	0.0135
7	0.036	0.0040	0.024	0.0018	0.741	0.0193
8	0	0	0.051	0.0026	0.792	0.0219
9	0	0	0.034	0.0016	0.826	0.0235
10	0.013	0.0040	0.105	0.0046	0.943	0.0321
11	0	0	0.012	0.0019	0.955	0.0339
12	0	0	0.016	0.0016	0.972	0.0355
13	0.012	0.0013	0.014	0.0021	0.998	0.0390
14	0	0	0.101	0.0054	1.099	0.0444
15	0	0	0	0	1.099	0.0444
16	0	0	0	0	1.099	0.0444
17	0	0	0	0	1.099	0.0444

Table 5. Amount of isolated NH$_4$Cl per "MoN" in the gas and in the liquid phase for each step, and the total amount of isolated NH$_4$Cl calculated as the sum.

The results from the gas and the liquid phase (Table 5) confirm that THF as predominant solvent retains the majority of ammonia as ammonium salt in the washing solution (NH_3/NH_4^+ ratio in most cases 1:3) as expected, in accordance with the previous experiments (see Table 3 and 4). The presence of [2,6-lutH][Al(OC{CF_3}_3)_4] in the first step favors the protonation of ammonia, if already generated at that point, to form $[NH_4][Al(OC\{CF_3\}_3)_4]$ in THF. In consequence, during addition of the reducing agent through a syringe, only traces of gaseous NH_3 should escape the flask and most is retained in the solution as NH_4^+.

In the first reaction step, after addition of 1.4 eq. 2,6-lutH$^+$ and 1.4 eq. CoCp*$_2$, 0.044 eq. NH_3 are isolated in the gas phase and another 0.135 eq. NH_4^+ in the washing solution (Table 5). In contrast to the protonation reaction (< 0.06 eq.), the total yield of ammonia released in this step amounts 0.18 equivalents with respect to "MoN" (Figure 17). Hence, protonation followed by reduction increases the yield of NH_3.

It is suggested that not all nitrido molybdenum complexes immobilized on the solid support react simultaneously, but the protonation and reduction proceeds in sections within the polymer bead. Active sites located at the "outer shell" of the spherical polymer bead, as illustrated in light orange in Figure 18, are well accessible and undergo rapid reactions upon H$^+$/e$^-$ addition. Whereas immobilized nitrido molybdenum complexes located in the "inner shells" of the cross-linked polymer, orange to dark orange colored, are less affected (slower reactions). Hence, product formation depends on diffusion rates and therefore also the time for each reaction step.

Figure 18. Scheme of multiple "reaction shells" within a spherical polymer bead.

The two competing physical properties that matter in this case are the diffusion rate of the 2,6-lutidinium cation and the reducing agent CoCp*$_2$ through the polymer network versus the reaction rate towards the immobilized molybdenum complexes. The proton and the electron source react faster with the molybdenum centers located in the "outer sphere" of the polymer network than reaching other immobilized reaction centers located in the "inner regions" of the bead resulting in the formation of 0.18 eq. ammonia already in the first step (Scheme 14).

$$\text{LMoN} + \text{H}^+,\text{e}^- + \text{H}^+,\text{e}^- + \text{H}^+,\text{e}^- \longrightarrow \text{NH}_3 + \text{LMoX}$$

L = polymer-supported
triamidoamine ligand

Scheme 14. Reaction equation leading to ammonia release in the first reaction step.

Additionally, 48%[*1] of the proton source are consumed for ammonia release in the first step showing the high efficiency of this stepwise method in comparison to the previous experiments 1−3 (see also Table 2).

In the following three steps, the amount of generated ammonia remains essentially constant. Then it decreases until the 6th step, shows an increase in the 7th step, decreases until the 9th step and increases considerably in the 10th and in the 14th step. Finally, until the 17th step no ammonia was released (Figure 17).

The amount of ammonia isolated in the gas phase shows an interesting pattern: 1, 4, 7, 10 and 13 (Figure 19 and Table 5). In two consecutive steps no ammonia, or a significant smaller amount of ammonia, is detected whereas the third step reveals ammonia in the gas phase. This pattern is repeated four times until the 13th step, the last step of ammonia isolation in the gas phase. With the application of this stepwise addition of one equivalent of the proton source and the electron source, it was expected to get insights into the reaction mechanism of ammonia release, especially concerning the reaction steps of the second half of the Schrock−Yandulov cycle (Scheme 3, equation (2)−(5)).

[*1] = (3×NH$_3$ $_{\text{gas phase}}$ + 4×NH$_4$$^+$ $_{\text{liquid phase}}$) / total 2,6-lutidinium consumption
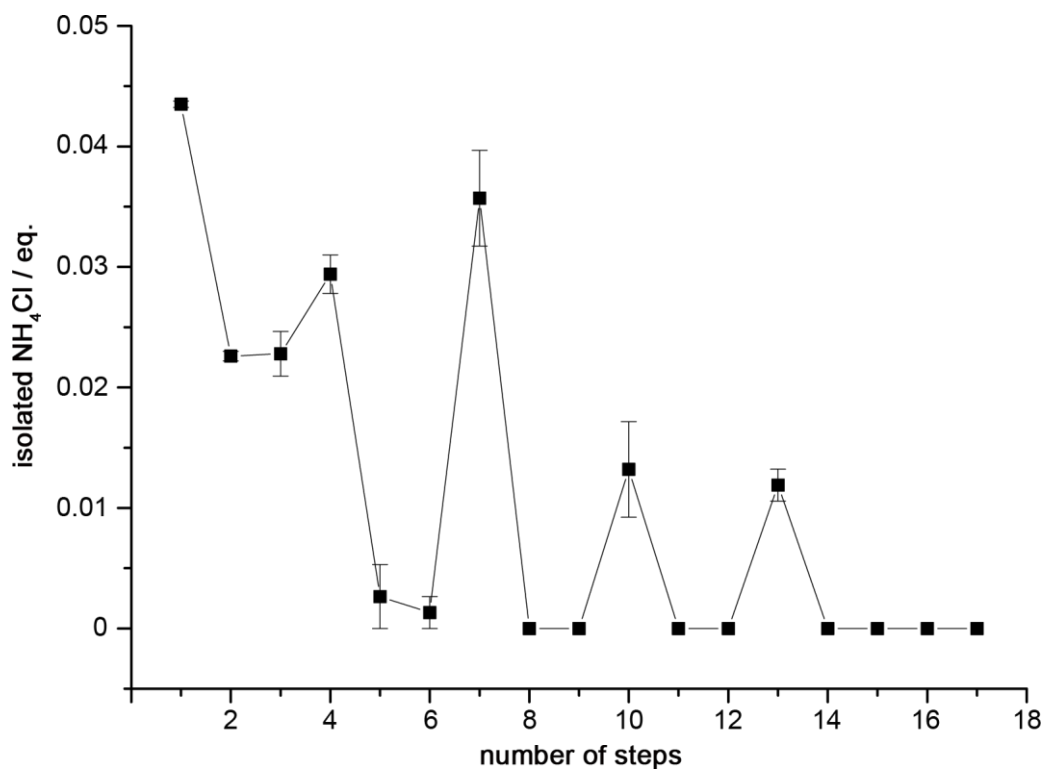
Figure 19. Amount of isolated NH_4Cl in the gas phase with error bars for each reaction step.

According to the reports on the proposed catalytic cycle by Schrock[6], it was supposed that the generation of ammonia proceeds as described in the introductory section in Figure 1. This proposed idealized mechanism is transferred to immobilized complexes and is shown in Figure 20, with L representing the polymer-supported triamidoamine ligand.
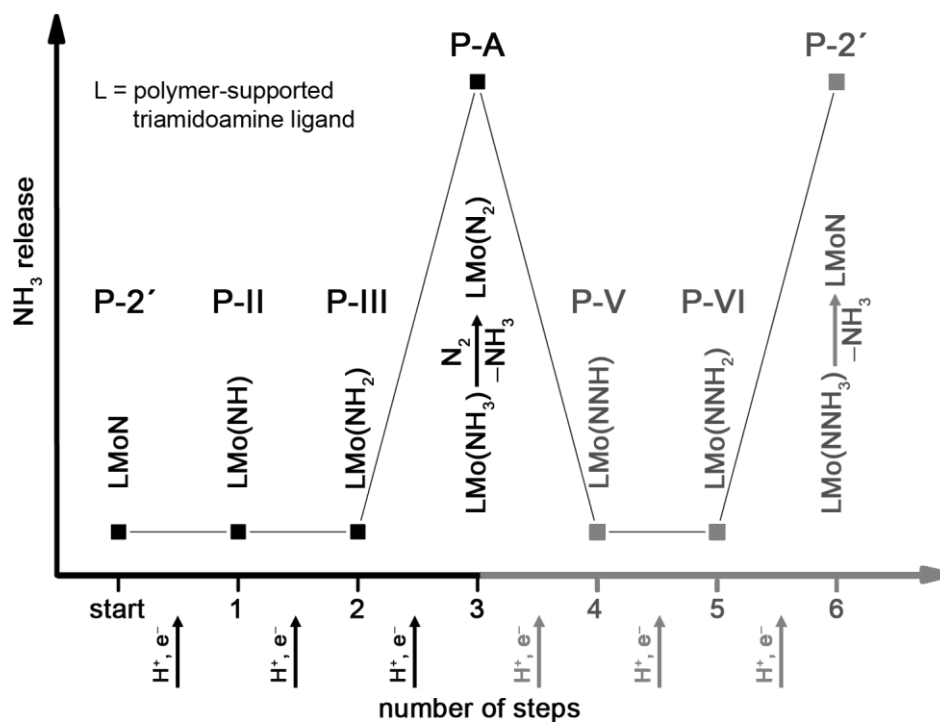
Figure 20. Proposed idealized reaction mechanism including NH_3 release after addition of 3 eq. H^+ and e^-.

After the first step, the addition of one equivalent of the proton source and the reducing agent, the immobilized imido molybdenum(V) complex (**P-II**) should be generated and we expect no ammonia, neither in the gas nor in the liquid phase in this idealized view. However, **P-II** formed at the "outer sphere" of the polymer bead reacts already in the first step to give LMo(NH$_2$) (**P-III**) and LMo(NH$_3$) (**P-IV**). The idealized second H$^+$/e$^-$ step should yield the amido molybdenum(IV) complex (**P-III**) and still no ammonia release. After addition of the third equivalent the ammine molybdenum(III) complex (**P-IV**) should be formed. At that stage, liberation of ammonia is expected enabling its detection either in the gas or in the liquid phase. Especially the results gained from the gas phase (Figure 19) show such a curve characteristics and thus this could be an evidence corroborating the proposed reaction mechanism. Due to the diffusion-limited reactions appearing in the "inner volume" of the spherical polymer (Figure 18), the less accessible active sites react slower, and thus stepwise protonation and reduction reactions are possible within shells of the polymer. This diffusion-controlled reaction is distinct from the homogeneous catalytic systems of Schrock, where all dissolved molybdenum complexes react "simultaneously", including H$^+$/e$^-$ exchange between the active sites, upon addition of the proton and the electron source in a thermodynamically controlled reaction.

The overall release of ammonia is depicted in Figure 21 (squares), and the data from the protonation experiment (see Table 4) were included for comparison (Figure 21, crosses).
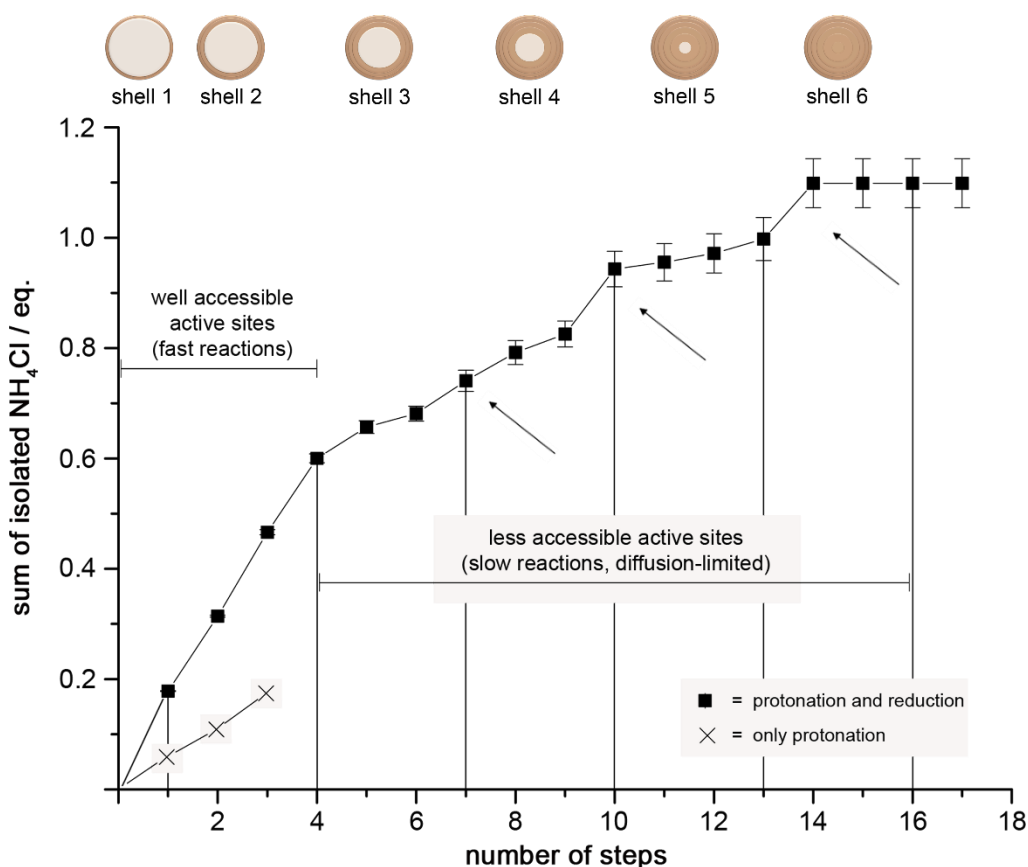
Figure 21. Sum of isolated NH$_4$Cl from stepwise protonation and reduction (with error bars), the arrows indicate distinct steps; reactive shells within the polymer are schematically illustrated above; results compared to protonation experiment indicated by crosses (results taken from Table 4).

The plot from stepwise protonation and reduction shows a saturation behavior, which corresponds to a stoichiometric process with a maximum amount of generated ammonia being one equivalent within error. After these 17 reaction steps 1.099 ±0.044 equivalents ammonia (based on "MoN") have been isolated (Figure 21).

In the first four reaction steps, the curve in Figure 21 shows an almost linear ammonia production. The well accessible active sites react with the proton and the electron source to release ammonia under thermodynamic control. Thus the addition of several protons and electrons to one immobilized nitrido molybdenum(VI) complex is possible in a single step. In these rapid reaction steps 55% of the total ammonia are generated. This method gives the highest yield compared to the previous methods (experiments 1−3). Using 5.6 equivalents of the proton source and the reducing agent in four portions results in the formation of 0.60 equivalents ammonia revealing the efficiency of this stepwise method. In the following, the curve flattens showing a total amount of 0.83 equivalents ammonia after nine steps and 1.1 equivalents after 14 steps. Distinct steps in the overall saturation curve, appearing at the 7th and 10th measurement as highlighted by arrows in Figure 21, could probably be explained with a stepwise reaction of the immobilized complexes (within shells) located in the "inner volume" of the spherical polymer bead according to the mechanism depicted in Figure 20. Each of these shells of the polymer requires three H^+/e^- steps for the formation of NH_3 as schematically illustrated in Figure 21. The 14th step shows again an abrupt increase of ammonia release. As this step represents the last step of ammonia detection this result can be attributed probably to the protonation and reduction reaction of the remaining immobilized molecules. In the end, 1.1 equivalents ammonia were released from all immobilized nitrido molybdenum complexes (1 eq.) within error.

In a catalytical reaction one dinitrogen molecule is coordinated to the molybdenum(III) center after the release of ammonia starting a new catalytic cycle from $LMo^{III}(N_2)$ (**P-A**, Figure 20). In this experiment no evidence of the coordination of dinitrogen has been obtained, and hence no catalytic formation of NH_3 is observed.

There are several possibilities explaining the loss of catalytic activity in this system. High acid concentrations can protonate the triamidoamine ligand at amido groups effecting the release of molybdenum from the solid support and thus decomposing the potential catalyst. This scenario was investigated by determination of the molybdenum content of the combined washing solutions of the 1st to the 8th step via ICP-MS revealing the presence of 0.0595±0.0003 equivalents molybdenum. This result means that only 6% of the immobilized molybdenum was released from the solid support during eight reaction steps showing the stability of the complexes towards chelate ligand protonation followed by molybdenum loss under these conditions. At this stage the curve depicted in Figure 21 already levels off indicating a stoichiometric reaction. Thus metal release due to protonation of the ligand backbone doesn't represent the predominant reason for the loss of catalytic ability. In consequence two other reasons are possible. First of all, it is supposed that the dinitrogen concentration in the reaction solution

might be relatively low, as the solvents used for this reaction were distilled and stored over argon atmosphere, and were added directly to the reaction mixture under dinitrogen without further degassing. This could be a reason that dinitrogen coordination to the molybdenum(III) complex leading to ammonia release according to equation (5) (Scheme 3) is not favored. However, protonation of NH_3 to NH_4^+ should shift the equilibrium to the right.

Another plausible reaction includes 2,6-lutidine coordination to the Mo^{III} as shown in equation (8) and (9) in the introductory section (Scheme 5). Such 2,6-lutidine complexes are well known in the literature. A series of 2,6-lutidine complexes have been synthesized with transition metals featuring low coordination numbers, for example square planar copper(II) and chromium(II) complexes,[39,40] but an octahedral mononuclear Fe(II) complex with 2,6-lutidine ligands has also been isolated.[41]

As shown in Scheme 6, 2,6-lutidine can coordinate to high spin molybdenum(IV) with the Schrock ligand leading to the cationic complex **VIII**. X-ray crystallographic studies have identified an Mo−N$_{2,6-lut}$ distance of 2.283 Å, which is within the range of the Mo−N$_{amine}$ dative bond distances observed for nine other Schrock-type molybdenum complexes.[6] 2,6-Lutidine is bound "off-axis" with an N$_{amine}$−Mo−N$_{2,6-lut}$ angle of 157°. These data already show that 2,6-coordination to the metal center is sterically restricted due to the bulky HIPT substituents. Upon reduction of **VIII** under dinitrogen atmosphere, giving the 2,6-lutidine molybdenum(III) complex **VII**, molybdenum(III) readily loses 2,6-lutidine and favors the coordination of the small N_2 ligand (equation (10), Scheme 6). Thus, 2,6-lutidine is unlikely to bind strongly to Schrock's molybdenum(III) complex due to the sterical hindrance.[6,11]

In contrast, corroborated by a DFT calculation (B3LYP, LANL2DZ, PCM THF)[42], 2,6-lutidine can indeed coordinate to the immobilized molybdenum(III) center, which is less encumbered compared to the Schrock system. Especially due to the benzylic arm of the polymer-supported ligand, the axial binding pocket of this molybdenum complex is large enough to enable strong 2,6-lutidine coordination. The DFT model of the immobilized 2,6-lutidine molybdenum(III) complex (**P-VII**) is depicted in Figure 22. The calculated Mo−N$_{2,6-lut}$ distance amounts 2.261 Å, which is nearly identical to the Mo−N$_{amine}$ bond distance of 2.256 Å. This Mo−N$_{2,6-lut}$ distance is shorter compared to the respective distance in Schrock's molybdenum(IV) complex **VIII** (2.283 Å)[6] and corroborates the stronger Mo^{III}−N$_{2,6-lut}$ bond. The pyridine ring of 2,6-lutidine is slightly distorted and not entirely planar in **P-VII** (< 4° torsion angle N−C^o−C^m−C^p). The N$_{amine}$−Mo−N$_{2,6-lut}$ angle of 168° reveals additionally that 2,6-lutidine coordinates in linear fashion, and thus with a better orbital overlap, to the metal center in this immobilized complex **P-VII** compared to the Schrock Mo^{IV} complex **VIII** (157°).[6] This DFT calculation shows that this sterically less encumbered ligand system enables 2,6-lutidine coordination to molybdenum(III), in contrast to the bulky Schrock ligand system. This stable immobilized 2,6-lutidine molybdenum(III) complex **P-VII** is catalytically unreactive as 2,6-lutidine cannot be substituted by N_2. Thus, formation of this complex **P-VII** represents a plausible explanation for the loss of catalytic activity in this immobilized system.

Figure 22. DFT model of immobilized 2,6-lutidine molybdenum(III) (**P-VII**) (B3LYP, LANL2DZ, PCM THF), protons are omitted for clarity.

3. CONCLUSIONS

An alternative route to a polymer-anchored triamidoamine ligand (**P-1'**) using an Ullmann-type coupling reaction has been presented. This method was, however, more time-consuming compared to the previously reported palladium-catalyzed Buchwald-Hartwig coupling (**P-1**). In addition, **P-1'** shows a lower ligand loading compared to **P-1**. Subsequent transformation to the immobilized nitrido molybdenum(VI) complex (**P-2'**) was realized according to published methods using [MoCl$_3$N(CH$_3$CN)]$_4$ as "MoN" source. The transformation to the immobilized copper(II) complexes **P-5a'** and **P-5b'** was achieved using Cu(ClO$_4$)$_2$·6H$_2$O and Cu(NO$_3$)$_2$·3H$_2$O, respectively. All newly immobilized compounds feature the same spectroscopic properties but show a lower degree of loading compared to the previously reported congeners **P-1**, **P-2**, **P-5a** and **P-5b**.

EPR spectroscopy of immobilized copper(II) complex **P-5b** was performed in different solvents at different temperatures to monitor the spatial separation of the immobilized copper(II) complexes, which is achieved due to solvent uptake and swelling of the cross-linked polymer. The polystyrene solid phase shows a good swelling behavior in THF, CH$_2$Cl$_2$ and toluene, whereas in saturated hydrocarbons like petroleum ether it behaves like a dry, collapsed polymer. Hence, EPR spectroscopic experiments revealed the dependence of accessibility and reactivity of active sites from the type of solvent. Petroleum ether and heptane for example are not suitable for solid phase reactions.

Polymer-supported nitrido molybdenum(VI) complexes **P-2** and **P-2'** were treated with a proton source (2,6-lutidinium) and an electron source (decamethylcobaltocene) under different reaction conditions (solvents) to investigate and to optimize the amount of released ammonia. In accordance to the EPR spectroscopic experiments, good swelling solvents for the solid phase were used to optimize and to guarantee good accessibility of the immobilized nitrido molybdenum(VI) complexes. The use of such

solvents, which are simultaneously good solvents for the proton and the electron source, led to a high proton concentration in the reaction solution and favored the fast formation of dihydrogen. In consequence, the proton source and the reducing agent were added stepwise to the immobilized nitrido molybdenum(VI) complex to reduce dihydrogen formation and favor NH$_3$ generation. This experiment revealed that protonation and reduction reactions proceed stepwise within shells of the polymer. Active sites located at the "outer shell" of the spherical polymer bead are well accessible and react fast upon H$^+$/e$^-$ addition, whereas active sites located at the "inner shells" are less accessible undergoing slow diffusion-controlled reactions with the proton and electron source. Three H$^+$/e$^-$ steps are required to give a peak NH$_3$ release from these inner shells, corresponding to the 3 H$^+$/e$^-$ reactions followed by one ligand exchange reaction, for example with 2,6-lutidine (Scheme 15).
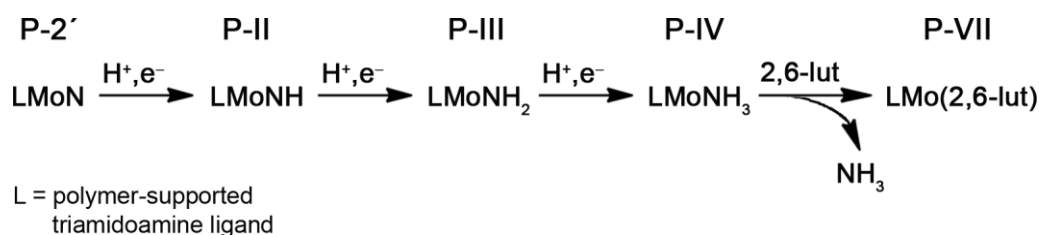
Scheme 15. NH$_3$ release after three H$^+$/e$^-$ steps and one ligand exchange reaction, here with 2,6-lutidine.

Protonation of the immobilized nitrido molybdenum(VI) complexes followed by reduction yielded stoichiometric amounts of ammonia after 17 steps. In this experiment no evidence for catalytic formation of ammonia was observed. Irreversible coordination of 2,6-lutidine to molybdenum(III) yielding the stable, catalytically inactive complex **P-VII** represents a plausible reason for the loss of catalytic ability.

In the future, the immobilized nitrido molybdenum(VI) complex should be further investigated with respect to catalytic ammonia formation. Thus a sterically more demanding proton source, for example 2,6-diisopropylpyridinium, should be used to prevent coordination to molybdenum(III). The use of an acid like for example [H(OEt$_2$)][Al(OC{CF$_3$}$_3$)$_4$][43], whose corresponding base diethylether does not compete with N$_2$ for molybdenum(III) coordination, would be another possible way to enable catalytic ammonia formation.

4. EXPERIMENTAL SECTION

General considerations: All reactions were performed under inert atmosphere (Schlenk techniques, glove box). For the solid-phase reactions a flask with a nitrogen inlet and a coarse porosity fritted glass filter that allows addition and removal of reagents and solvents without exposure of the resin to the atmosphere was used.[44] For the protonation and reduction reactions under dinitrogen atmosphere dinitrogen 5.0, purchased from Westfalen AG Münster, was used after drying and purification, to remove traces NH$_3$, by bubbling through H$_2$SO$_4$ (conc.). THF was distilled from potassium, petroleum

ether b.p. 40–60°C and toluene from sodium. Tris(2-aminoethyl)amine resin (1% divinylbenzene, 100–200 mesh, $0.6 - 1.0$ mmol g^{-1}) was obtained from IRIS Biotech GmbH (Germany). Other chemicals were obtained from commercial suppliers and used without further purification. [MoCl$_3$N(CH$_3$CN)]$_4$[23,45] and [2,6-lutH][Al(OC{CF$_3$}$_3$)$_4$][12] were synthesized as reported. IR spectra were recorded on a BioRad Excalibur FTS 3100 spectrometer using cesium iodide or potassium bromide disks. UV/Vis spectra in solution were recorded on a Varian Cary 5000 spectrometer in 1.0 cm cells (Hellma, suprasil). The solid phase spectra were recorded using this spectrometer equipped with a Praying Mantis Diffuse Reflectance Accessory. FD mass spectra were recorded on a FD Finnigan MAT90 spectrometer. ESI mass spectra were recorded on a Micromass Q-TOF-Ultima spectrometer. NMR spectra were recorded on a Bruker Avance DRX 400 spectrometer at 400.31 (^{1}H), 100.66 (^{13}C{^{1}H}), 367.67 (^{19}F) and 40.56 MHz (^{15}N). All resonances are reported in ppm *versus* the solvent signal as internal standard [D$_8$]THF (^{1}H: $\delta = 1.72, 3.58$; ^{13}C: $\delta = 25.5, 67.7$ ppm); C$_6$D$_6$ (^{1}H: $\delta = 7.20$; ^{13}C: $\delta = 128.0$ ppm); [D$_6$]DMSO (^{1}H: $\delta = 2.50$; ^{13}C: $\delta = 39.52$ ppm) or *versus* external CFCl$_3$ (^{19}F: $\delta = 0$ ppm) and *versus* external CH$_3$NO$_2$ (90% in CDCl$_3$) (^{15}N: $\delta = 380.23$ ppm). ^{15}N data are reported *versus* liquid NH$_3$ as reference ($\delta = 0$ ppm). X-band continuous wave (CW) EPR spectra were measured with a Miniscope MS 300 (Magnettech GmbH, Germany). The *g*-values are referenced to external Mn^{2+} in ZnS ($g = 2.118, 2.066, 2.027, 1.986, 1.946, 1.906$). Simulations were performed with the program package EasySpin.[46] Elemental analyses were performed by the microanalytical laboratory of the chemical institutes of the University of Mainz. ICP-MS measurements (Mo, Cu) were carried out on a HP 4500 instrument using external calibration. Density Functional Calculations were performed with the Gaussian09/DFT[42] series of programs. The B3LYP formulation of density functional theory was used with the LANL2DZ basis set. To include solvent effects, the integral equation formalism polarizable continuum model (IEFPCM, THF) was employed. No symmetry constraints were imposed on the molecules. All structures were characterized as minima by frequency analysis ($N_{imag} = 0$).

Synthesis of 1': Ligand **1'** was prepared according to reference [13] with slight modification using toluene as solvent instead of dimethylformamide. CuI (0.092 g, 0.48 mmol), *N,N*-diethylsalicylamide (0.37 g, 1.92 mmol), K$_3$PO$_4$ (4.00 g, 18.92 mmol) were dried under reduced pressure in a Schlenk flask for two hours and toluene (20 mL) was added. After stirring for 20 min 1-bromo-3,5-dimethylbenzene (1.76 g, 9.60 mmol) was added, and after additional 5 min 2,2′,2″-tris(3,5-dimethylphenylamino)-triethylamine (tren) (0.468 g, 3.20 mmol). The mixture was stirred for 7 days at 80–90°C. The reaction suspension was cooled to room temperature and water (40 mL), NH$_4$OH (20 mL, conc.) and diethylether (80 mL) were added. The mixture was extracted with diethylether (4×60 mL) and the organic layers were dried over MgSO$_4$. The product was purified via column chromatography over silica (petroleum ether / ethyl acetate with 3 vol-% methanol and 3 vol-% triethylamine) and recrystallized from petroleum ether to yield colorless crystals. Yield 1.01 g (2.20 mmol, 69%). Analytical data conform with those previously reported.[12] ^{1}H NMR ([D$_8$]THF): $\delta = 6.21$ (s, 3 H, H$_p$), 6.11 (s, 6 H, H$_o$), 4.57 (t, 3 H, $^3J_{H,H} = 5.0$ Hz, NH), 3.11 (td, 6 H, $^3J_{H,H} = 5.0$ Hz, $^3J_{H,H} = 6.0$ Hz, CH$_2$NH), 2.77 (t, 6 H, $^3J_{H,H} = 6.0$ Hz, CH$_2$N),

2.12 (s, 18 H, CH$_3$) ppm. ^{13}C{^{1}H} NMR ([D$_8$]THF): δ = 149.7 (s, C$_i$), 138.4 (s, C$_m$), 119.0 (s, C$_p$), 111.4 (s, C$_o$), 54.2 (s, CH$_2$N), 42.5 (s, CH$_2$NH), 21.5 (s, CH$_3$) ppm. ^{15}N NMR (HMBC, [D$_8$]THF): δ = 26 (N), 62 (NH) ppm. MS (FD): m/z (%) = 458.5 (100) [M]$^+$. IR (KBr): $\tilde{v}$ = 3390 (m, NH), 3340 (s, NH), 3012 (m, CH), 2941 (m, CH), 2842 (s, CH), 1607 (vs, CC), 1517 (s), 1473 (s), 1340 (s, CN), 1193 (s, CN), 1060 (m, CN), 817 (s), 690 (m) cm^{-1}.

Synthesis of P-1': Preparation according to reference [13] with slight modification using toluene as solvent instead of dimethylformamide. CuI (0.086 g, 0.45 mmol), N,N-diethylsalicylamide (0.348 g, 1.8 mmol), K$_3$PO$_4$ (3.82 g, 18.0 mmol) were dried under reduced pressure for two hours in a Schlenk flask and toluene (20 mL) was added. After stirring for 20 min 1-bromo-3,5-dimethylbenzene (1.166 g, 6.3 mmol) was added. Tris(2-aminoethyl)amine resin (0.62 mmol g^{-1}, as analyzed by nitrogen content) (5 g, 3.1 mmol) was swollen in toluene (30 mL) separately in a solid phase reaction flask for 20 min. The catalyst mixture was added to the solid phase reaction flask through a glass bridge and the reaction mixture was stirred for 21 d at 80−95°C showing a color change of the solid phase from colorless to yellow. The solid phase was washed with toluene (3×50 mL). Water (40 mL), NH$_4$OH (20 mL, conc.) and diethylether (80 mL) were added to the solid phase resulting in an immediate color change to green (resin) and blue (solution). This procedure was repeated until the solution showed no color from dissolved copper salts (5×). The solid phase remained greenish so it was washed with THF (4×40 mL), CH$_2$Cl$_2$ (4×50 mL), and CH$_3$CN (4×30 mL) under basic (1×) and slightly acidic conditions (3×) to remove traces of residual copper salts. Finally, the resin was washed with diethylether (3×75 mL) and dried under reduced pressure. To monitor the success of the arylation a small portion of the resin was treated with ninhydrin.[14,15] The absence of a blue color indicated the absence of primary amines. IR (CsI): $\tilde{v}$ = 3345 (br, NH) cm^{-1}. Elemental analysis found N 2.06% corresponding to 0.37 mmol ligand g^{-1} (based on the assumption of only mono arylated amines).

Synthesis of P-2': Polymer **P-1'** (2 g, 1.0 mmol) was swollen in toluene/THF (10:1, 55 mL) and [MoCl$_3$N(CH$_3$CN)]$_4$ (283 mg, 0.275 mmol) in THF (5 mL) was added. The resin turned light red and was stirred for 1 h at room temperature. LiNMe$_2$ (178 mg, 3.5 mmol) was added as a solid and the suspension was heated to 70 – 80°C for 4 d resulting in a dark red resin and some white LiCl precipitate on the flask wall. The resin was washed with THF (5×20 mL) until the solutions were colorless. Finally, the red resin was washed with diethylether (3×30 mL) and dried under reduced pressure at 50–100°C. IR (CsI, difference spectrum): $\tilde{v}$ = 1070 (m, Mo≡N), 1029 (m, Mo≡N) cm^{-1}. DR-UV/Vis: $\lambda \approx$ 480 nm. Mo release by ICP-MS: 0.140±0.01 mmol g^{-1}; thus not all sites are available for complexation with molybdenum due to overarylation or steric hindrance. NH$_3$ release from **P-2'** due to acidic hydrolysis with HCl (5 mL, conc. aq.), dioxane (10 mL) and H$_2$O (5 mL), measured by ^{1}H NMR spectroscopy (as NH$_4$Cl; ^{1}H NMR: δ = 7.46 ppm, t, $^1J_{^{14}N,H}$ = 50 Hz in [D$_6$]DMSO; integrated against toluene as internal standard; ^{15}N NMR: δ = 23 ppm, d, $^1J_{^{15}N,H}$ = 70 Hz): 0.135 mmol NH$_3$ g^{-1} polymer revealing an Mo:N ratio 1.03:1.

Synthesis of P-5a': A procedure according to reference [22] was adopted to prepare a [Cu(NCCH$_3$)(tren)](ClO$_4$)$_2$ complex. Cu(ClO$_4$)$_2 \times 6H_2O$ (20 mg, 0.054 mmol) was dissolved in dry THF (1 mL) in a Schlenk flask giving a blue solution which was transferred to another Schlenk flask containing the yellow resin **P-1'** (100 mg, 0.037 mmol) swollen in dry CH$_2$Cl$_2$. The color of the resin immediately changed to light green. All solvents were removed under reduced pressure and CH$_2$Cl$_2$ was added. After five minutes NEt$_3$ (25 μL diluted in 1 mL CH$_2$Cl$_2$) was added and the mixture was stirred for 20 minutes giving a dark green resin. The resin was washed with water (3×10 mL) and CH$_2$Cl$_2$ (3×10 mL) and dried under reduced pressure. The green resin was washed with dry acetonitrile (3×10 mL) and again dried under reduced pressure. IR (CsI): $\tilde{v}$ = 3269 (br. m, NH), 1102 (s, ClO$_4^-$) cm^{-1}. DR-UV/Vis: $\lambda \approx 680$ nm. EPR (solid, 295 K): g = 2.0250, 2.1250, 2.2280; A($^{63/65}$Cu) = 12, 28, 158 G. Elemental analysis calcd for an immobilized complex [Cu(NCCH$_3$)(tren)](ClO$_4$)$_2$ (0.33 mmol g^{-1}) N 2.31; found N 2.22 (= 0.31 mmol g^{-1}). Cu release from **P-5a'** in HNO$_3$ (5 mL) measured by ICP-MS: 0.295±0.01 mmol g^{-1}.

Synthesis of P-5b': Cu(NO$_3$)$_2 \times 3H_2O$ (12 mg, 0.05 mmol) was dissolved in THF (2 mL) giving a turquoise solution. The yellow resin **P-1'** (100 mg, 0.037 mmol) was added to the solution and the color of the resin immediately changed to green. The mixture was stirred for 20 minutes and the resin was washed with THF (3×10 mL) until the washing solutions were colorless. Drying of the resin under reduced pressure gave **P-5b'** as green powder. IR (CsI): $\tilde{v}$ = 3238 (w, NH), 1360 (br, NO$_3^-$) cm^{-1}. DR-UV/Vis: $\lambda \approx 680$ nm. EPR (solid, 77 K): g = 2.0450, 2.1330, 2.2400; A($^{63/65}$Cu) = 33, 15, 170 G. Cu release from **P-5b'** in HNO$_3$ (5 mL) measured by ICP-MS: 0.307±0.01 mmol g^{-1}.

EPR measurements of P-5a:

solvent, temperature	g-values	A($^{63/65}$Cu)-values
CH$_2$Cl$_2$, 295 K	2.0350, 2.1340, 2.2280	12, 28, 150 G
solid, 295 K	2.0280, 2.1400, 2.2280	15, 30, 159 G
CH$_2$Cl$_2$, 77 K	2.0250, 2.1350, 2.2290	31, 17, 158 G
solid, 77 K	2.0200, 2.1390, 2.2310	15, 30, 160 G

Table 6. EPR parameters of **P-5a** under different conditions.

EPR measurements of P-5b:

solvent, temperature	g-values	A($^{63/65}$Cu)-values
THF, 295 K	2.0400, 2.1050, 2.2250	30, 22, 147 G
petroleum ether, 295 K	2.0400, 2.1050, 2.2256	30, 15, 157 G
solid, 295 K	2.0400, 2.1050, 2.2260	30, 15, 150 G
THF, 77 K	2.0330, 2.1070, 2.2260	31, 17, 158 G
petroleum ether, 77 K	2.0480, 2.1050, 2.2262	31, 17, 157 G
solid, 77 K	2.0480, 2.1050, 2.2262	30, 15, 157 G

Table 7. EPR parameters of **P-5b** under different conditions.

Protonation of P-2': P-2' (54 mg, 7.56 µmol, 1 eq.) was weighed in a Schlenk flask. 1.4 eq. (11.4 mg, 0.0106 mmol) [2,6-lutH][Al(OC{CF$_3$}$_3$)$_4$] dissolved in THF (6 mL) were added and the mixture was stirred 3 h under dinitrogen atmosphere. The gas phase was transferred under reduced pressure into a liquid nitrogen cooled HCl/dioxane (1.5 mL, 4N) flask. The reaction mixture was washed with THF (3×5mL) and the combined washing solutions were collected in a Schlenk flask containing a mixture of THF (1 mL) and HCl (2 mL, conc. aq.). This procedure was repeated 3 times. The amount of ammonium chloride was determined by ^{1}H NMR spectroscopy using toluene (0.046±0.001 mmol) as internal standard. In the following Table 8 the results are summarized. Total yield of NH$_3$ as NH$_4$Cl: 1.31 µmol, 0.174 eq., 17%.

number of steps	NH$_3$ gas phase	estimated error (eq.)	NH$_4^+$ washing solution	estimated error (eq.)	total yield NH$_3$ + NH$_4^+$ (eq.)	estimated error (eq.)
1	0.013	0.0016	0.045	0.0032	0.058	0.0048
2	0.0	0.0	0.050	0.0027	0.108	0.0074
3	0.0	0.0	0.066	0.0023	0.174	0.0097

Table 8. Amount of isolated NH$_4$Cl in the gas and in the liquid phase for each step, and the total amount of isolated NH$_4$Cl calculated as the sum.

Protonation / reduction (method 1): P-2 (100 mg, 0.032 mmol, 1 eq.), [2,6-lutH][Al(OC{CF$_3$}$_3$)$_4$] (200 mg, 0.186 mmol, 5.8 eq.) and CoCp*$_2$ (49 mg, 0.148 mmol, 4.6 eq.) were weighed in a solid phase Schlenk flask, and petroleum ether was added under dinitrogen atmosphere. After 2 d of gently shaking the gas phase was transferred under reduced pressure into a liquid nitrogen cold trap containing HCl/dioxane (1.5 mL, 4N). The ^{1}H NMR spectrum shows essentially no NH$_4$Cl (< 1%), but the proton signals for 2,6-lutidinium chloride, which was not quantified in this step. Subsequent acidic hydrolysis of the reaction mixture with THF (20 mL), H$_2$O (5 mL) and HCl (5 mL, conc. aq.), and quantification of NH$_4$Cl and 2,6-lutidinium chloride via ^{1}H NMR spectroscopy using toluene (0.029 mmol) as internal standard revealed 0.97 eq. (0.031 mmol) NH$_4$Cl based on "MoN" and 4.44 eq. (0.142 mmol) 2,6-lutidinium chloride. In return, 1.36 eq. (5.8 eq. – 4.44 eq.) 2,6-lutidinium are consumed in the first reaction step using petroleum ether as solvent, meaning 23%, due to fast reaction between the proton source and the reducing agent.

Protonation / reduction (method 2): P-2 (100 mg, 0.032 mmol, 1 eq.) and [2,6-lutH][Al(OC{CF$_3$}$_3$)$_4$] (300 mg, 0.279 mmol, 8.73 eq.) were weighed inside the solid phase Schlenk flask, and CoCp*$_2$ (85 mg, 0.259 mmol, 8.1 eq.) was placed on the other side of the glass filter of this flask as depicted in Figure 21. Benzene was added as solvent under dinitrogen atmosphere. After 2 h of gently shaking the gas phase was transferred under reduced pressure into a liquid nitrogen cooled flask containing HCl/dioxane (1.5 mL, 4N). Quantification via ^{1}H NMR using 2,4,6-trimethylaniline (0.014 mmol) as internal standard gave 0.14 eq. (0.0044 mmol) NH$_4$Cl based on MoN and 7.32 eq. (0.234 mmol) 2,6-lutidinium chloride. Under the assumption of isolating the remaining 1.38 eq. (0.044 mmol) of the proton source by washing the reaction mixture with THF (3×20 mL) and collecting the liquid phase in HCl (3 mL, conc. aq.) additional 0.0828 eq. (0.00265 mmol) NH$_4$Cl have been isolated in the liquid phase (integration of the proton signals in the ^{1}H NMR spectrum relative to 2,6-lutidinium chloride). Total yield of NH$_3$ as NH$_4$Cl: 0.00705 mmol, 0.220 eq., 22%.

CoCp*$_2$

solid phase + proton source
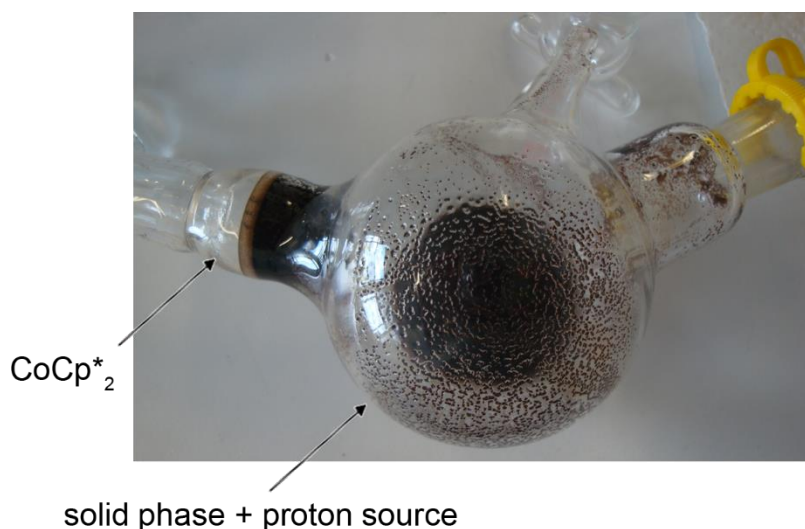
Figure 23. Picture of a solid phase reaction flask with glass filter demonstrating the spatial separation of the proton and the electron source.

Protonation / reduction (method 3): P-2' (110 mg, 0.0154 mmol, 1 eq.), [2,6-lutH][Al(OC{CF$_3$}$_3$)$_4$] (110 mg, 0.102 mmol, 6.6 eq.) and CoCp*$_2$ (33.6 mg, 0.102 mmol, 6.6 eq.) were weighed in a Schlenk flask, and a toluene/THF mixture (10:5 mL) was added under dinitrogen atmosphere. After 24 h the volatiles were transferred under reduced pressure into a cold trap containing HCl/dioxane (1.5 mL, 4N). Quantification of NH$_4$Cl and 2,6-lutidinium chloride via ^{1}H NMR spectroscopy using toluene (0.075 mmol) as internal standard: 0.084 eq. (0.0013 mmol) NH$_4$Cl based on "MoN", 5.19 eq. (0.08 mmol) 2,6-lutidinium chloride (consumption 79%). After addition of toluene/THF (10:5 mL) the reaction mixture was stirred for 27 h, and then the gas phase was transferred under reduced pressure in a nitrogen cooled HCl/dioxane flask. Quantification with toluene (0.047 mmol) yielded 0.095 eq. (0.00147 mmol) NH$_4$Cl and 0.97 eq. (0.015 mmol) 2,6-lutidinium chloride (total consumption 93%). After this step, 0.71 eq. (12 mg, 0.011 mmol) [2,6-lutH][Al(OC{CF$_3$}$_3$)$_4$], 0.75 eq. (3.9 mg, 0.012 mmol) CoCp*$_2$ and 10 mL toluene were added to the solid phase. After stirring for 48 h the gas phase was transferred under reduced pressure into a nitrogen cooled HCl/dioxane flask. Quantification with toluene (0.047 mmol) revealed 0.022 eq. (0.00034 mmol) NH$_4$Cl and 0.58 eq. (0.009 mmol) 2,6-lutidinium chloride. After this third step another 1.45 eq. (24 mg, 0.022 mmol) [2,6-lutH][Al(OC{CF$_3$}$_3$)$_4$], 1.5 eq. (7.7 mg, 0.024 mmol) CoCp*$_2$ and toluene/THF (10:5 mL) were added and the mixture was stirred for 24 h. The gas phase was again transferred under reduced pressure into a HCl/dioxane containing flask cooled by liquid nitrogen revealing 0.029 eq. (0.00045 mmol) NH$_4$Cl and 1.56 eq. (0.024 mmol) 2,6-lutidinium chloride after quantification with toluene (0.047 mmol) in the ^{1}H NMR spectra. The solid residue in the reaction was finally suspended in 15 mL THF and the washing solution was collected in an HCl (5 mL, conc. aq.) containing flask. Quantification using toluene (0.047 mmol) as internal standard in the ^{1}H NMR spectra revealed 0.150 eq. (0.00231 mmol) NH$_4$Cl. Total yield of NH$_3$ as NH$_4$Cl: 0.00587 mmol, 0.380 eq., 38%.

Protonation / reduction (method 4): P-2' (54 mg, 7.56 µmol, 1 eq.) was weighed in a Schlenk flask. First, 1.4 eq. (11.4 mg, 0.0106 mmol) [2,6-lutH][Al(OC{CF$_3$}$_3$)$_4$] dissolved in toluene THF (5:5 mL) were added and the mixture was stirred 3 h under dinitrogen atmosphere. Then, 1.4 eq. (3.5 mg, 0.0106 mmol) CoCp*$_2$ dissolved in toluene/THF (10:5 mL) were added under dinitrogen and the mixture was stirred for additional 3 h. The gas phase was transferred under reduced pressure into a liquid nitrogen cooled HCl/dioxane (1.5 mL, 4N) flask. The reaction mixture was extracted with THF (3×5mL) and the combined washing solutions were collected in a Schlenk flask containing a mixture of THF (1 mL) and HCl (2 mL, conc. aq.). This procedure was repeated 17 times. The amount of ammonium chloride was determined by ^{1}H NMR spectroscopy using toluene (0.046±0.001 mmol for steps 1−13 and 17, 0.0278±0.001 for steps 14−16) as internal standard. The results are summarized in Table 5 (page 117). The washing solutions from the 1st to the 8th step were combined and the molybdenum content was determined by ICP-MS measurements revealing 0.05952±0.0003 eq. (0.45 µmol) Mo (release of only 6% of the immobilized molybdenum).

Cartesian coordinates of 2,6-lutidine molybdenum(III) (P-VII) (B3LYP, LANL2DZ, PCM THF)

```
42    -0.306522000    -0.261978000    -0.748483000
7     -2.322195000    -0.352178000    -1.296732000
7      0.798835000    -1.883256000    -0.326959000
7      0.990285000     1.094995000    -1.590850000
7     -0.104924000    -1.140549000    -2.816150000
6     -2.570950000    -1.174994000    -2.516992000
6     -3.506590000    -0.023172000    -0.583300000
6      1.209077000    -2.761483000    -1.464188000
6      0.980559000     1.071227000    -3.081636000
6      1.980687000     1.900194000    -0.977182000
6     -1.427428000    -0.963261000    -3.508746000
6      0.230811000    -2.597851000    -2.631828000
6      0.983503000    -0.394656000    -3.540149000
1     -3.509583000    -0.873510000    -3.006014000
1     -2.675762000    -2.248696000    -2.280743000
6     -3.587990000     1.190039000     0.151852000
6     -4.663006000    -0.854627000    -0.601491000
1      1.211552000    -3.821521000    -1.157442000
1      2.237174000    -2.535180000    -1.790724000
1      1.872564000     1.557893000    -3.496185000
1      0.105924000     1.601339000    -3.488778000
6      2.511790000     1.533690000     0.287710000
6      2.470472000     3.097028000    -1.574871000
1     -1.509160000    -1.649263000    -4.367004000
1     -1.470155000     0.064859000    -3.881374000
1      0.639149000    -3.023483000    -3.562130000
1     -0.701087000    -3.122331000    -2.397515000
1      0.849485000    -0.482440000    -4.629877000
1      1.943777000    -0.846221000    -3.273532000
1     -2.735799000     1.859872000     0.132121000
6     -4.743441000     1.550224000     0.866950000
6     -5.838932000    -0.505518000     0.096300000
1     -4.648035000    -1.791671000    -1.152783000
1      2.147967000     0.625771000     0.760775000
6      3.478603000     2.318812000     0.942375000
6      3.451179000     3.888430000    -0.944279000
1      2.062247000     3.432549000    -2.525144000
6     -5.870952000     0.694859000     0.835476000
6      3.950868000     3.494803000     0.318091000
1     -6.774343000     0.973178000     1.376002000
1      4.705296000     4.103711000     0.813465000
6      3.973733000     5.145158000    -1.622706000
1      4.838959000     4.918866000    -2.263111000
1      3.208597000     5.604966000    -2.260166000
1      4.299076000     5.891080000    -0.887396000
6      3.998709000     1.902812000     2.308926000
1      3.241357000     2.069534000     3.088661000
1      4.252617000     0.835176000     2.330411000
1      4.893159000     2.471938000     2.588249000
6     -7.060594000    -1.409820000     0.031790000
1     -6.781848000    -2.467744000     0.121620000
1     -7.772999000    -1.177141000     0.831972000
1     -7.589982000    -1.295057000    -0.925363000
6     -4.782142000     2.842242000     1.667880000
1     -4.443048000     2.676398000     2.701062000
1     -4.127961000     3.605707000     1.229330000
1     -5.798432000     3.251947000     1.719904000
6      1.310549000    -2.398286000     0.965553000
1      1.044285000    -1.670449000     1.741031000
1      0.800428000    -3.343557000     1.231758000
6      2.819464000    -2.665772000     1.051516000
6      3.288147000    -3.730671000     1.854650000
6      3.769917000    -1.859577000     0.386648000
6      4.667300000    -3.977242000     2.004184000
1      2.570316000    -4.370764000     2.365592000
6      5.149024000    -2.104597000     0.528161000
1      3.428049000    -1.041434000    -0.239901000
```

```
6      5.606101000    -3.162968000     1.339526000
1      5.005825000    -4.800756000     2.629285000
1      5.864418000    -1.471487000     0.007639000
1      6.671564000    -3.351933000     1.448383000
6     -1.089066000     0.693956000     4.205896000
6     -0.702435000     1.730130000     3.345680000
6     -0.611426000     1.516197000     1.957349000
7     -0.821678000     0.263638000     1.389673000
6     -1.334689000    -0.724407000     2.233316000
6     -1.449290000    -0.531522000     3.618837000
1     -1.148817000     0.843258000     5.280021000
1     -0.491186000     2.724010000     3.730384000
1     -1.828528000    -1.347056000     4.227055000
6     -1.861201000    -2.015159000     1.646110000
1     -2.881641000    -1.858939000     1.273150000
1     -1.260872000    -2.370974000     0.806747000
1     -1.897687000    -2.794038000     2.415159000
6     -0.368004000     2.724858000     1.080519000
1      0.634576000     3.137921000     1.226813000
1     -0.473775000     2.485719000     0.021588000
1     -1.090140000     3.510024000     1.342858000
```

ACKNOWLEDGMENTS

REFERENCES

[1]   V. Smil, *Nature* **1999**, *400*, 415.

[2]   R. Schloegl, *Angew. Chem. Int. Ed*. **2003**, *42*, 2004−2008.

[3]   D. V. Yandulov, R. R. Schrock, *Science* **2003**, *301*, 76–78.

[4]   D. V. Yandulov, R. R. Schrock, *J. Am. Chem. Soc.* **2002**, *124*, 6252–6253.

[5]   D. V. Yandulov, R. R. Schrock, A. L. Rheingold, C. Ceccarelli, W. M. Davis, *Inorg. Chem.* **2003**, *42*, 796–813.

[6]   D. V. Yandulov, R. R. Schrock, *Inorg. Chem.* **2005**, *44*, 1103–1117.

[7]   K. Arashiba, Y. Miyake, Y. Nishibayashi, *Nat. Chem.* **2011**, *3*, 120–125.

[8]   J. S. Anderson, J. Rittle, J. C. Peters, *Nature* **2013**, 501, 84–88.

[9]   F. Studt, F. Tuczek, *Angew. Chem.* **2005**, *117*, 5783−5787; *Angew. Chem. Int. Ed.* **2005**, *44*, 5639−5642.

[10]   S. Schenk, B. Le Guennic, B. Kirchner, M. Reiher, *Inorg. Chem.* **2008**, *47*, 3634−3650.

[11]   R. R. Schrock, *Acc. Chem. Res*. **2005**, *38*, 955−962.

[12]   A. Wünsche von Leupoldt, C. Förster, T. J. Fiedler, N. H. Bings, K. Heinze, *Eur. J. Inorg. Chem*. **2013**, *36*, 6079−6090.

[13] F. Y. Kwong, S. L. Buchwald, *Org. Lett.* **2003**, *5*, 793−796.

[14] E. Kaiser, R. L. Colescott, C. D. Bossinger, P. I. Cook, *Anal. Biochem.* **1970**, *34*, 595–598.

[15] V. K. Sarin, S. B. H. Kent, J. P. Tam, R. B. Merrifield, *Anal. Biochem.* **1981**, *117* 147–157.

[16] K. Heinze, A. Reinhart, *Inorg. Chem.* **2006**, *45*, 2695−2703.

[17] E. Hübner, G. Türkoglu, M. Wolf, U. Zenneck, N. Burzlaff, *Eur. J. Inorg. Chem.* **2008**, 1226–1235.

[18] A. Schiller, R. Scopelliti, M. Benmelouka, K. Severin, *Inorg. Chem.* **2005**, *44*, 6482–6492.

[19] R. S. Houk, V. A. Fassel, G. D. Flesch, H. J. Svec, A. L. Gray, C. E. Taylor, *Anal. Chem.* **1980**, *52*, 2283−2289.

[20] N. H. Bings, A. Bogaerts, J. A. C. Broekaert, *Anal. Chem.* **2013**, *85*, 670−704.

[21] A. Almesåker, P. Gamez, J. L. Scott, S. J. Teat, J. Reedijk, L. Spiccia, *Eur. J. Inorg. Chem.* **2010**, 5394−5400.

[22] G. Izzet, B. Douziech, T. Prangé, A. Tomas, I. Jabin, Y. Le Mest, O. Reinaud, *Proc. Natl. Acad. Sci. USA* **2005**, *102*, 6831–6836.

[23] E. Gauch, A. Hagenbach, J. Strähle, A. Dietrich, B. Neumüller, K. Dehnicke, *Z. Anorg. Allg. Chem.* **2000**, *626*, 489–493.

[24] J. K. M. Sanders, B. K. Hunter, C. J. Jameson, G. Romeo, *Chem. Phys. Lett.* **1988**, *143*, 471−476.

[25] M. Pittelkow, T. Brock-Nannstad, J. Bendix, J. B. Christensen, *Inorg. Chem.* **2011**, *50*, 5867−5869.

[26] Y. Xia, Y. Li, A. O. Burts, M. F. Ottaviani, D. A. Tirrell, J. A. Johnson, N. J. Turro, R. H. Grubbs, *J. Am. Chem. Soc.* **2011**, *133*, 19953−19959.

[27] S. L. Regen, *J. Am. Chem. Soc.* **1974**, *96*, 5275−5276.

[28] I. M. C. van Amsterdam, M. Ubbink, G. W. Canters, M. Huber, *Angew. Chem. Int. Ed.* **2003**, *42*, 62−64.

[29] G. Jeschke, *Annu. Rev. Phys. Chem.* **2012**, *63*, 419−446.

[30] G. Jeschke, *Einführung in die ESR-Spektroskopie*, Vorlesungsskript, Universität Konstanz, **2007**.

[31] V. K. Sarin, S. B. H. Kent, R. B. Merrifield, *J. Am. Chem. Soc.* **1980**, *102*, 5463−5470.

[32] R. Santini, M. C. Griffith, M. Qi, *Tetrahedron Lett.* **1998**, *39*, 8951–8954.

[33] S. Rana, P. White, M. Bradley, *J. Comb. Chem.* **2001**, *3*, 9−15.

[34] U. Schatzschneider, T. Weyhermüller, E. Rentschler, *Eur. J. Inorg. Chem.* **2001**, 2569–2586.

[35] M. W. Weatherburn, *Anal. Chem.* **1967**, *39*, 971−974.

[36] R. R. Schrock, *Acc. Chem. Res.* **2005**, *38*, 955−962.

[37] M. Binnewies, M. Jäckel, H. Willner, C. Rayner-Canham, *Allgemeine und Anorganische Chemie*, Spektrum Akademischer Verlag, 2. Auflage, Wiesbaden, **2010**, 478f.

[38] D. V. Yandulov, R. R. Schrock, *Science* **2003**, *301*, 76–78 (supporting online material).

[39] M. Fontanet, A.-R. Popescu, X. Fontrodona, M. Rodriguez, I. Romero, F. Teixidor, C. Vinas, N. Aliaga-Alcalde, E. Ruiz, *Chem. Eur. J.* **2011**, *17*, 13217–13229.

[40] I. L. Eremenko, A. A. Pasynskii, V. T. Kalinnikov, G. G. Aleksandrov, Y. T. Struchkov, *Inorg. Chim. Acta*, **1981**, *54*, L85−L86.

[41] J. R. Hagadorn, L. Que, Jr., W. B. Tolman, *Inorg. Chem.* **2000**, *39*, 6086−6090.

[42]   M. J. Frisch, G. W. Trucks, H. B. Schlegel, G. E. Scuseria, M. A. Robb, J. R. Cheeseman, G. Scalmani, V. Barone, B. Mennucci, G. A. Petersson, H. Nakatsuji, M. Caricato, X. Li, H. P. Hratchian, A. F. Izmaylov, J. Bloino, G. Zheng, J. L. Sonnenberg, M. Hada, M. Ehara, K. Toyota, R. Fukuda, J. Hasegawa, M. Ishida, T. Nakajima, Y. Honda, O. Kitao, H. Nakai, T. Vreven, J. A. Montgomery Jr., J. E. Peralta, F. Ogliaro, M. Bearpark, J. J. Heyd, E. Brothers, K. N. Kudin, V. N. Staroverov, R. Kobayashi, J. Normand, K. Raghavachari, A. Rendell, J. C. Burant, S. S. Iyengar, J. Tomasi, M. Cossi, N. Rega, J. M. Millam, M. Klene, J. E. Knox, J. B. Cross, V. Bakken, C. Adamo, J. Jaramillo, R. Gomperts, R. E. Stratmann, O. Yazyev, A. J. Austin, R. Cammi, C. Pomelli, J. W. Ochterski, R. L. Martin, K. Morokuma, V. G. Zakrzewski, G. A. Voth, P. Salvador, J. J. Dannenberg, S. Dapprich, A. D. Daniels, O. Farkas, J. B. Foresman, J. V. Ortiz, J. Cioslowski, D. J. Fox, *Gaussian 09*, Revision A.02, Gaussian, Inc., Wallingford CT, **2009**.

[43]   I. Krossing, A. Reisinger, *Eur. J. Inorg. Chem.* **2005**, 1979–1989.

[44]   a) K. Heinze, *Chem. Eur. J.* **2001**, *7*, 2922–2932; b) K. Heinze, J. D. Bueno Toro, *Angew. Chem.* **2003**, *115*, 4671–4674; *Angew. Chem. Int. Ed.* **2003**, *42*, 4533–4536; c) K. Heinze, V. Jacob, C. Feige, *Eur. J. Inorg. Chem.* **2004**, 2053–2061; d) K. Heinze, J. D. Bueno Toro, *Eur. J. Inorg. Chem.* **2004**, 3498–3507.

[45]   K. Seyferth, R. Taube, *J. Organomet. Chem.* **1982**, *229*, C19–C23.

[46]   S. Stoll, A. Schweiger, *J. Magn. Reson.* **2006**, *178*, 42–55.

3.4 Effect of Chelate Ring Expansion on Jahn–Teller Distortion and Jahn–Teller Dynamics in Copper(II) Complexes

Katharina Mack[a], Anica Wünsche von Leupoldt[a], Christoph Förster[a], Maria Ezhevskaya[b], Dariush Hinderberger[b], Karl W. Klinkhammer[a], and Katja Heinze[a]*

[a] Institute of Inorganic Chemistry and Analytical Chemistry, Johannes Gutenberg-University of Mainz, Duesbergweg 10-14, 55128 Mainz, Germany

[b] Max Planck Institute for Polymer Research, Ackermannweg 10, 55128 Mainz, Germany

ABSTRACT

The expanded ligand *N,N'*-dimethyl-*N,N'*-dipyridin-2-yl-pyridin-2,6-diamine (ddpd) coordinates to copper(II) ions in a meridional fashion giving the dicationic complex *mer*-[Cu(ddpd)$_2$](BF$_4$)$_2$ (**1**). In the solid state at temperatures below 100 K the cations of **1** localize in Jahn–Teller elongated CuN$_6$ polyhedra with the longest Cu–N bond pointing in the molecular *x* or *y* directions while the *z* axis is constrained by the tridentate ddpd ligand. The elongated polyhedra are ordered in an antiferrodistortive way giving an idealized zincblende structure. At higher temperature dynamically averaged (fluxional) polyhedra in the molecular *x*/*y* directions are observed by multifrequency variable temperature EPR and by variable temperature X-ray diffraction studies. Compared to [Cu(tpy)$_2$]$^{2+}$ (tpy = 2,2′;6′,2″-terpyridine) the Jahn–Teller splitting $4\delta_1$ of **1** is larger. This is very probably caused by the much more favorable orbital overlap in the Cu–N bonds in **1** which results from the larger bite angle of ddpd as compared to tpy. The "freezing-in" of the Jahn–Teller dynamics of **1** ($T \approx 100$ K) occurs at higher temperature than observed for [Cu(tpy)$_2$]$^{2+}$ ($T < 77$ K) which is also probably due to the larger Jahn–Teller distortion of **1** resulting in a larger activation barrier.
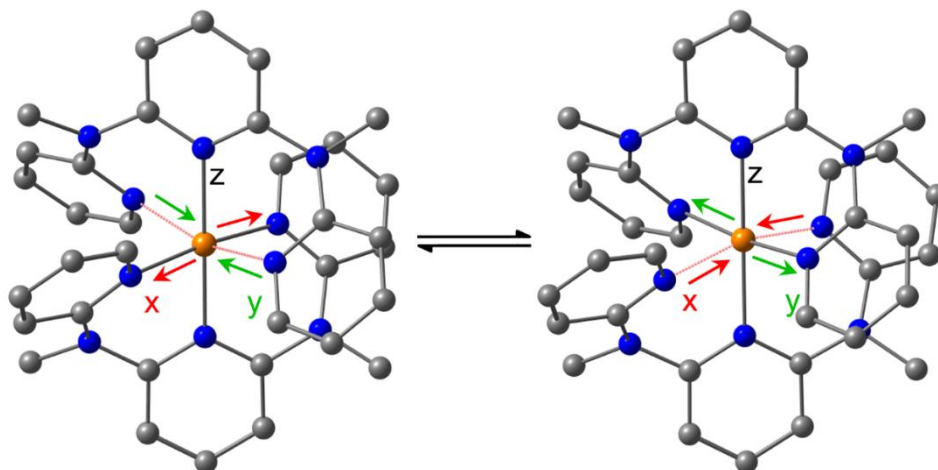
1. INTRODUCTION

The Jahn–Teller theorem states that an orbital electronic degenerate system is unstable with respect to nuclear displacement.[1] For six-coordinate copper(II) complexes $Cu^{II}L_6$ octahedral symmetry results in a $^2E_{2g}$ ground state which is subject to a Jahn–Teller distortion induced by the $E_g \otimes \varepsilon_g$ vibronic coupling, where ε_g is the Jahn–Teller active vibrational mode (Figure 1).[2–5] Octahedral symmetry is reduced via the tetragonal $Q_\theta = \rho \cos \phi$ and orthorhombic $Q_\varepsilon = \rho \sin \phi$ components of this ε_g vibrational mode (Figure 1a) giving rise to three equivalent minima at $\phi = 0°$, 120° and 240° representing tetragonal elongated octahedra along the molecular z, y and x axes, respectively.[2–6] The circular section of the ground state potential surface of the Mexican hat potential (Figure 1b) given by ϕ is depicted in Figure 1c (upper graph).[2–5] If the octahedron is subject to strain effects acting parallel to the z axis, for example, by rigid chelate ligands or crystal packing, the potential surface distorts (Figure 1c, lower graph). Tridentate meridional coordinating ligands like 2,2′;6′,2″-terpyridine (tpy) enforce the central Cu–N bond (along the molecular z axis) to be short and hence only two low-energy minima remain with elongation along the molecular x or y axes (Chart 1, left).[2–5]
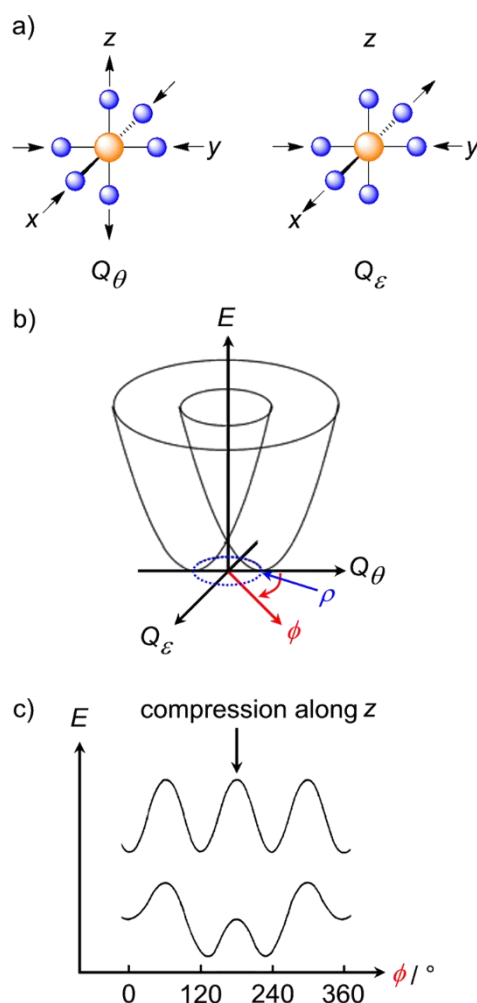
Figure 1. (a) Illustration of the tetragonal and orthorhombic components Q_θ, Q_ε of the Jahn–Teller active vibrational mode ε_g; (b) potential energy surface of a $Cu^{II}L_6$ system; (c) circular cross section along the angular coordinate ϕ in the absence and in the presence of strain along the z axis.[8]

In several cases the energy required to overcome the saddle point between the two minima with elongated octahedra (along x or y) is relatively small so that at moderate temperatures a dynamically averaged polyhedron is observed with a tetragonally compressed z axis. At low temperatures the fluxional process "freezes in" and the two elongated polyhedra are formed in equal amounts. Frequently, these elongated polyhedra arrange in an antiferrodistortive, that is, alternating manner, in the crystalline state.[7]

In the prototypical well-studied complexes $[Cu(tpy)_2](X)_2$ pseudocompressed polyhedra are observed by X-ray crystal structure determination at higher temperature ($2\times Cu–N \approx 1.995$ Å and $4\times Cu–N \approx 2.15$ Å). The radial and angular distortion is determined as $\rho \approx 0.27$ Å and $\varphi \approx 150°$ reflecting both the Jahn–Teller averaging and the ligand strain.[8–11] The X-band powder electron paramagnetic resonance (EPR) spectra (microwave frequency ≈ 9.4 GHz) show a pattern of an axially compressed octahedron with $g_x \approx g_y \approx 2.191 > g_z \approx 2.023$ at higher temperature ($T = 298$ K). The finer details of the structural data and the g values depend somewhat on the counterions X and the presence of crystal solvent

molecules.[8] At lower temperature the typical EPR spectra of elongated polyhedra are detected for $[Cu(tpy)_2](X)_2$ complexes ($T = 4$ K: $g_x \approx 2.26$, $g_y \approx 2.129$ and $g_z \approx 2.020$).[8] Genuine compressed CuL_6 polyhedra are quite uncommon, reported examples being (3-chloroanilinium)$_8$[CuCl$_6$]Cl$_4$ featuring an EPR spectrum of an axially compressed octahedron with $g_x \approx g_y \approx 2.19 > g_z \approx 2.06$ and [Cu(*fac*-HC(P(O)Ph$_2$)$_3$)$_2$]$^{2+}$ featuring two short and four long Cu–O bonds (2×1.94 Å; 2×2.14 Å; 2×2.15 Å), although all these measurements have been performed at room temperature and thus dynamic effects might also be operative.[12,13]

The ligand field splitting in $[Cu(tpy)_2]^{2+}$ amounts to $\Delta_o = 11200–11300$ cm^{-1} also slightly depending on the counterion.[3a] The Jahn–Teller splitting, that is, the splitting of the $^2E(d_{z^2-y^2}, d_{x^2})$ ground state into $_a{}^2A_1$ and $_b{}^2A_1$ states has been determined as $4\delta_1 = 5900–6550$ cm^{-1} again slightly modulated by the counterion and the crystal packing.[3a]

Recently, we successfully employed the ligand *N,N′*-dimethyl-*N,N′*-dipyridin-2-yl-pyridin-2,6-diamine (ddpd) for complexation of ruthenium(II)[14] with the aim of increasing the ligand field splitting (as compared to tpy) to boost photophysical properties by increasing the energy of deactivating ligand field states.[15] This aim was achieved by the larger bite angle of ddpd (almost 90°) in the six-membered chelate rings in comparison with that of tpy (78°, five-membered chelate rings). This increases the orbital overlap of metal and ligand orbitals which is especially pronounced in the M-L σ bonds.

Here, we study the influence of the increased bite angle of ddpd on the ligand field splitting, on the Jahn–Teller distortion and on the Jahn–Teller dynamics of the homoleptic ddpd copper(II) complex $[Cu(ddpd)_2]^{2+}$ as compared to the analogous benchmark terpyridine copper(II) complex $[Cu(tpy)_2]^{2+}$ (Chart 1).
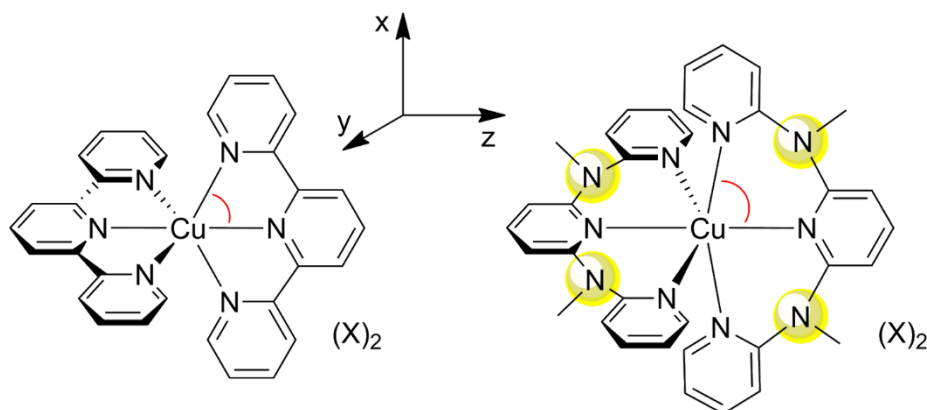
Chart 1. $[Cu(tpy)_2](X)_2$ and $[Cu(ddpd)_2](X)_2$ Complexes Relevant to This Study

2. EXPERIMENTAL SECTION

All reagents were used as received from commercial suppliers (ABCR, Acros, Sigma-Aldrich). The ddpd ligand was prepared according to the literature procedure.[14] IR spectra were recorded with a BioRad Excalibur FTS 3100 spectrometer as CsI disks. (vs) = very strong, (s) = strong, (m) = medium, (w) = weak. Electrochemical experiments were carried out on a BioLogic SP-50 voltammetric analyzer using a glassy carbon working electrode, a platinum wire as counter electrode, and a 0.01 M Ag/AgNO$_3$ electrode as reference electrode. The measurements were carried out at a scan rate of 100 mV s^{-1} for cyclic voltammetry experiments and at 10 mV s^{-1} for square wave voltammetry experiments using 0.1 M (nBu$_4$N)(PF$_6$) as supporting electrolyte in CH$_3$CN. Potentials are given relative to the ferrocene/ferrocenium couple. UV/Vis/NIR spectra were recorded on a Varian Cary 5000 spectrometer using 1.0 cm cells (Hellma, suprasil). Electrospray ionization (ESI) mass spectra were recorded on a Micromass Q-TOF-Ultima spectrometer. X-band CW EPR spectra (9.4 GHz) were measured on a Miniscope MS 300 (Magnettech GmbH, Germany). g-values are referenced to external Mn^{2+} in ZnS (g = 2.118, 2.066, 2.027, 1.986, 1.946, 1.906). X-band pulsed EPR experiments (9.4 GHz) were performed on a Bruker Elexsys 580 spectrometer, equipped with a helium-gas flow cryostat (Oxford Inc.) at 10 K. Davies ENDOR (electron nuclear double resonance) experiments were performed using the microwave pulse sequence $\pi - T - \pi/2 - \tau - \pi - \tau -$ echo, with a π radio frequency (rf) pulse applied during time T. The parameters used were t_π = 200 ns, $t_{\pi/2}$ = 100 ns, T = 12 μs, t_{rf} = 10 μs. Standard HYSCORE (hyperfine sublevel correlation) experiments were performed using the $\pi/2 - \tau - \pi/2 - t1 - \pi - t2 - \pi/2 - \tau -$ echo sequence with $t_{\pi/2}$ = 16 ns and t_π = 16 ns and τ = 200 ns, 256 ns. The time intervals $t1$ and $t2$ were varied in steps of 16 ns. W-band EPR experiments (94 GHz) were performed on a Bruker Elexsys 680 spectrometer equipped with a helium-gas flow cryostat at 50, 150, and 293 K. Simulations were performed with the program package EasySpin.[16] Melting points were determined using a Gallenkamp capillary melting point apparatus MFB 595 010 and were not corrected. Variable-temperature magnetic susceptibility measurements were carried out with a Quantum Design MPMS-XL7 SQUID magnetometer in the temperature range 2–300 K under an applied magnetic field of 1 T. Experimental susceptibility data were corrected for diamagnetic contributions of the sample holder and the underlying diamagnetism using Pascal's constants. Differential scanning calorimetry (DSC) was performed using a Mettler Toledo 30. DSC curves were recorded in the temperature range from –150 to –10°C using a heating and cooling rate of 10 K min^{-1}. Samples were surrounded by a flow of nitrogen gas (30 mL min^{-1}). The sample volume was 40 μL. Atomic Absorption Spectroscopy was performed using a Perkin-Elmer 510 ZL with a Zeeman furnace module. Elemental analyses were performed by the microanalytical laboratory of the chemical institutes of the University of Mainz.

Crystal Structure Determination. Intensity data were collected with a Bruker AXS Smart1000 CCD diffractometer with an APEX II detector and an Oxford cooling system and corrected for absorption and other effects using Mo K_α radiation (λ = 0.71073 Å). The diffraction frames were integrated using the

SAINT package, and most were corrected for absorption with MULABS.[17,18] The structures were solved by direct methods and refined by the full-matrix method based on F^2 using the SHELXTL software package.[19,20] All nonhydrogen atoms were refined anisotropically, while the positions of all hydrogen atoms were generated with appropriate geometric constraints and allowed to ride on their respective parent carbon atoms with fixed isotropic thermal parameters. The asymmetric unit of a crystal of **1** contains one molecule of an acetonitrile solvent molecule and a disordered $[BF_4]^-$ counterion. Crystallographic data (excluding structure factors) for the structure reported in this paper have been deposited with the Cambridge Crystallographic Data Centre as supplementary publication nos. CCDC-874634 (263 K) and CCDC-874635 (123 K). Copies of the data can be obtained free of charge upon application to CCDC, 12 Union Road, Cambridge CB2 1EZ, U.K. [fax (0.44) 1223-336-033; e-mail deposit@ccdc.cam.ac.uk].

Density functional theory (DFT) calculations were carried out with the Gaussian09/DFT[21] series of programs. The B3LYP formulation of DFT was used by employing the LANL2DZ basis set.[21] No symmetry constraints were imposed on the molecules. The presence of energy minima or first order saddle points was checked by analytical frequency calculations. For calculations of EPR parameters the EPR-II basis set[21b] was used for C, H, N and the 6-311G(d) basis set for Cu. For time-dependent DFT (TD-DFT) calculations solvent modeling was also included employing the integral equation formalism polarizable continuum model (IEFPCM, acetonitrile).

Synthesis of 1. Copper(II) bis(tetrafluoroborate) hexahydrate (528 mg, 1.529 mmol) was dissolved in ethanol (12 mL), and ddpd (980 mg, 3.364 mmol) was dissolved in ethanol (18 mL). Upon mixing the solutions at room temperature a light-green suspension formed. After stirring for 2 h at room temperature diethylether (50 mL) was added. The precipitate was filtered and washed with diethylether (30 mL). After recrystallization from ethanol/diethylether a light-green solid was obtained in 68% yield (964 mg, 1.039 mmol). Recrystallization from acetonitrile yielded crystals suitable for X-ray diffraction.
Anal. Calcd for $C_{34}H_{34}N_{10}B_2F_8Cu$ (819.86): C, 49.81; H, 4.18; N, 17.08. Found: C, 49.27; H, 4.07; N, 17.17. MS (ESI): m/z = 354.07 (100, $[M-ddpd-2(BF_4)]^{•+}$), 373.08 (50, $[M-ddpd-2(BF_4)+F]^{•+}$). SQUID: χT = 0.443 cm^3 K mol^{-1} (4–300 K). X-band EPR (powder, 295 K, 9.42 GHz): $g_x \approx g_y$ = 2.150, g_z = 2.066, $A_x \approx A_y(^{63/65}Cu)$ = 82 G. X-band EPR (powder, 103 K, 9.43 GHz): g_x = 2.228, $g_y \approx g_z$ = 2.054, and $A_x(^{63/65}Cu)$ = 145 G. UV/Vis (CH$_3$CN): λ (ε) = 240 nm (32000 M^{-1} cm^{-1}), 309 (29000), 433 (140), 657 (25), 1287 (5); by Gaussian fitting the two LF transitions are found at 653 nm (15308 cm^{-1}) and 1254 nm (7973 cm^{-1}). IR (CsI): $\tilde{v}$ = 3120 (w, CH), 2924 (w, CH), 1597 (s), 1490 (s), 1450 (s), 1435 (vs), 1365 (s), 1340 (s), 1238 (s), 1170 (s), 1134 (s), 1095 (s), 1061 (vs), 1034 (sh, BF), 947 (w), 868 (w), 806 (w), 781 (m), 750 (m), 617 (w), 584 (w), 522 (w), 437 (w), 413 (w) cm^{-1}. CV (CH$_3$CN, vs FcH/FcH$^+$): E_p = –0.91 V (irreversible reduction), –0.65 V (reoxidation of the derived Cu^I species). Mp = 168°C (dec).

Synthesis of 2. Copper(II) bis(tetrafluoroborate) hexahydrate (8.2 mg, 0.024 mmol) and iron(II) bis(tetrafluoroborate) hexahydrate (148.5 mg, 0.440 mmol) were dissolved in ethanol (5 mL), and ddpd (305 mg, 1.050 mmol) was dissolved in ethanol (5 mL). Upon mixing the solutions at room temperature an orange-red suspension formed. After stirring for 2 h at room temperature diethylether (25 mL) was added. The dark red precipitate was filtered and washed with diethylether (25 mL). A dark-red solid was obtained in 95% yield (360 mg, 0.443 mmol). $C_{34}H_{34}N_{10}B_2F_8Cu_{1-x}Fe_x$, $x = 0.125$ from AAS measurements. X-band EPR (powder, 295 K, 9.42 GHz): $g_x \approx g_y = 2.156$, $g_z = 2.058$, $A_x \approx A_y(^{63/65}Cu) = 79$ G. X-band EPR (powder, 103 K, 9.42 GHz): $g_x = 2.228$, $g_y \approx g_z = 2.063$, and $A_x(^{63/65}Cu) = 146$ G.

3. RESULTS AND DISCUSSION

The infrared spectrum of **1** is unremarkable showing the absorption of the BF stretch of the counterion at 1034 cm^{-1}, the absorptions of the C=C and C=N vibrations of the ligand around 1597 and 1490 cm^{-1} as well as the signature of CH stretching vibrations around 3120 cm^{-1} (aromatic CH) and 2924 cm^{-1} (aliphatic CH). **1** can be irreversibly reduced to a copper(I) complex at –0.91 V vs. FcH/FcH$^+$. The magnetic susceptibility of **1** was measured in the temperature range 2–300 K giving a temperature independent magnetic moment of $\chi T = 0.443$ cm^3 K mol^{-1} ($T > 4$ K) independent of the heating or cooling mode (Figure 2). For an $S = 1/2$ system the expected spin-only value amounts to $\chi T = 0.375$ cm^3 K mol^{-1} indicating that spin-orbit coupling is operative for **1** as expected ($g_{iso} \approx 2.17$, from SQUID measurement).[22] Below 4 K a weak antiferromagnetic interaction is observed (Figure 2).
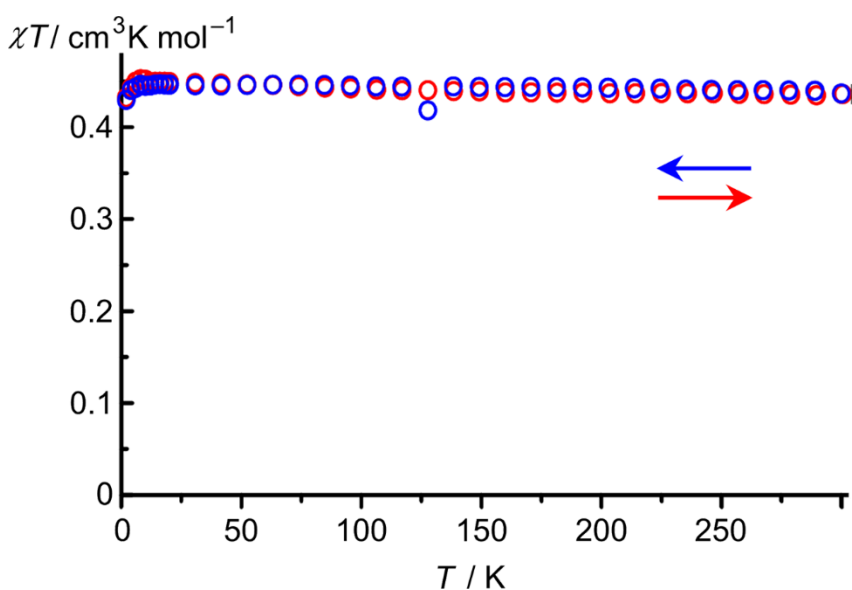
Figure 2. Variable-temperature magnetic susceptibility measurements of **1**.

Optical spectra of **1** were measured in acetonitrile (Figure 3). Intense ligand-centered π–π^* absorptions are found at 240 nm ($\varepsilon = 32000$ M^{-1} cm^{-1}) and 309 nm ($\varepsilon = 29000$ M^{-1} cm^{-1}) and a moderately intense ligand-to-metal charge transfer band is located at 433 nm ($\varepsilon = 140$ M^{-1} cm^{-1}; N–CH$_3$ lone pair $\rightarrow$ half-filled Cu d orbital). By Gaussian fitting of the spectrum two ligand field transitions are observed at 653 nm ($\varepsilon = 25$ M^{-1} cm^{-1}) and 1254 nm ($\varepsilon = 5$ M^{-1} cm^{-1}), the former bands (433 nm and 653 nm) accounting for the light green color of **1** (Figure 3; the Gaussian fits including all absorption bands slightly deviate from the maxima determined directly from the spectrum). If in the Jahn–Teller distorted case the symmetry of the dication is lowered to C_{2v} as in [Cu(tpy)$_2$]$^{2+}$ and the Jahn–Teller axis is assigned to the x axis a term sequence $_a{}^2A_1$ (z^2–y^2), $_b{}^2A_1$ (x^2), $^2B_2$ (yz), $^2B_1$ (xz), $^2A_2$ (xy) is expected (Figure 3).[8] The observed ligand field transitions can be assigned to the symmetry allowed transitions in the C_{2v} point group $_a{}^2A_1$ (z^2–y^2) $\rightarrow$ $^2B_2$ (yz)/$^2B_1$ (xz) and $_a{}^2A_1$ (z^2–y^2) $\rightarrow$ $_b{}^2A_1$ (x^2) (Figure 3; the $_a{}^2A_1$ (z^2–y^2) $\rightarrow$ $^2A_2$ (xy) transition is symmetry forbidden).[8] The energy of the latter absorption band corresponds to the Jahn–Teller splitting $4\delta_1 = 7975$ cm^{-1} and together with the former absorption band the ligand field splitting is estimated as $\Delta_o = 11325$ cm^{-1}.
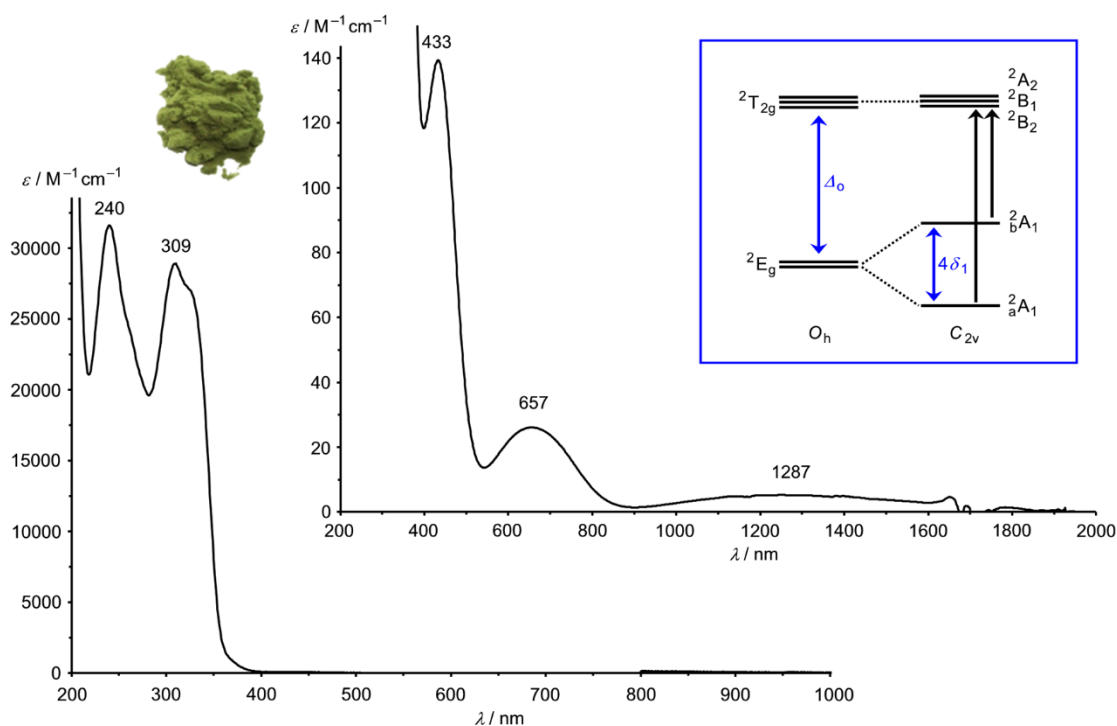
Figure 3. Electronic spectrum of **1** in CH$_3$CN (inset: ligand field region and term diagram in C_{2v} symmetry).

The significantly larger Jahn–Teller splitting of **1** is accounted for by a stronger σ-type interaction of ddpd with the copper center and thus an increased energy gain by Jahn–Teller distortion as compared to tpy complexes. This effect has already been predicted by Jahn and Teller in their seminal paper ("If the electrons causing the degeneracy are not essential for molecular binding, only a slight instability will result.").[1] Vice versa, the stronger σ antibonding electrons in the "e$_g$" set of **1** result in a more

pronounced Jahn–Teller splitting $4\delta_1$ as compared to the less antibonding "e_g" electrons of $[Cu(tpy)_2]^{2+}$ complexes with smaller bite angles.

At 103 K the X-band powder EPR spectrum of **1** displays the expected axial pattern with $g_x = 2.228$, $g_y \approx g_z = 2.054$, and $A_x(^{63/65}Cu) = 145$ G (Figure 4, top). These g values are comparable to those of $[Cu(tpy)_2](PF_6)_2$ at 4.2 K ($g_x \approx 2.26$, $g_y = 2.129$ and $g_z = 2.020$.[8] In accordance with the larger energies of the ligand field absorption bands of **1** the averaged orbital contribution to the g_{iso} value is smaller ($g_{iso} - g_e = 0.114$) than for $[Cu(tpy)_2](PF_6)_2$ ($g_{iso} - g_e = 0.139$).[3a] Upon being warmed to 293 K, the powder EPR spectrum of **1** gradually evolves into a spectrum of an axially compressed octahedron with $g_x \approx g_y = 2.150$, $g_z = 2.066$ and $A_x \approx A_y(^{63/65}Cu) = 82$ G (Figure 4, bottom and Figure 5). The g values are again comparable to those of $[Cu(tpy)_2](PF_6)_2$ at 298 K ($g_x = g_y = 2.191$, $g_z = 2.023$).[8] Obviously, for both copper(II) complexes g_z remains essentially unaffected reflecting the ligand-strain induced compression along z while g_x and g_y gradually converge to a common value upon increasing the temperature.
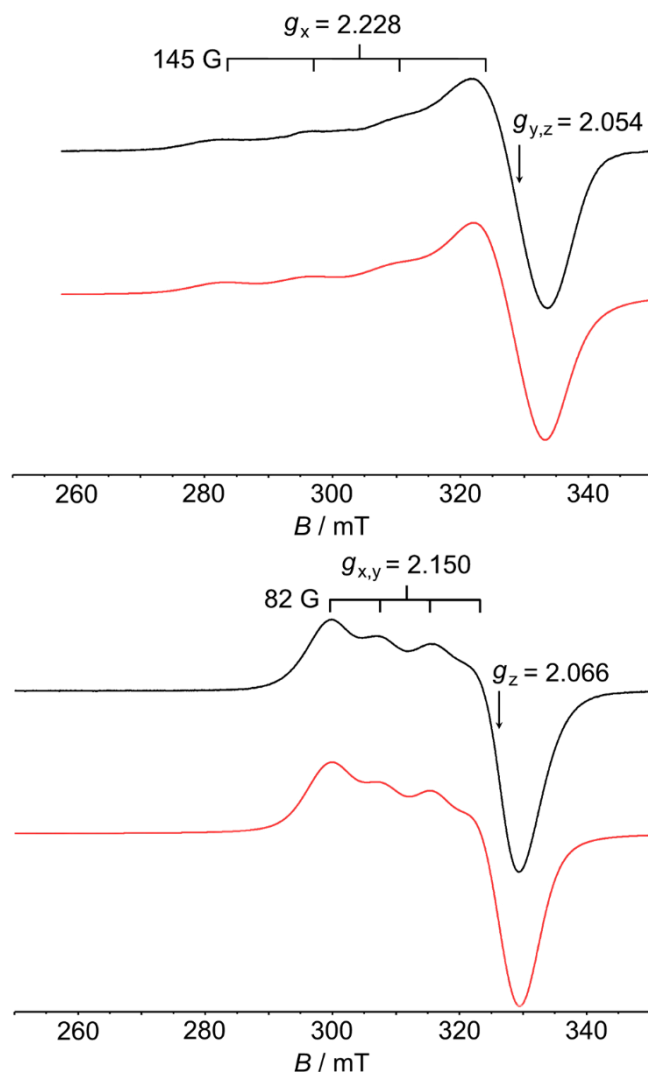
Figure 4. X-band powder EPR spectra of **1** (9.42 GHz) at 103 K (top) and 293 K (bottom) and simulated spectra in red.[16]

145
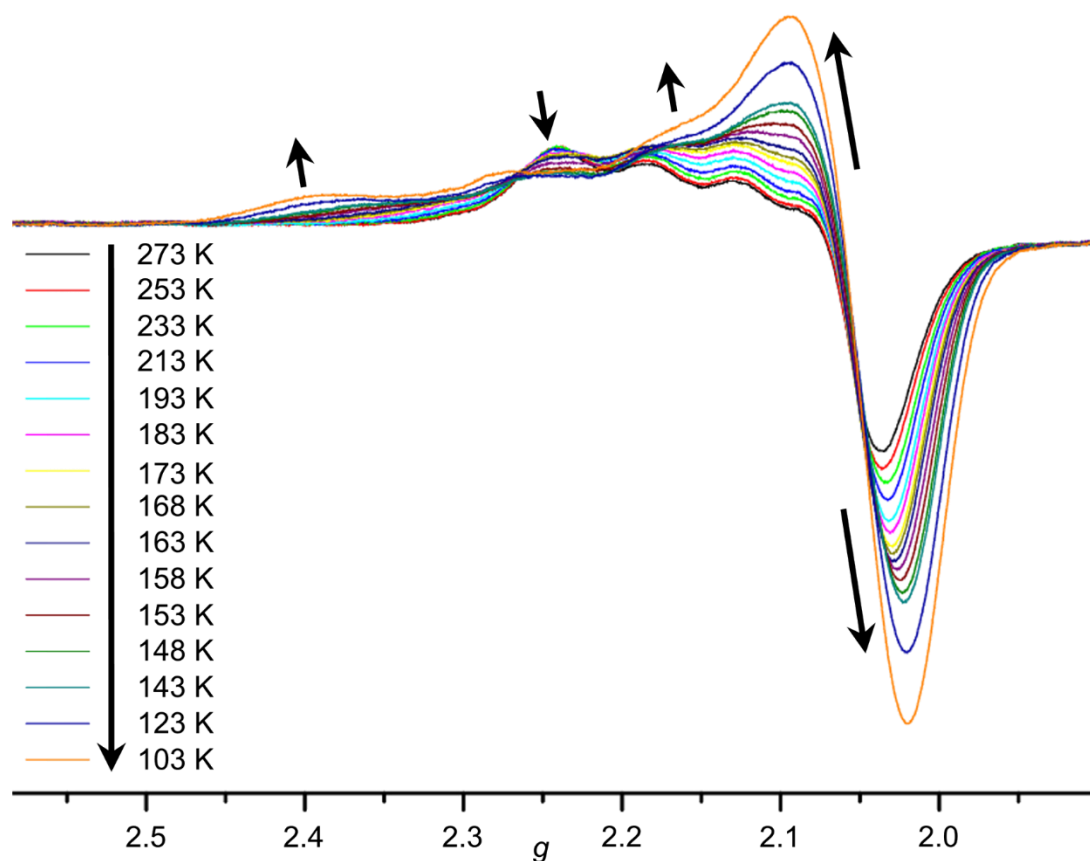
Figure 5. Variable temperature X-band EPR spectra of **1** indicating the evolution of the spectra with temperature ($T = 273–103$ K).

The spectra obtained in the temperature range 103–273 K could be successfully simulated by weighted superpositions of low-temperature and high-temperature spectra (see Supporting Information for selected spectra and their simulations). If one assigns the low-temperature EPR spectrum (Figure 4, top) to the static elongated complexes and the high-temperature spectrum to the dynamic, that is, rapidly interconverting elongated complexes on the EPR time scale (Figure 4, bottom), one can extract the molar fraction of static and (on the EPR time-scale) dynamic complexes present at different temperatures. A continuous transition from the static to the dynamic regime is observed implying only weak, if any, cooperative effects (Figure 6). The absence of exchange coupling between the neighboring paramagnetic centers in this temperature regime (Figure 2) further supports practically vanishing cooperative forces. The critical temperature at which approximately 50% of the complexes are dynamic on the X-band EPR time scale is estimated as $T_{1/2} = 170 \pm 10$ K.
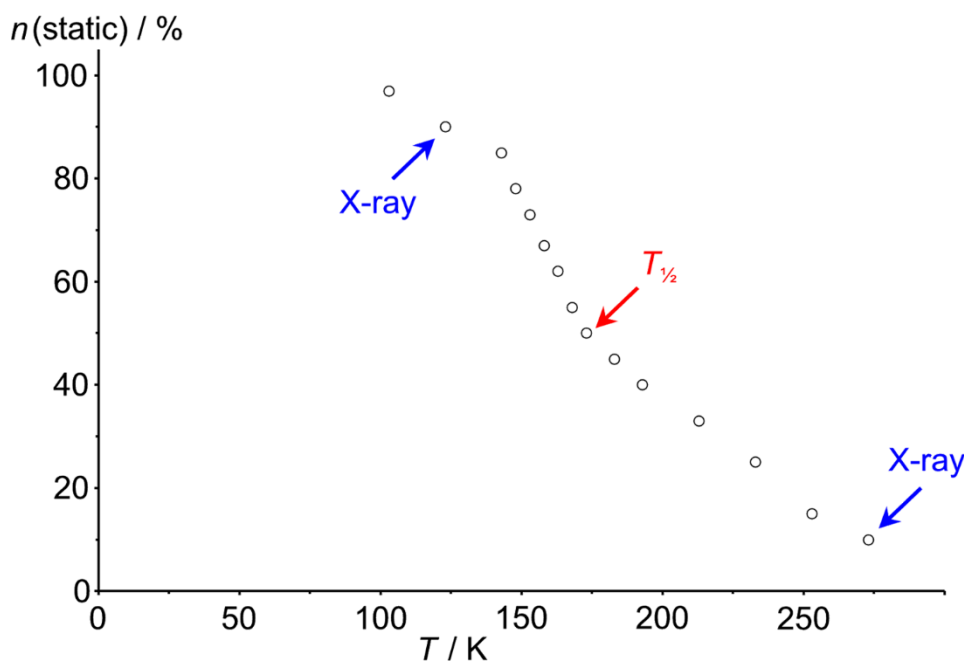
Figure 6. Molar fraction of static complexes **1** extracted from variable temperature X-band EPR spectra.

To diminish intermolecular dipole dipole interactions and thus to improve the resolution of the EPR spectra the copper(II) ddpd complex **1** was doped into the diamagnetic isomorphous iron(II) ddpd complex host lattice giving the magnetically dilute material [Fe$_{1-x}$Cu$_x$(ddpd)$_2$](BF$_4$)$_2$ (**2**, x = 0.125 by atomic absorption spectroscopy).[23] The resulting variable temperature EPR spectra of **2** are indeed of higher resolution (Figure 7 and Supporting Information). The extracted parameters are basically similar to those of pure **1** (T = 103 K: g_x = 2.228, g_y = g_z = 2.063 and A_x($^{63/65}$Cu) = 146 G; T = 295 K: g_x = g_y = 2.156, g_z = 2.058 and A_x = A_y($^{63/65}$Cu) = 79 G). The critical temperature of the transition from the dynamic to the static regime is $T_{1/2}$ = 190 ± 10 K, practically identical to $T_{1/2}$ of **1** within experimental error again arguing against significant cooperative forces (see Supporting Information).

When a frozen solvent mixture (water/glycerol) was used as a matrix for **1**, a fully analogous behavior was observed (see Supporting Information; resolution is somewhat poorer) suggesting that the observed dynamics is mainly a molecular phenomenon and largely independent of the surrounding matrix (crystal, diamagnetic host, frozen solution).
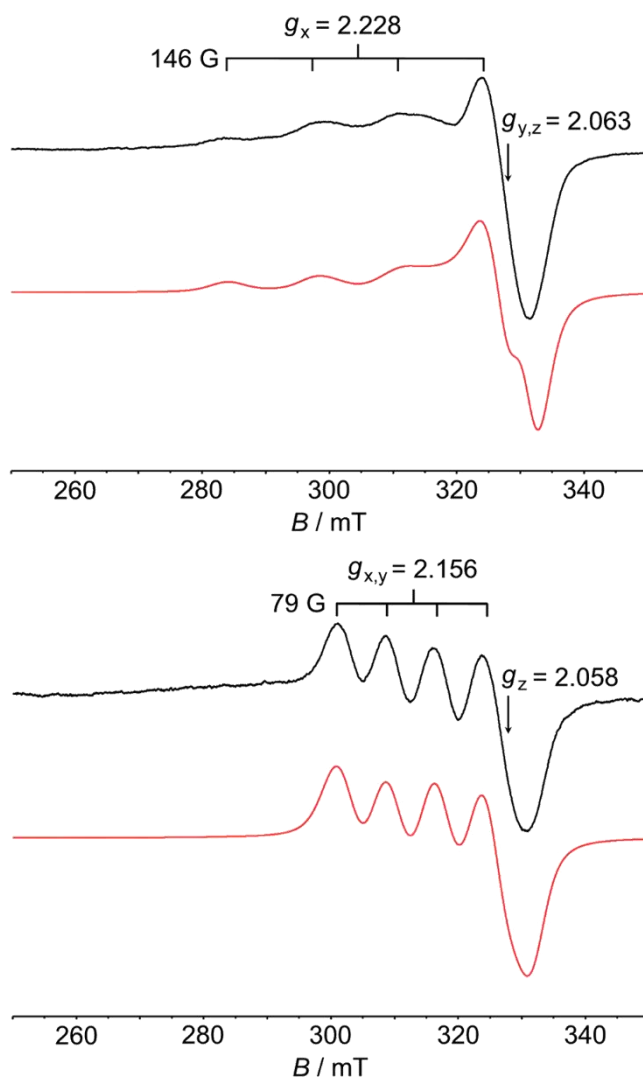
Figure 7. X-band powder EPR spectra of **2** (9.42 GHz) at 103 K (top) and 293 K (bottom) and simulated spectra in red.[16]

DSC on powdered **1** in the temperature range 123–263 K revealed a small broad endothermic feature between 140 and 180 K (see Supporting Information) which is obviously associated with the process observed by EPR. A detailed molecular view could be obtained by variable temperature X-ray diffraction studies. A single crystal of **1** was subjected to X-ray diffraction at 123 K and at 263 K (Table 1). Both structures could be solved and refined as racemic twins in the orthorhombic space group *Fdd*2 (Figure 8). At low temperature the C_2 symmetric complex cations (C_2 axis through N3–Cu–N6) form tetragonal elongated CuN$_6$ octahedra with long Cu–N4 (2.332(16) Å) and short Cu–N1 (2.026(15) Å) bonds to the terminal pyridine rings and short Cu–N3/N6 bonds (1.989(3) Å, 2.060(3) Å) to the central pyridine rings (Figure 8, bottom). The radial distortion $\rho = 0.355$ Å is large and similar to the ones calculated for [Cu(tpy)$_2$](X)$_2$.[8] The N1–Cu–N3 bite angle amounts to 86.06(5)° while the N4–Cu–N6 bite angle involving the Jahn–Teller elongated Cu–N4 bonds amounts to 80.03(4)°. The N4–Cu–N4′ angle (160.06(8)°) deviates more from the ideal 180° angle than the N1–Cu–N1′ angle with 172.12(9)°. The angular distortion is estimated as $\varphi = 120°$.

Table 1. Data of the Crystallographic Structure Determinations.

	1 / 263 K	**1** / 123 K
empirical formula	$C_{38}H_{40}CuN_{12}B_2F_8$	$C_{38}H_{40}CuN_{12}B_2F_8$
formula weight	901.98	901.98
crystal color, habit	yellow block	yellow block
crystal dimensions / mm	$0.25 \times 0.22 \times 0.20$	$0.25 \times 0.22 \times 0.20$
crystal system	orthorhombic	orthorhombic
space group	$Fdd2$	$Fdd2$
a / Å	26.412(4)	25.9249(12)
b / Å	21.696(3)	21.4550(9)
c / Å	14.123(2)	14.0455(6)
V / Å^3	8093(2)	7812.4(6)
Z	8	8
$F(000)$	3704	3704
density (calcd) / g cm^{-3}	1.481	1.534
absorption coefficient μ / mm^{-1}	0.623	0.645
2θ range / deg	3.78–55.70	4.92–56.10
index ranges	$-34 \le h \le 34$	$-34 \le h \le 34$
	$-28 \le k \le 28$	$-26 \le k \le 28$
	$-18 \le l \le 18$	$-18 \le l \le 18$
reflections collected	27532	13479
independent reflections	4796	4725
parameters	300	299
max./min. transmission	0.8855/0.8598	0.8818/0.8553
goodness-of-fit on F^2	0.940	0.991
largest difference peak and hole/e Å^{-3}	0.281/–0.184	0.342/–0.313
R_1 ($I > 2\sigma(I)$)	0.0344	0.0280
R_1 (all data)	0.0541	0.0325
wR_2 ($I > 2\sigma(I)$)	0.0809	0.0648
wR_2 (all data)	0.0871	0.0660
absolute structure parameter	0.503(19)	0.568(8)

In the crystal packing CuN_6 cations with the long axis in the molecular x direction occupy the lattice sites of an fcc close-packing (idealizing the orthorhombic crystal system to cubic) while complex cations with the long axis in the molecular y direction occupy one-half of the tetrahedral sites giving an overall approximate zincblende structure, that is, each CuN_6 elongated polyhedron is surrounded by four CuN_6 elongated polyhedra of the other Jahn–Teller axis orientation (Figure 9). These two sublattices are canted by $\approx 72°$ approaching an antiferrodistortive limiting case (90°) which is typically observed, for example, for tetrachlorocuprates like $(NH_4)_2[CuCl_4]$.[24]
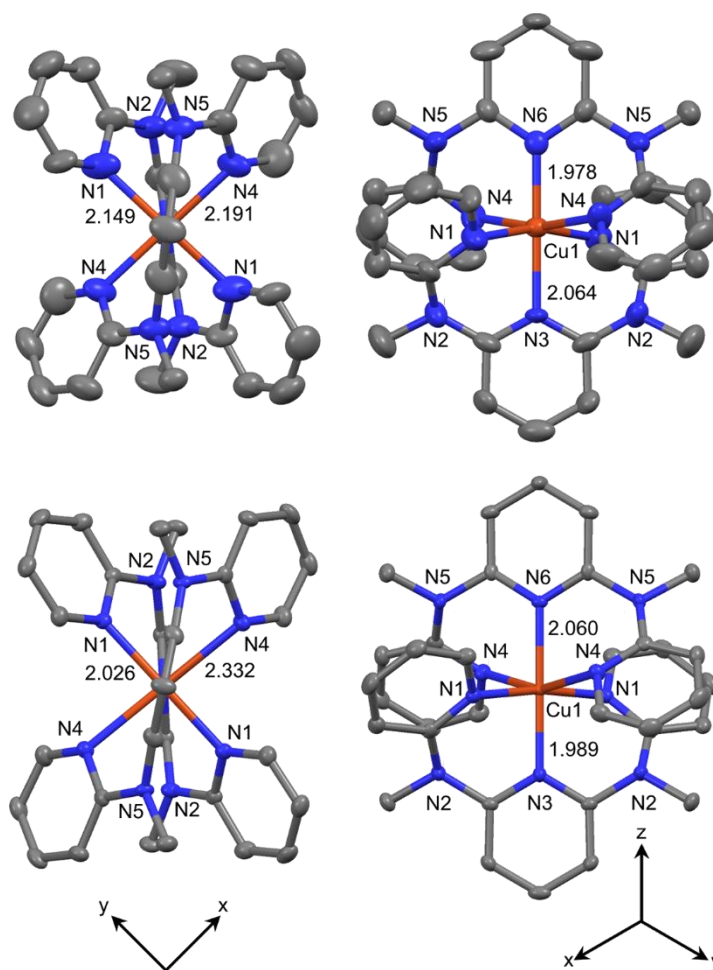
Figure 8. Depiction of the molecular structure of the cation of **1** at 263 K (top) and at 123 K (bottom). View along the N3–Cu–N6 (z) axis (left) and view perpendicular to the N3–Cu–N6 (z) axis (right). Thermal ellipsoids are drawn at the 50% probability level. Hydrogen atoms are omitted for clarity.

At 263 K the Cu–N1/N4 distances to the four terminal pyridine rings are almost dynamically averaged to 2.149(4) Å and 2.191(4) Å, respectively, while the bond lengths to the N3/N6 atoms of the central pyridine rings remain almost unaffected (2.064(5) Å and 1.978(6) Å) (Figure 8, top). Also, the N1–Cu–N1 and N4–Cu–N4 angles almost converge to a common value (166.5(2)° and 167.0(2)°). The averaging along the molecular x and y axes results in an apparent compressed CuN_6 coordination polyhedron (apparent radial distortion $\rho = 0.187$ Å) and the two crystallographic sites become almost indistinguishable (apparent angular distortion $\varphi \approx 166°$). The packing of the averaged CuN_6 polyhedra can then be described by an idealized diamond structure. The cocrystallized acetonitrile becomes highly disordered at 263 K. From the variable temperature X-ray analysis it appears that the transition from the static to the dynamic Jahn–Teller distortion occurs continuously and without a change in space group for **1**.
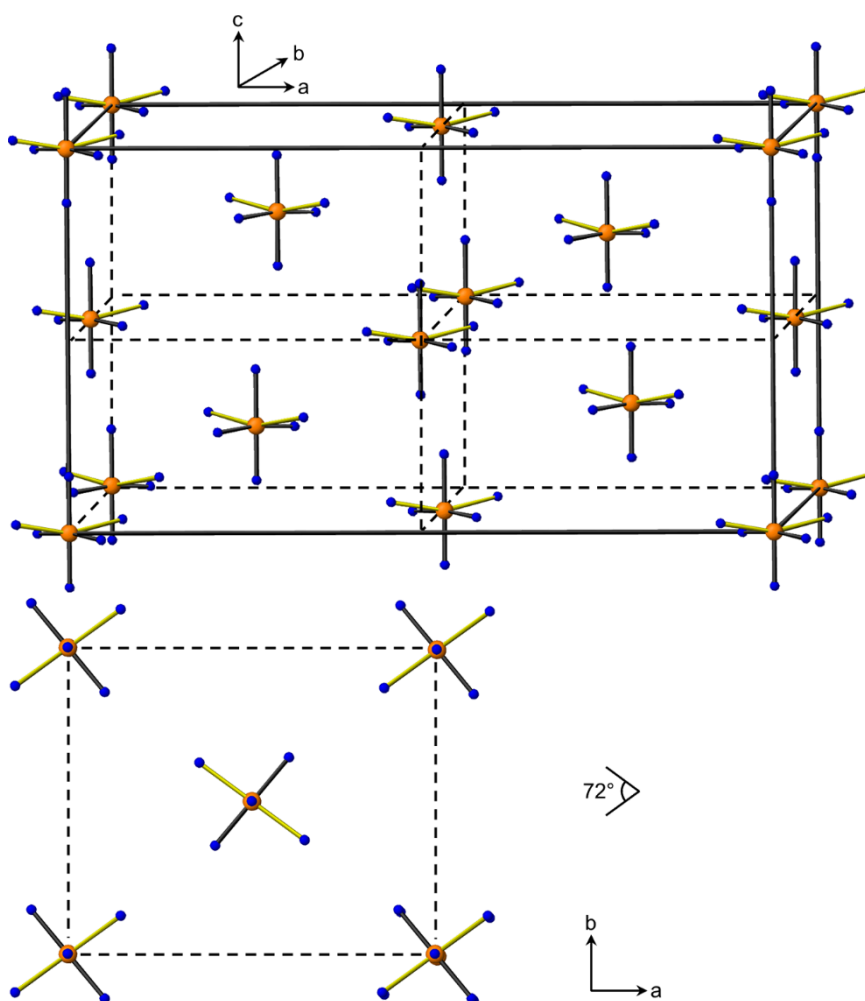
Figure 9. Depiction of the zincblende like packing of the CuN$_6$ polyhedra of **1** at 123 K showing the antiferrodistortive order (top), view along the *c* axis (bottom); the long axes of the polyhedra are shown in yellow; C and H atoms omitted for clarity.

Considering the observed averaged geometry at 263 K as an approximation of the transition state between the two axially elongated Jahn–Teller isomers the changes in radial and angular distortions $\Delta\rho$ and $\Delta\varphi$ of **1** are more than twice as large as those estimated for [Cu(tpy)$_2$]$^{2+}$ [**1**: $\Delta\rho = \rho(123\text{ K}) - \rho(263\text{ K}) \approx 0.171$ Å, $\Delta\varphi = \varphi(123\text{ K}) - \varphi(263\text{ K}) \approx -46°$; [Cu(tpy)$_2$]$^{2+}$: $\Delta\rho = \rho(77\text{ K}) - \rho(170\text{ K}) \approx 0.082$ Å, $\Delta\varphi = \varphi(77\text{ K}) - \varphi(170\text{ K}) \approx -21°$]. Thus, geometric reorganization of **1** during the Jahn–Teller isomerization requires more energy than that of [Cu(tpy)$_2$]$^{2+}$ giving a higher energy saddle point and thus a higher "freezing-in" temperature for **1**.[25]

The geometry of the cation of **1** was optimized at the DFT/B3LYP/LANL2DZ level of theory. As expected, an elongated polyhedron represents the minimum geometry (Figure 10, bottom). The long and short Cu–N bond lengths to terminal pyridine rings are calculated as 2.315 Å and 2.071 Å (exp.: 2.332(16) Å and 2.026(15) Å) while the Cu–N distances to the central pyridine rings are slightly different from each other (2.065 Å and 2.145 Å) similar to the difference obtained from the crystal diffraction data (1.989(3) Å, 2.060(3) Å). Also, the N1–Cu–N1 and N4–Cu–N4 angles are calculated as 173.22° and 164.90° comparable to the experimental ones (172.12(9)° and 160.06(8)°).

In the calculated transition state connecting the two Jahn–Teller isomers (8 kJ mol^{-1} above the two minima; imaginary frequency 66 cm^{-1}) the Cu–N1 and Cu–N4 distances are averaged to 2.210 Å. This compares well to the averaged data obtained from the X-ray diffraction at 263 K (2.149(4) Å and 2.191(4) Å) (Figure 10, top). The Cu–N3/N6 distances to the central pyridine rings (2.053 Å) are also similar to the X-ray data at 263 K (2.064(5) Å and 1.978(6) Å). The N1–Cu–N1 and N4–Cu–N4 angles are equal in the transition state (170.15°). These values reflect the higher symmetry of the transition state (Figure 10, top).
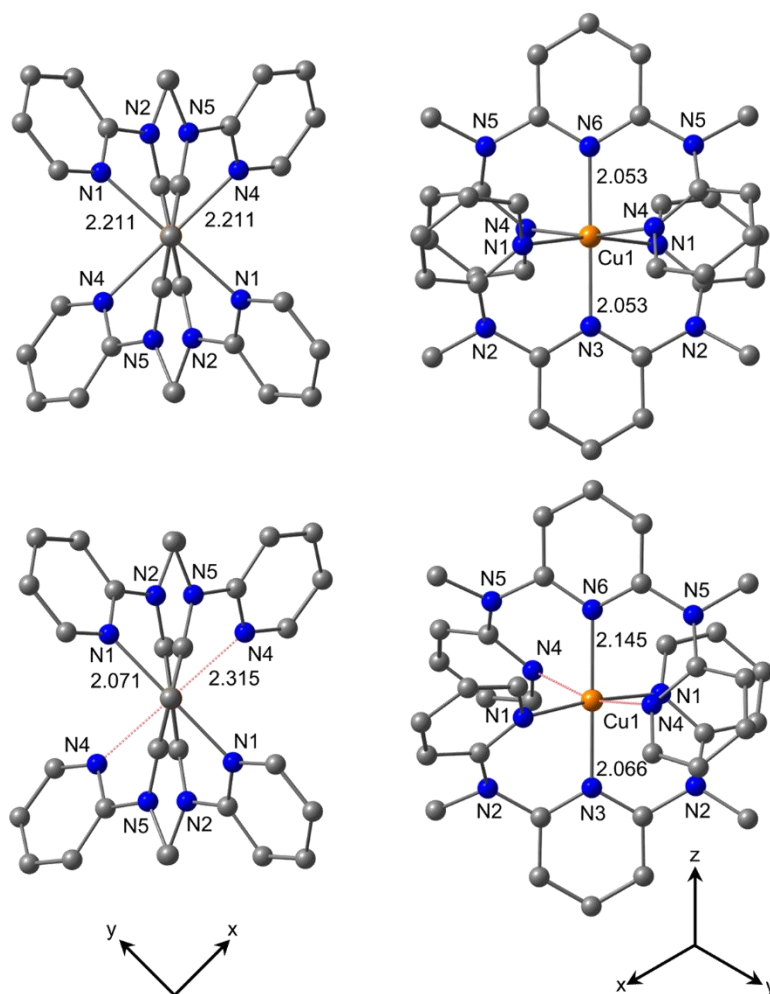
Figure 10. DFT optimized geometry of the cation of **1** (bottom) and of the transition state (top) for the interconversion between the two Jahn–Teller isomers; View along the N3–Cu–N6 *z* axis (left) and view perpendicular to the N3–Cu–N6 *z* axis (right). Hydrogen atoms omitted for clarity.
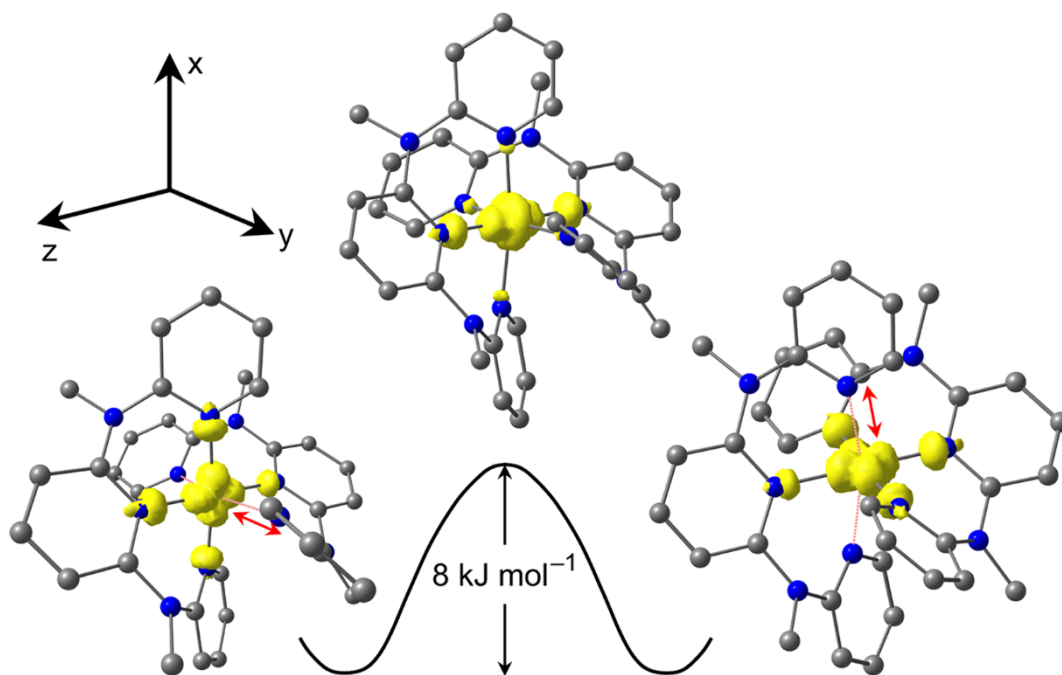
Figure 11. Spin densities (isosurface value 0.01 a.u.) of the two degenerate Jahn–Teller isomers and of the connecting transition state. Hydrogen atoms omitted for clarity.

Spin densities were calculated for the two Jahn–Teller isomers revealing the expected degenerate $z^2 - y^2$ ($z^2 - x^2$) ground state (Figure 11). In the geometrically averaged transition state the spin density is averaged accordingly (Figure 11, center). g-values were calculated from the optimized geometry using the EPR-II basis set for C, H, N and the 6-311G(d) basis set for Cu. For the elongated polyhedron a nearly axial pattern $g_x = 2.293$, $g_y = 2.109 \approx g_z = 2.089$ was calculated (cf. experimental values: $g_x = 2.228$, $g_y \approx g_z = 2.054$). For [Cu(tpy)$_2$]$^{2+}$ DFT calculations yield a rhombic pattern with $g_x = 2.273$, $g_y = 2.194$; $g_z = 2.021$ (cf. experimental values: $g_x \approx 2.26$, $g_y \approx 2.129$, $g_z \approx 2.020$). For the transition state geometry of the Jahn–Teller isomerization the g pattern is calculated as $g_x = 2.277 \approx g_y = 2.222$; $g_z = 2.010$ (cf. experimental values for the dynamically averaged state: $g_x \approx g_y = 2.150$; $g_z = 2.066$).

For improving the resolution we additionally measured variable temperature EPR spectra of **2** at W-band (microwave frequency $\approx$ 94 GHz, see Supporting Information). The simulations of the W-band spectra fully confirm the results obtained from the X-band spectra, namely, the characteristic pseudoaxial pattern for elongated octahedra at 50 K ($g_x = 2.049$; $g_y = 2.068$; $g_z = 2.258$; A_z($^{63/65}$Cu) = 184 G) and a pattern of an axially compressed polyhedron at 150 K ($g_x = 2.185$; $g_y = 2.145$; $g_z = 2.049$; $A_x \approx A_y$($^{63/65}$Cu) = 90 G). To further support our DFT calculations by comparing calculated with experimental hyperfine coupling constants to ligand nuclei for the static state ^{14}N Davies ENDOR spectra, ^{14}N HYSCORE and ^{1}H HYSCORE spectra of **1** and **2** were recorded at 10 K. ^{14}N Davies ENDOR spectra of **2** at different magnetic field positions together with simulations are given in the Supporting information. The spectra are characterized by three pairs of peaks centered at the range from 12 to 23 MHz which are split by twice the nitrogen nuclear Zeeman frequency. These values are typical for strongly coupled nitrogen nuclei with $|A/2| > |v_N|$. The simulations allow to estimate the principal

values of the hyperfine coupling tensors $A(^{14}N)$ for three different nitrogen atoms, namely, $A(^{14}N6)_{\perp,||} \approx 15, 15$ G; $A(^{14}N3)_{\perp,||} \approx 10, 10$ G; $A(^{14}N1)_{\perp,||} \approx 13, 12$ G (see Figure 10 for atom numbering). These values are excellently reproduced by the DFT calculation giving $A(^{14}N6)_{iso} = 15$ G, $A(^{14}N3)_{iso} = 10$ G and $A(^{14}N1)_{iso} = 14$ G while coupling along the elongated axis to N4 and to the noncoordinating N5 is calculated to be very small with $A(^{14}N4) = 0.4$ G and $A(^{14}N5)_{iso} = 0.1–0.2$ G. Indeed, small coupling constants to ^{14}N can be extracted from ^{14}N HYSCORE spectra of **2** ($A(^{14}N4) \approx 0.6$ G, see Supporting Information) and these are assigned to N4. From the ^{1}H HYSCORE spectra of **1** and **2** proton hyperfine couplings of $A(^{1}H) \approx 2.9$ G can be resolved (see Supporting Information). The largest proton coupling has been calculated by DFT for the protons adjacent to the strongly bound nitrogen atom N1 ($A(^{1}H) = 1.3$ G). This value somewhat underestimates the experimental one, probably because of the strong angular dependence of this electron–nucleus interaction which is also evident from the anisotropy of the proton coupling seen in the ^{1}H HYSCORE spectra recorded at different observer positions (see Supporting Information). All these data together provide confidence to the DFT calculation and corroborate our interpretations on the dynamics of **1**.

TD-DFT and PCM-TD-DFT (CH_3CN) calculations were then employed to interpret the experimental electronic spectrum (Figure 3). The calculated three lowest-energy absorptions are assigned to the symmetry-allowed ligand field transitions $_a^2A_1$ ($z^2–y^2$) $\rightarrow$ $_b^2A_1$ (x^2) (gas phase: 5210 cm^{-1}; CH_3CN: 5510 cm^{-1}) and $_a^2A_1$ ($z^2–y^2$) $\rightarrow$ $^2B_2$ (yz) / $^2B_1$ (xz) (gas phase: 14950 cm^{-1}; CH_3CN: 15265 cm^{-1}). The next absorption (gas phase: 18325 cm^{-1}; CH_3CN: 18720 cm^{-1}) consists of ligand-to-metal charge transfer transitions from the N-methyl lone pairs to the half-filled copper d-orbital. This pattern is in qualitative but far from quantitative agreement with the experimental data, especially with respect to the Jahn–Teller splitting $4\delta_1$ (vide supra). Even consideration of solvent effects by employing a polarisable continuum solvent model only slightly improves the agreement. Possibly the presence of counterions influences the Jahn–Teller splitting more than the solvent effects. Indeed, in the solid state the tetrafluoroborate counterions attach to the ddpd ligands via CH···F contacts (H···F = 2.33–3.03 Å; see Supporting Information) bridging the pyridyl ring (N1) of one ddpd ligand with a pyridyl ring of the second one (N4). In solution a similar contact ion pair might be expected. As this bridging is not reflected in the TD-DFT calculations it could be the reason for the discrepancy.

4. CONCLUSIONS

The expanded ligand ddpd coordinates to copper(II) in a meridional fashion giving the homoleptic dicationic complex *mer*-[Cu(ddpd)$_2$](BF$_4$)$_2$ **1**. In the solid state at T < 100 K the complex cations localize in Jahn–Teller elongated polyhedra with the longest Cu–N bond pointing in the molecular x or y directions while the z axis is constrained by the tridentate ligand. These polyhedra order in an antiferrodistortive fashion in an idealized zincblende structure. Increasing the temperature yields

dynamically averaged (fluxional) polyhedra in the molecular x/y directions as observed by variable temperature EPR (X-band, W-band) and variable temperature X-ray diffraction.

The Jahn–Teller splitting $4\delta_1$ of **1** is larger than the corresponding energy of $[Cu(tpy)_2]^{2+}$. This is based on the much more favorable orbital overlap in the Cu–N bonds in **1** which results from the larger bite angle of the ddpd ligand as compared to tpy.

The "freezing-in" of the Jahn–Teller dynamics of **1** ($T \approx 100$ K) occurs at higher temperature as observed for $[Cu(tpy)_2]^{2+}$ ($T < 77$ K) which is also probably due to the larger Jahn–Teller distortion of **1** giving a larger activation barrier. Future work will include functionalized ddpd ligands which could be able to transmit structural information between individual Jahn–Teller active copper(II) complexes resulting in cooperative ordering and maybe also magnetic ordering effects.[26] Ligand functionalization could also be a means to isolate individual "Jahn–Teller isomers".[27]

ASSOCIATED CONTENT

Supporting Information

Simulations of variable temperature X-band and W-band EPR spectra of **1** and **2**, HYSCORE spectra of **1** and **2**, DSC of **1**, illustration of the coordination of the tetrafluoroborate counterions in the solid state to the dication, Cartesian coordinates of DFT optimized $[Cu(ddpd)_2]^{2+}$. This material is available free of charge via the Internet at http://pubs.acs.org.

AUTHOR INFORMATION

Corresponding author

*Fax: +49-6131-39-27277. E-mail: katja.heinze@uni-mainz.de.

Notes

The authors declare no competing financial interest.

ACKNOWLEDGMENTS

REFERENCES

(1) Jahn, H. A.; Teller, E. *Proc. Roy. Soc.* **1937**, *161*, 220–235.

(2) Ammeter, J. H.; Bürgi, H. B.; Gamp, E.; Meyer-Sandrin, V.; Jensen, W. P. *Inorg. Chem.* **1979**, *18*, 733–750.

(3) (a) Henke, W.; Reinen, D. *Z. Anorg. Allg. Chem.* **1977**, *436*, 187–200; (b) Reinen, D.; Krause, S. *Inorg. Chem.* **1981**, *20*, 2750–2759.

(4) Kremer, S.; Henke, W.; Reinen, D. *Inorg. Chem.* **1982**, *21*, 3013–3022.

(5) Riley, M. J.; Hitchman, M. A.; Reinen, D.; Steffen, G. *Inorg. Chem.* **1988**, *27*, 1924–1934.

(6) The radial distortion is defined as $\rho = (2\Delta x^2 + 2\Delta y^2 + \Delta z^2)^{1/2}$ and the angular distortion[4] as $\varphi = $ arc tan$[3^{1/2}(\Delta x - \Delta y) / (2\Delta z - \Delta x - \Delta y)]$ with Δx, Δy, Δz being deviations of individual Cu-L bond lengths from the average value.[2–5]

(7) Bertini, I.; Gatteschi, D.; Scozzafava, A. *Coord. Chem. Rev.* **1979**, *29*, 67–84.

(8) Folgado, J.-V.; Henke, W.; Allmann, R.; Stratemeier, H.; Beltrán-Porter, D.; Roja, T.; Reinen, D. *Inorg. Chem.* **1990**, *29*, 2035–2042.

(9) Allmann, R.; Henke, W.; Reinen, D. *Inorg. Chem.* **1978**, *17*, 378–382.

(10) Arriortua, M. I.; Rojo, T.; Amigo, J. M.; Germain, G.; Declercq, J. P. *Acta Crystallogr.* **1982**, *B28*, 1323–1324.

(11) Valdéz-Martínez, J.; Toscano, R. A.; Salazar-Mendoza, D. *Acta Crystallogr., Sect. E* **2001**, *E57*, m331–m332.

(12) Tucker, D. A.; White, P. S.; Trojan, K. L.; Kirk, M. L.; Hatfield, W. E.; *Inorg. Chem.* **1991**, *30*, 823–826.

(13) Shieh, S.-J.; Che, C.-M.; Peng, S.-M. *Inorg. Chim. Acta* **1992**, *192*, 151–152.

(14) Breivogel, A.; Förster, C.; Heinze, K. *Inorg. Chem.* **2010**, *49*, 7052–7056.

(15) Hammarström, L.; Johansson, O. *Coord. Chem. Rev.* **2010**, *254*, 2546–2559.

(16) Stoll, S.; Schweiger, A. *J. Magn. Reson.* **2006**, *178*, 42–55.

(17) *SMART Data Collection and SAINT-Plus Data Processing Software for the SMART System* (various versions); Bruker Analytical X-Ray Instruments, Inc.: Madison, WI, 2000.

(18) Blessing, B. *Acta Crystallogr.* **1995**, *A51*, 33.

(19) Sheldrick, G. M. *SHELXTL*, Version 5.1; Bruker AXS: Madison, WI, 1998.

(20) Sheldrick, G. M. *SHELXL-97*; University of Göttingen: Göttingen, Germany, 1997.

(21) (a) Frisch, M. J.; Trucks, G. W.; Schlegel, H. B.; Scuseria, G. E.; Robb, M. A.; Cheeseman, J. R.; Scalmani, G.; Barone, V.; Mennucci, B.; Petersson, G. A.; Nakatsuji, H.; Caricato, M.; Li, X.; Hratchian, H. P.; Izmaylov, A. F.; Bloino, J.; Zheng, G.; Sonnenberg, J. L.; Hada, M.; Ehara, M.; Toyota, K.; Fukuda, R.; Hasegawa, J.; Ishida, M.; Nakajima, T.; Honda, Y.; Kitao, O.; Nakai, H.; Vreven, T.; Montgomery, Jr., J. A.; Peralta, J. E.; Ogliaro, F.; Bearpark, M.; Heyd, J. J.; Brothers, E.; Kudin, K. N.; Staroverov, V. N.; Kobayashi, R.; Normand, J.; Raghavachari, K.; Rendell, A.; Burant, J. C.; Iyengar, S. S.; Tomasi, J.; Cossi, M.; Rega, N.; Millam, J. M.; Klene, M.; Knox, J. E.; Cross, J. B.; Bakken, V.;

Adamo, C.; Jaramillo, J.; Gomperts, R.; Stratmann, R. E.; Yazyev, O.; Austin, A. J.; Cammi, R.; Pomelli, C.; Ochterski, J. W.; Martin, R. L.; Morokuma, K.; Zakrzewski, V. G.; Voth, G. A.; Salvador, P.; Dannenberg, J. J.; Dapprich, S. Daniels, A. D.; Farkas, O.; Foresman, J. B.; Ortiz, J. V.; Cioslowski, J.; Fox, D. J. *Gaussian 09*, Revision A.02; Gaussian, Inc.: Wallingford, CT, 2009; (b) Barone, V. In *Recent Advances in Density Functional Methods*; Chong, D. P., Ed.; World Scientific Singapore: Singapore, 1995; Part 1.

(22) Kahn, O. *Molecular Magnetism*, Wiley-VCH: New York, 1993.

(23) The bis(ddpd) iron(II) complex is in the low-spin state at all investigated temperatures. Details concerning bis(ddpd) iron(II) complexes will be reported elsewhere.

(24) Smith, D. W. *Coord. Chem. Rev.* **1976**, *21*, 93–158.

(25) Dunitz, J. D.; Bürgi, H.-B., Eds.; *Structure Correlation*; VCH: Weinheim, Germany, 1994.

(26) Halder, G. J.; Chapman, K. W.; Schlueter, J. A.; Manson, J. L. *Angew. Chem.* **2011**, *123*, 439–441; *Angew. Chem. Int. Ed.* **2011**, *50*, 419–421.

(27) Comba, P.; Hauser, A.; Kerscher, M.; Pritzkow, H. *Angew. Chem.* **2003**, *115*, 4675–4679; *Angew. Chem. Int. Ed.* **2003**, *42*, 4536–4540.

4. SUMMARY AND OUTLOOK

In this dissertation the synthesis of a polymer-supported nitrido molybdenum(VI) complex using a new pathway consisting of only a single reaction step, including the immobilized ligand and the trichlorido nitrido molybdenum(VI) precursor complex, is presented. For comparison of the spectroscopic and reactivity properties, the soluble nitrido molybdenum(VI) complex was prepared as well, using a sterically unencumbered tripodal ligand. Protonation of both nitrido molybdenum(VI) complexes yields the respective imido molybdenum(VI) complexes. Subsequent one-electron reduction of the soluble complex is irreversible as the product undergoes bimolecular proton/electron transfer reactions. In contrast, single-electron reduction of the immobilized molybdenum(VI) complex with cobaltocene gives the polymer-supported imido molybdenum(V) complex as shown by EPR spectroscopy. Due to the immobilization and the effective separation of the reaction centers onto the solid support (site isolation effect), bimolecular side reactions which often occur in homogeneous systems are suppressed, enabling the preparation and characterization of this imido molybdenum(V) complex. This is the first time that this proposed intermediate of the Schrock cycle could be isolated and characterized.

To monitor the spatial separation of the immobilized copper(II) complexes, EPR spectra of an immobilized nitrato copper(II) complex were acquired under different conditions (solvent, temperature). Effective isolation of immobilized complexes is achieved due to solvent uptake and swelling of the cross-linked polymer. In THF, CH_2Cl_2 and toluene, the polystyrene/divinylbenzene (1%) solid phase shows a good swelling behavior, whereas in saturated hydrocarbons such as petroleum ether it behaves like a dry, collapsed polymer. These experiments revealed that the accessibility and the reactivity of the immobilized reaction centers strongly depend on the type of solvent. This fact is an important aspect with respect to ammonia formation from immobilized nitrido molybdenum(VI) complexes.

To investigate and to optimize the amount of ammonia release, polymer-supported nitrido molybdenum(VI) complexes were treated with a proton source (2,6-lutidinium) and an electron source (decamethylcobaltocene) under different reaction conditions (solvents). The use of good swelling solvents for the solid phase, which guarantee good accessibility of the immobilized nitrido molybdenum(VI) complexes, revealed also rapid dihydrogen formation as these solvents are simultaneously good solvents for the proton and the electron source. Thus, the proton source and the reducing agent were added stepwise to the reaction leading to stoichiometric NH_3 formation (one equivalent based on immobilized "MoN" after 17 steps). Protonation and reduction reactions proceed in sections within the polymer bead. Active sites located at the "outer shell" of the spherical polymer bead are well accessible and react rapidly with the proton and electron source, whereas active sites located in the "inner shells" are less accessible and undergo slow diffusion-controlled reactions. Three H^+/e^- steps are required to give a peak NH_3 release from these inner shells. As stoichiometric amounts of ammonia were released, this experiment provides no evidence for the catalytic activity of

immobilized nitrido molybdenum(VI) complexes. Coordination of 2,6-lutidine to the molybdenum(III) center yielding the stable, catalytically inactive 2,6-lutidine molybdenum(III) complex represents a serious side reaction explaining the irreversible loss of catalytic ability.

Future work could focus on the synthesis and characterization of other immobilized N_xH_y containing molybdenum complexes that represent proposed but not yet isolated intermediates of the Schrock cycle. Especially the preparation and characterization of other EPR active complexes, for example the cationic amido molybdenum(V) complex and the hydrazido molybdenum(V) complex, would be highly interesting.

Immobilized nitrido molybdenum(VI) complexes could be further investigated with respect to catalytic ammonia formation. As 2,6-lutidine coordination to molybdenum(III) with this sterically less encumbered ligand represents an irreversible reaction leading to the loss of catalytic ability, other proton sources which are unable to coordinate to molybdenum(III) could be investigated in catalysis reactions. Sterically more demanding proton sources could be used, for example 2,6-diisopropylpyridinium, or acids like $[H(OEt_2)]^+$ whose corresponding bases do not compete with N_2 for coordination to molybdenum(III). Thus N_2 coordination to the metal center, closing the cycle, might be favored. As this dinitrogen molybdenum(III) complex represents the starting point for a new reaction cycle, catalytic NH_3 formation could probably be enabled.

As a second topic, Jahn−Teller distortion and Jahn−Teller dynamics of the bis(ddpd) copper(II) complex *mer*-$[Cu^{II}(ddpd)_2](BF_4)_2$ were investigated with the help of variable temperature EPR and X-ray diffraction studies. In the solid state at temperatures below 100 K the copper(II) complexes appear as Jahn–Teller elongated polyhedra with the longest Cu–N bond pointing in the molecular *x* or *y* directions. These two degenerate "Jahn−Teller isomers" are ordered in an antiferrodistortive fashion in an idealized zincblende structure. At higher temperatures EPR spectra show *g*-values corresponding to pseudo-compressed octahedral copper(II) species. This fact is ascribed to a dynamical process occurring along the Cu–N bonds in the molecular x/y directions resulting in a pseudo-compression along the *z* axis. This dynamic Jahn−Teller phenomenon process is frozen at 100 K.

To investigate the cooperativity and hysteresis behavior of Jahn−Teller dynamics in such copper(II) systems, future work could focus on the use of functionalized or linked ddpd ligands. These ligands might transmit structural information between the individual Jahn–Teller active copper(II) complexes, which could result in cooperative ordering and maybe also in magnetic ordering effects. Additionally, ligand functionalization could enable the isolation of individual "Jahn–Teller isomers".

5.   SUPPORTING INFORMATION

Contents:

To 3.2:Proton and Electron Transfer to a Polymer-Supported Nitrido Molybdenum(VI) Complex

Anica Wünsche von Leupoldt, Christoph Förster, Tobias J. Fiedler, Nicolas H. Bings, Katja Heinze
Published in: *Eur. J. Inorg. Chem*. **2013**, *36*, 6079−6090.
[DOI:10.1002/ejic.201301156]
http://onlinelibrary.wiley.com/doi/10.1002/ejic.201301156/suppinfo

To 3.4:Effect of Chelate Ring Expansion on Jahn−Teller Distortion and Jahn−Teller Dynamics in Copper(II) Complexes

Katharina Mack, Anica Wünsche von Leupoldt, Christoph Förster, Maria Ezhevskaya, Dariush Hinderberger, Karl W. Klinkhammer, Katja Heinze
Published in: *Inorg. Chem*. **2012**, *51*, 7851−7858.
[DOI:10.1021/ic300929g]
http://pubs.acs.org/doi/suppl/10.1021/ic300929g

To 3.2: Proton and Electron Transfer to a Polymer-Supported Nitrido Molybdenum(VI) Complex

Figure S1. UV/Vis spectra of **1**, **2** and **3** in THF.
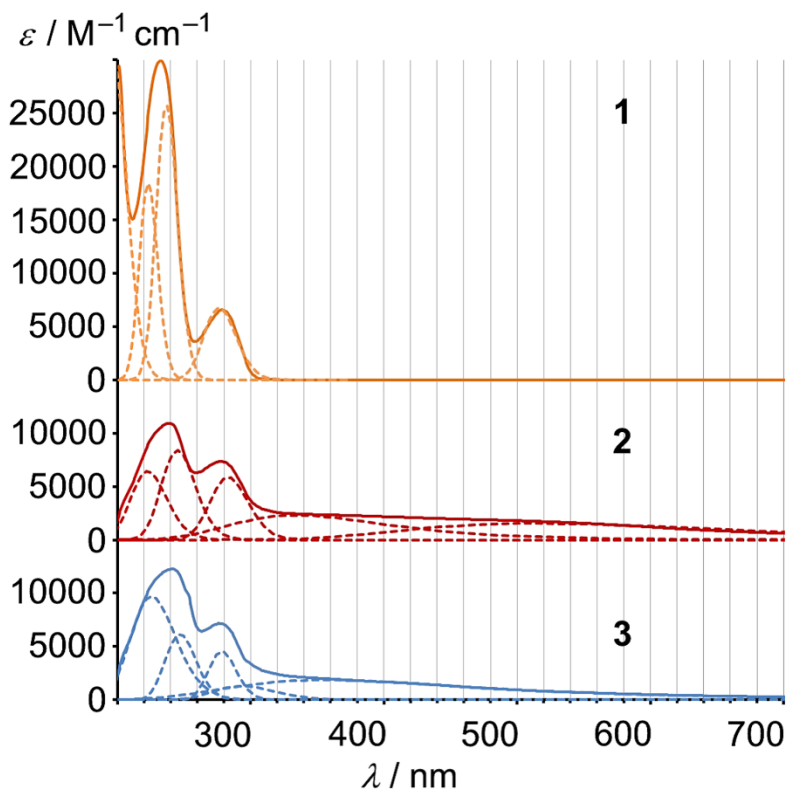
Figure S2. Frontier orbitals of a) **2** and b) **3**.

a)

b)
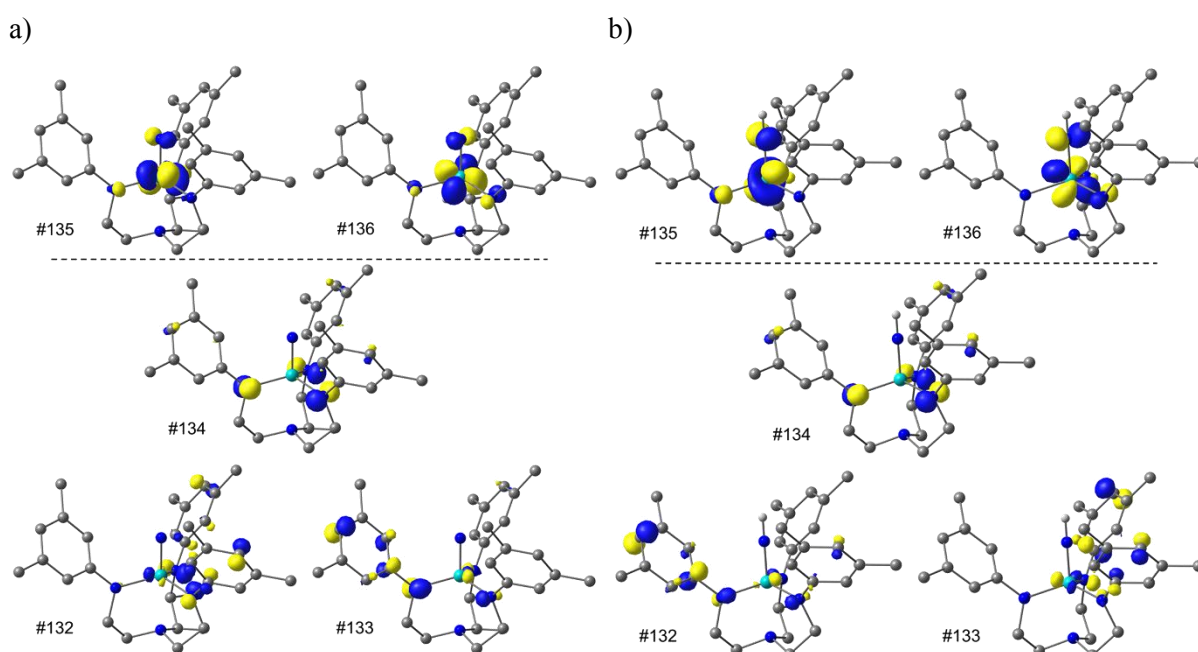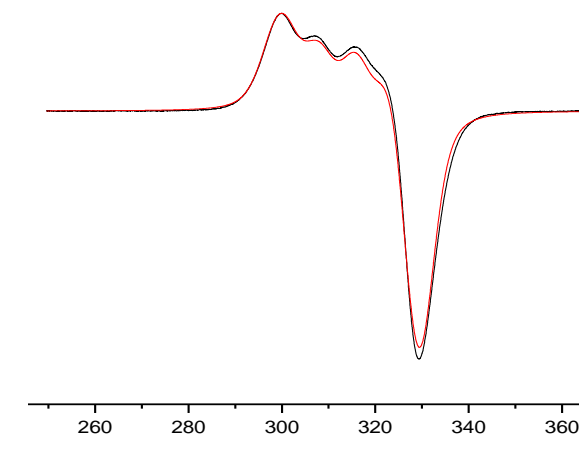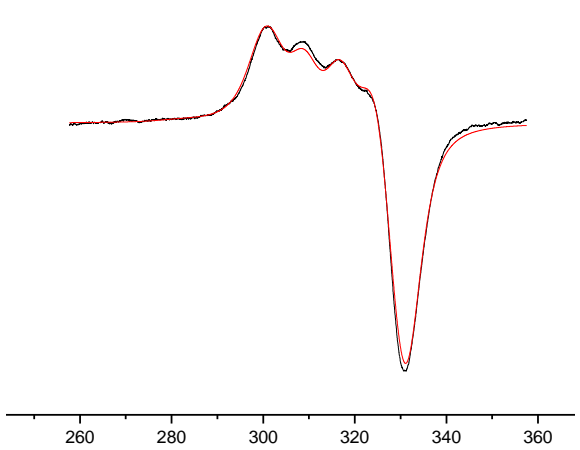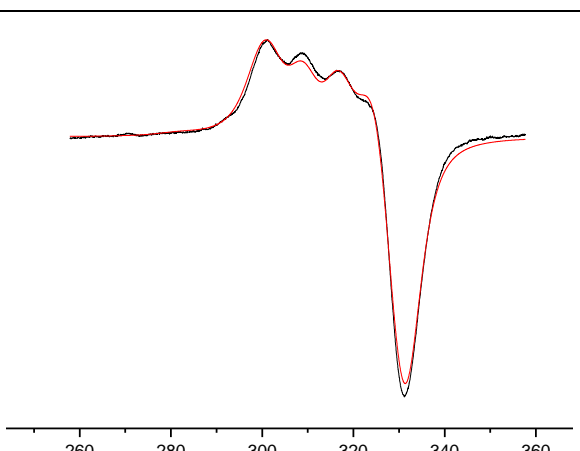
Figure S3. Kaiser test of a) **P-tren**, b) **P-1** (incomplete Buchwald-Hartwig amination) and c) **P-1** (complete Buchwald-Hartwig amination).
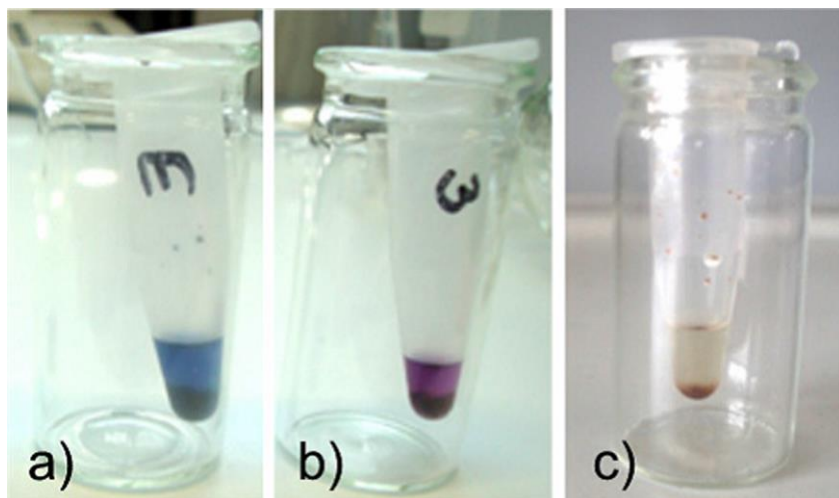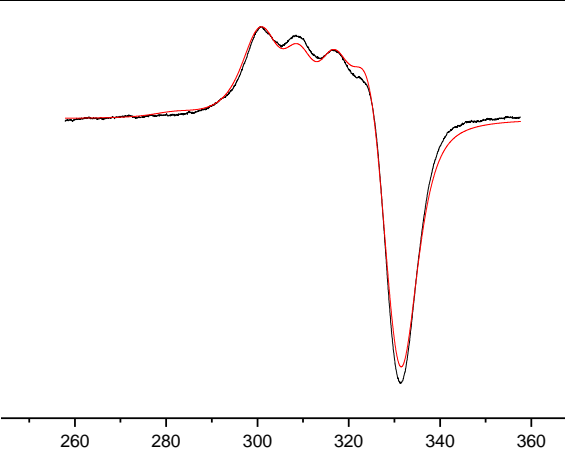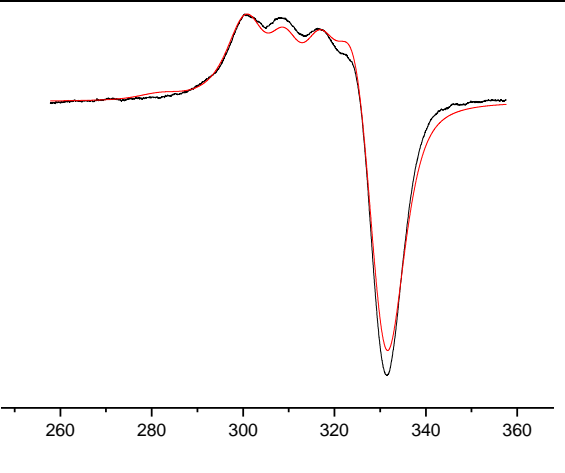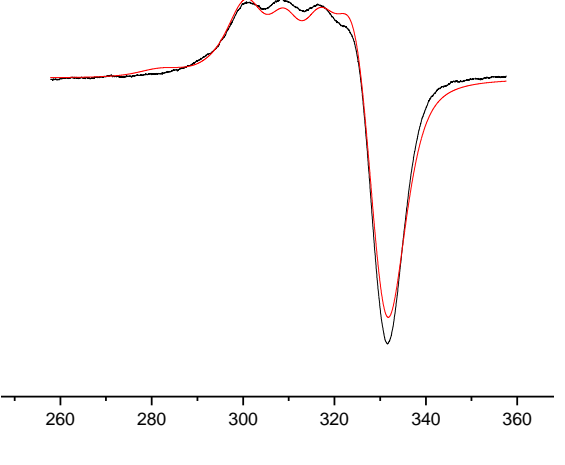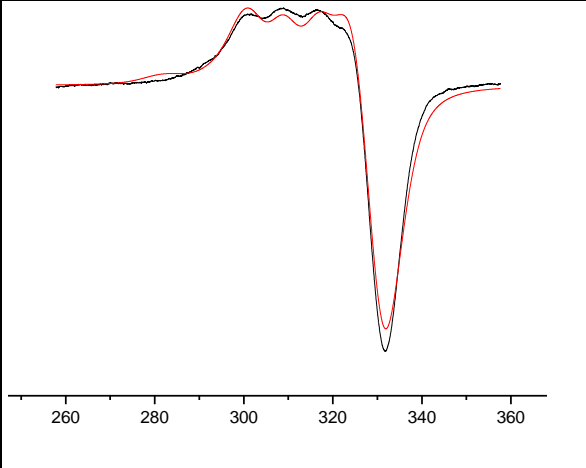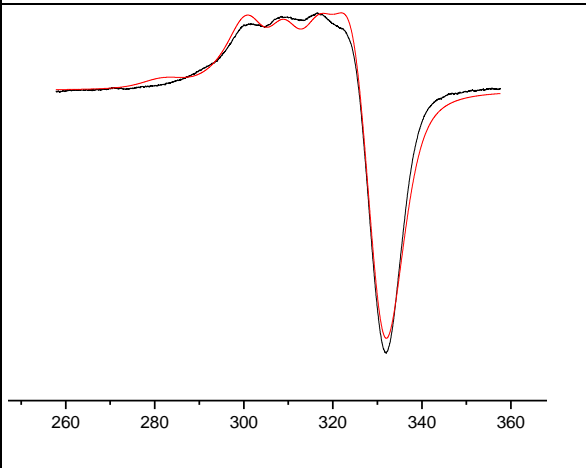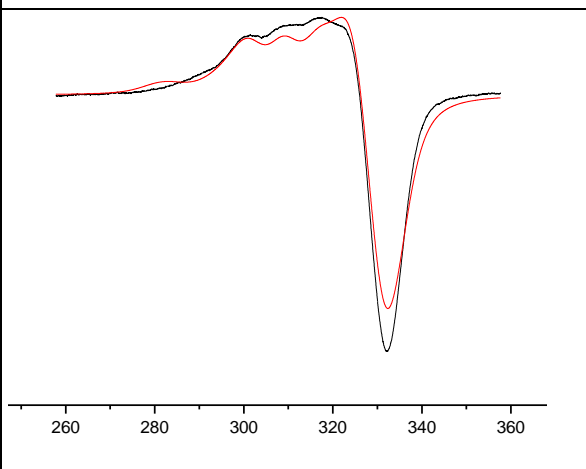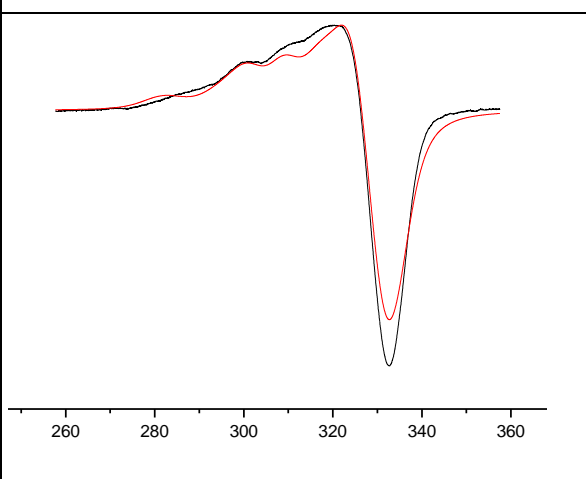
For Cartesian coordinates of **1** – **4** and **P-1** – **P-4** (B3LYP, LANL2DZ, PCM THF) see electronic supporting information under http://onlinelibrary.wiley.com/doi/10.1002/ejic.201301156/suppinfo.
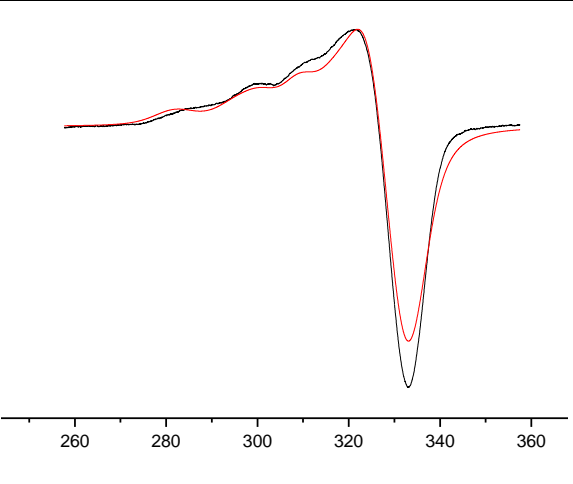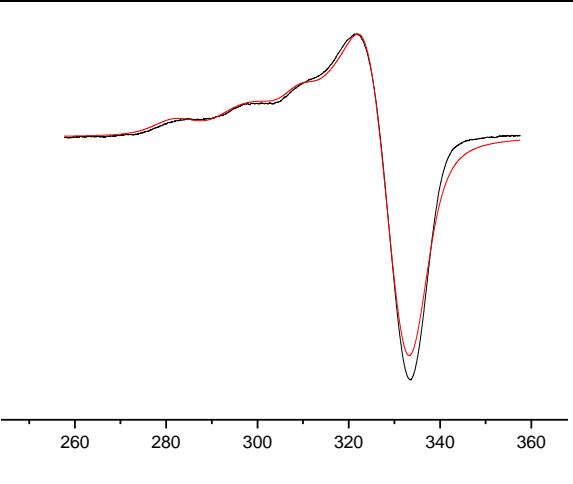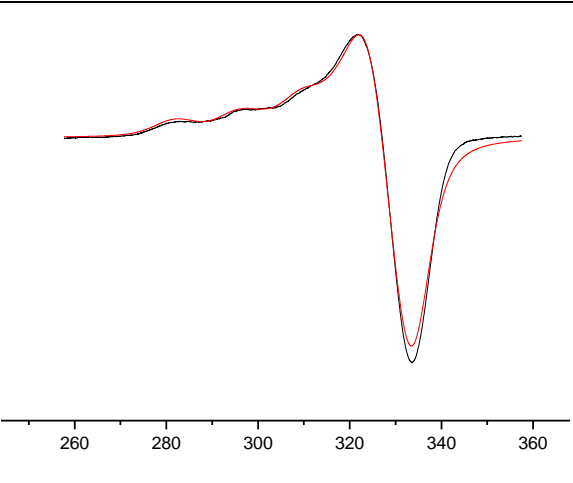
To 3.4:   Effect of Chelate Ring Expansion on Jahn−Teller Distortion and Jahn−Teller Dynamics in Copper(II) Complexes

Selected simulated EPR spectra of **1**.
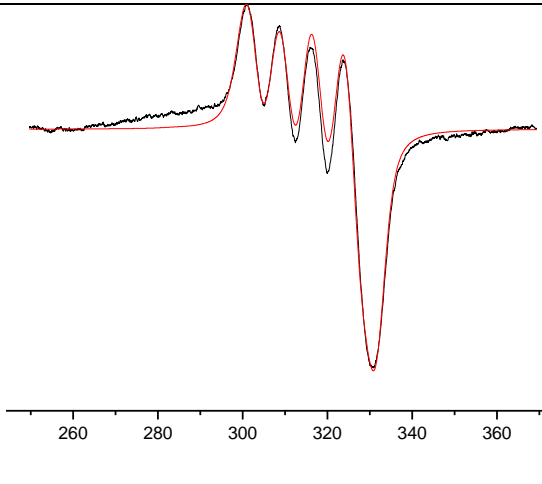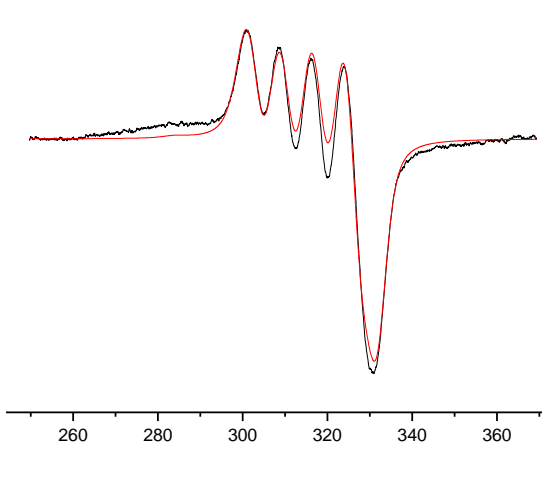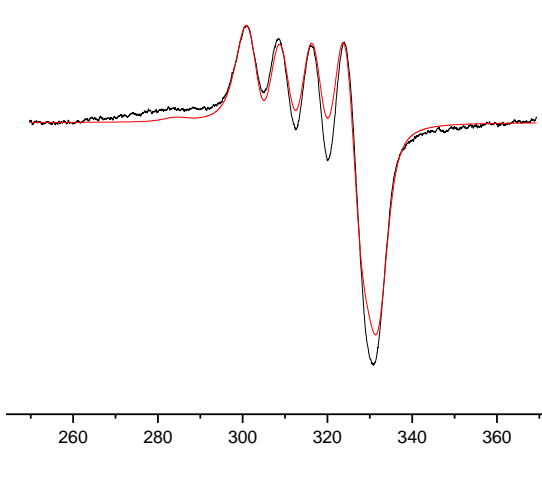
exp. spectrum (black) / simulation (red)	T [K]	g	A [G]	fraction [%]
	293	2.146, 2.146, 2.056	82, 82, 5	100
		2.054, 2.054, 2.228	15 15 150	0
	273			90
				10
	253			85
				15
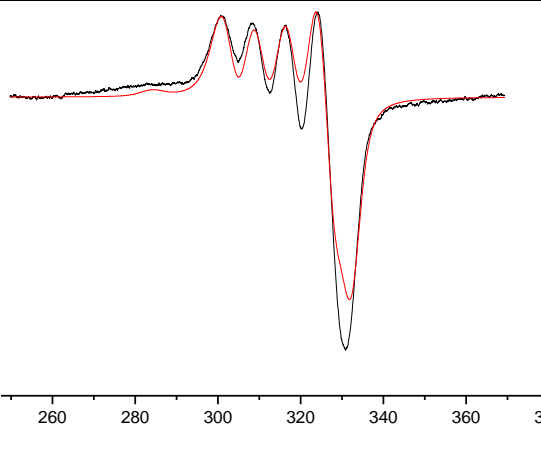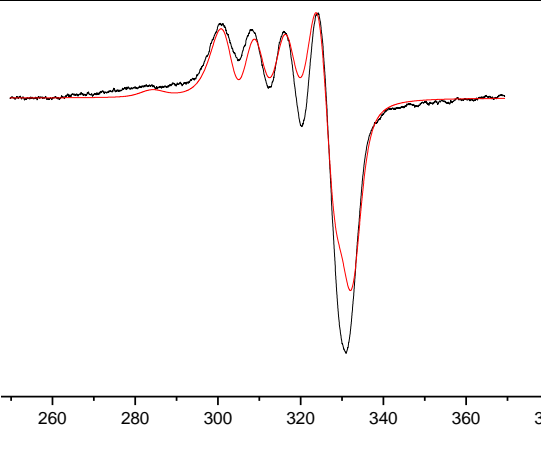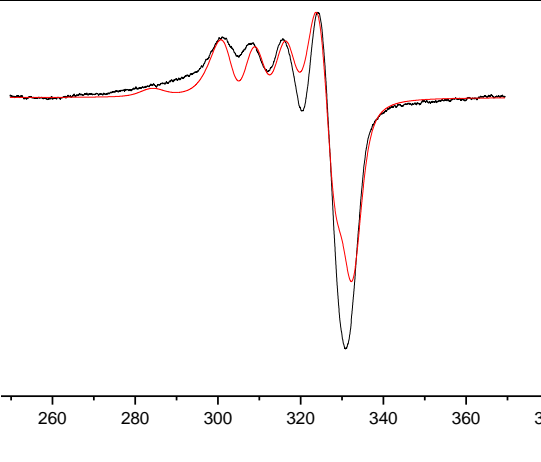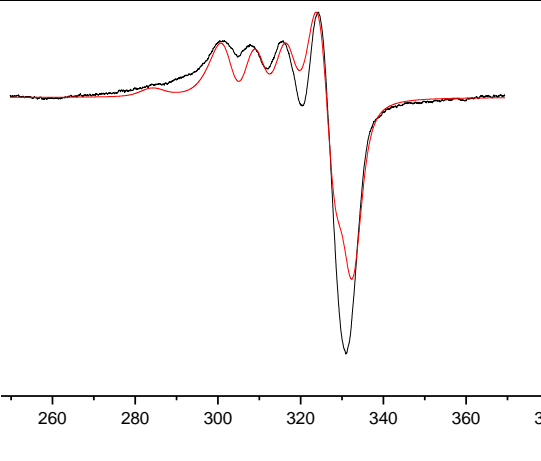
	233			75
				25
	213			67
				33
	193			60
				40
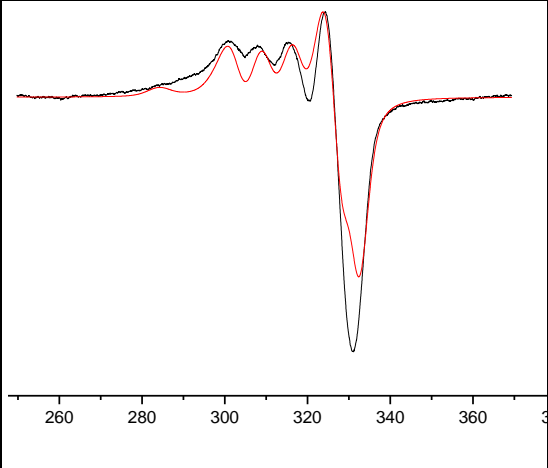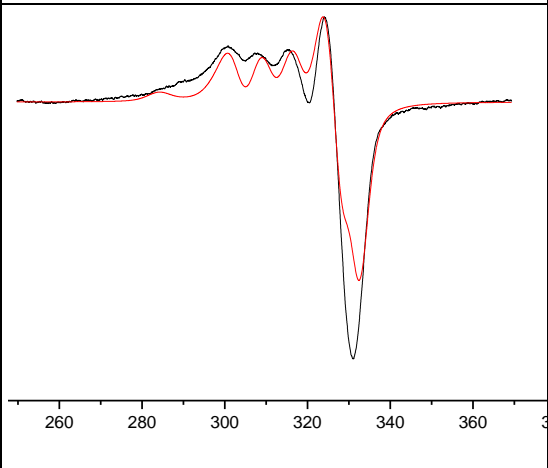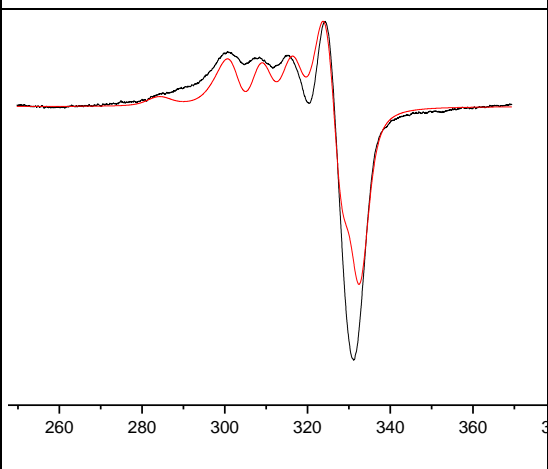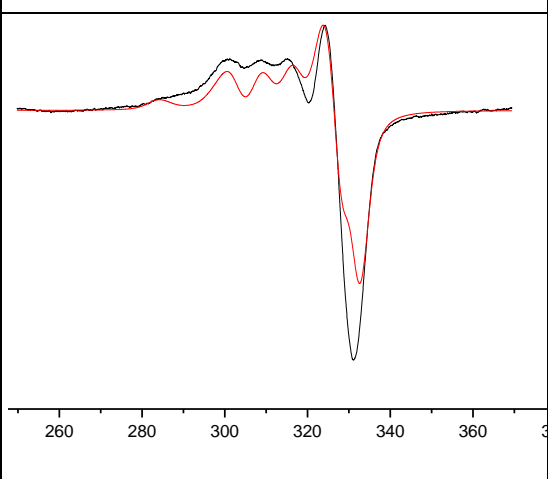
	183			55
				45
	173			50
				50
	163			38
				62
	153			27
				73

	143			15
				85
	123			10
				90
	103			3
				97

Selected simulated EPR spectra of **2**.
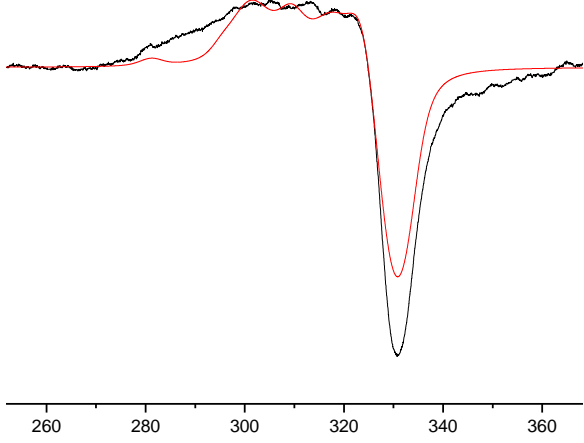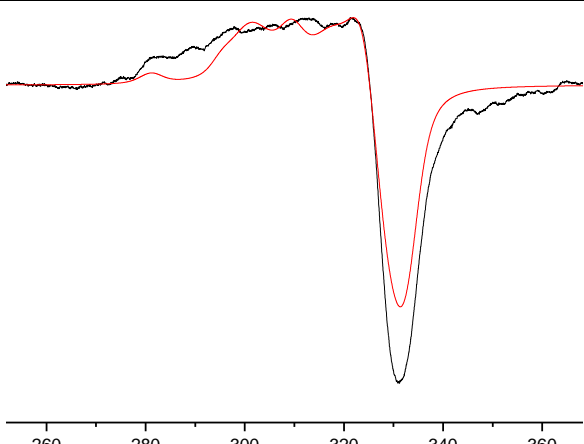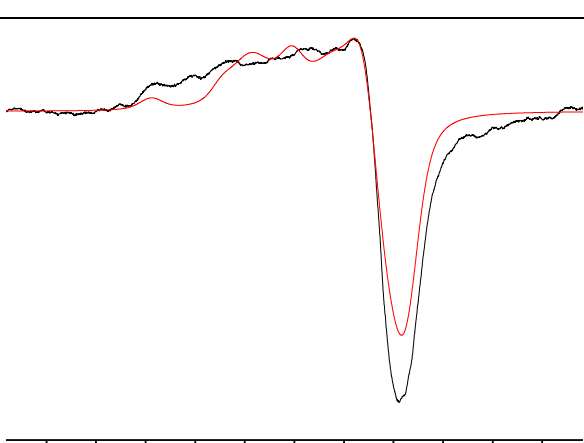
exp. spectrum (black) / simulation (red)	T [K]	g	A [G]	fraction [%]
	293	2.148, 2.148, 2.054 2.061, 2.061, 2.210	80, 80, 15 10 10 150	98 2
	273			90 10
	253			81 19

	233			68
				32
	213			58
				42
	193			51
				49
	183			48
				52

	173			45
				55
	163			43
				57
	153			42
				58
	143			33
				67

	123			17
				83
	103			5
				95

VT X-band powder EPR spectra of **2**.

| 293 K |
| 283 K |
| 273 K |
| 263 K |
| 253 K |
| 243 K |
| 233 K |
| 223 K |
| 213 K |
| 203 K |
| 193 K |
| 183 K |
| 173 K |
| 163 K |
| 153 K |
| 143 K |
| 133 K |
| 113 K |
| 103 K |

B / mT
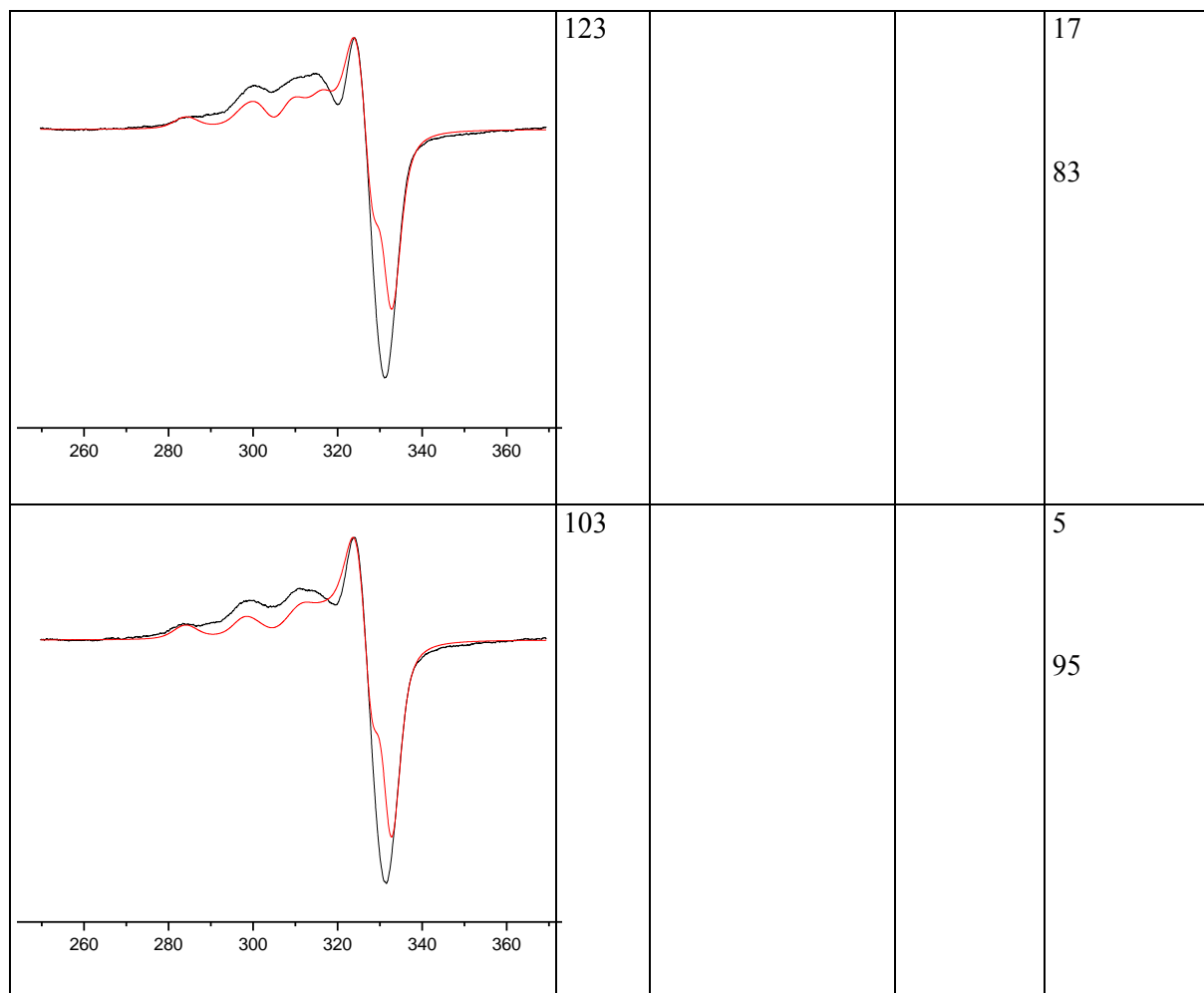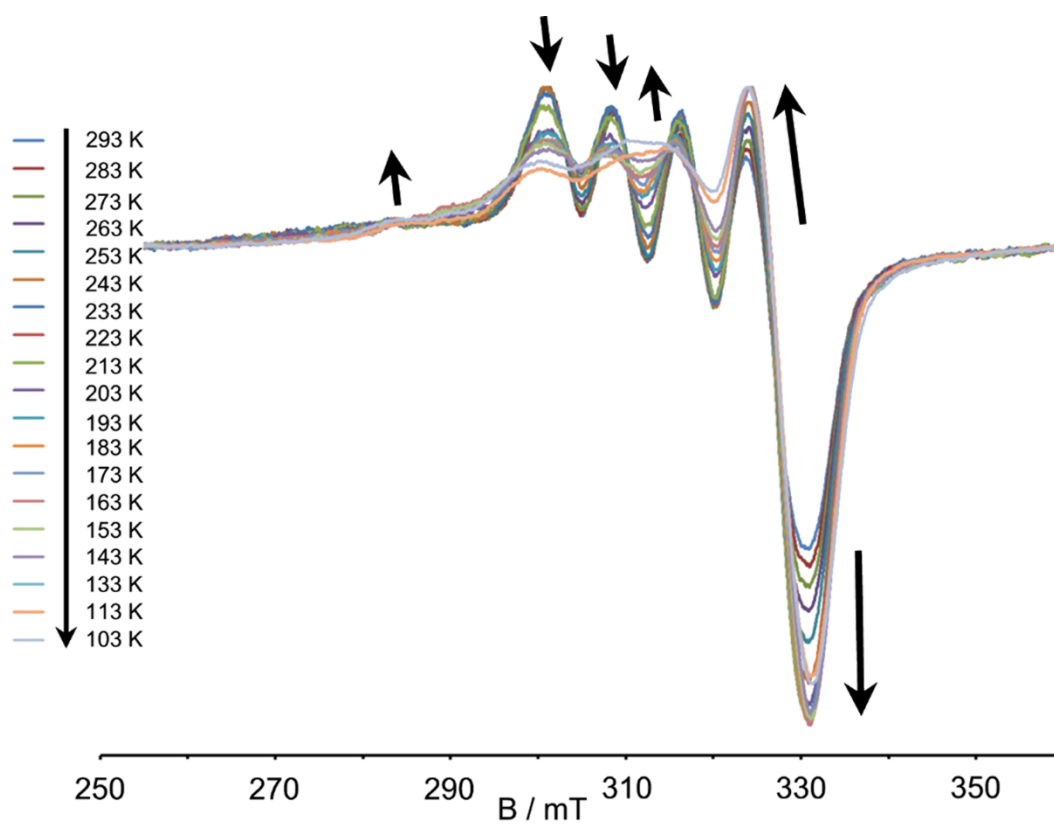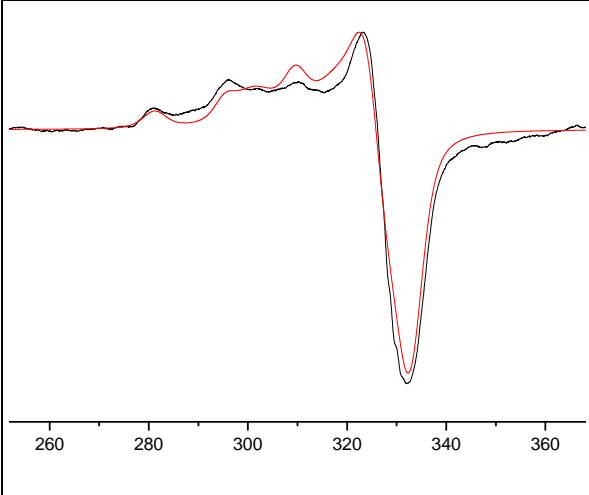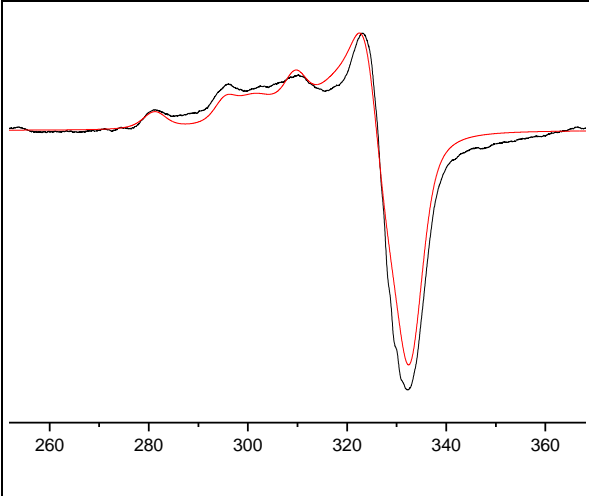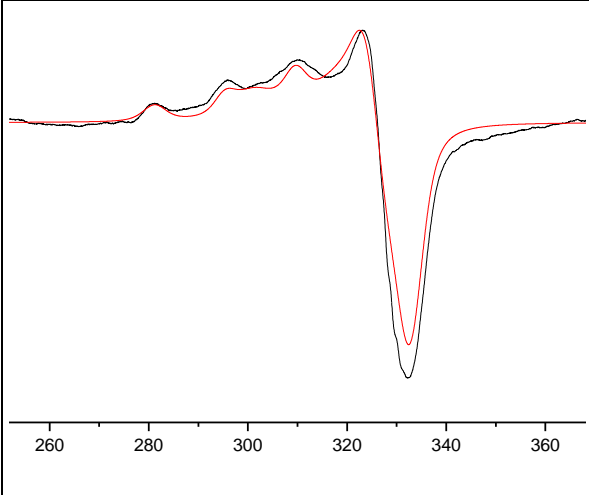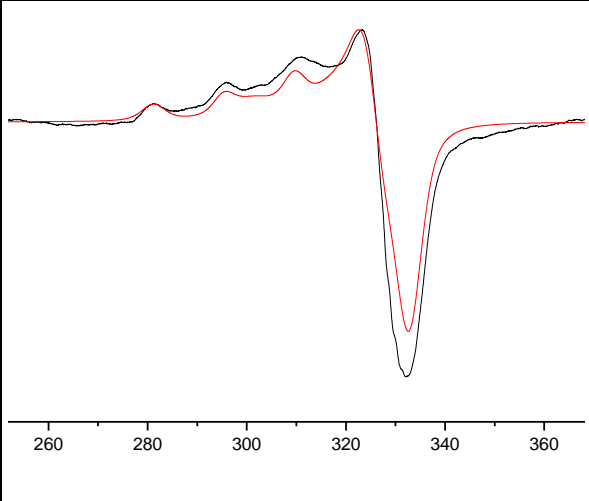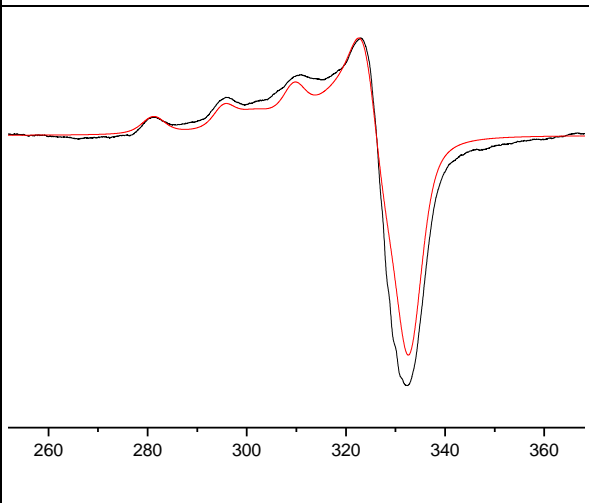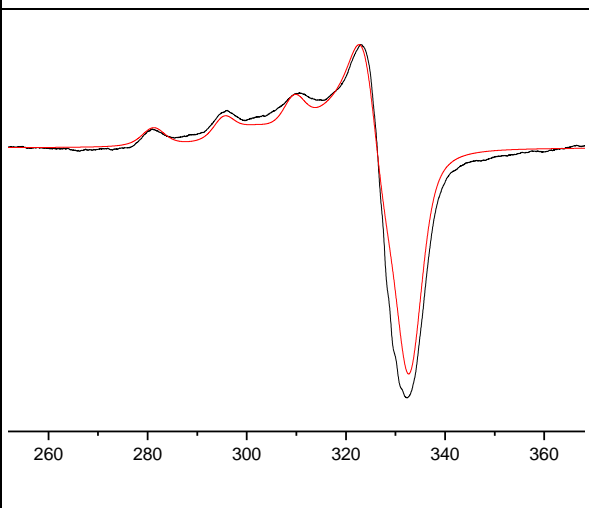
Selected EPR spectra of **1** in water (plus some glycerol for a better glass formation) and attempted simulations (in red).

exp. spectrum (black) / simulation (red)	T [K]	g	A [G]	fraction [%]
	253	2.142, 2.142, 2.068 2.060, 2.060, 2.226	81 81 5 15 15 155	70 30
	243			60 40
	233			55 45

	223			50
				50
	213			45
				55
	203			40
				60

	193		40 60
	183		40 60
	173		40 60

	163			35 65
	153			30 70
	143			27 73

	133			78
				22
	123			80
				20
	113			85
				15

	103			95
				5
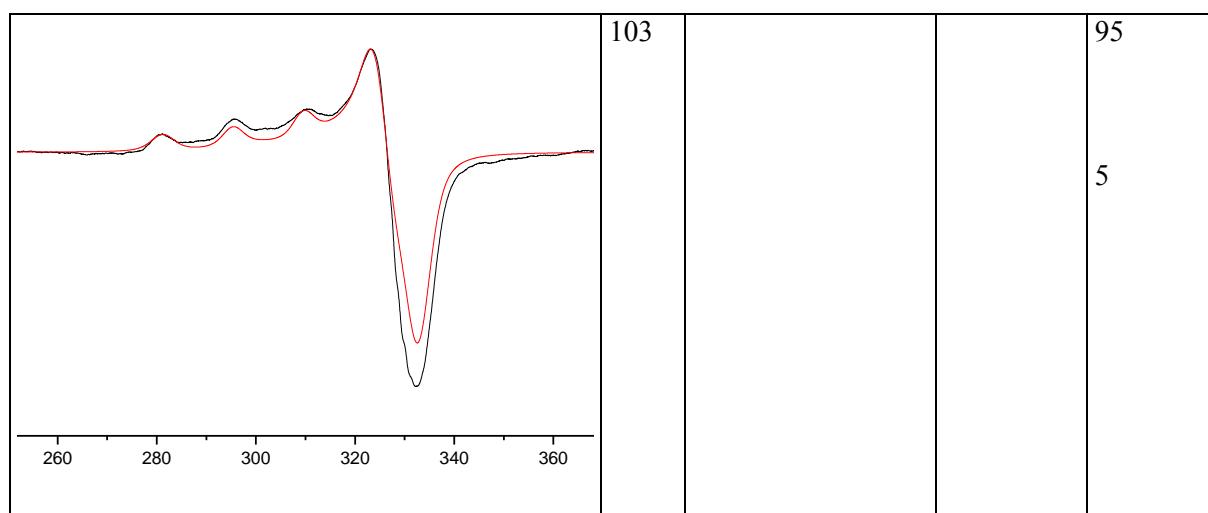
EPR spectrum of **1** in acetonitrile at 293 K and simulation in red (g_{iso} = 2.118, A_{iso}(Cu) = 48.5 G).
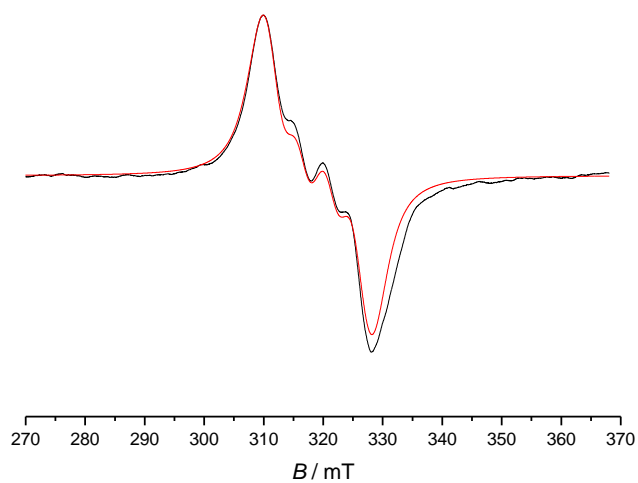
DSC curves of powdered **1** (4.376 mg); heating-cooling-heating cycle (1→2→3).

178
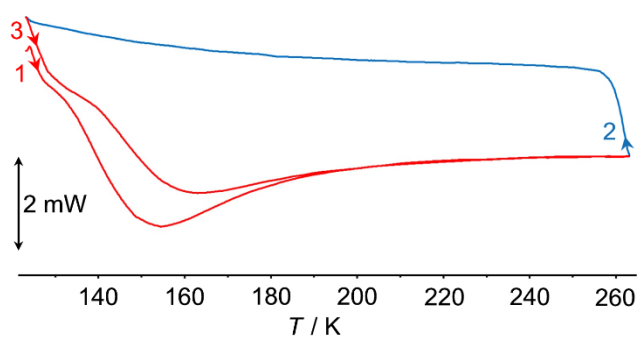
W-band CW EPR spectrum of **1** at 293 K ($g_x = 2.185 \approx g_y = 2.145$; $g_z = 2.056$; $A_x \approx A_y(^{63/65}Cu) = 90$ G).
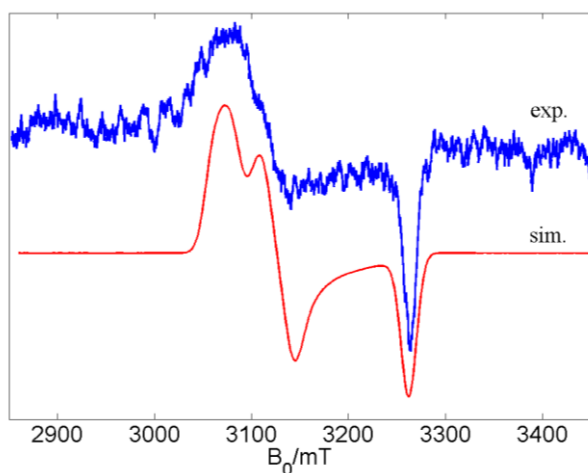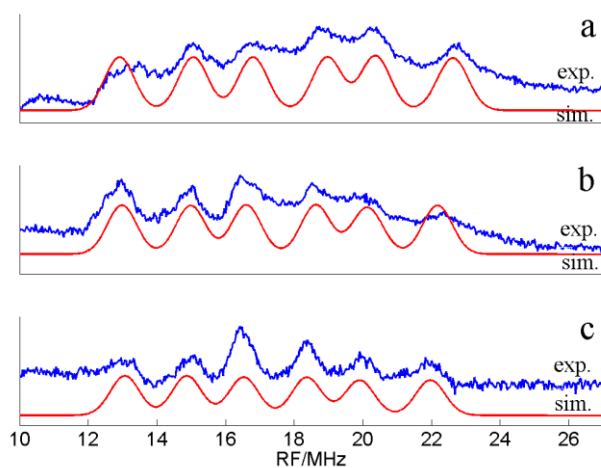

W-band CW EPR spectrum of **2** at 150 K ($g_x = 2.185 \approx g_y = 2.145$; $g_z = 2.049$; $A_x \approx A_y(^{63/65}Cu) = 90$ G).
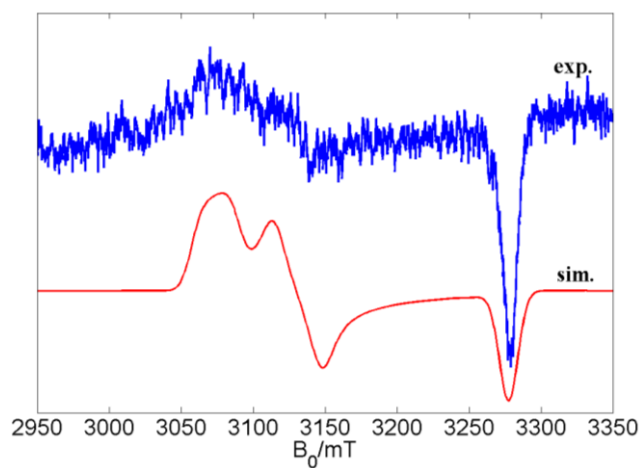
W-band CW EPR spectrum of **2** at 50 K ($g_x = 2.049$; $g_y = 2.068$; $g_z = 2.258$; $A_z(^{63/65}Cu) = 184$ G).
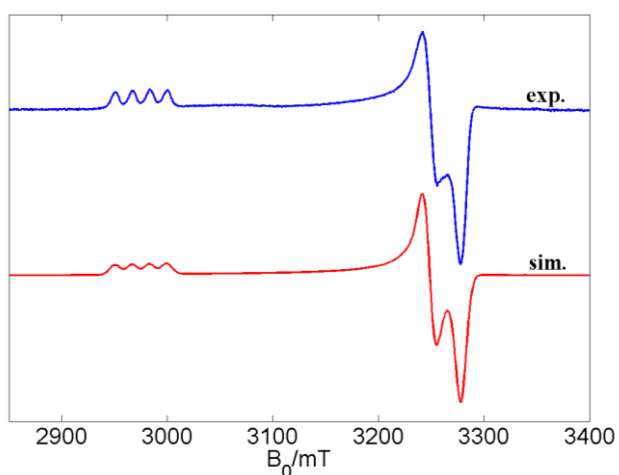
ESE detected EPR spectrum of **2** at 10 K taken with $\tau = 200$ ns. A – E indicate observer positions used for pulsed ENDOR and HYSCORE measurements.
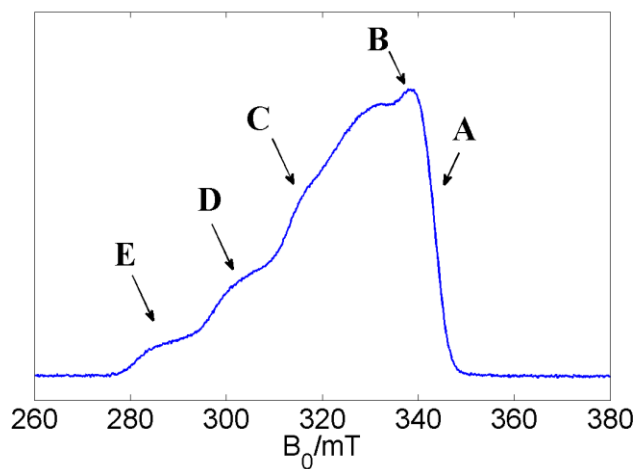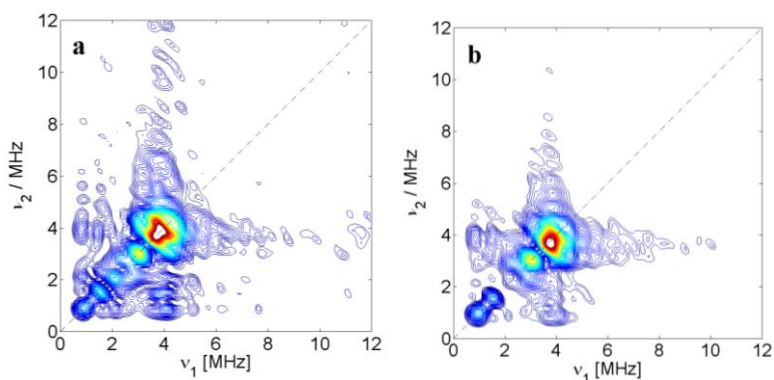

X-band Davies ENDOR spectra of **2** taken at 10 K at observer positions (a) B, (b) C, (c) E.
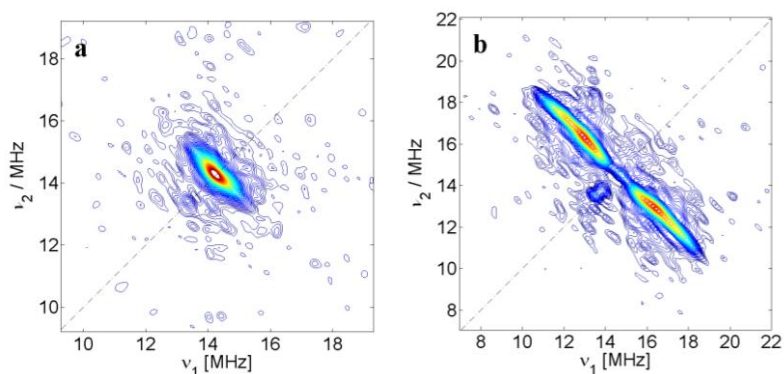

(simulations: $A(N1)_\perp \approx 43$ MHz, $A_{||} \approx 42$ MHz; $Q \approx (0.1\ 0.1\ -0.1)$; $A(N2)_\perp \approx 28$ MHz, $A_{||} \approx 28$ MHz; $A(N3)_\perp \approx 35.8$ MHz, $A_{||} \approx 35$ MHz).

^{14}N HYSCORE spectra of **2** taken at 10 K with $\tau = 200$ ns at observer positions B (a) and A (b).

^{1}H HYSCORE spectra of **2** taken at 10 K with $\tau = 200$ ns at observer positions A (a) and B (b).

^{1}H HYSCORE spectra of **1** taken at 10 K with $\tau = 200$ ns at observer positions A (a), B (b) and D (c).
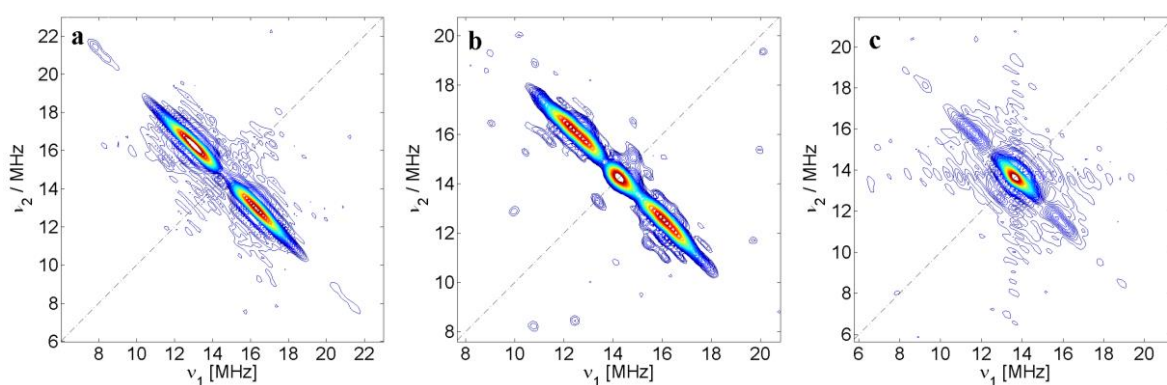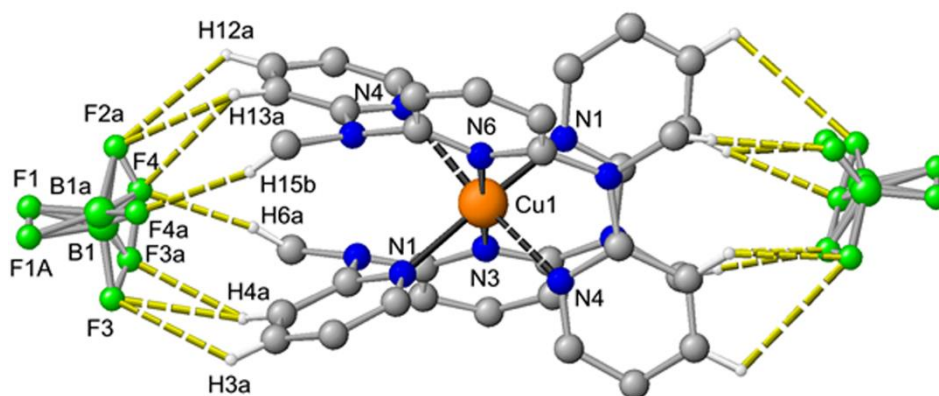

Illustration of the coordination of the tetrafluoroborate counter ions in the solid state to the dication.

For Cartesian Coordinates of DFT optimized [Cu(ddpd)$_2$]$^{2+}$ and [Cu(ddpd)$_2$]$^{2+}$, transition state, see electronic supporting information under http://pubs.acs.org/doi/suppl/10.1021/ic300929g.

6. ACKNOWLEDGMENTS

7. LIST OF PUBLICATIONS

Publications:

A. Wünsche von Leupoldt, C. Förster, T. J. Fiedler, N. H. Bings, K. Heinze*; *"Proton and Electron Transfer to a Polymer-Supported Nitrido Molybdenum(VI) Complex"*; *Eur. J. Inorg. Chem.* **2013**, *36*, 6079−6090; *"Proton and Electron Transfer to a Polymer-Supported Nitrido Mo^{VI} Complex"*; cover picture published in: *Eur. J. Inorg. Chem.* **2013**, *36*, 6061.

K. Mack, A. Wünsche von Leupoldt, C. Förster, M. Ezhevskaya, D. Hinderberger, K. W. Klinkhammer, K. Heinze*; *"Effect of Chelate Ring Expansion on Jahn−Teller Distortion and Jahn−Teller Dynamics in Copper(II) Complexes"*; *Inorg. Chem.* **2012**, *51*, 7851−7858.

Oral presentation:

A. Wünsche von Leupoldt; *"Immobilisierte Molybdän(VI)-Komplexe zur Ammoniaksynthese – Protonen- und Elektronentransfer"*; oral presentation at the 10. Koordinationschemie-Tagung, **march 03 2014**, Kaiserslautern.

Poster presentations:

K. Mack, A. Wünsche von Leupoldt, C. Förster, V. Ksenofontov, K. Heinze*; *"Spin crossover and dynamic Jahn-Teller effects in [M(ddpd)$_2$]$^{2+}$ complexes [M = Co, Cu]"*; poster presented at the 16. Vortragstagung der Wöhler-Vereinigung, **september 26-28 2012**, Göttingen, and at the GdCh-Wissenschaftsforum, Chemie – Elemente unseres Lebens, **september 01-04 2013**, Darmstadt.

Further publications:

J. Melomedov, A. Wünsche von Leupoldt, M. Meister, F. Laquai, K. Heinze*; *"Porphyrin amino acids – amide coupling, redox and photophysical properties of bis(porphyrin) amides"*; *Dalton. Trans.* **2013**, *42*, 9727−9739.

J. Dietrich, A. Wünsche von Leupoldt, M. Grabolle, U. Resch-Genger, K. Heinze*; *"Thermal and Photoinduced Electron Transfer in Directional Bis(terpyridine)ruthenium(II) – (Bipyridine)platinum(II) Complexes"*; *Eur. J. Inorg. Chem.* **2013**, *17*, 3009−3019.

Curriculum Vitae

Anica Wünsche von Leupoldt

Date of birth: 24.05.1985

Place of birth: Bad Dürkheim

Education

11/2009 – 09/2014	**Ph.D. thesis** at the Institute of Inorganic Chemistry and Analytical Chemistry in the group of ████████████████, Johannes Gutenberg University of Mainz *"Bio-inspired Polymer-Supported Nitrido Molybdenum(VI) Complexes for Ammonia Synthesis − Reactivity towards protons and electrons – EPR investigations on paramagnetic molybdenum(V) and copper(II) complexes"*
10/2004 – 12/2008	Studies of Biomedical Chemistry Johannes Gutenberg University of Mainz Special fields: Organic Chemistry Biochemistry Bioinorganic Chemistry Biophysics
01/2009 – 09/2009	**Diploma in Chemistry** (Academic degree: Diplom-Chemikerin) Diploma thesis in the group of ████████████████ Johannes Gutenberg University of Mainz *"Polymer-supported molybdenum complexes for ammonia synthesis"*
10/2006	**Intermediate Diploma in Chemistry** (Vordiplom) Johannes Gutenberg University of Mainz
07/1995 – 03/2004	**General Qualification for University Entrance** (Allgemeine Hochschulreife) Geschwister-Scholl-Gymnasium, Ludwigshafen a. Rh.

Teaching Activities

since 11/2009	Research associate Institute of Inorganic Chemistry and Analytical Chemistry Johannes Gutenberg University of Mainz